



Study of electrically conductive coatings produced by cold spray onto brittle and thermosensitive substrate

Patrizio Lomonaco

► To cite this version:

Patrizio Lomonaco. Study of electrically conductive coatings produced by cold spray onto brittle and thermosensitive substrate. Material chemistry. Université Paris sciences et lettres, 2022. English. NNT : 2022UPSLM065 . tel-04049986

HAL Id: tel-04049986

<https://pastel.hal.science/tel-04049986>

Submitted on 29 Mar 2023

HAL is a multi-disciplinary open access archive for the deposit and dissemination of scientific research documents, whether they are published or not. The documents may come from teaching and research institutions in France or abroad, or from public or private research centers.

L'archive ouverte pluridisciplinaire **HAL**, est destinée au dépôt et à la diffusion de documents scientifiques de niveau recherche, publiés ou non, émanant des établissements d'enseignement et de recherche français ou étrangers, des laboratoires publics ou privés.



THÈSE DE DOCTORAT
DE L'UNIVERSITÉ PSL

Préparée à Mines Paris-PSL

Study of electrically conductive coatings produced by cold spray onto brittle and thermosensitive substrate

Étude des revêtements électriquement conducteurs produits par projection à froid sur des substrats fragiles et thermosensibles

Soutenue par

Patrizio LOMONACO

Le 25 novembre 2022

Ecole doctorale n° 621

ISMME

Spécialité

Mécanique

Composition du jury :

| | |
|---------------------------------------------------------------------------------|--------------------------------------|
| Caroline, RICHARD Professeur des universités, Université de Tours | President <i>Rapporteur</i> |
| Bertrand JODOIN Full Professor, University of Ottawa | <i>Rapporteur</i> |
| Bernardo, FAVINI Tenured Associate Professor, Università Sapienza di Roma | <i>Examineur</i> |
| Yuji, ICHIKAWA Tenured Associate Professor, Tohoku University | <i>Examineur</i> |
| Jean-François, HOCHÉPIED Maître de recherche, MinesParis-PSL | <i>Directeur de thèse</i> |
| Michel, JEANDIN Maître de recherche, MinesParis-PSL | <i>Co-directeur de thèse</i> |
| Francesco, DELLORO Chargé de recherche, MinesParis-PSL | <i>Examineur</i> |
| Sara, BAGHERIFARD Associate Professor, Politecnico di Milano | <i>Examineur</i> |
| Chrystelle, BERNARD Assistant Professor, ElyTMax International Joint Unit | <i>Examineur</i> |

TABLE OF CONTENTS

| | |
|------------------------------------------------------------------------|-----|
| List of Tables | vii |
| List of Figures | x |
| Chapter 1: General introduction | 1 |
| Chapter 2: Selected bibliography | 9 |
| 2.1 Thermal spray and cold spray processes | 10 |
| 2.2 Cold spray onto polymer and polymer-based composite substrates . . | 13 |
| 2.3 CFD simulation of the cold spray process | 19 |
| 2.4 Particle impact and coating build-up modeling | 23 |
| Chapter 3: Materials and methods | 31 |
| 3.1 Feed-stock powders | 32 |
| 3.1.1 Metal powders | 32 |
| 3.1.2 Polymeric powders | 36 |
| 3.1.3 Mixture of metal and polymeric powder | 38 |
| 3.2 SUBSTRATES | 39 |
| 3.2.1 Short fiber reinforced PEEK | 39 |
| 3.2.2 POLYAMIDE 66 | 40 |

| | | |
|-------------------------------------------------------------------------------|-------------------------------------------------------|-----------|
| 3.2.3 | WOOD | 41 |
| 3.3 | Cold spray technology | 45 |
| 3.3.1 | High pressure cold spray | 45 |
| 3.3.2 | Low pressure cold spray | 47 |
| 3.4 | Samples production and characterization | 51 |
| 3.4.1 | Cold spray strategies | 51 |
| 3.4.2 | Sample preparation and metallography | 53 |
| 3.5 | Experimental measurements | 53 |
| 3.5.1 | PARTICLE IN-FLIGHT SPEED MEASUREMENTS | 53 |
| 3.5.2 | Electrical conductivity measurement methods | 56 |
| 3.5.3 | Pull-off test | 60 |
| Chapter 4: Cold spray on short carbon fiber reinforced PEEK substrates | | 63 |
| 4.1 | Introduction to the experimental work | 67 |
| 4.2 | Pure metal coatings | 68 |
| 4.2.1 | Aluminium coatings | 69 |
| 4.2.2 | Copper coatings | 77 |
| 4.3 | Metal-polymer composite coatings | 79 |
| 4.3.1 | Mixed PEEK - Aluminium coatings | 79 |
| 4.3.2 | Mixed PEKK - aluminum coatings | 92 |
| 4.4 | Conclusion | 95 |
| Chapter 5: CFD analysis tool applied to cold spray process | | 99 |
| 5.1 | Introduction | 102 |

| | | |
|------------------------------------------------------------------------------------------------------|-------------------------------------------------------------------|------------|
| 5.2 | Theoretical model | 103 |
| 5.2.1 | Choice of the framework | 103 |
| 5.2.2 | Problem formulation | 107 |
| 5.3 | Model implementation in OpenFOAM | 114 |
| 5.4 | Simulations of high and low pressure cold spray systems | 115 |
| 5.4.1 | High pressure cold spray | 116 |
| 5.4.2 | Low pressure cold spray | 123 |
| 5.5 | Discussion | 136 |
| 5.6 | Conclusion | 136 |
| Chapter 6: Finite element simulation of particle impacts onto a composite substrate | | 139 |
| 6.1 | Model foundations | 143 |
| 6.1.1 | CEL approach | 144 |
| 6.1.2 | Constitutive laws | 147 |
| 6.1.3 | Mesh and element types | 151 |
| 6.2 | Impact simulations | 152 |
| 6.2.1 | Single aluminum particle onto a pure PEEK substrate | 153 |
| 6.2.2 | Single particle onto SCRP substrate | 156 |
| 6.2.3 | Bi-particle impact | 162 |
| 6.2.4 | Multi-particle impact | 166 |
| 6.3 | Conclusion and perspectives | 170 |
| Chapter 7: Industrial applications | | 173 |

| | | |
|---------------------------------------------------------|---------------------------------------------------------------------------------------------------------------|------------|
| 7.1 | Introduction | 174 |
| 7.2 | Cold spray metallization of short carbon fibre reinforced PEEK composite for the aerospace industry | 174 |
| 7.3 | Metallization of wood for luxury and design applications | 176 |
| 7.3.1 | Introduction | 176 |
| 7.3.2 | Cold spray experiments | 177 |
| 7.3.3 | Modelling of particle impact onto the wood surface | 183 |
| 7.3.4 | Conclusions | 187 |
| 7.4 | Metallization of PA66 additively manufactured substrates | 188 |
| Chapter 8: Conclusion and perspectives | | 193 |
| 8.1 | Conclusion | 193 |
| 8.2 | Perspectives | 196 |
| references | | 214 |

LIST OF TABLES

| | | |
|-----|--------------------------------------------------------------------------------------------------------|----|
| 3.1 | Particle size distribution deciles of aluminum powder, measured by laser granulometry. | 33 |
| 3.2 | Particle size distribution deciles of spherical copper powder, measured by laser granulometry. | 34 |
| 3.3 | Particle size distribution deciles of irregular copper powder, measured by laser granulometry. | 34 |
| 3.4 | Particle size distribution deciles of dendritic copper powder, measured by laser granulometry. | 35 |
| 3.5 | Particle size distribution deciles of PEEK powder, measured by laser granulometry. | 37 |
| 3.6 | Geometrical parameters of the nozzle and the divergent inserts, in relation to Figure 3.19 | 50 |
| 4.1 | High pressure cold spray parameters | 69 |
| 4.2 | Summary table of the effect of cold spray parameters on the coating . | 70 |
| 4.3 | Measured average resistance values for the four specimens | 73 |
| 4.4 | Measured adhesion strength values for the three specimens | 74 |
| 4.5 | Low pressure cold spray parameters for the aluminium powder tests . | 75 |
| 4.6 | Low pressure cold spray parameters for the copper powder tests . . . | 77 |
| 4.7 | High pressure cold spray parameters for the aluminium-PEEK powder mixture tests | 80 |

| | | |
|------|--------------------------------------------------------------------------------------------------------------------------------------------------|-----|
| 4.8 | Electrical resistance measurements of HPCS PEEK-aluminum mixed powders. | 82 |
| 4.9 | Measured adhesion strength values for the five specimens | 83 |
| 4.10 | Summary table of the differences in the main tested parameters for the LPCS | 85 |
| 4.11 | Measured adhesion strength values of the LPCS 20%PEEK-aluminum mixed powders | 87 |
| 4.12 | Electrical resistance measurements of LPCS 20% PEEK-aluminum mixed powders. | 87 |
| 4.13 | Measured adhesion strength values of the LPCS 10%PEEK-aluminum mixed powders | 89 |
| 4.14 | Electrical resistance measurements of LPCS 10% PEEK-aluminum mixed powders. | 89 |
| 4.15 | Measured adhesion strength values of the LPCS 5%PEEK-aluminum mixed powders | 90 |
| 4.16 | Electrical resistance measurements of LPCS 5% PEEK-aluminum mixed powders. | 91 |
| 4.17 | Adhesion test results for LPCS of PEKK-Al mixed feed-stock powder. | 93 |
| 4.18 | Adhesion test results for for LPCS multilayered sample, made of a PEKK-Al bond coating and a pure Al top layer. | 95 |
| 4.19 | Resistivity measurement by the Van der Pauw method for LPCS multilayered sample, made of a PEKK-Al bond coating and a pure Al top layer. | 95 |
| 5.1 | Flow types depending on the volume fraction of the solid phase. | 104 |
| 5.2 | Meshsize of different parts for the HPCS case | 117 |
| 5.3 | Gas phase boundary conditions for the HPCS model | 118 |
| 5.4 | Particle phase boundary conditions for the HPCS model | 118 |
| 5.5 | Inlet cold spray parameters for HPCS. | 119 |

| | | |
|------|----------------------------------------------------------------------------------------------------------------------|-----|
| 5.6 | Meshsize of different parts for the LPCS case | 125 |
| 5.7 | Gas phase boundary conditions for the HPCS model | 125 |
| 5.8 | Particle phase boundary conditions for the HPCS model | 125 |
| 5.9 | Physical parameters of the solid phase. | 126 |
| 5.10 | LPCS parameters for the experimental measurement of particle velocities. | 134 |
| 6.1 | Unit system for Abaqus simulations. | 147 |
| 6.2 | Material dependent parameters for aluminum and PEEK. | 150 |
| 6.3 | Material dependent parameters for the carbon fibers. | 151 |
| 6.4 | Initial conditions for impact simulations of an aluminum particle onto a pure PEEK substrate. | 154 |
| 6.5 | Initial conditions for the aluminum particle impacting onto the com- posite substrate. | 157 |
| 6.6 | Initial conditions for the simulations with a thicker top PEEK layer. . | 159 |
| 6.7 | Initial conditions for impact simulations of a PEEK particle onto a SCRP substrate. | 160 |
| 6.8 | Initial conditions for the simulation of bi-particle impacts, with a PEEK particle below an aluminum one. | 162 |
| 7.1 | HPCS parameters with a wooden substrate. | 178 |
| 7.2 | LPCS parameters with a wooden substrate. | 178 |

LIST OF FIGURES

| | | |
|------|------------------------------------------------------------------------------------------------------------|----|
| 2.1 | Schematic views of high pressure (on the top) and low pressure (on the bottom) cold spray systems. | 12 |
| 2.2 | Usage of various materials in the Boeing 787 Dreamliner from [9, 10]. | 14 |
| 2.3 | Composite case of Vega launcher made by filament winding process [credits avio.com]. | 14 |
| 3.1 | MEB image of the aluminum powder 20-50 UPS by Toyal Europe. . . | 33 |
| 3.2 | SEM image of the spherical copper powder. | 34 |
| 3.3 | SEM image of the irregular copper powder. | 34 |
| 3.4 | SEM image of the dendritic copper powder. | 35 |
| 3.5 | PEEK repeating unit. | 36 |
| 3.6 | PEKK repeating unit. | 36 |
| 3.7 | SEM image of the Vicote 702 PEEK powder. | 37 |
| 3.8 | SEM image of the KEPSTAN 8002PL PEKK powder. | 38 |
| 3.9 | SEM image of the KEPSTAN 6002PL PEKK powder. | 38 |
| 3.10 | SEM image of an aluminum - PEEK702 powder mixture. | 39 |
| 3.11 | Photographic image of a VICTREX® PEEK™ 90HMF40 plate, as received. | 40 |
| 3.12 | Photographic image showing one of the PA66 3D printed specimens. . | 41 |
| 3.13 | The three main sections of wood, after [94]. | 42 |

| | | |
|------|-------------------------------------------------------------------------------------------------------------------------------------------------------------------------------------------------------------------------------------------------------|----|
| 3.14 | Optical microscope image of the walnut transverse surface showing the different features of hardwood | 43 |
| 3.15 | Optical microscope image of the walnut transverse surface showing the different features of hardwood | 44 |
| 3.16 | The cold spray system CGT Kinetics 3000. (a) control unit, (b) powder feeder, (c) gas heater, (d) gun. | 46 |
| 3.17 | Characteristics of the nozzles used. (a): general sketch of the nozzles; (b) photographic images of the 24TC (on the top) and of the 33PBI (on the bottom); (c) geometrical parameters of the two nozzles. After Pierre-Emmanuel Leger, [95]. | 47 |
| 3.18 | Low pressure Cold Spray equipment Dycomet 523. | 48 |
| 3.19 | Schematic of the Dycomet 523 nozzle. | 49 |
| 3.20 | Photographic image of the three Dycomet 523 diverging inserts. From the left to right: rectangular section stainless steel, circular section stainless steel and circular section ceramic. | 49 |
| 3.21 | Cutting scheme of plates. | 51 |
| 3.22 | Schematic view of spraying strategies: on the left, the track test and, on the right, the surfacing test. | 52 |
| 3.23 | Photographic image of the disk sample holder. | 52 |
| 3.24 | Schematic of the measuring principle of the DPV2000 system. | 54 |
| 3.25 | Photographic image of the high speed shadowgraphy system installed in the cold spray booth. | 56 |
| 3.26 | Schematic view of the four-point method to measure the electrical resistance of a coating. | 57 |
| 3.27 | On the left, schematic view of the Van der Pauw method. On the right, photographic image of an aluminum coating with cloverleaf shape, cold sprayed onto a PEEK-based composite disk of 22 mm radius. | 58 |
| 3.28 | Setup for the measurement of electrical resistance by the Van der Pauw method. | 59 |

| | | |
|------|----------------------------------------------------------------------------------------------------------------------------------------------------------------------------|----|
| 3.29 | On the left, schematic view of glued stud specimen and, on the right, photographic image of a pull-off specimen. | 60 |
| 3.30 | Schematic view illustrating the different types of fracture resulting from coating adhesion tests, after [97]. | 61 |
| 4.1 | Photographic pictures of pure aluminum coatings onto PEEK, representative of the spraying conditions listed in Table 4.1 | 70 |
| 4.2 | SEM and optical microscopy cross sectional observations of pure aluminum coatings. | 72 |
| 4.3 | Photographic images of the fracture surfaces of pure aluminum coatings. | 74 |
| 4.4 | Optical microscopy cross sections of aluminum LPCS samples, for the three different temperatures. | 76 |
| 4.5 | Optical microscopy cross sections of the copper sprayed samples for the three different temperatures. | 78 |
| 4.6 | Top view of cold spray track of aluminium-PEEK. | 81 |
| 4.7 | Optical images of cross section | 81 |
| 4.8 | Photographic images of the fracture surfaces of Al-10%PEEK HPCS coatings. | 83 |
| 4.9 | SEM cross sectional image of the best PEEK 20 %vol - Aluminum coatings. | 86 |
| 4.10 | SEM cross sectional images of PEEK 10% - aluminum coatings for three different temperatures. From top to bottom: 450°C, 500°C and 550°C. | 88 |
| 4.11 | SEM cross sectional images of PEEK 5%-aluminum coatings for three different temperatures. From top to bottom: 450°C, 500°C and 550°C. | 90 |
| 4.12 | Bar chart of conductivity and adhesion strength values for different PEEK contents into the feed-stock powder mixture and spraying temperatures. | 91 |
| 4.13 | SEM cross sectional images of multilayered coating, consisting of a composite adhesion layer made of PEKK and aluminum (1) and in a pure aluminum top coating (2). | 94 |

| | | |
|------|---------------------------------------------------------------------------------------------------------------------------------------------------------------------------|-----|
| 5.1 | Summary of model approaches for gas-solids flows from [104] | 106 |
| 5.2 | Gas flow in a nozzle (left), heating and acceleration of a particle in a gas flow (right). | 106 |
| 5.3 | Simulation domain for HPCS. | 117 |
| 5.4 | Mesh of the simulation domain for HPCS. Labels C, F and FF referred to different mesh size, respectively coarse, fine, finest. Values are reported in Table 5.2 | 117 |
| 5.5 | Axy-symmetrical gas velocity profile | 120 |
| 5.6 | Axy-symmetrical gas temperature profile | 120 |
| 5.7 | Close up of gas temperature profile on the particle injection point . . | 121 |
| 5.8 | Gas velocity along the nozzle axis for the four different setups. | 121 |
| 5.9 | Gas temperature along the nozzle axis for the four different setups. . | 122 |
| 5.10 | Simulation domain for LPCS. | 124 |
| 5.11 | Mesh of LPCS model | 124 |
| 5.12 | Mach number field for an inlet temperature of 500 °C. | 127 |
| 5.13 | Gas velocity field [m/s] for an inlet temperature of 500 °C. | 127 |
| 5.14 | Gas temperature field [K] for an inlet temperature of 500 °C. | 128 |
| 5.15 | Velocity field on the axis for three inlet temperatures. | 129 |
| 5.16 | Temperature field on the axis for three inlet temperatures. | 129 |
| 5.17 | Change in gas velocity field due to particle injection for an inlet temperature of 500 °C. | 130 |
| 5.18 | Change in gas temperature field due to particle injection for an inlet temperature of 500 °C. | 130 |
| 5.19 | Particle velocity for three different inlet temperatures. | 131 |
| 5.20 | Particle temperature for three different inlet temperatures. | 131 |

| | | |
|------|--------------------------------------------------------------------------------------------------------------------------------------------------------------------------------------------------------------------------------------------------------------------------------------------------------------------------------|-----|
| 5.21 | Particle velocity evolution along the symmetry axis for aluminum and PEEK. | 133 |
| 5.22 | Particle temperature evolution along the symmetry axis for aluminum and PEEK. | 133 |
| 5.23 | Particle velocity experimental measures. | 135 |
| 5.24 | Simulated LPCS particle velocity, with a stagnation pressure of 0.6 MPa, a stagnation temperature of 500 °C, at 8 mm from the nozzle exit. | 135 |
| 6.1 | Schematic view of Volume Fraction Tool DS Simulia, after [59]. | 145 |
| 6.2 | Modified EVF field in cross sectional view for the impact simulation of an aluminum particle onto a pure PEEK substrate. Last frame of the simulation ($3 \cdot 10^{-7}$ s). From the left to the right, HPCS, LPCS with substrate initial temperature at 300 K and LPCS with substrate initial temperature at 450 K. | 154 |
| 6.3 | Temperature field in cross sectional view for the impact simulation of an aluminum particle onto a pure PEEK substrate. Last frame of the simulation ($2 \cdot 10^{-7}$ s). From the left to the right, HPCS, LPCS with substrate initial temperature at 300 K and LPCS with substrate initial temperature at 450 K. | 156 |
| 6.4 | Modified EVF field in cross sectional view for the impact simulation of an aluminum particle onto a SCRP substrate. Last frame of the simulation ($2 \cdot 10^{-7}$ s). From the left to the right, HPCS, LPCS with substrate initial temperature at 300 K and LPCS with substrate initial temperature at 450 K. | 157 |
| 6.5 | Temperature field [K] in cross sectional view for the impact simulation of an aluminum particle onto a SCRP substrate. Last frame of the simulation ($2 \cdot 10^{-7}$ s). From the left to the right, HPCS, LPCS with substrate initial temperature at 300 K and LPCS with substrate initial temperature at 450 K. | 158 |
| 6.6 | Max stress (absolute value) [MPa] field of fibers in cross sectional view for an aluminum particle impact onto a SCRP substrate. From the left to the right, HPCS, LPCS with substrate initial temperature at 300 K and LPCS with substrate initial temperature at 450 K. | 159 |

| | | |
|------|-----------------------------------------------------------------------------------------------------------------------------------------------------------------------------------------------------------------------------------------------------------------------------------------------------------------------|-----|
| 6.7 | Modified EVF field in cross sectional view for the impact simulation of an aluminum particle onto a SCRP substrate with increased PEEK layer. Last frame of the simulation ($2 \cdot 10^{-7}$ s). On the left, HPCS. On the right, LPCS. | 160 |
| 6.8 | Modified EVF field in cross sectional view for the impact simulation of an PEEK particle onto a SCRP substrate. Last frame of the simulation ($2 \cdot 10^{-7}$ s). On the left, HPCS. On the center and on the right, LPCS. | 161 |
| 6.9 | Temperature field [K] in cross sectional view for the impact simulation of an PEEK particle onto a SCRP substrate. Last frame of the simulation ($2 \cdot 10^{-7}$ s). On the left, HPCS. On the center and on the right, LPCS. | 162 |
| 6.10 | Modified EVF field in cross sectional view for the impact simulation of two particles onto a SCRP substrate. The lower particle is PEEK, the upper aluminum. Last frame of the simulation ($2 \cdot 10^{-7}$ s). From the left to the right, HPCS, LPCS lower temperature and LPCS higher temperature. | 163 |
| 6.11 | Temperature field [K] in cross sectional view for the impact simulation of two particles onto a SCRP substrate. The lower particle is PEEK, the upper aluminum. Last frame of the simulation ($2 \cdot 10^{-7}$ s). From the left to the right, HPCS, LPCS lower temperature and LPCS higher temperature. | 164 |
| 6.12 | Max stress (absolute value) [MPa] field of fibers in cross sectional view for two particles onto a SCRP substrate. The lower particle is PEEK, the upper aluminum. Last frame of the simulation ($2 \cdot 10^{-7}$ s). From the left to the right, HPCS, LPCS lower temperature and LPCS higher temperature. | 164 |
| 6.13 | Modified EVF field in cross sectional view for the impact simulation of two particles onto a SCRP substrate. The lower particle is aluminum, the upper PEEK. Last frame of the simulation ($2 \cdot 10^{-7}$ s). From the left to the right, HPCS, LPCS lower temperature and LPCS higher temperature. | 165 |
| 6.14 | Temperature field [K] in cross sectional view for the impact simulation of two particles onto a SCRP substrate. The lower particle is aluminum, the upper PEEK. Last frame of the simulation ($2 \cdot 10^{-7}$ s). From the left to the right, HPCS, LPCS lower temperature and LPCS higher temperature. | 165 |

| | | |
|------|--------------------------------------------------------------------------------------------------------------------------------------------------------------------------------------------------------------------------------------------------------------------------------------------------------------------------------------|-----|
| 6.15 | PEEK EVF field. Initial configuration of the multi-particle impact simulation. | 167 |
| 6.16 | PEEK EVF field. Final frame of the multi-particle impact simulation. Aluminum particles, as well as the PEEK matrix, appear in blue. Carbon fibers are in white. | 168 |
| 6.17 | Modified EVF field in double cross sectional view for the multi-particle impact simulation. | 169 |
| 7.1 | Top view of a wood sample cold sprayed with aluminum powder. . . . | 179 |
| 7.2 | HPCS tin coating onto wood sample. | 179 |
| 7.3 | LPCS of metals on wood. From the left to the right, tin (bond layer) and copper, tin, aluminum, zinc. | 180 |
| 7.4 | SEM cross section of LPCS tin bond coat onto the transverse surface of a sycamore sample. | 181 |
| 7.5 | LPCS of aluminum particles onto the transverse surface of a sycamore sample. | 182 |
| 7.6 | SEM cross section of LPCS tin bond coat onto the radial surface of a sycamore sample. | 182 |
| 7.7 | SEM cross section of a copper-zinc coating onto radial surface of sycamore specimen. | 183 |
| 7.8 | Mechanical behavior of the honeycomb structure of wood under a compressive load from the top, after [132]. The structure is shown in different subsequent states: undeformed (left), slightly deformed with small bending and buckling of cell walls (middle) and severely crushed, with self-contact of cell walls (right). | 184 |
| 7.9 | Unit cell geometries representing fibers and rays at the macro-scale (a) and meso-scale (b) | 185 |
| 7.10 | Particle (diameter $20\mu m$) impacting onto a single wood fiber at $500ms^{-1}$.186 | |
| 7.11 | Particle (diameter $20\mu m$) impacting onto an hexagonal array of wood fibers at $500ms^{-1}$ | 187 |
| 7.12 | Schematic view of a FFF machine, after [133]. | 188 |

| | | |
|------|-------------------------------------------------------------------------------------------------------------------------------------------------------------------------------------------------------|-----|
| 7.13 | Sample produced by FFF to test different surfaces features. | 190 |
| 7.14 | Optical microscope cross section of an aluminum sprayed PA66 samples. | 191 |
| 7.15 | Photographic images of the pull-off test. On the left, sample preparation with all the pins glued to the metallized surfaces. On the right, the adhesive failure of an aluminum-PEEK coating. | 192 |
| 7.16 | Adhesion strength results for 9 different specimens and spraying parameters. | 192 |

CHAPTER 1

GENERAL INTRODUCTION

The cold spray process (CS) is part of the bigger family of the thermal spray process. It was discovered in the 80's during a bi-phase wind tunnel test. In this process, particles are accelerated to supersonic speeds by a high pressure carrier gas expanding in a convergent-divergent nozzle. Particles remain in a solid state and their deformation at high-speed impact allows the formation of a coating by particle stacking. Very thick and adherent coating can be produced by this technology. Moreover, the particle solid state is a strong advantage when spraying complex alloys, avoiding segregation or changes in their composition. These features, together with the repairing usage and the additive manufacturing application, attracted more and more industrial companies and research centers. Being a cold process, the possibility to be used on thermo-sensitive materials, such as polymer and polymer based composite, has begun to be explored several years before. The idea to add metallic features, such as thermal and electrical conductivity, to lightweight materials arouse enthusiasm for testing the cold spray process on new materials. Aeronautical and space applications, where more and more composite materials are being used to replace heavier metals, can take advantage of the possibilities offered by the cold spray, thus avoiding painting or other expensive or complicated expedients to protect structures from electrical discharges, lightning strikes, and static currents. The operating mechanisms of metal-on-metal cold spray were largely studied during the last 20 years. Several phenomena were identified as responsible for the strong adhesion of cold sprayed materials, as compared to other thermal spray processes. In the case of metal-on-polymer cold spray instead, metallurgical bonding, adiabatic shear stresses and oxide layer breaking, to cite a few, are not involved anymore. Rather, particle mechanical anchoring,

substrate local melting and softening and fiber breaking are some of the phenomena that need to be kept into account. If much has been made to understand and improve cold spray on thermo-sensitive materials, other questions need to be answered. What is the effect of cold spray gas on a thermo-sensitive substrate? Are both the gas and the particle temperature key factors to produce a continuous coating? Should the velocity be lowered to avoid erosion and damage to the composite? Could the fibers play a role in stiffening the composite and avoiding particle penetration? How do polymers behave in the cold spray process, both as feedstock and substrate materials? The present work tries to bring some answers to these questions, starting from cold spray experiments and then, with the help of fluid dynamic and mechanical modeling, looking for various elementary mechanisms acting during polymer cold spray.

This thesis is divided into six chapters. The first one reports a state of the art of thermal spray and, in particular, of the cold spray process and its applications. It begins with a focus on the cold spray process characteristics in the case of classical metal substrates. Then, a literature overview of cold spray applied to thermo-sensitive and brittle substrates is presented. A review of computational fluid-dynamics modeling applied to the cold spray process follows. The chapter closes with a retrospection of the mechanics of particles impacting on metal and composite substrates.

The second chapter illustrates the experimental methods and techniques employed. First, the substrates and the powders used are presented in detail. The two cold spray equipment, high pressure and low pressure, are shown. Metallographic preparation, as well as characterization devices, are presented. Then, two different setups used for experimental particle velocity measurements are illustrated. Finally, the methods and the techniques used to characterize the mechanical and electric properties of the various coatings are described. The third chapter is dedicated to the experimental work on the metallization of a PEEK-based composite material.

Pure aluminum coatings are obtained by employing high and low pressure cold spray equipment. A parameter analysis to choose the best spraying parameters is presented. Mechanical and electrical properties are then assessed by, respectively, a pull-off adhesion test and the Van der Pauw method. Metal spraying experiments end with an attempt with copper powder. Then, another strategy is employed to improve coating quality. A PEEK-aluminium powder mixture in different percentages is sprayed, by high and low pressure equipment, and the electro-mechanical performance of the coated parts is evaluated. The chapter closes by reporting the tests performed with a different polymer in the feed-stock powder mixture, namely the PEKK.

The fourth chapter deals with CFD analysis of the cold spray process. Both the high and low pressure equipment are modeled since they present different geometries and operating parameters. If for the high pressure, an axisymmetric model seems the best choice, a full 3D geometry is necessary for the low pressure. Particle velocities and temperatures for the two different systems are then compared among them and with experimental measurements.

The fifth chapter concludes the numerical analysis, focusing on particle impact modeling. The hypotheses of the coupled Eulerian-lagrangian analysis are presented, as well as the constitutive laws. Different configurations were modeled. First, the behavior of a pure PEEK substrate is compared to the composite, adding fibers to the matrix. Single metal and polymer particles impact the two types of substrate, both in high and low pressure conditions. Then, the effect of the thickness of the polymer skin layer is addressed. Finally, multiple particle simulations illustrate the phenomena intervening when spraying powder mixtures.

The sixth chapter presents some industrial applications and some possibly new material assembly obtainable by cold spray. First, the application of a conductive coating onto an aeronautical part made of a PEEK-based composite is assessed. Then, the cold spray metallization is extended to another composite material: the wood.

The last part of the chapter is dedicated to the coating of 3D printed parts made of polyamide 66 by fused filament fabrication. These specimens allow to study the effect of the printing setup and of the complex geometries that can be obtained.

The manuscript closes with a general conclusion and some perspectives are illustrated.

Résumé en français

Le procédé de projection à froid (CS) fait partie de la grande famille des procédés de projection thermique. Il a été découvert dans les années 80 lors d'un essai biphasé en soufflerie. Dans ce procédé, les particules sont accélérées à des vitesses supersoniques par un gaz porteur à haute pression qui se dilate dans une buse convergente-divergente. Les particules restent à l'état solide et leur déformation à l'impact à grande vitesse permet la formation d'un revêtement par empilement de particules. Des revêtements très épais et adhérents peuvent être produits par cette technologie. De plus, l'état solide des particules est un avantage important lors de la projection d'alliages complexes, évitant la ségrégation ou la modification de leur composition. Ces caractéristiques, ainsi que l'utilisation de la réparation et l'application de la fabrication additive, ont attiré de plus en plus d'entreprises industrielles et de centres de recherche. Comme il s'agit d'un procédé à froid, la possibilité de l'utiliser sur des matériaux thermosensibles, tels que les polymères et les composites à base de polymères, a commencé à être explorée plusieurs années auparavant. L'idée d'ajouter des caractéristiques métalliques, telles que la conductivité thermique et électrique, à des matériaux légers suscite l'enthousiasme pour tester le procédé de projection à froid sur de nouveaux matériaux. Les applications aéronautiques et spatiales, où de plus en plus de matériaux composites sont utilisés pour remplacer des métaux plus lourds, peuvent profiter des possibilités offertes par la projection à froid, évitant ainsi la peinture ou d'autres expédients coûteux ou compliqués pour protéger les structures des

décharges électriques, des éclairs et des courants statiques. Les mécanismes de fonctionnement de la projection à froid métal sur métal ont été largement étudiés au cours des 20 dernières années. Plusieurs phénomènes ont été identifiés comme responsables de la forte adhérence des matériaux projetés à froid, par rapport aux autres procédés de projection thermique. Dans le cas de la projection à froid métal sur polymère, ce ne sont plus les liaisons métallurgiques, les contraintes de cisaillement adiabatiques et la rupture de la couche d'oxyde, pour n'en citer que quelques-uns, qui interviennent. En revanche, l'ancrage mécanique des particules, la fusion et le ramollissement locaux du substrat et la rupture des fibres sont quelques-uns des phénomènes dont il faut tenir compte. Si beaucoup a été fait pour comprendre et améliorer la projection à froid sur les matériaux thermosensibles, d'autres questions doivent être résolues. Quel est l'effet du gaz de projection à froid sur un substrat thermosensible ? La température du gaz et celle des particules sont-elles des facteurs clés pour produire un revêtement continu ? La vitesse doit-elle être réduite pour éviter l'érosion et la détérioration du composite ? Les fibres pourraient-elles jouer un rôle dans la rigidité du composite et éviter la pénétration des particules ? Comment les polymères se comportent-ils dans le procédé de projection à froid, à la fois comme matière première et comme substrat ? Le présent travail tente d'apporter des réponses à ces questions, en partant d'expériences de projection à froid puis, à l'aide de la dynamique des fluides et de la modélisation mécanique, en recherchant les différents mécanismes élémentaires agissant lors de la projection à froid de polymères.

Cette thèse est divisée en six chapitres. Le premier chapitre présente un état de l'art de la projection thermique et, en particulier, du procédé de projection à froid et de ses applications. Il commence par se concentrer sur les caractéristiques du procédé de projection à froid dans le cas de substrats métalliques classiques. Ensuite, un aperçu de la littérature sur la projection à froid appliquée aux substrats thermosensibles et fragiles est présenté. Une revue de la modélisation numérique de

la dynamique des fluides appliquée au processus de projection à froid s'ensuit. Le chapitre se termine par une revue sur la mécanique de l'impact des particules sur les substrats métalliques et composites.

Le deuxième chapitre illustre les méthodes et techniques expérimentales employées. Tout d'abord, les substrats et les poudres utilisés sont présentés en détail. Les deux équipements de projection à froid, haute pression et basse pression, sont montrés. La préparation métallographique, ainsi que les dispositifs de caractérisation, sont présentés. Ensuite, deux montages différents utilisés pour les mesures expérimentales de la vitesse des particules sont décrits. Enfin, les méthodes et les techniques utilisées pour caractériser les propriétés mécaniques et électriques des différents revêtements sont décrites.

Le troisième chapitre est consacré au travail expérimental sur la métallisation d'un matériau composite à base de PEEK. Les revêtements d'aluminium pur sont obtenus au moyen d'un équipement de projection à froid à haute et basse pression. Une analyse des paramètres permettant de choisir les meilleurs paramètres de projection est présentée. Les propriétés mécaniques et électriques sont ensuite évaluées, respectivement, par un test d'adhésion par arrachement et par la méthode de Van der Pauw. Les expériences de projection de métal se terminent par un essai avec de la poudre de cuivre. Ensuite, une autre stratégie est employée pour améliorer la qualité du revêtement. Un mélange de poudre de PEEK-aluminium en différents pourcentages est projeté, par des équipements à haute et basse pression, et les performances électromécaniques des pièces revêtues sont évaluées. Le chapitre se termine par un compte-rendu des essais réalisés avec un polymère différent dans le mélange de poudre d'alimentation, à savoir le PEKK.

Le quatrième chapitre traite de l'analyse CFD du processus de projection à froid. Les équipements haute et basse pression sont modélisés tous les deux, car ils présentent des géométries et des paramètres de fonctionnement différents. Si, pour la haute

pression, un modèle axisymétrique semble être le meilleur choix, une géométrie 3D complète est nécessaire pour la basse pression. Les vitesses et températures des particules pour les deux systèmes différents sont ensuite comparées entre elles et avec les mesures expérimentales.

Le cinquième chapitre conclut l'analyse numérique, en se concentrant sur la modélisation de l'impact des particules. Les hypothèses de l'analyse couplée eulérienne-lagrangienne sont présentées, ainsi que les lois constitutives. Différentes configurations ont été modélisées. Tout d'abord, le comportement d'un substrat PEEK pur est comparé à celui du composite, en ajoutant des fibres à la matrice. Des particules uniques de métal et de polymère impactent les deux types de substrat, à la fois dans des conditions de haute et de basse pression. Ensuite, l'effet de l'épaisseur de la couche de peau polymère est abordé. Enfin, des simulations de particules multiples illustrent les phénomènes intervenant lors de la projection de mélanges de poudres.

Le sixième chapitre présente certaines applications industrielles et certains assemblages de matériaux éventuellement nouveaux pouvant être obtenus par projection à froid. Tout d'abord, l'application d'un revêtement conducteur sur une pièce aéronautique en composite à base de PEEK est évaluée. Ensuite, la métallisation par projection à froid est étendue à un autre matériau composite : le bois. La dernière partie du chapitre est consacrée à l'enrobage de pièces imprimées en 3D en polyamide 66 par fabrication de filaments fusionnés. Ces spécimens permettent d'étudier l'effet de la configuration d'impression et des géométries complexes qui peuvent être obtenues.

Le manuscrit se termine par une conclusion générale et quelques perspectives sont ouvertes.

CHAPTER 2

SELECTED BIBLIOGRAPHY

Abstract

This chapter presents the state of the art of cold spray onto thermo-sensitive substrates. In addition, a brief review of fluid-dynamic and mechanical models applied to the cold spray process is provided. The bibliographic material is organized into four subsections. First, a general explanation of the cold spray process is reported, addressing the fundamental notions, the main parameters and how these affect coating creation and growth. The main applications are also presented. The second part focuses on the application of cold spray to thermo-sensitive materials. In particular, previous works on cold spray onto polymer and polymer-based substrates are reported and analyzed, as well as feed-stock materials typically used in these applications. A third part will concern the computational fluid-dynamic modeling tools and their application to the cold spray process, for both high and low pressure systems. The fourth part addresses the mechanical modeling of elementary events in the process, namely the impact of metal and polymer particles onto composite substrates.

Résumé en français

Ce chapitre présente l'état de l'art de la projection à froid sur des substrats thermosensibles. En outre, une brève revue des modèles mécaniques et de dynamique des fluides appliqués au processus de projection à froid est fournie. Le matériel bibliographique est organisé en quatre sous-sections. Tout d'abord, une explication générale du procédé de projection à froid est présentée, abordant les notions fondamentales, les principaux paramètres et la façon dont ils affectent la création et la

croissance du revêtement. Les principales applications sont également présentées. La deuxième partie se concentre sur l'application de la projection à froid aux matériaux thermosensibles. En particulier, les travaux antérieurs sur la projection à froid sur des substrats en polymère et à base de polymère sont rapportés et analysés, ainsi que les matériaux de base généralement utilisés dans ces applications. Une troisième partie concerne les outils de modélisation numérique de la dynamique des fluides et leur application au processus de projection à froid, pour les systèmes à haute et basse pression. La quatrième partie traite de la modélisation mécanique des événements élémentaires du procédé, à savoir l'impact des particules de métal et de polymère sur les substrats composites.

2.1 Thermal spray and cold spray processes

Thermal spray is a family of coating processes, in which melted or solid materials are sprayed onto a surface. Thermal spraying can provide thick coatings, over a large area at high deposition rates, as compared to other coating processes such as, for example, electroplating, physical and chemical vapor deposition. Achievable thicknesses range from 20 μm to several mm, depending on the process and feed-stock materials employed. Coating materials available for thermal spraying include pure metals, metallic alloys, ceramics, and plastics. They are fed in powder or wire form, heated to a molten or semi-molten state, and accelerated towards the substrate in the form of micrometer-sized particles. When using powder as a feedstock, different materials can be mixed and sprayed together, to directly obtain a composite coating. Cold gas dynamic spray, or simply cold spray (CS in the following), makes part of the thermal spraying family. The birth of cold spray took place in the 1980s, at the Institute of Theoretical and Applied Mechanics of the Siberian Branch of the Russian Academy of Sciences (ITA of RAS), situated in Novosibirsk (CCCP, at that time). This was an accidental discovery, during a series of experiments in which the

interaction of a two-phase supersonic flow, *i.e.* a gas charged with aluminum particles, with an immersed body was under study in a wind tunnel [1].

In CS, particles are accelerated in a “de Laval” nozzle towards a substrate by a heated high-pressure gas. Particles generally maintain their solid state because of short contact time with the hot gas, whose temperature drops during the expansion in the nozzle. Particles undergo ballistic impingement on the substrate at speeds ranging between 300 and 1200 ms^{-1} . When impact velocity exceeds a threshold value, which is called “critical velocity”, particles adhere to the surface. This velocity depends on many parameters as, for example, the powder/substrate material couple, the impact temperature, and the surface state of the substrate. Coating deposition is generally accomplished at the solid state, so it has characteristics that are unique when compared to other thermal spray techniques, as will be discussed later. The geometry of the nozzle, as well as the characteristics of feed-stock powders (e.g. density, oxidation, granulometry, particle morphology) and process parameters (e.g. stagnation pressure and temperature of the gas, spraying angle, stand-off distance) are fundamental to determine the impact temperature and velocity of sprayed particles. These are the physical parameters controlling the impact process and the coating build-up, affecting the final characteristics of deposited material, as its microstructure and, as a consequence, its physical and mechanical properties [2]. A way to study the relationship between process parameters, impact temperature, and velocity of sprayed particles is the numerical simulation of the gas flow and particle-gas interactions, as will be detailed later.

There are currently two main types of CS systems: high pressure cold spray (HPCS in the following) and low pressure cold spray (LPCS in the following). Figure 2.1 illustrates schematic views of the two systems. LPCS systems are typically much smaller, portable and are limited to 300–600 ms^{-1} particle velocities. They are employed for the deposition of ductile and easily deformable materials. They generally

utilize readily available compressed air or nitrogen as propellant gases. High pressure systems, instead, can spray harder materials thanks to the higher velocities that particles can reach, in the range of $800\text{--}1400\text{ ms}^{-1}$. Nitrogen and helium can be used as propellant gases for HPCS.

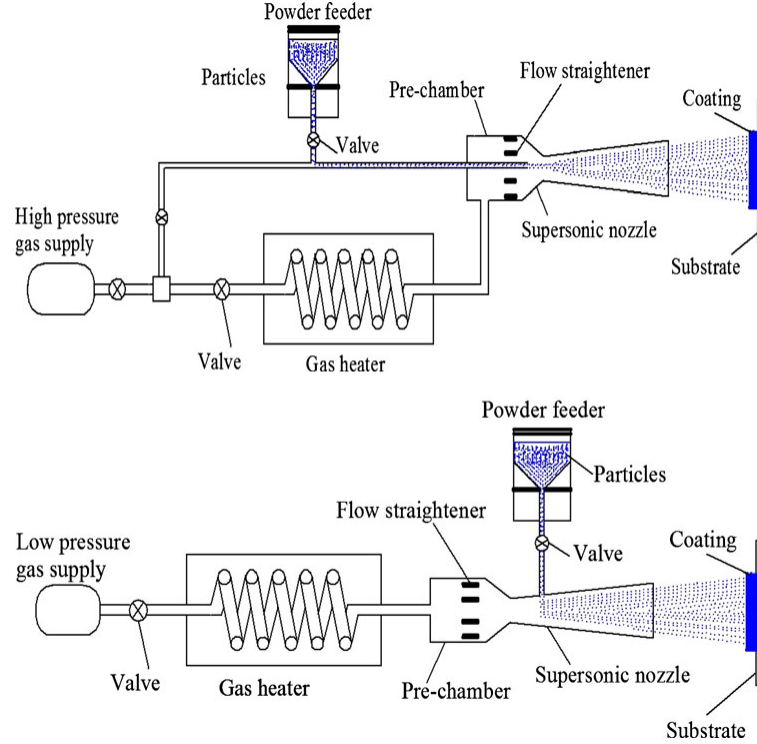


Figure 2.1: Schematic views of high pressure (on the top) and low pressure (on the bottom) cold spray systems.

While other thermal spray technologies are commonly used with a great variety of materials, cold spray is industrially assessed only for the assembly of metal onto metal. Nevertheless, CS offers several technological advantages over other processes, because it utilizes kinetic rather than thermal energy for material deposition. As a result, high temperature exposure, tensile residual stresses, oxidation, and undesired chemical reactions can be avoided. For this reason, CS could be then an optimal choice to create a material combination for a large variety of applications. Among these, to cite just a few, we can count: coating of nickel and iron based alloys for high temperature corrosion protection in thermal power plants; photo-catalyst coating using nickel,

aluminum, copper, and titanium oxides onto stainless steel and aluminum substrates; wear protection with stellite coatings; hydroxyapatite coatings to create bioactive and osteo-conductive materials; inconel, nickel, aluminum alloys to repair aircraft parts; copper for antimicrobial and conductivity purposes [3].

2.2 Cold spray onto polymer and polymer-based composite substrates

Ever lighter structures are the continuous goal of the aerospace industry. Composites were developed in the 1960s for their weight savings over aluminum parts, but only lately polymer-based composite materials replaced metals for most aircraft applications, because their manufacturing methods in the aviation industry have progressed from a purely manual fabrication to highly automated techniques using computer controlled machinery for laying up prepreg material, as reported in [4] and [5]. Large aircrafts are designed using composites in the fuselage and wing structures. Weight savings due to the use of composite materials in aerospace applications generally range from 15% to 25%, as stated in [6, 7, 8]. Two outstanding examples in, respectively, civil aviation and aerospace are the airbus A380, made of 50% by composite materials as shown in Figure 2.2, and the Vega launcher, illustrated in Figure 2.3, whose structure is made entirely by filament winding produced composites.

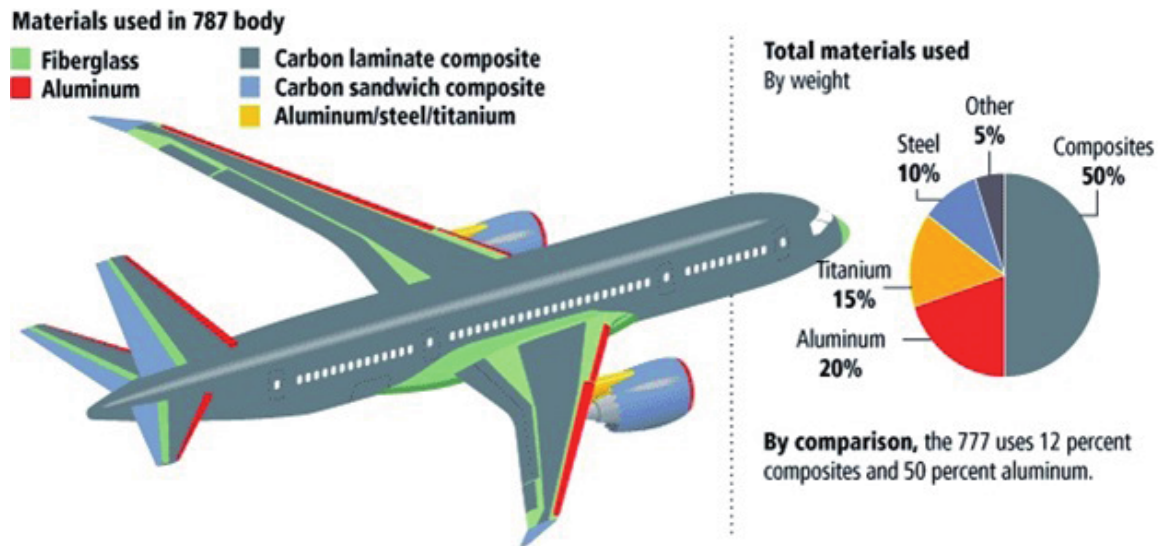


Figure 2.2: Usage of various materials in the Boeing 787 Dreamliner from [9, 10].

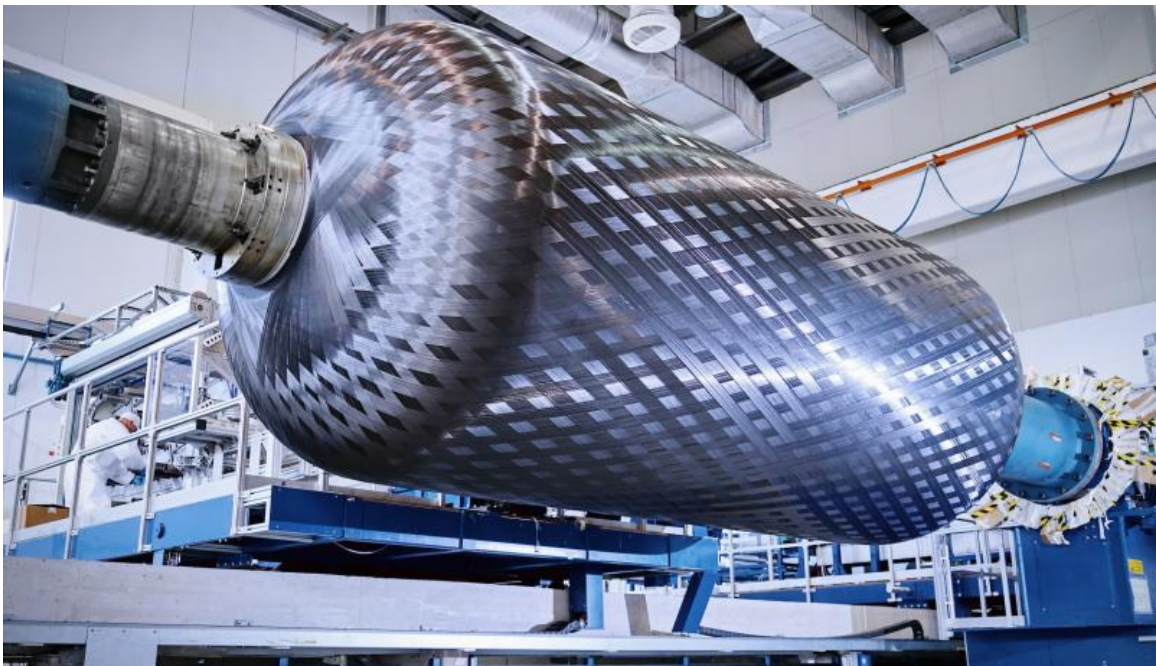


Figure 2.3: Composite case of Vega launcher made by filament winding process [credits avio.com].

Composite materials offer a strength-to-weight ratio superior to stainless steel and aluminum alloys, the drawback being the lack of electrical conductivity and reduced wear resistance. Static charges produced, for example, by air friction, electric discharge or lightning strike often cause serious damage to the composite matrix.

Nowadays, several techniques are employed to face these issues. Metallic paints, electrochemical depositions, metallic grids embedded among the plies of the composite, conductive fillers, etc. Nevertheless, these solutions are expensive or not completely adequate. The metallization of polymers and polymer-based composites has been the objective of many works in the past years. The protection of carbon fiber reinforced polymer (CFRP in the following) fuselages against lightning strike is obtained by riveting aluminum-based conductive plates to critical areas and of thin metallic meshes, placed on the outer surface of the CFRP structure [11]. The mesh can be made of aluminum, copper or bronze wires, and can be either co-woven with the carbon fibers in a prepreg fabric ply, or bonded separately as the outermost laminate layer, as explained in [12, 13, 14]. If the manufacture of these lightning protection systems (LSP) is difficult, their inspection and repair after a lightning episode is even more problematic. The damage could be in the LSP material, as well as in the underlying composites, resulting for example in the delamination between layers [15], burning of the epoxy and of the mesh/foil materials [16], etc. Repair is of course necessary before the next take-off. In addition, the risk of galvanic corrosion of the metal meshes, especially those made of aluminum, in contact with the carbon fibers is a concern, as exposed in [17]. Adding an isolation ply can solve the issue, at the price of increasing the weight.

Since composites and polymers are thermo-sensitive materials, the cold spray process has an interesting potential for their metallization, due to its considerably lower temperature of operation as compared to all other thermal spraying technologies. Very encouraging results have already been obtained for automotive and aeronautical applications. Nevertheless, to improve these results, one must take into account the superficial nature of the polymer substrate and its transformation during particle impacts. Several attempts were made onto thermosets and thermoplastic polymer, with or without fiber reinforcement as will be reported afterwards. The first study con-

cerning composite metallization by cold spray was published in 2006 [18]. The deposit was made of aluminum sprayed onto carbon fiber reinforced polyether-ether-ketone (PEEK), a thermoplastic polymer.

Cold spray metallization of polymers has been shown to be easier for ductile metals with relatively low melting temperatures, hardness, and mechanical strength. In a work of Lupoi [19], copper, aluminum, and tin have been sprayed onto several polymeric substrates (ABS, polyamide-6, polypropylene, polystyrene and a glass fiber composite) by HPCS. Tin was the only material that could be easily sprayed onto all these polymers. Copper was revealed to generate an excessive impact energy and strong erosion was experienced. On the other side, aluminum with its low specific weight could not attain the critical velocity to correctly build up a coating. In another study [20], copper, zinc, lead and aluminum were tested on polypropylene and 30% carbon fiber reinforced Poly-Ether-Ether-Ketone (PEEK450CA30), but only aluminum onto PEEK substrate was successfully cold sprayed. In [21], the substrate was a CFRP with an epoxy matrix. An LPCS was used to spray an aluminum coating to protect the surface from lightning strikes. Unfortunately, it was impossible to deposit aluminum powders directly onto the composite because of the severe erosion of the substrate. To avoid this phenomenon, due to a kinetic energy excess of the impacting solid particles, an aluminum interlayer was created by plasma spray before cold spraying. Thanks to this strategy, a thick and dense cold spray coating was created.

The nature of the substrate composite matrix was shown to be of uttermost importance. Thermoplastic and thermosetting produce different responses during cold spray of metallic powders. Cold spray of copper and tin was tested onto PVC (a thermoplastic) and epoxy (a thermoset), as reported in [22]. Two different copper powders, with dendritic and spherical morphologies, as well as two different process strategies, *i.e.* with or without interlayer, were adopted. Thick coatings were obtained with the two different copper powders onto PVC. This was almost impossible

to realize onto the epoxy, which experienced strong damage due to the brittleness of this substrate. A second test with spherical copper powder used as interlayer for the dendritic one worked again onto PVC, but still not onto the epoxy. The only way to achieve a copper coating on this brittle material was by using tin as an interlayer. In this case, a thick copper coating was finally obtained, using the dendritic powder. In 2018, H. Che [23] demonstrated the existence of a deposition window for copper onto PEEK (and other polymers) using both LPCS and HPCS. To avoid damage to composites reinforced with long fibers, in 2019 Gillet [24] added a PEEK layer on the substrate surface to protect them, allowing to build up thick copper coatings by LPCS.

A recent work [25] investigated the deposition of aluminum 7075 onto PEEK, PEI, and ABS substrates by HPCS. A recursive parameter analysis allowed to reach thicknesses higher than 1 mm and adhesion strengths in the order of 20 MPa.

An original work was found in [26]. The purpose was the metallization of aeronautical composites, to prevent damage due to lightning strikes. The substrate used in this work was a PEEK-based composite of aeronautical grade, reinforced by long carbon fibers. In order to achieve a conductive coating without damaging the composite, the idea was to spray a feed-stock powder made by mixing copper and PEEK particles. Three mixtures were prepared, all with 80% copper and 20% PEEK and with different kinds of copper particles. In the first mixture, an oxidized spherical copper powder was chosen, in the second the shape was the same, but the powder was not oxidized, while the third was an irregularly shaped copper powder. First, an optimization phase for cold spray parameters was developed to achieve maximum deposition efficiency. Microscopic observations revealed the heterogeneous morphology of the coating. In the case of the oxidized spherical copper powder, particles were revealed to be not deformed and embedded in a PEEK matrix. In the case of spherical and irregular non-oxidized copper powders, they resulted to be well deformed. Boundaries

between particles could not be distinguished anymore. The copper content measured by an image analysis tool resulted to be lower respect to the initial mixture ratio of about 15%. The difference was assumed to be due to particle rebounding, caused by their high velocity, the inability to deform and anchor. A 3D numerical simulation of the microstructure was then realized, allowing to numerically reproduce the observed microstructure with a good agreement. The last part of the article was focused on electrical resistance measurements, through the Van der Pauw method. This technique, reported in [27], compared with the classical four-probe method explained for example in [28], provides an average measurement of the conductivity of the coating, instead of its measurement in one direction only. The highest conductivity among all the samples was found for the coatings with non-oxidized spherical copper. Surprisingly, the conductivity was found to decrease when the thickness of the coating increased. Final remarks suggest that, in order to achieve better conductivity, cold spray parameters should not be optimized only by looking at deposition efficiency. Instead, a balance between the copper content and the deposition efficiency shall be found. The authors suggest the usage of a lower-pressure device that could achieve higher temperatures with lower pressures. Finally, the numerical tools developed demonstrated to be useful to define an optimal coating microstructure, maximizing the electrical conductivity. This is certainly more efficient and cheaper in comparison with the huge experimental work needed for the optimization.

The results presented above constitute precious teachings, to be considered as a solid basis for the present Ph.D. thesis. They are summarized in the following:

- mechanical and physical properties of the composite substrate must be kept into account to produce a conductive metallic coating by cold spray. Thermoplastic matrices are preferable because they can better withstand the impact and deform. Thermoset matrices are more brittle and can be cold sprayed without damage only using low melting point metals, such as tin, as feed-stock powders;

- composites with high volume fractions of fibers are more difficult to be sprayed because particles cannot anchor on the fibers, but only on the matrix;
- cold spray parameters must be optimized to allow the creation of a first layer onto the polymer and, then, to allow particles to deform and create metal-metal bondings. The optimized parameters for these two goals are probably different;
- the addition of a small percentage of polymer powder can increase coating adhesion, help the build-up process, and preserve fibers from damage.

2.3 CFD simulation of the cold spray process

It is largely admitted that in cold spray, to achieve material deposition, the mean particle velocity must exceed a certain material-dependent value, the so-called critical velocity. That is why a sufficient amount of kinetic energy must be provided to the particles to provoke their adhesion on the substrate and among them, as stated for example in [29]. Several possibilities can be explored to obtain the needed particle kinetic energy in the cold spray process. Inlet (stagnation) pressure and temperature of the carrier gas, as well as the geometry of the convergent-divergent nozzle, are the main factors impacting particle speed and temperature. In order to understand this interplay, a huge amount of experimental investigations would be necessary. In addition to the materials, the time and the financial cost associated with this experimental work, some phenomena taking place inside and outside the nozzle would not be captured. This explains the interest in developing analytical and numerical models for the supersonic bi-phase flow in a cold spray nozzle, a less expensive but powerful way to analyze the behavior of gas and particles. Dykhuizen and Smith [30] proposed an analysis of the effect of all the previously listed parameters. They used an isentropic, one-dimensional gas-flow model. Due to the limitations of this analytical approach, no information about particle velocity at the nozzle exit was provided.

Although, some precious information could be extracted:

- gas velocity in the nozzle depends on the total gas temperature and the nozzle geometry but not on the gas pressure;
- the drag coefficient of particles is linearly dependent on the stagnation pressure but independent of the total temperature.

The analytical model fails to include many other important phenomena such as viscosity, turbulence, boundary layer, nozzle length, outside supersonic jet and the compressed layer (i.e. the bow shock) on the substrate surface [31]. Alkhimov and colleagues [32] succeeded to consider the presence of boundary layers along the nozzle wall and a bow shock on the substrate surface. They started from the previous model and added new features. A similar approach was considered by Kosarev [33], who approached the problem with a two-dimensional velocity distribution. This approach allowed to include the outside supersonic jet and the bow shock. The drawback was the extreme mathematical difficulty in the resolution of the equations. The application of computational fluid dynamics (CFD) techniques began to be feasible more recently with the increase of computational power. In this way, a real gas flow field, as well as the particle features, can be simulated from the inlet to the impinging wall. Several different approaches to resolve particle motion are present in literature. The most used is the Lagrangian discrete phase modeling (DPM) to compute particle velocity and temperature. Different degrees of gas-particle dynamic coupling can be envisaged, formally, one-way, two-ways or four-ways approaches. In the case of one-way Lagrangian DPM, the equation for the gas phase alone is solved and used to compute the particle speed. In such a way, particles do not affect the gas dynamics. In the case of a two-way, instead, the effect of particles on the gas is considered, but particle-particle interactions are neglected. The four-ways approach, indeed the most complex of the three, considers all the interactions.

In [34] a two dimensional axisymmetric model was implemented in FLUENT CFD for solving the two-phase flow. The results were compared with experimental results coming from flow imaging system and particle velocimetry. A two-way coupled Lagrangian approach was used for particle trajectories and particle effect on the gas phase. The shocks and rarefaction waves modeled were found to be identical to the experimental ones. Increasing the powder mass flow rate, a double effect was observed. It reduces the gas and the particle velocity, but at the same time weakens the bow shock, thus facilitating particle deposition. Few works implemented an Eulerian DPM approach. In this modelling framework, both phases (gas and particles) are considered as a continuum. So, additional discrete equations must be added. Concerning one-way and two-ways Lagrangian DPM, the Eulerian approach keeps automatically into account particle-particle interactions. V.K. Champagne and colleagues [35] used this approach in a CFD computation to compare it to the 1D model and experimental measurements. A good agreement between CFD and 1D analytical model was found. Differences were due to the more accurate prediction of the flow field from the CFD, taking into account viscous effects, boundary layers and shocks. Also the comparison between the experimental measurements and the CFD results was satisfactory, even if CFD velocities were lower than the measured ones. This could be due to the approximation of considering a constant diameter for particles in the CFD simulation.

Numerical modeling of turbulence is also an important part of cold spray simulation. For example, in [36] a direct numerical simulation (DNS) modeling has been chosen. In the DNS approach, the exact Navier-Stokes equations are solved, which is very demanding from the point of view of computational resources. Nevertheless, it is the most powerful tool to simulate the reality of the cold spray process. In fact, in this work an explanation of the low deposition efficiency of the low pressure cold spray nozzle was assessed, based on the oscillations due to the strong turbulence of the flow.

The most used approach is the Reynold Average Navier Stokes (RANS) model. The computational cost compared to DNS is much lower and many different turbulence models can be adopted. Among them, the most used are the so-called k-epsilon, the shear stress transport SST, the normal velocity relaxation model ($\nu^2 - f$) and the large eddy simulation (LES). In [37] the different turbulence models were compared in the case of a supersonic jet impinging onto a substrate. The normal velocity relaxation turbulence model was found to be the most reliable, but its computational cost was the highest. The k-epsilon, instead, was the most efficient in terms of computational time, but with a high error on the variables, between 15% and 60%. The k-epsilon model was adopted in many works, for example in [38], where a multicomponent 3D approach was developed. The model was calibrated with the experimental results of [39] and validated with temperature parameters measured experimentally on a titanium substrate through thermocouples. For what concerns the drag force, which allows particle acceleration in the gas flow, several models are present in the literature. Different equations for the particle drag coefficient have been studied in several works related to the cold spray process, such as [40, 41, 42]. Each equation keeps into account different parameters, such as the particle shape and the influence of the Mach and Reynolds numbers. If the temperature within the metal particle has been considered constant by all the authors in the literature, the exchange coefficient between the two phases must be carefully considered. The Ranz-Marshall model [43], where three dimensionless quantities are present such as Nusselt, Prandtl and Reynolds numbers, is one of the most adopted. The majority of CFD works on the cold spray process, employs commercial software. A pretty new open-source software, called OpenFOAM, was adopted in [44] for the analysis of particle velocity and temperature in a cold spray nozzle. OpenFOAM [45] is a free and completely tunable and modifiable software. A large number of different solvers is included and many of them are suitable for modeling the cold spray process. Leitz and colleagues [44]

chose to use the OpenFOAM solver called “reactingParcelFoam”, using a PIMPLE algorithm for the solution of compressible NS equations with a Lagrangian tracing for the particles. Different drag force models, namely Schiller and Naumann [46], Ergun-Wen-Yu [47], a non-sphere drag [48] and the Plessis-Masliyah [49], were exploited and compared with experimental results. The Plessis-Masliyah was the best in terms of agreement with the experimental measurements obtained with an OSEIR particle velocity measurement device. For the heat transfer between gas and particles, the classical Ranz-Marshall model was the only one implemented in OpenFOAM for this solver, but others could be eventually coded and added. Finally, simulation results obtained for cold spraying of copper powder at different spray parameters showed a good agreement to analytical estimations for gas and particle temperature, as well as to experimental velocity measurements.

2.4 Particle impact and coating build-up modeling

The phenomena and mechanisms involved in particle impact during the cold spray process, due to the high speed, are not easy to observe experimentally. For this reason, accurate modeling of particle impact is mandatory to catch them, as well as a subsequent validation employing experimental data. Finite impact simulation is based on the resolution of Partial Differential Equations (PDE) with boundary conditions on a discretized domain. Each element of this domain can be a “finite element” if it is disjointed from the others and if it has a vertex (namely, a node) or a face in common. Depending on the problem to be solved, 1D, 2D or 3D models can be developed with this technique. In each element, the PDE is discretized in algebraic form and solved on each node. The solution is interpolated on the rest of the element by a specific function (*e.g.* linear, quadratic, cubic) which defines the element type [50]. This method is the most used in solving particle impact problems in cold spray conditions and many approaches have been adopted [51]. The first is

the Lagrangian framework, in which the movement of the continuum is specified as a function of material coordinates and time. The nodes of the Lagrangian mesh move together with the material and the interface between the two parts is defined and tracked precisely. Many works adopted this framework, as [52, 53, 54, 55, 56, 57, 58]. Due to large deformation or loss of materials occurring during high speed particle impacts, a pure Lagrangian description is not appropriate in many cases. Indeed, severe mesh distortions are detrimental to the convergence of the simulations. Alternatively, the Eulerian framework can be adopted. Here, the mesh is fixed and the material is tracked as it flows through it. Elements can thus be partially void and an additional variable is needed, namely the phase volume fraction. By definition, if a material fills an element completely, its volume fraction is one; if the material is absent from an element, its volume fraction is zero. All the intermediate cases are possible. Moreover, Eulerian elements may contain more than one material simultaneously, for example in the case of two particles made of different materials, both impacting onto a substrate. If the sum of all the material volume fractions in an element is less than one, the rest is considered as void volume fraction. Void material possesses no mass and no strength [59]. Coupling the Eulerian and the Lagrangian approaches results in the so-called Coupled Eulerian-Lagrangian (CEL) analysis. Eulerian materials can interact with Lagrangian elements through an Eulerian-Lagrangian contact [60, 61]. CEL enables to solve complex fluid-structure interaction problems, including large displacements and large strains, in a single numerical simulation. Another mixed approach is the Arbitrary Lagrangian Eulerian (ALE). In this method, specific re-meshing algorithms allow adjustments of nodal positions during the calculation, to alleviate the extreme element deformation in the case of large strains. In this case, the correspondence between material and nodes typical of the Lagrangian framework is lost, but, as in the Eulerian approach, the material position is tracked during the re-meshing steps. Historically, this method

was used for large deformation process simulation and then for the cold spray [62]. Certain parameters define the method efficacy such as the re-meshing frequency and the number of steps in each time increment [63]. Unfortunately, for very large deformations, these parameters could lead to a dramatic increase in the computational time or, in some cases, to the non-convergence of the simulation. A very relevant work was conducted by Xie in [64]. Here, comparisons between Lagrangian, Eulerian, ALE, and CEL for four combinations of particle/substrate materials (Cu/Cu, Al/Al, Cu/Al, and Al/Cu) were developed. The CEL method appeared to be the most accurate and robust in larger deformation zones, compared to pure Lagrangian and ALE approaches. The mesh was not affected by distortions, even at very high strains. The drawback was an increase in the computational resources needed.

In the works mentioned above, single particle impact models were useful in studying the effects of the impacting particle characteristics on the deformation behavior, such as velocity (magnitude and angle), material type, temperature, and morphology. However, these models are not capable of predicting the final structure and properties of cold sprayed coatings, as they do not include the interactions between large numbers of impacting particles. These often result in complex phenomena such as, for example, the creation of coating build-up defects. Finite element simulations involving several particles were thus proposed to address this issue. Such a numerical investigation was performed in 2D in [65], showing that interactions between adjacent particles can significantly affect coating formation. Two different configurations, involving three and 100 particles were implemented. The effects of particle positioning and variations of process parameters on the coating properties were studied. In more recent works, 3D simulations were carried on to assess coating porosity. Xu in [66] used a CEL model to simulate Ti-6Al-4V powder onto a Ti-6Al-4V substrate. With the help of a python script, 100 particles were generated in the Eulerian volume, based on a Rosin-Rammler particle size distribution. Velocity and temperature

were chosen for each particle. The Lagrangian part was the substrate. The accuracy of the porosity calculation was mesh size dependent and a trade-off between accuracy and computational cost had to be made. Some important conclusions could be assessed. The substrate temperature was found to be a negligible parameter in porosity creation. Instead, higher particle velocities and temperatures were beneficial for obtaining lower coating porosities. A multi-material multi-particle simulation was carried out by Terrone and colleagues [67]. Titanium-copper and titanium-aluminum feed-stock powder combinations were tested. Also in this case, a CEL model, a Rosin-Rammler distribution for particles in the Eulerian volume, and a Lagrangian substrate were chosen. Moreover, particles were randomly distributed in space. The goal of this paper was to simulate the titanium porous structure, obtained after removing one of the two components in the composite coating (copper or aluminum). A strong and interconnected porous coating was obtained with a 50%-50% Ti-Cu volume percentage mixture.

The constitutive material law is an essential point of all these mechanical models. The Johnson-Cook visco-plastic model is probably the most used. It is particularly effective in reproducing particle deformation morphologies in the case of metallic materials [68]. This model describes the yield-stress of the material as the product of three different functions, depending respectively on the deformation, the deformation rate, and the temperature. Alternatively, other models can be used. For example, in [69], six different visco-plastic models were compared among them and with a single deformed particle observation. The Johnson-Cook was not the best, but this comparison does not allow to choose a particular model over the others. Indeed, the common problem is that, independently of the model chosen, the material dependent parameters are fit from experimental data obtained, typically in Hopkinson pressure bar experiments, with deformation rates up to $10^4 s^{-1}$, much lower compared to the cold spray ones [70]. This generally results in a reduced predictivity of impact simulations,

leading in particular to an erroneous morphology of deformed particles. Durand *et al.* in [71] and [72] proposed a different experimental and numerical approach to fit JC parameters. First, the quasi-static mechanical behavior of particles was studied. Static JC parameters (A , B and n) were assessed by single particle microcompressions, 2D FEM analysis, and kriging meta-model. The behavior in the high strain rate regime was then studied utilizing the “LASHPOL” (Laser Shock Powder Launcher) system. Single particle impacts onto a specific substrate were accelerated by a laser impulse. The particle flight, recorded by a high speed imaging system, allowed computing the impact speed. The deformed particle (*i.e.* the splat), was then observed by different techniques. To compute the two remaining JC coefficients, C and m , FEM analysis was performed trying to match the experimental deformed particle shape. The work is still ongoing at the moment of writing this thesis. Instead, a new model was recently unveiled, involving the deformation speed of 10^9 s^{-1} [73]. In this work, the JC model was improved and updated. The plastic strain was composed of three different contributions. The first takes into account strain hardening, which can be determined through quasi-static tensile or compression experiments. The second implements a strain rate hardening, with the plastic strain dependence explored by considering the Tanimura-Mimura material model. The third part consists of the so-called ultra-high strain rate hardening and it has been explained by Regazzoni *et al.* [74] from the point of view of dislocation theory. Finally, the influence of temperature is considered by adding the thermal softening factor. This model was shown to accurately describe extreme deformation and grain refinement in CS.

Although the studies related to the impact of metal particles onto metal substrates are numerous, this is not the case of polymer-based substrates. Finite element simulation of the polymer behavior in cold spray conditions requires the use of an appropriate material law, calibrated using experimental high-speed deformations and temperature influence data. However, to understand the mechanisms involved in

the deformation of polymers in cold spray, it is first necessary to understand their mechanical behavior in relation to their chemical composition. Polymers are macromolecules formed by the chemical bonding of repeating units, called monomers. The number of monomers within the polymer molecule can vary greatly, as well as their order, relative orientations, and the presence of differing monomers within the same polymer molecules [75]. The possibility to rotate these units around the covalent bonds allows great flexibility of the chains [76]. Polymers always exhibit a viscoelastic behaviour, but the importance of each factor depends on the temperature and the stress rate. Plasticity in polymers can be different from the one of metals. It can involve micro-cracking, shear band, cavitation [77] and, for semi-crystalline polymers, also the deformation of crystallites through sliding systems. Polymers are therefore to be considered as visco-plastics materials too [78]. For structural calculations, two solutions are then possible: the construction of viscoelastic-viscoplastic models [79, 80] or the use of macroscopic models created for other materials [81].

Since the polymer under study in the present thesis is the PEEK, which is semi-crystalline, the rest of the discussion will be focused on this kind of material. The mechanical behavior of semi-crystalline polymers is well known under isothermal conditions. Nevertheless, few studies focused on thermomechanical modeling and these are limited only to test loadings where low strain rate values are reached [82, 83]. Moreover, there is a critical strain rate at which the system is expected to behave adiabatically, depending on thermal properties and loading conditions [84, 85]. In these conditions, the thermal softening driven by temperature rise associated with plastic dissipation is increased. Indeed, a full thermomechanical coupling should be adopted and taken into account by the constitutive model to obtain successful results in dynamic conditions, especially relevant at the high strain rates experienced in the cold spray process.

In [86] a constitutive model which takes into account thermal softening, strain rate

and pressure sensitivities, and temperature evolution is proposed. The formulation has been developed under the assumptions of large deformation within a thermo-mechanical framework. The constitutive model developed herein, therefore, allows for predicting the mechanical behavior of semi-crystalline polymers, not only under isothermal assumptions but also providing the evolution of temperature due to plastic dissipation. This is one of the key contributions of the present work since at high strain rates the change in temperature due to adiabatic heating can lead to important changes in the polymer behavior. The model has been applied to describe the behavior of a semi-crystalline PEEK, in a wide range of strain rates and testing temperatures. Its parameters have been identified from experimental data of uniaxial compression and tensile tests published by Rae. In order to analyze the predictive capacity under dynamic conditions, the model has been implemented in a FE code to study two different problems: low velocity impact test on PEEK thin plates and dynamic necking on PEEK slender bar. In another recent work [87], the authors adopted the same model to the cold spray of PEEK particles onto PEEK substrates. The already mentioned plasticity model proposed by Garcia-Gonzalez and colleagues [79] for PEEK is adopted. This model was coupled with the Taylor–Quinney equation [88] to include temperature rise due to plastic deformation. The Mie–Grüneisen equation of state was taken into account to simulate the volumetric response of PEEK in the shock loading regime [89, 90]. The obtained results indicated that the adhesion of PEEK particles on PEEK substrates occurs at a narrow critical velocity range, depending on the particle size. Because polymer behavior is strongly temperature-dependent, Bernard and colleagues in [91] investigated the in-flight behavior of an isolated polymeric particle. The effect on the thermal particle history inside the nozzle was studied. They discovered that the thermal gradient leads to a gradient of mechanical properties along the particles’ radius before the impact. The knowledge of the particle temperature map is then to be considered fundamental to better

understanding of the cold spray process, especially in the case of polymeric particle.

Despite the increasing number of papers on the topic in the last years, a lot of work is still needed to better understand the cold spray process. To conclude this bibliographic review, some general considerations are proposed:

- there is still a lack of knowledge of material behavior at cold spray strain rates, for both metals and polymers;
- drag and heat transfer model in CFD simulations must be improved before being able to accurately predict particle speeds and temperatures at their impact on the substrate;
- several question remains open concerning particle adhesion in cold spray. New approaches, such as molecular dynamics as in the Ph.D. thesis [92], are beginning to be considered and they could be useful to better understand the small scale phenomena related to adhesion.

CHAPTER 3

MATERIALS AND METHODS

Abstract

This chapter aims to present in detail the materials studied and the methods employed in this work. In particular, the feed-stock powders and the substrates to be coated are characterized. Powder and substrate characterization is crucial to understand the results that will be produced by the cold spray process. The nature, morphology and granulometry of powders and the nature, surface state and thermo-mechanical behavior of the substrate are studied. It is also important to discuss the features of the cold spray equipment used to produce the coatings. Indeed, high or low pressure, process parameters, and set-up of the tests have a big influence on the final characteristics of the coating-substrate assembly. Finally, the devices used for the analysis of in-flight particle velocity, as well as the methods to observe and characterize the coated samples are presented.

Résumé en français

L'objectif de ce chapitre est de présenter en détail les matériaux étudiés et les méthodes employées dans ce travail. En particulier, les poudres d'alimentation et le substrat à revêtir sont caractérisés. La caractérisation des poudres et du substrat est cruciale pour comprendre les résultats qui seront produits par le procédé de projection à froid. La nature, la morphologie et la granulométrie des poudres ainsi que la nature, l'état de surface et le comportement thermo-mécanique du substrat sont étudiés. Il est également important de discuter des caractéristiques de l'équipement de projection à froid utilisé pour produire les revêtements. En effet, la haute ou basse pression,

les paramètres du procédé et la mise en place des essais ont une grande influence sur les caractéristiques finales de l'ensemble revêtement-substrat. Enfin, les dispositifs utilisés pour l'analyse de la vitesse des particules en vol, ainsi que les méthodes d'observation et de caractérisation des échantillons revêtus sont présentés.

3.1 Feed-stock powders

Metal and polymeric powders were used in this study, separately and in mixtures. Aluminium and copper were sprayed, alone or in a mixture with polymers, to add conductivity to the PEEK substrates. Two different polymer powders, namely the PEEK and the PEKK, were tested in those mixtures, to improve adhesion and reduce damage of the substrates.

3.1.1 Metal powders

The cold spray process was originally designed for metal powders. In order to produce a conductive layer, copper and aluminum seem to be the best choices due to, respectively, the high electrical conductivity and the high conductivity over mass ratio. Moreover, the usage of these materials is well documented in many papers, as presented in chapter one. In particular, the bibliographic review showed that these are the most promising metals to create adhesive and conductive coating onto different polymers and composites. Commercial data and morphological characteristics of the metal powders used in the present thesis are presented below.

Aluminium

The aluminum powder used in this study was provided by the company Toyal Europe, under the commercial name of 20-50 UPS. The numbers indicate the approximate size range in micrometers and UPS stands for Ultra-high Purity Spherical. This powder had a purity of 99.996% and was produced by gas atomization. SEM observations

reported in Figure 3.1 show a quasi-spherical morphology with satellites around bigger particles. The particle size distribution was measured by a laser granulometer, which gives a volume fraction in function of particles diameter. The measurements performed resulted in accordance with the commercial specification, as shown in Table 3.1. Dv90, Dv50 and Dv10 parameters are, respectively, the 9th, 5th and 1st decile of the volumetric size distribution, *i.e.* Dv90 = 40 μm means that 90% of the powder volume is smaller than 40 μm .

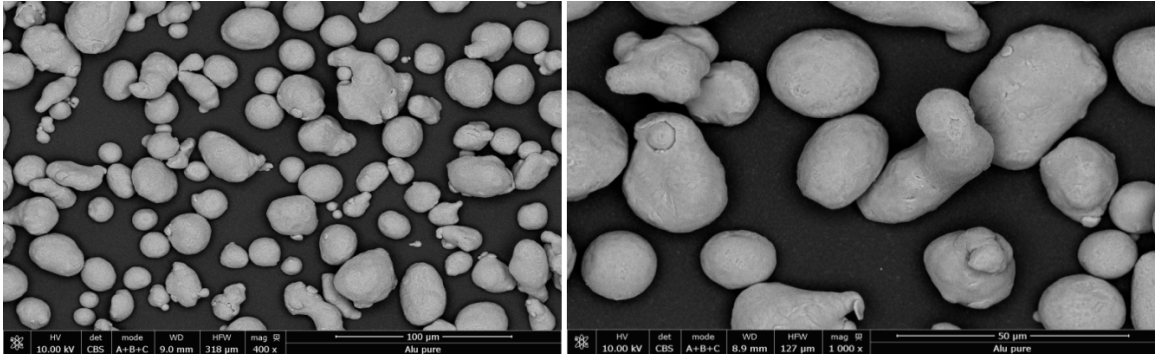


Figure 3.1: MEB image of the aluminum powder 20-50 UPS by Toyal Europe.

| Dv(%) | Value [μm] |
|-------|-------------------------|
| Dv10 | 18.8 |
| Dv50 | 29.3 |
| Dv90 | 44.8 |

Table 3.1: Particle size distribution deciles of aluminum powder, measured by laser granulometry.

Copper

Three copper powders of different morphologies were tested, all provided by Ronald Britton, with commercial references MPSCXX300P, MPICXX325P and MPCODE300P for, respectively, spherical, irregular and dendritic shape. SEM images of the three powders are shown in Figures 3.2, 3.3 and 3.4. As for the aluminum powder, Dv values are presented in Tables 3.2, 3.3 and 3.4.

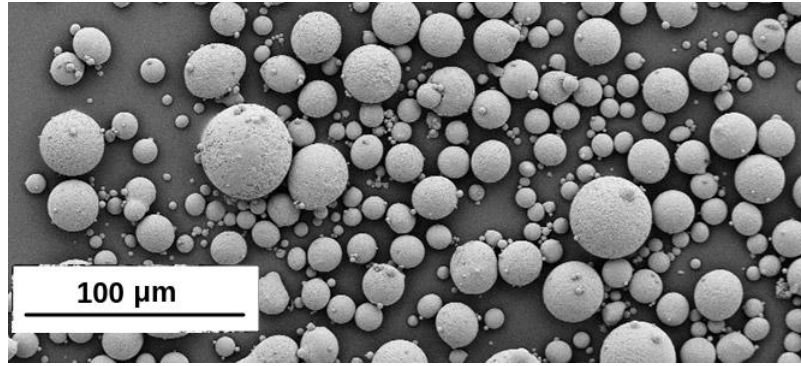


Figure 3.2: SEM image of the spherical copper powder.

| Dv(%) | Value [μm] |
|-------|-------------------------|
| Dv10 | 20.2 |
| Dv50 | 35.0 |
| Dv90 | 51.2 |

Table 3.2: Particle size distribution deciles of spherical copper powder, measured by laser granulometry.

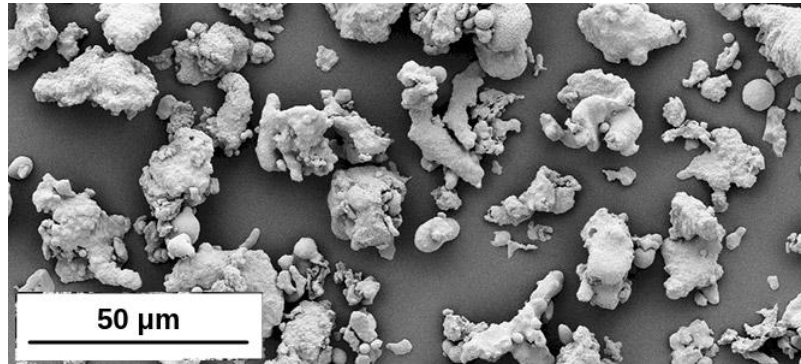


Figure 3.3: SEM image of the irregular copper powder.

| Dv(%) | Value [μm] |
|-------|-------------------------|
| Dv10 | 17.6 |
| Dv50 | 30.1 |
| Dv90 | 45.3 |

Table 3.3: Particle size distribution deciles of irregular copper powder, measured by laser granulometry.

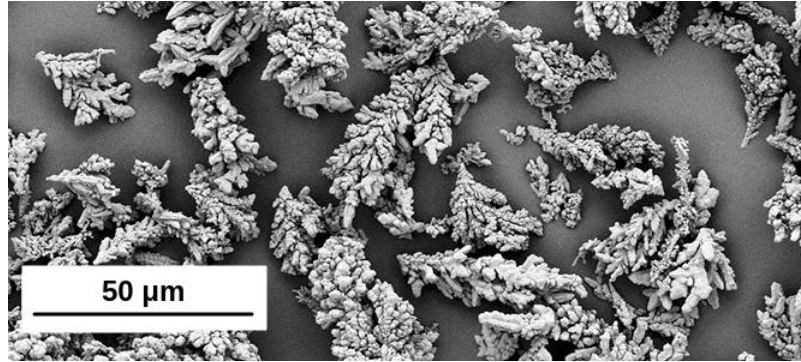


Figure 3.4: SEM image of the dendritic copper powder.

| Dv(%) | Value [μm] |
|-------|-------------------------|
| Dv10 | 28.1 |
| Dv50 | 41.9 |
| Dv90 | 53.3 |

Table 3.4: Particle size distribution deciles of dendritic copper powder, measured by laser granulometry.

3.1.2 Polymeric powders

The usage of polymers as feed-stock materials for the cold spray process is a relatively new field of research. Adhesion mechanisms for this class of materials are still not fully understood, but several studies have assessed the feasibility of the process. In this study, two different polymeric powders have been tested, both belonging to the same family of PEAK (polyaryletherketone). The first is the Poly-Ether-Ether-Ketone (PEEK), the same polymer of the substrate matrix. It is a thermoplastic, semi-crystalline polymer. Figure 3.5 illustrates the repeating unit of the PEEK. It owns very good mechanical and acid resistance properties. The maximum working temperature is about 220°C and the melting temperature reaches 343°C, one of the highest values among thermoplastic polymers. The second polymer is the more recent Poly-Ether-Ketone-Ketone (PEKK), recently developed by ARKEMA company in two different grades. Figure 3.6 illustrates the repeating unit of the PEEK.

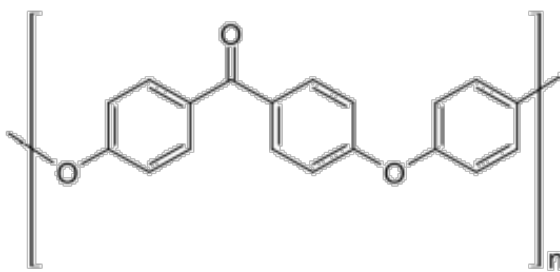


Figure 3.5: PEEK repeating unit.

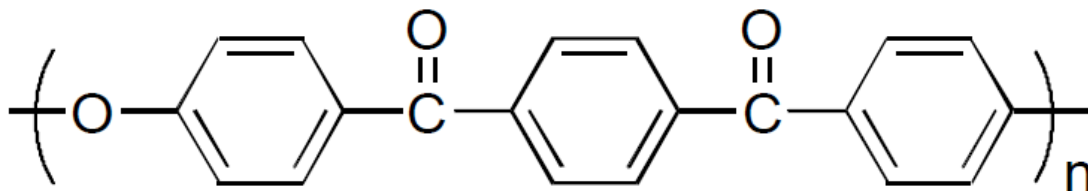


Figure 3.6: PEKK repeating unit.

The PEEK powder, commercially referenced as “Vicote 702” by the company Victrex, was used in this study. Figure 3.7 shown an SEM image of this PEEK powder.

The PhD thesis of Bortolussi has been chosen as a reference for the characterization of this powder [93]. According to his study, the powder is coarse and irregular. According to the manufacturer, the size distribution should have been centered and with a width of approximately 30 μm . In reality, many particles smaller than 20 μm can be observed in Fig. 3.7. Moreover, as reported in Table 3.1.2, the particle size was not centered.

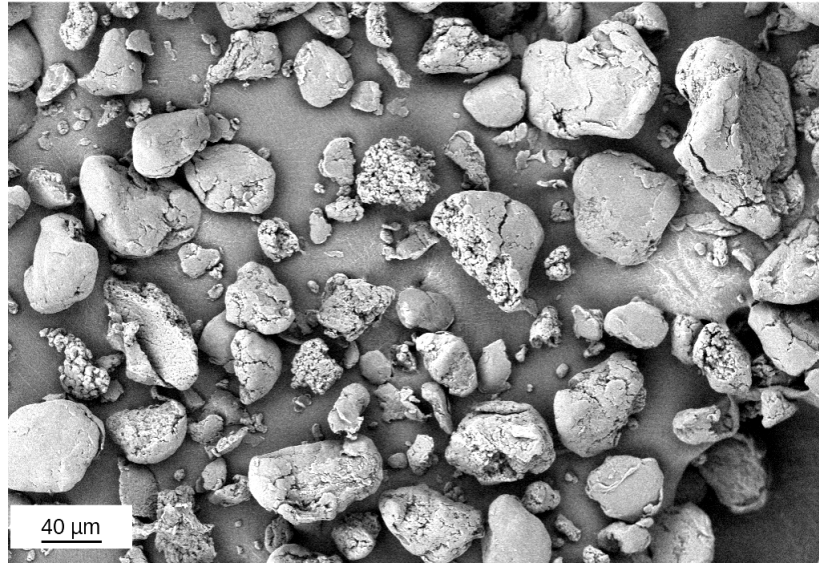


Figure 3.7: SEM image of the Vicote 702 PEEK powder.

| Dv(%) | Measured diameter (μm) |
|-------|-------------------------------------|
| Dv10 | 26.5 |
| Dv50 | 53.0 |
| Dv90 | 88.5 |

Table 3.5: Particle size distribution deciles of PEEK powder, measured by laser granulometry.

PEKK polymer powders exist in different grades. Two types were tested in the present work. The first, commercially referenced KEPSTAN 8002PL by Arkema, has a melting temperature of 358°C, higher than the PEEK one. Figure 3.8 shows a SEM image of it. The second, commercially referenced KEPSTAN 6002PL by Arkema, has a melting temperature of 305°C, lower than the PEEK one. Figure 3.9 shows a SEM

image of the latter. The manufacturer communicated a Dv50 in the range 50-55 μm for both powders. An experimental measurement has not been carried out for PEKK.

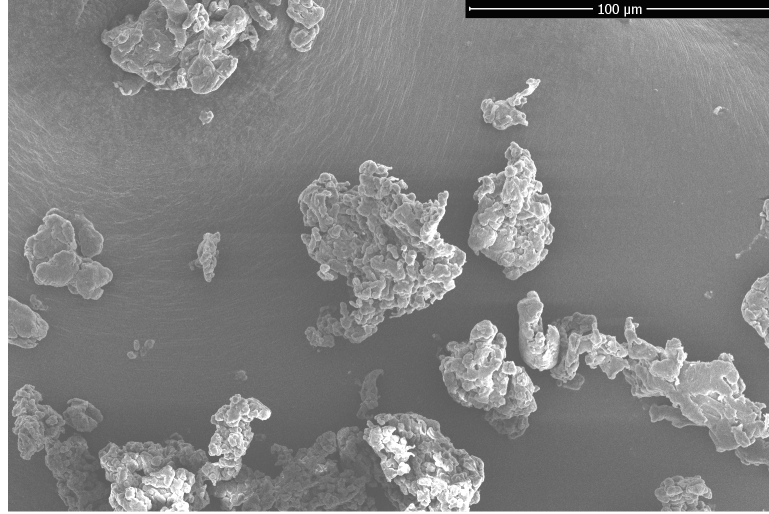


Figure 3.8: SEM image of the KEPSTAN 8002PL PEKK powder.

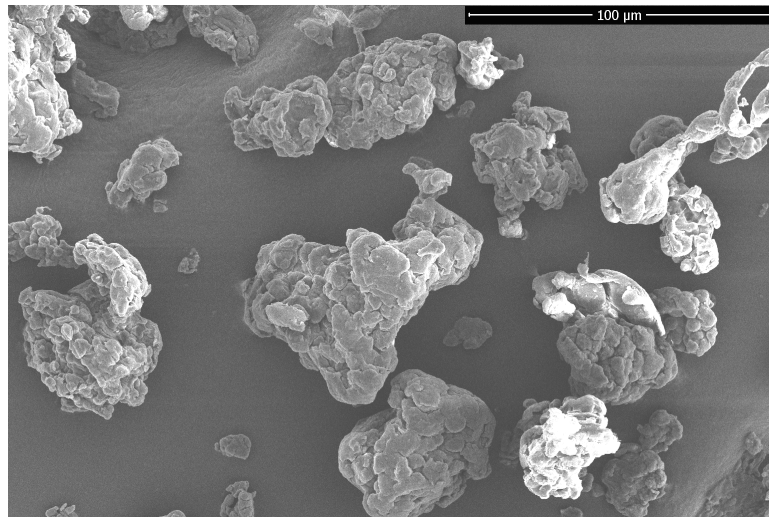


Figure 3.9: SEM image of the KEPSTAN 6002PL PEKK powder.

3.1.3 Mixture of metal and polymeric powder

In order to produce composite coatings, several mixtures of polymer and aluminum powders were performed, with different volume fractions. The maximum polymer

volume fraction value tested was 20 %. Each mixture is characterized by its volume fractions of metal and PEEK, named respectively F_{Al} and F_{Pol} . Mixing in a Turbula mixer for two hours allowed a better homogenization. Figure 3.10 illustrates a SEM view of the mixed powder.

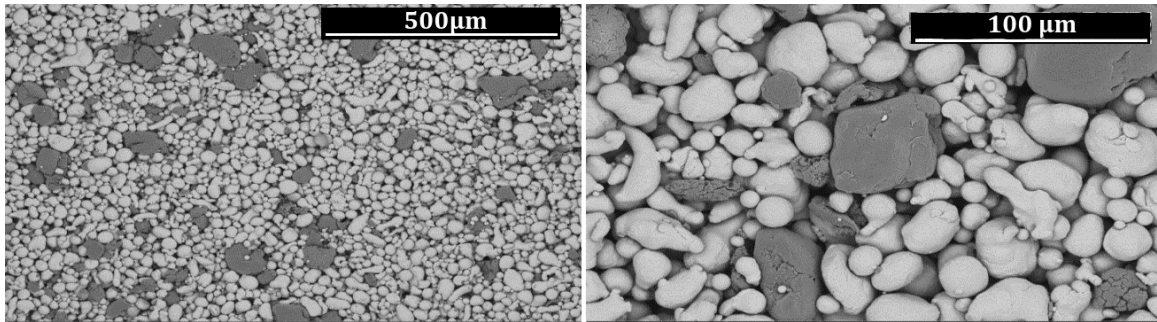


Figure 3.10: SEM image of an aluminum - PEEK702 powder mixture.

3.2 SUBSTRATES

The lead thread between the substrates presented below is their thermo-sensitivity. The metallization of three types of substrate by cold spray is under study in the present work. First, PEEK-based composites, used to replace many metal components especially in the aerospace industry and already introduced in the bibliographic chapter, are characterized. Secondly, additively manufactured parts made by Polyamide 66 (PA66 in the following) will be presented. Finally, wood has been the object of cold spray metallization tests. This multi-scale material is introduced below.

3.2.1 Short fiber reinforced PEEK

A PEEK-based composite, reinforced with short carbon fibers, is the principal material studied in this thesis. Samples, produced by Victrex with the commercial reference VICTREX® PEEK™ 90HMF40, were provided as square plates. The fiber volume fraction is about 40%. They were manufactured by the injection molding technique. Figure 3.11 shows a photographic picture of a plate.



Figure 3.11: Photographic image of a VICTREX® PEEK™ 90HMF40 plate, as received.

3.2.2 POLYAMIDE 66

PA66 and PA66 reinforced by carbon fibers are also tested as substrates in the present work. Samples have been provided by one of the industrial partners, IPC, who produced them using Fused Filament Fabrication (FFF) additive manufacturing technique. Complex shapes can be obtained by this process. The samples presented six different faces, with varying shapes and surface roughness. Three different wall thicknesses, obtained by changing the number of layers, were studied, with the aim of exploring the interaction of the cold spray process with all these features. Figure 3.12 shows a photographic image of one of these samples.



Figure 3.12: Photographic image showing one of the PA66 3D printed specimens.

3.2.3 WOOD

Four different types of wood, all of the hardwood families, were studied. These are walnut, sycamore, ash and oak. The final majority of the cold spray tests were carried out only on sycamore samples, which gave the best results in a preliminary spraying campaign. The particularity of hardwoods is the presence of structures called vessels, absent in softwoods, dedicated to the transport of sap and water and without any structural function. To better understand the morphological structure of the specimens, a characterization of the material has been done by means of observations by SEM and by optical microscopy. Due to its orthotropic characteristics, three main sections (planes) are generally identified in wood: transversal, radial and tangential, as shown in Figure 3.13.

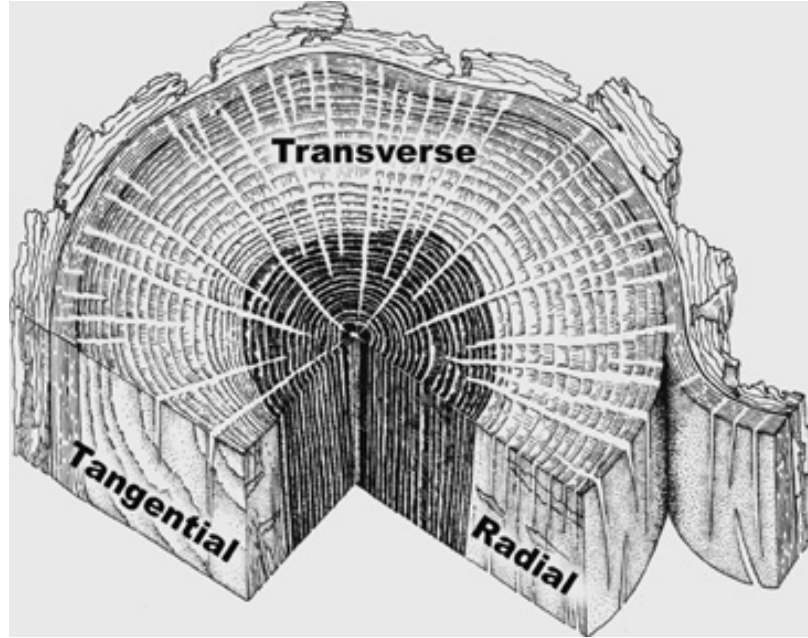


Figure 3.13: The three main sections of wood, after [94].

The repeating units forming the structure, as shown in figures 3.14 and 3.15, are called fibers and have sizes in the order of $10\text{-}40\ \mu\text{m}$. Rays are made of cells of a different kind and can be considered as inclusions of a different material. Vessels are larger pores ($100\text{-}200\ \mu\text{m}$), delimited by cell walls, also visible in figures 3.14 and 3.15.

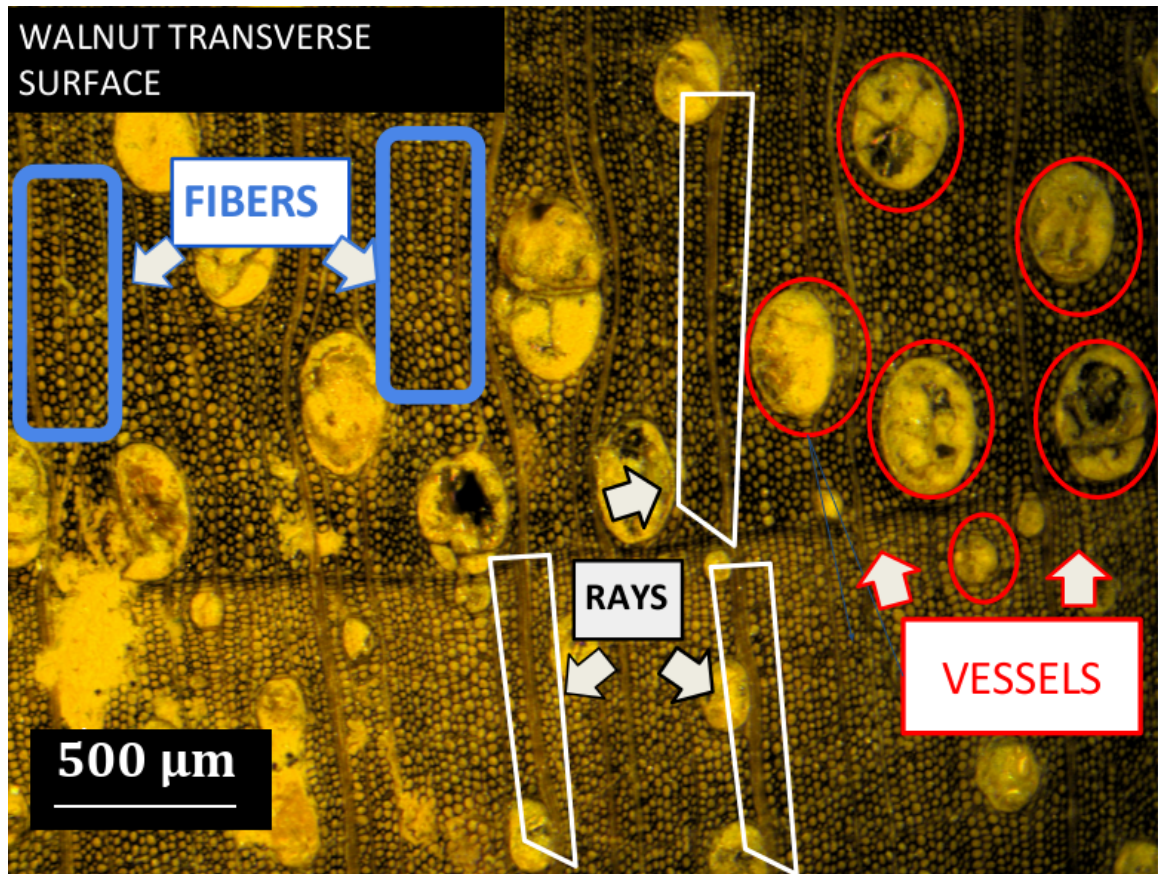


Figure 3.14: Optical microscope image of the walnut transverse surface showing the different features of hardwood

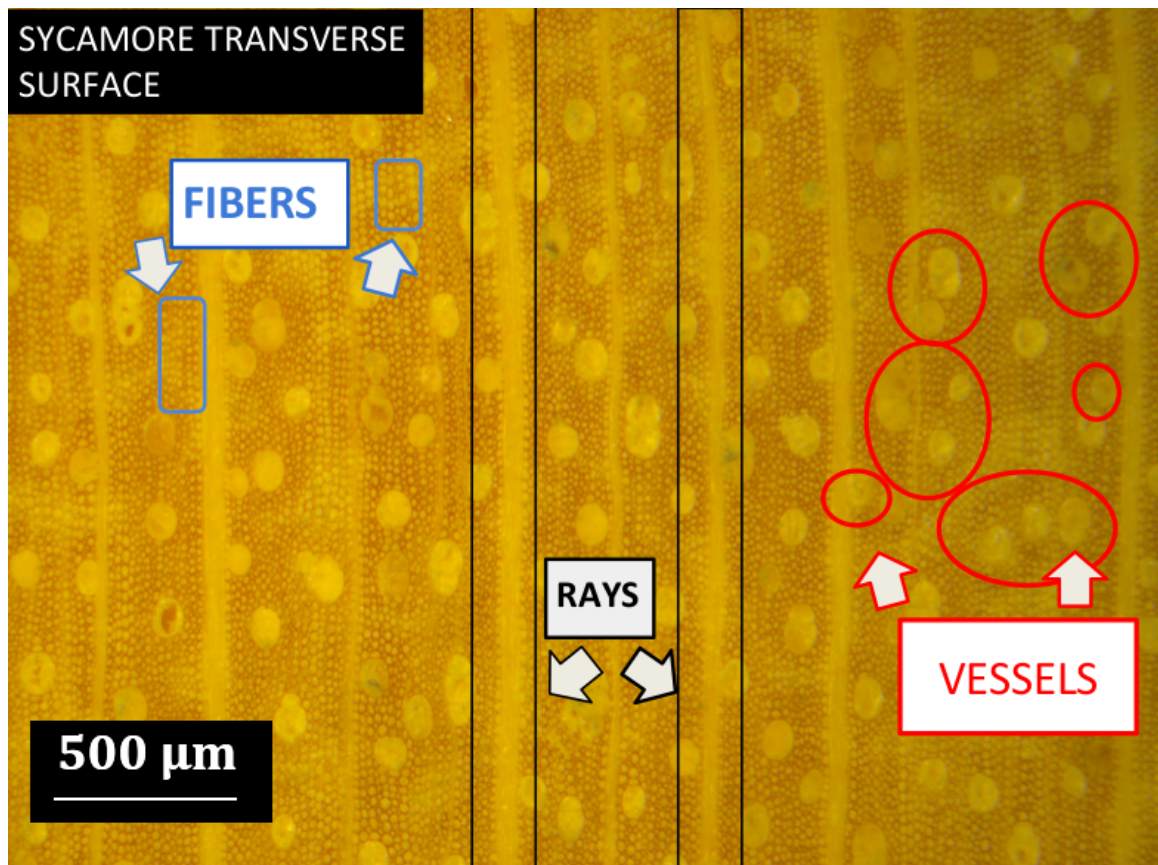


Figure 3.15: Optical microscope image of the walnut transverse surface showing the different features of hardwood

3.3 Cold spray technology

Two different cold spray systems were used in the present work, a high pressure and a low pressure equipment. The first is suitable for harder materials, it can reach pressures up to 6 MPa and temperatures up to 1200°C, in the latest models. Low pressure cold spray systems operate at smaller values of pressure, generally between 0.4 and 1 MPa, and temperatures, up to 600°C or 800°C, depending on the model. An important difference between the two system types lies on the powder feeder which, in the high pressure, is located before the throat and presents an axial powder injection feeder. In low pressure systems, powder feeding is essentially radial and located in the divergent part of the nozzle. Other differences concern nozzle geometries and materials. In conclusion, each system has its own particular behavior, resulting in different possibilities offered by the two systems.

3.3.1 High pressure cold spray

A Kinetics 3000 produced by Cold Gas Technology-GmbH (Germany), is used as high pressure cold spray. Figure 3.16 presents the different components of the equipment. Here, the gas is heated by a dedicated unit. The hot gas and the cold carrier gas charged in powder are transported up to the gun, where they mix together just before the convergent-divergent nozzle. Even if this system is not capable of the high pressures and performances of the more recent ones and can, thus, be classified as a “medium pressure” equipment, spraying parameters are largely sufficient for the usage onto thermo-sensitive substrates. The principal and carrier gas can either be nitrogen, helium or a mixture of the two, with pressure in the range 1 - 3 MPa and temperature in the range 25-600°C.



Figure 3.16: The cold spray system CGT Kinetics 3000. (a) control unit, (b) powder feeder, (c) gas heater, (d) gun.

Two different nozzles are available for this equipment:

- 33PBI (polybenzimidazole), suitable for metal powders for temperatures below 350°C.
- 24TC (tungsten carbide), allowing it to reach higher temperatures and suitable for metal and ceramic powders. Due to recurrent clogging issues, the use of pure aluminum powder is not recommended.

In this work, only the 33 PBI nozzle is used due to the low temperatures needed by the materials sprayed (aluminum and aluminum-polymer mixtures) and to take advantage of the anti-clogging capabilities of the PBI. The two nozzles are detailed in Figure 3.17, reporting also the geometrical characteristics.

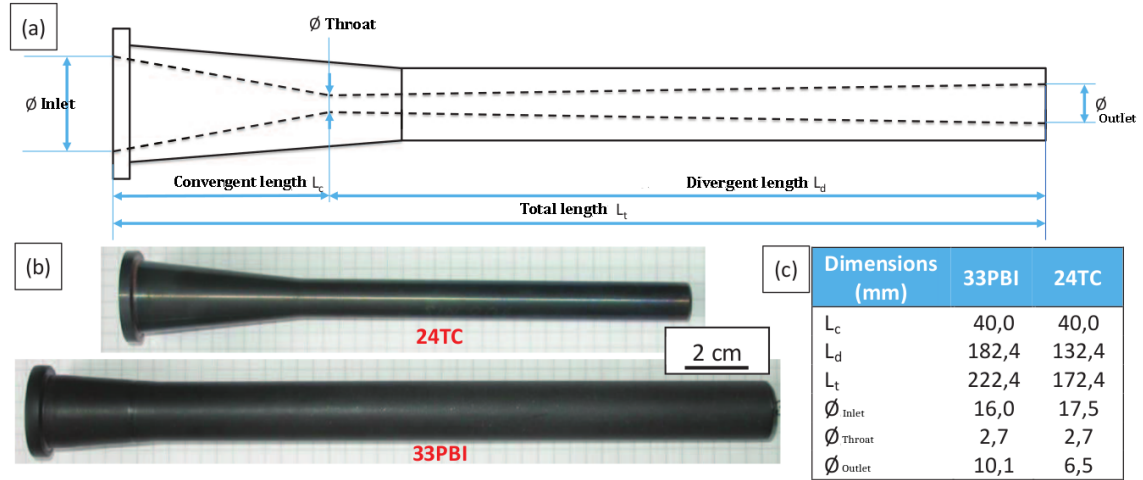


Figure 3.17: Characteristics of the nozzles used. (a): general sketch of the nozzles; (b) photographic images of the 24TC (on the top) and of the 33PBI (on the bottom); (c) geometrical parameters of the two nozzles. After Pierre-Emmanuel Leger, [95].

For the HPCS, the injection is axial and located in the middle of the convergent part of the nozzle. The cold spray gun is mounted on a tri-axial robot, installed in a dedicated hood and allowing the realization of large samples.

3.3.2 Low pressure cold spray

A Dycomet 523 low pressure cold spray system, produced by Dycomet (Akkum, The Netherlands), is also used in the present work. A photographic image of the equipment is shown in Figure 3.18. In this system, the heating elements are integrated into the spraying gun. The main gas can be compressed air or nitrogen. Its pressure ranges from 0.3 to 0.6 MPa and its stagnation temperature from 100 to 600°C. Two different powder feeder systems can be used. The standard Suction Unit FB-12A and the more sophisticated pressurized powder feeder PB-95. The first is composed of two cylinders, equipped with vibrating needles. The powder is transported thanks to the suction effect, due to the pressure difference between the ambient and the injection point after the nozzle throat, which is lower than the first one due to a Venturi effect. Unfortunately, this system presented issues in feeding powders with limited flowability. For this reason, the second powder feeder was preferred in the

experiments. In this case, the pressurized air or nitrogen can increase the drag force and help push the powder forward to the nozzle. Moreover, the injection pressure and the disk rotation speed could be tuned, increasing the control on the powder flow.



Figure 3.18: Low pressure Cold Spray equipment Dycomet 523.

The nozzle design is very different with respect to the high pressure one and is reported in Figure 3.19. In the Dycomet 523 system, the nozzle is composed of two main parts. The first is a convergent-divergent insert, connected to the gun from one side and to a divergent insert on the other. The radial injector is located here, just after the nozzle throat.

Three different diverging inserts are available:

- circular section stainless steel,
- rectangular section stainless steel,
- circular section ceramic.

They are shown in Figure 3.20.

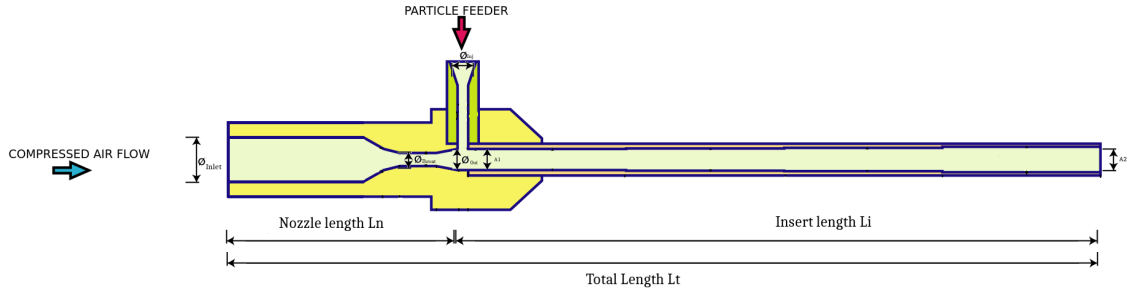


Figure 3.19: Schematic of the Dycomet 523 nozzle.

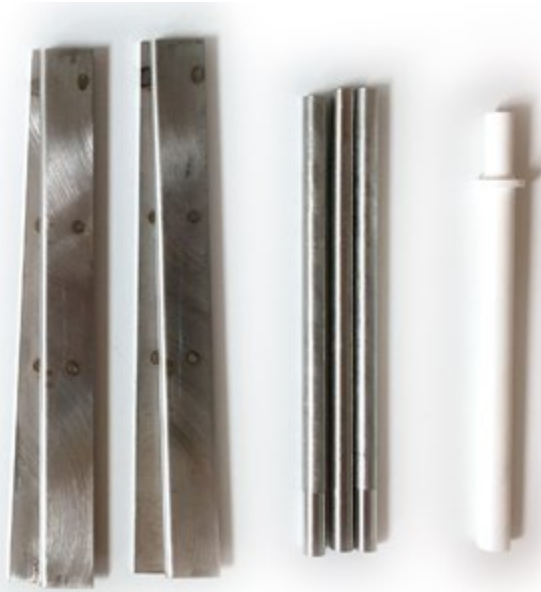


Figure 3.20: Photographic image of the three Dycomet 523 divergent inserts. From the left to right: rectangular section stainless steel, circular section stainless steel and circular section ceramic.

The geometrical parameters of the nozzle and the divergent inserts, in relation to Figure 3.19, are presented in Table 3.6.

| Dimension | Circular | Rectangular |
|--------------------------|----------|-------------|
| Ln (mm) | 20 | 20 |
| Li (mm) | 120 | 140 |
| Lt (mm) | 140 | 160 |
| Ai (mm ²) | 56.74 | 56.74 |
| At (mm ²) | 4.91 | 4.91 |
| Ao (mm ²) | 12.56 | 12.56 |
| A1 (mm ²) | 12.56 | 12.75 |
| A2 (mm ²) | 18.09 | 31.05 |
| Ainj (mm ²) | 3.14 | 3.14 |

Table 3.6: Geometrical parameters of the nozzle and the divergent inserts, in relation to Figure 3.19

The cold spray gun is fixed on a support allowing it to modify the stand-off distance. The sample is fixed on a motorized XY table.

A brief comparison concludes the presentation of the cold spray systems used in this work. The two equipments are very different in size and, more importantly, in the particle speed and temperature that they can provide. LPCS is certainly limited in particle speed when compared to HPCS. However, this is not always a defect. For example, it is capable of reaching high gas temperatures with low pressure, a configuration which is not possible with HPCS. Indeed, for the latter, it is impossible to stabilize the gas flow at low pressure and high temperature. The powder injection is another important difference. In HPCS, the injector is axial and placed before the throat. This can cause clogging near the nozzle throat. It is also risky to use polymer powders with this system because in the convergent part of the nozzle the temperature is almost the same as the stagnation one. This can lead to powder melting and, consequently, to nozzle clogging. Instead, in LPCS, the injection is radial and located in the divergent part, reducing the clogging issue.

3.4 Samples production and characterization

3.4.1 Cold spray strategies

Three types of specimen, each suitable for a different test, were machined, starting with the square plates provided. The plates are cut into squares measuring 20x20 mm², to be used for tests of optimization of cold spray parameters. The other two sample types are both in disk shape, with either 25 mm diameter for adhesion strength measurements, or 22 mm diameter, for the Van der Pauw conductivity measurements. The cutting schemes of the plates are shown in Figure 3.21.

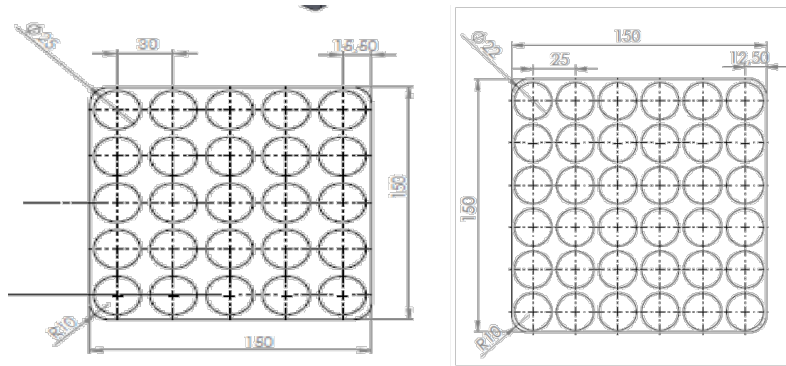


Figure 3.21: Cutting scheme of plates.

Three different strategies were used to produce and assess cold spray coatings. The splat test is useful to understand the bonding mechanism between single particles and the substrate. In this test, a very low powder flow rate and a high transverse speed were used to obtain single impacts on the substrate. The track test consists of a single passage of the nozzle over the specimen and allows it to rapidly compare different spraying parameters. Finally, in the surfacing test, the entire surface of the specimen is sprayed, to obtain a complete coating, to be used for adhesion strength and conductivity measurements. The track and surfacing strategies are illustrated in Figure 3.22.

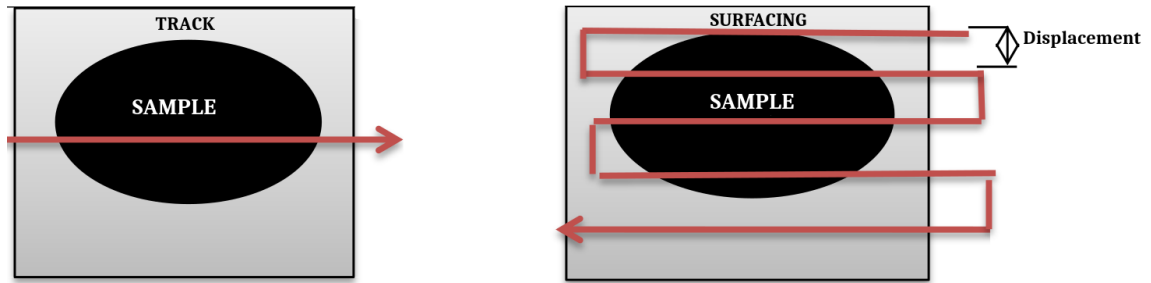


Figure 3.22: Schematic view of spraying strategies: on the left, the track test and, on the right, the surfacing test.

A specific sample holder, to be used in both HPCS and LPCS, was designed and produced to place equidistantly disk-shaped substrates. As shown in Figure 3.23, five samples for adhesion test with 25 mm diameter and four for the Van der Pauw measurement, with 22 mm diameter and the cloverleaf mask, can be produced in a single cold spray experiment.



Figure 3.23: Photographic image of the disk sample holder.

3.4.2 Sample preparation and metallography

Samples were systematically embedded in resin before cutting and polishing, for their cross-sectional observations. This precaution is necessary to avoid delamination, because coatings and substrates have highly different mechanical properties. Moreover, an Epofix resin is chosen for embedding because of its low temperature polymerization, allowing to avoid undesired effects on wood, PEEK composite and PA66 specimens are thermosensitive materials. In order to avoid bubble formation, mounted samples are put under vacuum during polymerization. It is, then, advisable to polish in such a way that the deposit is stressed towards the substrate. The adopted polishing procedure is as follows: first use an abrasive paper with a grain size 1200, secondly continue with a diamond paste with grain size 3 μm and then 1 μm . To further improve the quality of the polishing, an OPS colloidal silica can be used. An optical microscope ZEISS AXIOVERT 450 M was used to produce colored images, allowing to easily distinguish the polymer from the resin. Two different SEM were used: a FEG HR ZEISS Gemini DSM982 and a FEI Nova NanoSEM 450.

3.5 Experimental measurements

3.5.1 PARTICLE IN-FLIGHT SPEED MEASUREMENTS

Two different measurement systems were employed to measure particle diameter, number, and speed at typical stand-off distances: the cold spray meter DPV2000[®] by TECNAR (Canada), and a custom shadowgraphy equipment, designed and developed by Hugo Durand, PhD candidate at Mines Paris. The two systems are now detailed.

DPV2000

The DPV-2000 is composed of a laser and a sensing head, connected by an optical cable to a detection module. The device is operated during dedicated cold spray

experiments without any substrate. The measurement principle is illustrated in Figure 3.24. The laser illuminates in-flight particles at a given stand-off distance. This is necessary because, unlike warmer thermal spray processes, in cold spray particle temperature is not sufficient to have photon emission distinguishable from the background ambient radiation. The light reflected by a given particle is then detected by the sensor head, which is covered by a 2-slits photo mask. In this way, a double peak signal is generated. The signals are analyzed, directly by the hardware of the device, according to a number of criteria, validating or not the measurement of each particle depending on the signal shape and intensity. In the end, only a few percent of the particles passing in front of the sensor are retained by the device. This ensures the quality of the measurements, by eliminating parasitic signals and noise. This method requires, however, a long measurement time (about ten seconds), to ensure a statistical representation of the powder flow at a given point. Finally, the velocity is computed as the distance between the slits divided by the time between the two peaks of the detected signal. Moreover, for each particle, its diameter is also estimated by an analysis of the signal intensity. The DPV2000 system can also be used in jet-mapping mode. The laser-sensor assembly is mounted on a moving mechanical arm, which is able to scan a plan perpendicular to the cold spray jet. Particle speeds are then measured on a $6 \times 6 \text{ mm}^2$ grid, with a point distance of 1 mm in each direction.

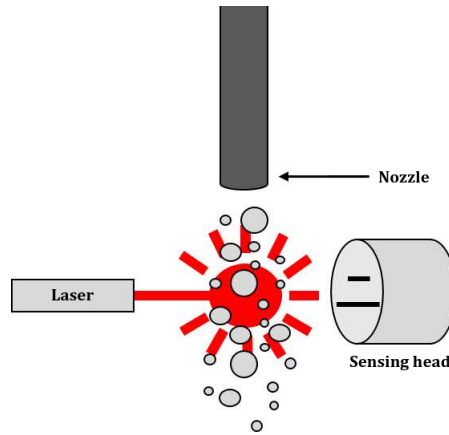


Figure 3.24: Schematic of the measuring principle of the DPV2000 system.

The DPV2000 system saves the data in two files, one containing all particle diameters and velocities measured at each point and the other an average of those values on the integration time at each point. From these files it is possible to plot a cartography showing the spatial distribution of jet characteristics, namely particle speed, number and diameter.

High speed shadowgraphy

This in-lab system was designed to have an independent measurement system to compare and validate DPV 2000 data. In addition, it can be operated during a cold spray experiment without the need to remove the substrate. The principle of this technique is to take multiple pictures of the cold spray jet and measure the displacement of each particle from an image to the subsequent one. Knowing the pixel size and the time interval between two frames, particle speed is readily calculated. The system consists of a high speed camera PHOTRON FASTACAM SA1.1, placed in front of a Cavilux pulsed laser generator, with a wavelength of 808 nm and a pulse duration of 5 ns. Given the spatial resolution of the camera optics, the minimum acquisition frequency required to catch a particle in two subsequent frames, assuming a maximum speed of 1200 m s^{-1} , is 120 KHz. The system synchronization and triggering is assured by a Low Frequency Generator (LFG), set to produce a square wave signal at 120 kHz. The camera recording and the laser pulse are switched on with a rising edge of the LFG signal. Figure 3.25 shows the the high speed shadowgraphy system installed in the cold spray booth.

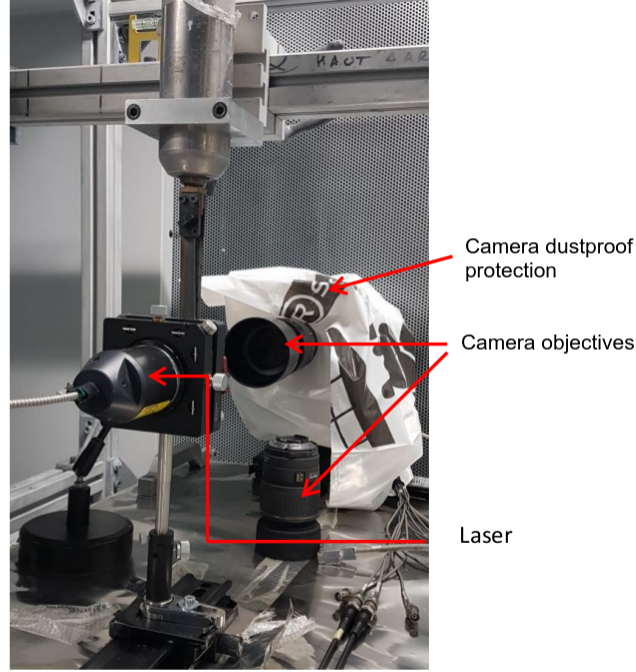


Figure 3.25: Photographic image of the high speed shadowgraphy system installed in the cold spray booth.

3.5.2 Electrical conductivity measurement methods

One of the main goals of this work is to produce electrical conductive coatings by cold spray. For this reason, precise resistance measurements must be performed. A classical method for measuring the conductivity of thin layers is the 4-point technique. Figure 3.26 illustrate the principle of this measuring method. The set-up consists in four aligned electrical contact probes, equidistant by a small distance s . A current I is sent between tip 1 and tip 4 and the potential difference V between tip 2 and tip 3 is measured. This method is not always effective for thick, brittle, and anisotropic coatings.

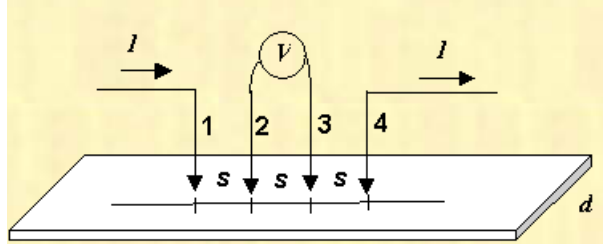


Figure 3.26: Schematic view of the four-point method to measure the electrical resistance of a coating.

These drawbacks can be overcome by using the four-points surface resistance measurement known as the “Van der Pauw method” [31]. Four-point probes are placed around the perimeter of the sample. Unlike with respect to the linear four point probe, which is able to measure resistance only along a specific direction, here the current circulates along different paths through the sample surface. To ensure good measuring conditions, the sample must present a simply connected conductive surface. The coating must be continuous, with a uniform thickness, much smaller than the width and length of the sample. To reduce errors in calculations, it is preferable to use a symmetrical shape. The most recommended shape is a uniform cloverleaf with a thin thickness. This shape forces the current to pass through the middle of the sample and, thus, to take a path of roughly the same length between all the points. Figure 3.27 illustrates the measuring configuration and a photographic image of a cloverleaf shaped coating.

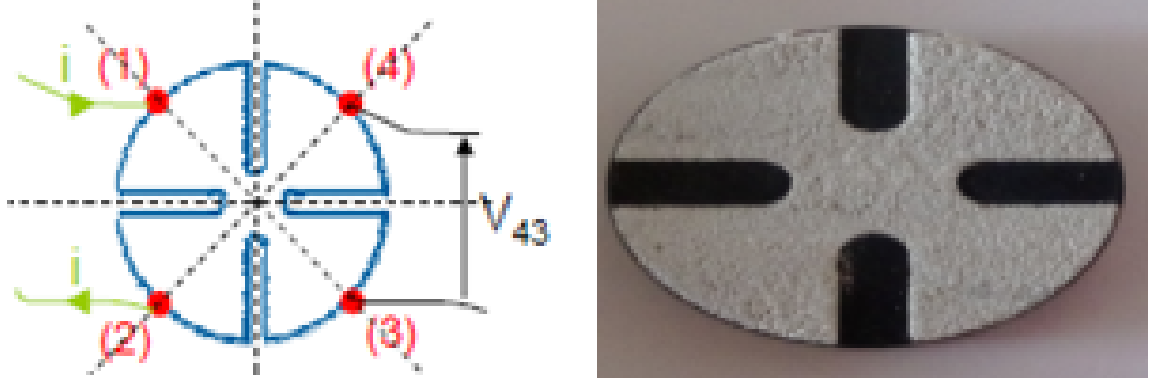


Figure 3.27: On the left, schematic view of the Van der Pauw method. On the right, photographic image of an aluminum coating with cloverleaf shape, cold sprayed onto a PEEK-based composite disk of 22 mm radius.

The determination of the surface resistance requires four measurements to be made. A current of known intensity is applied between two peaks on one side and the voltage must be measured between the two opposite peaks. By Ohm's law, four resistance values will be obtained. The isotropy of the sample can be verified by comparing the resistances in orthogonal directions. The surface resistance is calculated by solving Van der Pauw's equation:

$$e^{-\pi \frac{R_h}{R_s}} + e^{-\pi \frac{R_v}{R_s}} = 1 \quad (3.1)$$

where $R_h = \frac{R_{14} + R_{43}}{2}$ and $R_v = R_{32} + R_{21}2$. An approximate solution to this equation is:

$$R_s = \frac{\pi(R_h + R_v)}{2 \ln 2} f \quad (3.2)$$

where f is a shape factor, depending on the sample resistance isotropy, which can be obtained by numerically solving the following equation:

$$\cosh \left(\frac{\frac{R_h}{R_v} - 1}{\frac{R_h}{R_v} + 1} \frac{\ln(2)}{f} \right) = \frac{1}{2} \exp \left(\frac{\ln(2)}{f} \right) \quad (3.3)$$

The measurement requires four ohmic contacts on the sample under the following

specific conditions:

- each contact point should lie on the edge of the sample, or at least as close to it as possible;
- the contact spot should be as small as possible.

Starting from the resistance measurements, the resistivity was calculated using the following formula:

$$\rho = \frac{\pi d R_{eq}}{\ln(2)} f \quad (3.4)$$

where d is the deposit thickness, $R_{eq} = \frac{R_{13} + R_{24}}{2}$ is the average resistance, f is the shape factor. The latter is equal to one if and only if the two orthogonal resistances are the same ($R_{13} = R_{24}$). This was the case for all the specimens.

The equipment used is a Linkam HFS600E-PB4 measuring chamber, with 4 points, coupled to a Keithley multimeter and a current generating unit. The maximum current is 1 A. The set-up for resistance measurement by the Van der Pauw method is shown in Figure 3.28. The ability of the coatings to conduct electricity is also assessed using a portable ohmmeter immediately after spraying.

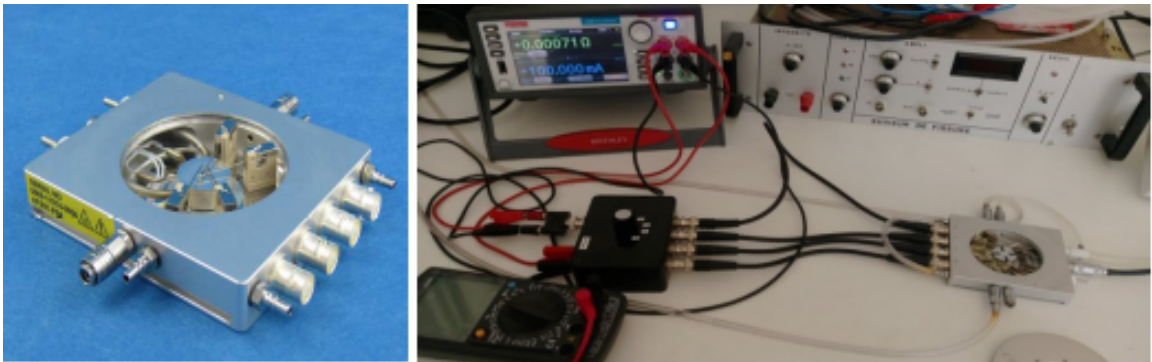


Figure 3.28: Setup for the measurement of electrical resistance by the Van der Pauw method.

3.5.3 Pull-off test

The adhesion of cold sprayed coating is a key property, especially in the case of the metallization of thermosensitive materials for which it is known to be a weakness. A pull-off tensile test was chosen to assess the adhesion strength. The experimental procedure is regulated by the standard USA ASTM C633-13(2021) [96] As reported on the documentation of the standard: “The test consists of coating one face of a substrate fixture, bonding this coating to the face of a loading fixture, and subjecting this assembly of coating and fixtures to a tensile load normal to the plane of the coating”. A specific assembly must be prepared and a perfect alignment must be ensured. A sample dedicated to the pull-off test is illustrated in Figure 3.29.

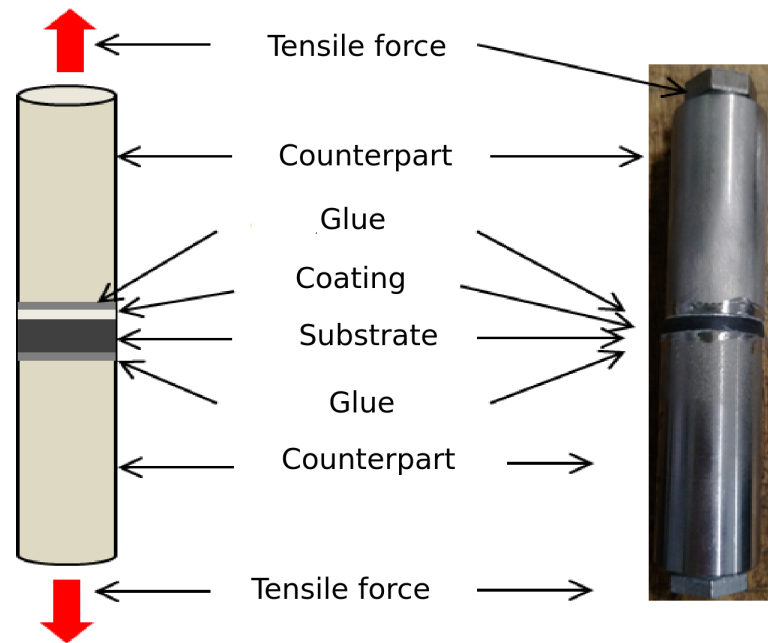


Figure 3.29: On the left, schematic view of glued stud specimen and, on the right, photographic image of a pull-off specimen.

The 25 mm diameter cold sprayed disks are first sand blasted on the non-coated side of the substrate to increase the adhesion with the glue. Then, both sides are glued with an epoxy adhesive to the counterparts as visible in Figure 3.29. The counterparts are connected on both sides to the tensile test machine by means of screws. The tensile

test machine used is an Instron 5982 with a load cell of 10kN. A loading speed of 0.1 mm/min was used. The force is monitored throughout the test, but only its value at failure is necessary for the analysis. Stress, considered homogeneous on the surface, is obtained by dividing the force by the surface area. At rupture, different scenarios are possible. They are summarized in Figure 3.30. The failure can be at the interface between the coating and the substrate, which corresponds to an adhesive failure. If, instead, is located inside the coating, the failure is cohesive. When failure occurs either at an interface with the glue, or inside the glue, only a lower bound to the adhesive and cohesive strengths can be given. Finally, it is also possible to observe mixed-mode failures, with a part of the coating still adhering to the substrate.

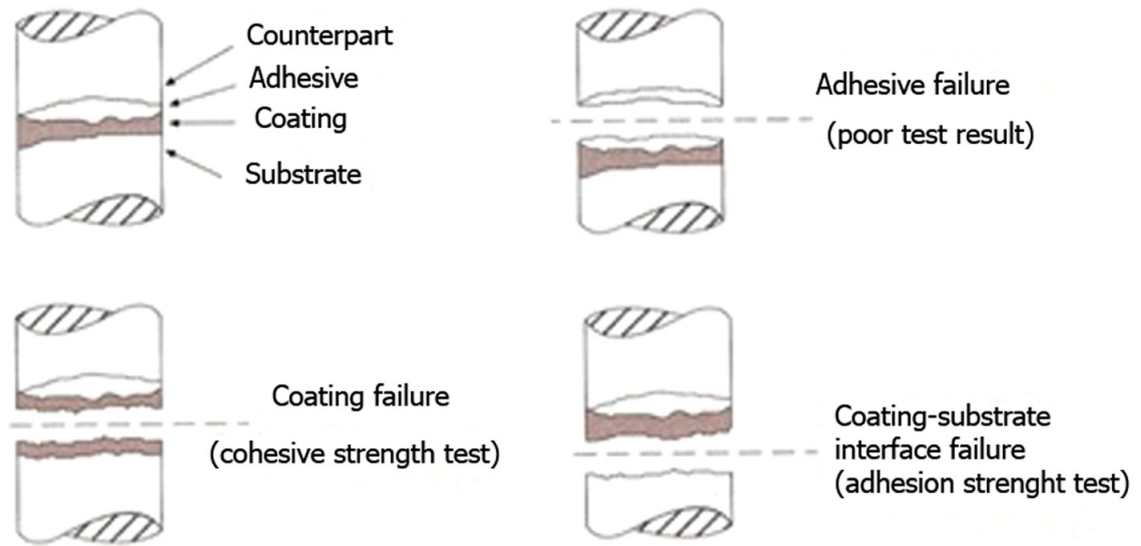


Figure 3.30: Schematic view illustrating the different types of fracture resulting from coating adhesion tests, after [97].

CHAPTER 4

COLD SPRAY ON SHORT CARBON FIBER REINFORCED PEEK SUBSTRATES

Abstract

As seen in chapter 1, the metallization of polymers and polymer-based composites has been the objective of many works. Within the thermal spray family, all processes involving high temperatures of the flame may not be appropriate because of the thermo-sensitivity of those substrate materials. Differently, the cold spray process overcomes this issue, due to its considerably lower operational temperature. If some initial very encouraging results have already been obtained for automotive and aeronautical applications, as reported in chapter 1, there is still much to understand to improve the cold spray process for polymer and polymer-based composites. In particular, superficial rugosity, the presence or not of fibers, adhesion, erosion, porosity, temperature effect on the substrate and its transformation during the spraying must be kept in account. The aim of this chapter is to present the experimental results of the metallization of PEEK-based composites and propose some mechanisms that lead to coating creation and growth on these thermosensitive materials. Especially in the composite, the presence of fibers is a crucial factor to keep into account. If fiber damage by high velocity particles degrades the mechanical properties of the substrate, fibers are also an issue for mechanical anchoring of these particles and, then, for the coating adhesion. The high temperature and velocity of gas and particles can also be a threat for the composite matrix, leading to severe melting and/or erosion. Concerning the feed-stock material, aluminum and copper, due to their high conductivities, are selected as the most promising coating materials.

The experience with high pressure equipment and pure aluminum powders revealed that the delamination of coating and substrate erosion could not be overcome by tuning the cold spray parameters. The acquired experience convinced that a lower pressure associated with a higher temperature of the cold spray gas was the right path to follow. Unfortunately, the system could not be stabilized at low pressure and high temperature. Therefore the optimal choice seemed to be the switch to a low pressure spray system. The results with pure aluminum were improved and some attempts were conducted with copper powder too.

Another strategy retained for the metallization of composite materials was inspired by the work of Bortolussi at MINES Paris [26], consisting of the spraying of a mixture of metallic and polymer powders. This was useful to avoid fiber damage in the case of long fiber reinforced PEEK. In the case of short fiber reinforced PEEK, this could be a solution to increase the coating adhesion preserving the conductivity. In fact, the thin PEEK top layer of the composite is not always enough to have a good mechanical anchoring. Moreover, the short carbon fibers close to the top surface can affect the particle penetration being damaged too. Conductivity can be preserved if percolation between metal particles is guaranteed. With an opportune percentage of PEEK particles this seemed to be possible.

The effort to optimize coating adhesion and electrical conductivity led to the investigation of the effect of polymer/metal ratio of the feed-stock powder and of the different process parameters. The nature of the polymer powder used in the mixture was also questioned and innovative solutions were tested. The chapter will then conclude on a discussion about the phenomena leading to conductive and adhesive coatings.

Résumé en français

Comme nous l'avons vu au chapitre 1, la métallisation des polymères et des composites à base de polymères a fait l'objet de nombreux travaux. Dans la famille de la projection thermique, tous les procédés impliquant des températures élevées de la flamme peuvent ne pas être appropriés en raison de la thermosensibilité de ces matériaux de substrat. En revanche, le procédé de projection à froid permet de surmonter ce problème, grâce à sa température opérationnelle considérablement plus basse. Si certains résultats initiaux très encourageants ont déjà été obtenus pour des applications automobiles et aéronautiques, comme indiqué au chapitre 1, il reste encore beaucoup à comprendre pour améliorer le procédé de projection à froid pour les polymères et les composites à base de polymères. En particulier, la rugosité superficielle, la présence ou non de fibres, l'adhésion, l'érosion, la porosité, l'effet de la température sur le substrat et sa transformation pendant la projection doivent être pris en compte. L'objectif de ce chapitre est de présenter les résultats expérimentaux de la métallisation de composites à base de PEEK et de proposer quelques mécanismes qui conduisent à la création et à la croissance du revêtement sur ces matériaux thermosensibles. En particulier dans le composite, la présence de fibres est un facteur crucial à prendre en compte. Si l'endommagement des fibres par des particules à haute vitesse dégrade les propriétés mécaniques du substrat, les fibres sont également un problème pour l'ancrage mécanique de ces particules et, ensuite, pour l'adhésion du revêtement. La température et la vitesse élevées du gaz et des particules peuvent également constituer une menace pour la matrice composite, entraînant une fusion sévère et/ou une érosion. En ce qui concerne le matériau d'alimentation, l'aluminium et le cuivre, en raison de leur haute conductivité, sont sélectionnés comme les matériaux de revêtement les plus prometteurs.

L'expérience avec des équipements à haute pression et des poudres d'aluminium

pur a révélé que la délamination du revêtement et l'érosion du substrat ne pouvaient être surmontées en ajustant les paramètres de projection à froid. L'expérience acquise a convaincu qu'une pression plus faible associée à une température plus élevée du gaz de projection à froid était la bonne voie à suivre. Malheureusement, le système ne pouvait pas être stabilisé à basse pression et haute température. Par conséquent, le choix optimal semblait être le passage à un système de projection à froid à basse pression. Les résultats avec l'aluminium pur ont été améliorés et quelques tentatives ont été menées avec de la poudre de cuivre également.

Une autre stratégie retenue pour la métallisation des matériaux composites a été inspirée par les travaux de Bortolussi à MINES Paris [26], consistant à projeter un mélange de poudres métalliques et de polymères. Ceci a été utile pour éviter d'endommager les fibres dans le cas du PEEK renforcé par des fibres longues. Dans le cas du PEEK renforcé par des fibres courtes, cela pourrait être une solution pour augmenter l'adhésion du revêtement en préservant la conductivité. En effet, la fine couche supérieure de PEEK du composite n'est pas toujours suffisante pour avoir un bon ancrage mécanique. De plus, les fibres de carbone courtes proches de la surface supérieure peuvent affecter la pénétration des particules en étant également endommagées. La conductivité peut être préservée si la percolation entre les particules métalliques est garantie. Avec un pourcentage approprié de particules de PEEK, cela semble être possible.

L'effort d'optimisation de l'adhérence du revêtement et de la conductivité électrique a conduit à l'étude de l'effet du rapport polymère/métal de la poudre d'alimentation et des différents paramètres du processus. La nature de la poudre de polymère utilisée dans le mélange a également été questionnée et des solutions innovantes ont été testées. Le chapitre se conclura ensuite par une discussion sur les phénomènes conduisant aux revêtements conducteurs et adhésifs.

4.1 Introduction to the experimental work

Determining the best cold spray parameters is crucial in order to match the requirements of uniformity, repeatability and of course conductivity of the deposited material. Coating creation and growth mechanisms differ significantly from classical metal-on-metal combinations. Evidently, metallurgical bonding is not possible between metals and polymers, so there is no possibility to reach the same adhesive strength values as a metal-on-metal assemblies. In a recent work [98], a surprisingly 24 MPa adhesion strength value could be obtained in the case of aluminum 7075 particles and of 12 MPa in the case of Aluminium onto pure PEEK substrates. The authors used a HPCS system at its maximum pressure of 4.1 MPa and a temperature of 350 °C. In [99], the same authors, using the same powders onto a short carbon reinforced PEKK substrate, obtained an adhesion of 18 MPa for the Aluminium CP and of 9 MPa using the 7075 alloy. This improvement in the case of CP Aluminium was correlated to the lower mismatch in the coefficients of thermal expansion (CTE) between PEKK and Aluminium (34%), with respect to the PEEK and Aluminium (154%). In terms of electrical conductivity of aluminum cold spray coatings onto composites, there are not so many works to compare with, so all the results will be compared to the bulk aluminum conductivity value. The exploratory work conducted in the present PhD thesis tries to put a milestone in the comprehension of the phenomena involved and in the strategies bringing to conductive and adherent coatings onto short carbon fiber reinforced polymers.

PEEK450G substrates were provided by one of the industrial partners of the project, Liebherr Aerospace. Short carbon fibers, with a volumetric content of 30%, are embedded in a PEEK matrix, to improve the mechanical properties. Plates are produced by the injection molding technique and SEM observations reveal that fibers are oddly distributed in the volume. Some of them were present in the composite

surface too, so there is no pure polymer top layer that could protect them from impacting cold sprayed particles.

Total pressure and temperature are the most important parameters in the cold spray process. Nevertheless, it is their effect on particle speed and temperature at impact that matters. While the total temperature affects the gas Mach number at the nozzle exit, the total pressure acts on the gas density. Both parameters control, in different ways, the particle speed. Moreover, gas temperature can have a significant impact on thermo-sensitive substrates, in particular due to the bow shock phenomenon suddenly raising the temperature in the proximity of the substrate surface.

The two different equipments used are the high pressure cold spray Kinetics 3000 and the low pressure system Dymet523, already introduced in the previous chapter. The differences within the two systems lie in terms of pressure and temperature, as well as of the feeding system, nozzle designs and of the strategy in powder injection. This last aspect proves to be a key feature when clogging and melted particles are involved in the tests, as will be shown later. The first part of the chapter explores the possibility of pure metal coatings onto the composite. Pure aluminum and copper powders are tested with both HPCS and LPCS. The second part presents the composite coatings produced by spraying aluminum and a small percentage of PEEK powder. Finally, a mixture of aluminum and of a different polymer, namely the PEKK, is sprayed and results are compared.

4.2 Pure metal coatings

In this part, pure aluminum and copper powders are used as feed-stock material for the cold spray process to create a conductive layer onto PEEK composite. As reported in chapter 1, many works employed these materials to create a metal layer on different polymers and polymer based composites. The differences between the

two powders lie mostly in their density and conductivity values. Copper has roughly 1.6 times the conductivity of aluminum, but on the other hand its density is 3.3 times higher.

4.2.1 Aluminium coatings

High pressure cold spray results

Several conditions, as reported in Table 4.1, were tested, as well as two different nozzles, a polymer one (PBI33) for lower temperatures and a tungsten carbide one (TC) for higher temperatures. Nozzle clogging revealed to be an issue with pure aluminum powders at temperatures higher than 400°C, especially with the TC nozzle. Results at higher values, thus, are not reported here. The best results were obtained for temperatures ranging between 300 and 400°C, with a pressure of 2.5 MPa and a PBI polymeric nozzle (WC in the case of 400°C). A surfacing robot trajectory, shown in chapter 2, was chosen to coat 25 and 22 mm diameter disks, suitable for adhesion and electrical conductivity measurements.

| Parameters | S1 | S2 | S3 | S4 | S5 | S6 | S7 | S8 | S9 |
|-------------------------|-------|-------|-------|-------|-------|-------|-------|-----|-----|
| Nozzle | PBI33 | PBI33 | PBI33 | PBI33 | PBI33 | PBI33 | PBI33 | WC | WC |
| Pressure (MPa) | 2.5 | 2.5 | 2.5 | 2.5 | 2.5 | 2.5 | 2.5 | 2.5 | 2.5 |
| Temperature (°C) | 350 | 300 | 300 | 350 | 350 | 350 | 350 | 400 | 400 |
| Displacement (mm) | 1 | 1 | 1 | 2 | 1 | 5 | 5 | 2 | 1 |
| Flow-rate (g/min) | 6.5 | 9.2 | 9.2 | 9.2 | 9.2 | 6.7 | 5.1 | 13 | 13 |
| Transverse speed (mm/s) | 300 | 200 | 200 | 200 | 200 | 300 | 200 | 200 | 200 |
| Stand-off distance (mm) | 30 | 30 | 30 | 30 | 30 | 20 | 20 | 30 | 30 |

Table 4.1: High pressure cold spray parameters

Figure 4.1 illustrates photographic images of some of the coatings. For the highest temperatures, corresponding to conditions S8 and S9, irregular coatings and easy delamination were experienced. Their poor coating behavior was mainly due to increased thermal stresses, provoked by the higher temperatures and the strong difference in the thermal expansion coefficients of aluminum and PEEK.

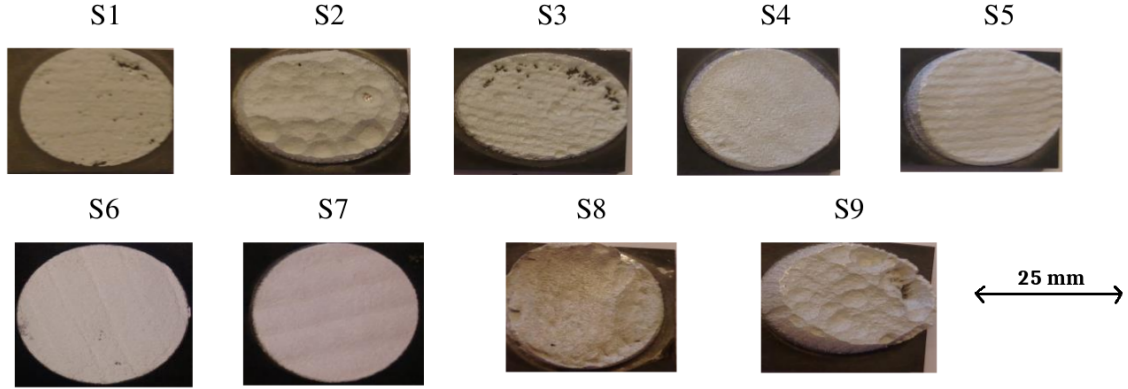


Figure 4.1: Photographic pictures of pure aluminum coatings onto PEEK, representative of the spraying conditions listed in Table 4.1

S1, S2 and S3 conditions presented defects and large pores in the coating. This is assumed to be due mainly to the high transverse speed of the gun, resulting in the deposition of few particles, and to the trajectory step, *i.e.* the distance between successive lines in the surfacing trajectory, causing the debonding of deposited material with each passage of the cold spray nozzle. Moreover, S2 and S3 conditions exhibit coating delamination during the metallographic preparation. Results evidenced the importance of the trajectory step parameter. When it was set to 5 mm, with a transverse speed of 200 mm/s, a stand-off distance of 20 mm, a temperature of 350°C degrees and a pressure of 2.5 MPa, corresponding to S6 and S7 conditions, a regular and homogeneous coating could be obtained, presenting no visible defects. For the sake of simplicity, Table 4.2 resumes the effects of spraying parameters on the coating, helping to better understand the determination of the best set.

| Parameters | High value effect | Low Value effect |
|---------------------|--------------------------|----------------------------|
| Nozzle displacement | Non homogeneous coating | Delamination |
| Transverse speed | Low deposition/reheating | High deposition/reheating |
| Stand-off distance | Low particle velocity | Substrate damaging |
| Pressure | Substrate damaging | No coating |
| Temperature | Melting substrate | lower particle penetration |

Table 4.2: Summary table of the effect of cold spray parameters on the coating

SEM and optical cross sectional observations of the specimens, reported in Figure 4.2, confirmed the previous speculations. In S1, a lack of anchoring of aluminum particles on the substrate can be noticed. Indeed, particles at the interface are almost completely undeformed and not penetrating into the substrate. In S4 and S5 specimens, particles are more deformed and adherent, but still not uniformly. Interfaces in S6 and S7 specimens seem more adherent. The reduced stand-off distance probably allowed particles to impact at higher speeds, resulting in a certain penetration in the composite. The S7 specimen, compared to the S6, was produced at a lower transverse speed and a thicker coating can be observed. Due to delamination during sample manipulation, cross sectional images could not be acquired for S2, S3, S8 and S9 conditions.

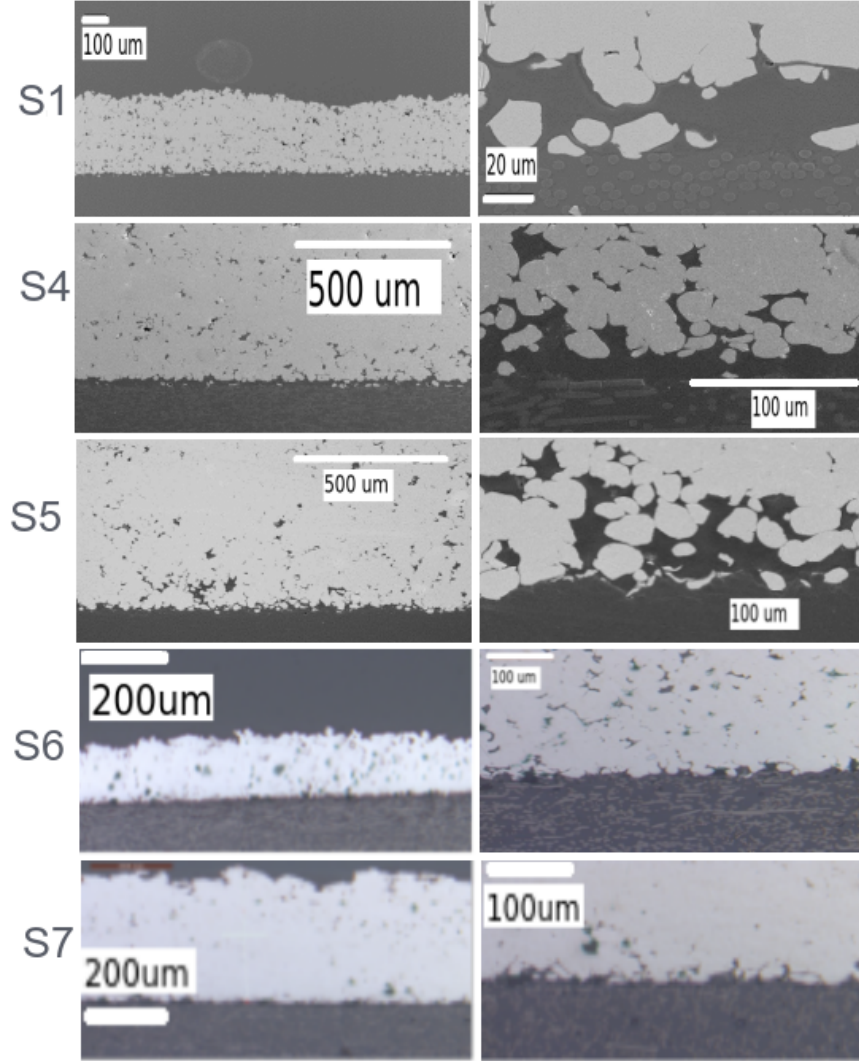


Figure 4.2: SEM and optical microscopy cross sectional observations of pure aluminum coatings.

Before the assessment of mechanical adhesion strength and conductivity of the coatings, some preliminary remarks can be made. High speed particles seem to rebound on the top surface of the PEEK composite. This is due to the double effect of the toughness of the PEEK, compared to other polymers, and to the presence of short fibers close to the surface. Thus, pure aluminum particles could not reach the necessary amount of kinetic energy to penetrate the surface. Local adhesion is due to particles that, reaching the surface in zones richer in PEEK, deform and probably melt locally the polymer. They can then penetrate to a certain degree in the matrix.

In the following parts, adhesion strength and electrical conductivity will be assessed on samples produced with S7 spraying conditions.

Electrical conductivity measurement

The Van der Pauw method envisages four resistance measurements for four different specimens to assess a representative value. The average resistance of each specimen is reported in Table 4.3. The average resistance values of the four different specimens were revealed to be close to each other. This means that a good reproducibility of the coating properties can be obtained in the case of HPCS of the aluminum powder. The averaging values from the four specimens gives final resistivity, as recommended by the Van der Pauw procedure. The average resistivity was $2.04 \cdot 10^{-6} \Omega \cdot m$, corresponding to a conductivity of $4.9 \cdot 10^5 S \cdot m^{-1}$, two orders of magnitude lower than pure bulk aluminum one. This is certainly due to a certain impurity of the material, the presence of porosities and to the numerous interfaces between deformed aluminum particles in the coating, which have an increased resistance compared to bulk aluminum.

| Imposed current (mA) | Res 1(Ω) | Res 2(Ω) | Res 3(Ω) | Res 4(Ω) | Req (Ω) |
|----------------------|---------------------|---------------------|---------------------|---------------------|-------------------------------------------|
| 100 | $6.1 \cdot 10^{-4}$ | $5.6 \cdot 10^{-4}$ | $5.5 \cdot 10^{-4}$ | $5.5 \cdot 10^{-4}$ | $5.8 \cdot 10^{-4} \pm 2.2 \cdot 10^{-5}$ |

Table 4.3: Measured average resistance values for the four specimens

Adhesion test

For a reliable and standard measurement, five specimens per parameter set were used to quantify coating adhesion. Unfortunately, the measured values were rather low. It must be noticed that two of the five coatings were delaminated during sample preparation. The results are presented in Table 4.4. For all the samples, as shown in Figure 4.3, the failure was adhesive, occurring at the interface between the coating and the substrate. Strong differences in the adhesion strength value were due to difficulties of the gluing procedure and to the very low adhesion of the coatings.

| Test | Fmax(N) | Adhesion strength (MPa) |
|------|---------|-------------------------|
| 1 | 280.86 | 0.57 |
| 2 | 166.39 | 0.33 |
| 3 | 100.01 | 0.25 |

Table 4.4: Measured adhesion strength values for the three specimens

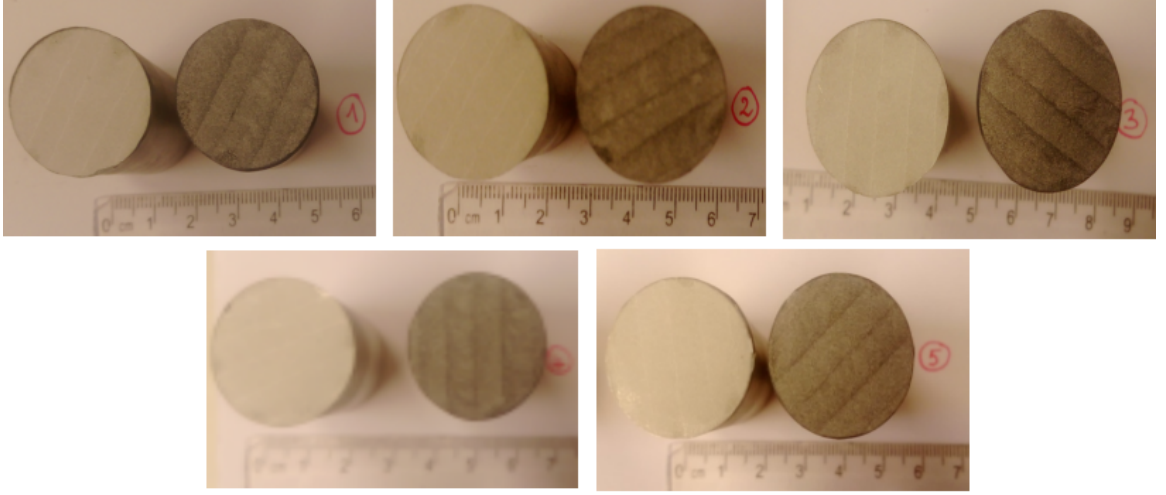


Figure 4.3: Photographic images of the fracture surfaces of pure aluminum coatings.

Remarks on high pressure cold spray of pure aluminum

HPCS of aluminum coatings onto the short carbon fiber reinforced PEEK composite revealed to be very challenging. Even if aluminum particles were found to be deformed by high speed impact, their penetration into the PEEK matrix was not sufficient to assure a mechanical anchoring to the composite. Moreover, the spraying window is rather small. Particles at a higher speed, corresponding to the highest pressure/temperature parameters tested, erode the substrate and damage the fibers. Slower ones simply rebound both on the fibers and on the PEEK surface. An opportune optimization of the parameters led to homogeneous coatings with good conductivities. Nevertheless, the adhesion was rather low.

Low pressure cold spray results

The potential of LPCS was explored to compare with HPCS results, in particular hoping to improve the adhesion issues experienced. LPCS can reach parameter combinations that are not accessible to HPCS systems, in the high temperature and low pressure zones. These conditions are potentially interesting for composite metallization because they can result in slower and warmer particles. In this way, erosion and damage of the substrate can potentially be reduced. Moreover, warmer particles can deform more easily, soften the PEEK and penetrate more in the substrate, creating the conditions for a better mechanical anchoring. A fixed value of 0.6 MPa was used as a total pressure and three different temperatures were tested, as reported in Table 4.5. The stand-off distance was fixed at 30 mm. The circular section stainless steel divergent inserts were used for these experiments.

| Parameters | Test 1 | Test 2 | Test 3 |
|-------------------------|--------|--------|--------|
| Pressure (MPa) | 0.6 | 0.6 | 0.6 |
| Temperature (°C) | 350 | 400 | 450 |
| Stand-off distance (mm) | 30 | 30 | 30 |

Table 4.5: Low pressure cold spray parameters for the aluminium powder tests

Figure 4.4 presents cross sectional images of aluminum LPCS samples. Coatings are thicker and denser compared to the HPCS case. Unfortunately, their adhesion was still very poor. The combined low velocity and high temperature of particles did not give the expected result. Looking at the three cross sections, it is likely that the strong thermal stresses induced by the hot cold spray jet led to a complete delamination of the coating. Moreover, the PEEK surface presents strong erosion.

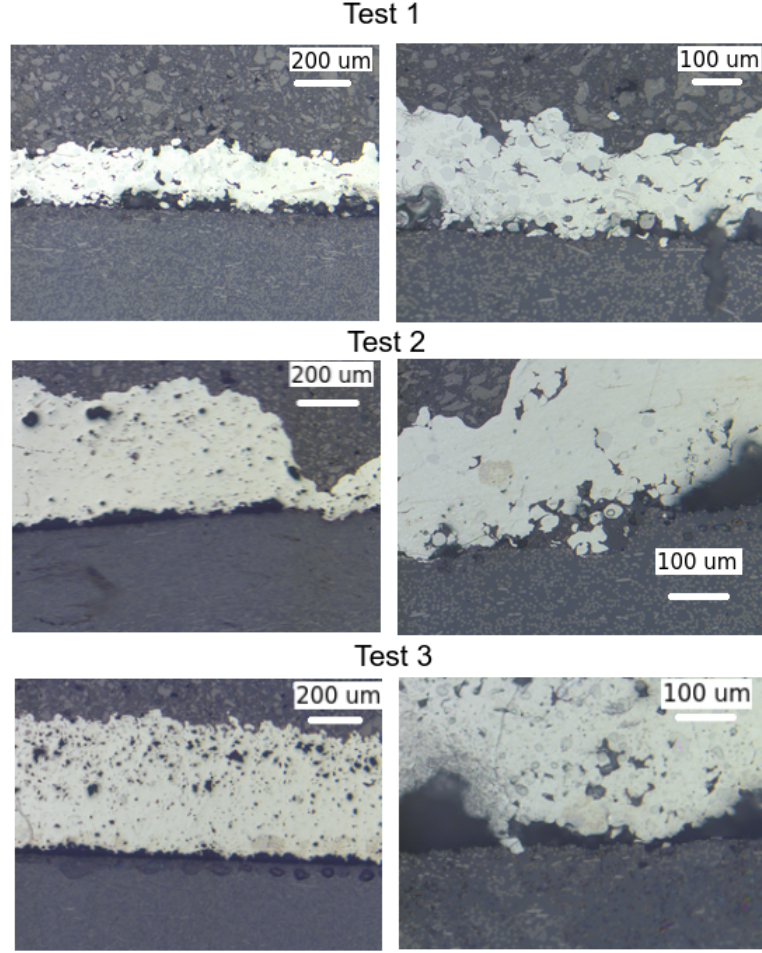


Figure 4.4: Optical microscopy cross sections of aluminum LPCS samples, for the three different temperatures.

Remarks on LPCS of pure aluminum

LPCS could produce coatings that are much thicker than in the HPCS case. Nevertheless, these coatings were porous and not adherent. If the higher temperature of the particles increases the deposition efficiency, the hot gases can melt the PEEK surface to a certain degree, probably inducing even higher thermal stresses than in HPCS. Another issue was the clogging of the metal nozzle inserts due to the high temperature, this made it impossible to go beyond of certain temperatures and to test other conditions.

4.2.2 Copper coatings

Low pressure cold spray results

To investigate the effect of the coating material, copper was used as a feed-stock powder in LPCS experiments. The driving idea here is to take advantage of the higher density of copper to obtain an increased particle penetration into the PEEK composite. Three different powder shapes were tested, as reported in chapter 2: spherical, irregular and dendritic. All the tests were carried out using the suction type powder feeder, that experienced many problems in terms of feeding the heavy and hardly flowable powders. The spherical copper powder was impossible to be sprayed without a pressurized feeder. This could be related to the relatively small particle size of this powder, leading to a low flowability inside the pipes of the system. On the other hand, a mixture of irregular and dendritic copper powders showed a better flowability and could be successfully sprayed. Also in this case, only three temperatures were tested, while the pressure was set at 0.6 MPa and the stand-off distance was set at 30 mm, as reported in Table 4.6.

| Parameters | Test 1 | Test 2 | Test 3 |
|-------------------------|--------|--------|--------|
| Pressure (MPa) | 0.6 | 0.6 | 0.6 |
| Temperature (°C) | 350 | 400 | 450 |
| Stand-off distance (mm) | 30 | 30 | 30 |

Table 4.6: Low pressure cold spray parameters for the copper powder tests

Figure 4.5 shows cross sectional images of copper LPCS samples, taken with an optical microscope. Particles are incrustated on the substrate surface, but no continuous coating is present. As expected, copper particles revealed a deeper penetration into the PEEK matrix, compared to aluminum ones, probably due to its higher density and, thus, kinetic energy. Nevertheless, LCPS was not able to provide the critical velocity to the copper to ensure the coating build-up. Although several particles are embedded in the PEEK composite, the majority rebounded, eroding the substrate

and probably detaching some of the adhering particles. From the perspective of the work performed on copper, a spraying strategy combining LPCS and HPCS can be envisaged. First, a quick LPCS pass can allow particle incrustation, preparing the surface to receive further HPCS passes, in spraying conditions compatible with the build up of a copper coating.

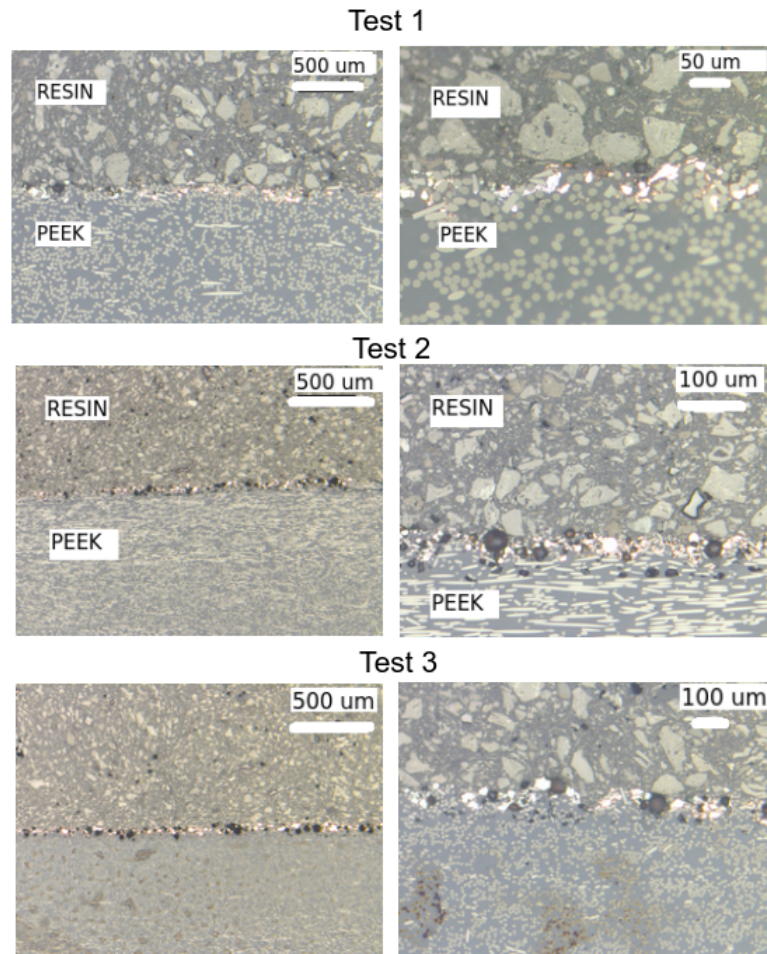


Figure 4.5: Optical microscopy cross sections of the copper sprayed samples for the three different temperatures.

4.3 Metal-polymer composite coatings

Since pure metal powders could not provide the desired results in terms of coating homogeneity and adherence, a different strategy to obtain conductive and adherent coating was employed. This was suggested by the work in [26], where a mixture of PEEK and copper powders was successfully sprayed by HPCS for the metallization of PEEK-based composites reinforced by long carbon fibers. The application was the lightning strike protection of aeronautic parts.

A mixture of aluminum and polymer powders was sprayed, in order to avoid erosion and damage of substrate and to promote coating adhesion, while giving a decent metal conductivity to the substrates. Two different polymers, belonging to the same PEAK family, were tested with this aim. The first is PEEK, being the same material as the substrate matrix. The second is the more recent PEKK. For the latter, two different grades were used: the 8002 grade, with a higher melting temperature than PEEK, and the 6002 grade, with a lower melting temperature than PEEK. Both HPCS and LPCS, each with different spraying parameters and polymer contents in the feed-stock mixture, were tested to find the best recipe. Due to the low melting temperatures of polymers as compared to the aluminum one, nozzle clogging was a crucial issue to deal with.

4.3.1 Mixed PEEK - Aluminium coatings

High pressure cold spray results

Being aluminum more ductile and having a lower density as compared to the copper used in [26], only 10% vol of PEEK was employed in the feed-stock powder mixture. Compared to the usage of a pure aluminum powder, the maximum temperature had to be reduced to avoid PEEK melting inside the nozzle. For all the experiments the nozzle used was PBI33, the powder mass flow rate was fixed at 4.5 g/min, the trans-

verse speed at 100 mm/s and the stand-off distance at 30 mm. The total pressures and temperatures explored are reported in Table 4.7.

| Parameters | c1 | c2 | c3 | c4 | c5 | c6 | c7 |
|-------------------------|-------|-------|-------|-------|-------|-------|-------|
| Nozzle | PBI33 | PBI33 | PBI33 | PBI33 | PBI33 | PBI33 | PBI33 |
| Pressure (MPa) | 1.5 | 1.5 | 2.0 | 2.0 | 2.0 | 2.0 | 2.5 |
| Temperature (°C) | 300 | 300 | 300 | 350 | 250 | 300 | 250 |
| Flow-rate (g/min) | 4.5 | 4.5 | 4.5 | 4.5 | 4.5 | 4.5 | 4.5 |
| Transverse speed (mm/s) | 100 | 100 | 100 | 100 | 100 | 100 | 100 |
| Stand-off distance (mm) | 30 | 30 | 30 | 30 | 30 | 30 | 30 |

Table 4.7: High pressure cold spray parameters for the aluminium-PEEK powder mixture tests

A track spraying strategy was adopted to compare more easily all the different conditions. Figure 4.6 shows the visual appearance of those tracks. Unlike the pure aluminum powder, it was easy to produce regular coatings with no visible defects. The addition of PEEK powder seemed to increase the deposition efficiency and the adhesion strength. In all the cross sectional optical images, shown in Figure 4.7, composite coatings are visible. Zones richer in PEEK appear in dark gray. Aluminum particles are less deformed than in pure metallic coatings and, occasionally, surrounded by heavily deformed PEEK particles, acting as binders. On the interface, there is no sign of damage and delamination. C4 spraying parameters were selected as the most promising to produce, through a surfacing spraying strategy, a coating onto disk-shaped specimens to later assess mechanical and electrical properties.

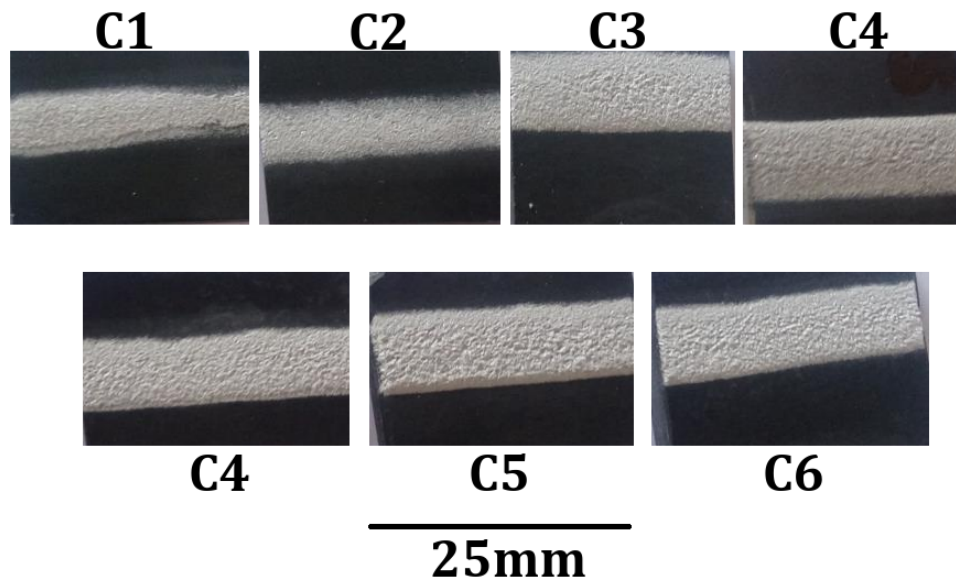


Figure 4.6: Top view of cold spray track of aluminium-PEEK.

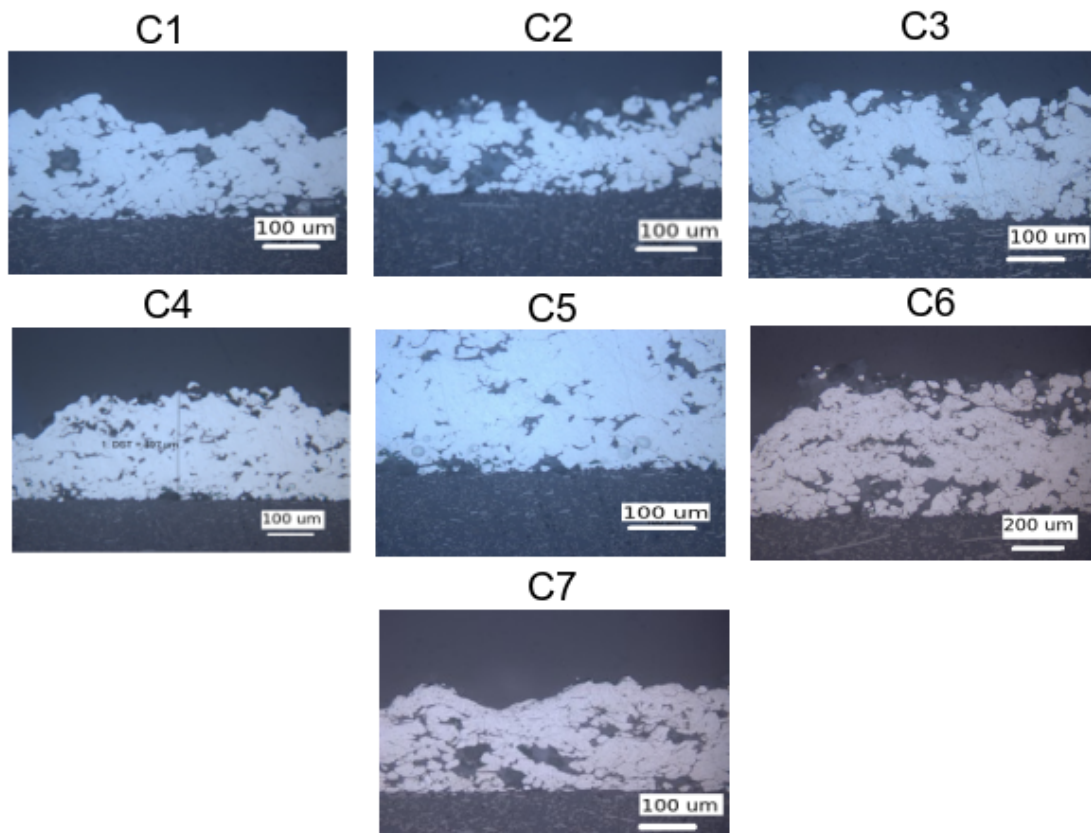


Figure 4.7: Optical images of cross section

Electrical conductivity test

The results shown below are the average resistance of each specimen and the final equivalent resistance with which computing the resistivity of the pure aluminum coating.

| | |
|---------------------------|-------------------------------------------|
| Test number | 2 |
| Imposed current (mA) | 100 |
| Resistance 1 [Ω] | $7.3 \cdot 10^{-4}$ |
| Resistance 2 [Ω] | $1.5 \cdot 10^{-3}$ |
| Resistance 3 [Ω] | $7.1 \cdot 10^{-4}$ |
| Resistance 4 [Ω] | $1.5 \cdot 10^{-3}$ |
| R_{eq} [Ω] | $1.1 \cdot 10^{-3} \pm 2.1 \cdot 10^{-4}$ |

Table 4.8: Electrical resistance measurements of HPCS PEEK-aluminum mixed powders.

In the case of mixed PEEK-aluminum coatings, resistance values measured by the Van der Pauw method are reported in Table 4.3.1. Compared to pure aluminum coatings, resistances are more dispersed because of the metal-polymer heterogeneous microstructure. In particular, PEEK richer zones, as those observed in Figure 4.7, can decrease significantly the conductivity between the two given points. The average value was calculated to have a comparison between the different tests. For a shape factor value of 1, the average resistivity was $2.23 \cdot 10^{-6} \Omega \cdot m$, corresponding to a conductivity of $4.48 \cdot 10^5 S \cdot m^{-1}$. This value is close to the one of pure aluminum coatings. It can be assumed, thus, that a 10% PEEK addition in the feed-stock powder mixture does not significantly affect the conductivity.

Adhesion test

Adhesion strength values are reported in Table 4.9. No delamination prior to the pull-off test was experienced for these samples. The specimen No. 3, showing a lower adhesion value, underwent some difficulties in the glue curing process, and should not be considered as representative. The values of adhesion strength are at least four

times higher than the pure aluminum case, confirming that the presence of PEEK particles in the mixture did increase coating adhesion on the composite substrate. Another important difference with the pure aluminum powder is the failure mode. While it was adhesive in the first case, here it is cohesive or mixed, as can be seen in Figure 4.8, showing the fracture surfaces of the samples after the pull-off test. In all cases, large zones of both surfaces still show a coating layer, which thus remained attached to the substrate. Cracks probably followed a more tortuous path, passing in some areas at the coating-substrate interface and in other areas at PEEK-aluminum particle interfaces within the coating.

| Sample | Fmax(N) | Adhesion strength (MPa) |
|--------|---------|-------------------------|
| 1 | 1025.75 | 2.1 |
| 2 | 1204.3 | 2.45 |
| 3 | 426.04 | 0.87 |
| 4 | 1489.01 | 3.04 |
| 5 | 1276.54 | 2.6 |

Table 4.9: Measured adhesion strength values for the five specimens

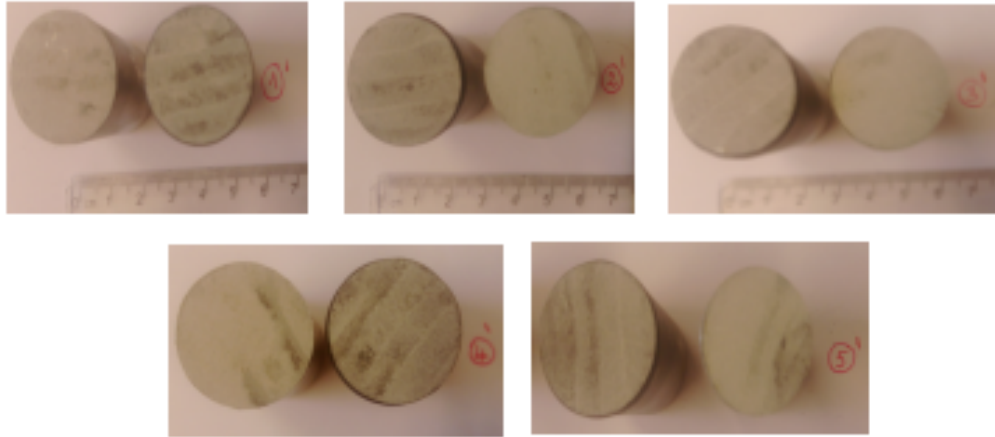


Figure 4.8: Photographic images of the fracture surfaces of Al-10%PEEK HPCS coatings.

Remarks on HPCS of mixture aluminum-PEEK

The addition of a small percentage of PEEK powder to the aluminum one allows to obtain more adherent coatings, with a small loss of conductivity. The strategy proposed by Bortolussi in [26] was successfully employed here, with a short carbon fibre composite instead of long ones, aluminum replacing copper and a lower PEEK content in the powder mixture. These results can be considered as a starting point, to be improved in further tests with LPCS.

Low pressure cold spray of mixture aluminum-PEEK

The strategy of cold spraying a metal-polymer powder was shown to be effective in HPCS. Do to the reasons already discussed concerning the differences between HPCS and LPCS, it is tempting to predict a better behavior of the mixture for the latter. In particular, the radial injection situated in the divergent part of the nozzle allowed spraying at higher temperatures in LPCS, reducing the risk of melted PEEK particles inside the nozzle and, thus, of clogging. The rectangular section nozzle introduced in Chapter 2 was chosen this time. As noted by the manufacturer, this nozzle is effective in reducing clogging when spraying very ductile metals, such as tin and zinc. The potential for a metal-polymer mixture will then be evaluated. Compared to HPCS experiments, different percentages of PEEK are tested here and a comparative study is presented hereafter. The goal is to tune the mixed powder composition and the spraying parameters towards the maximization of adhesion strength and conductivity values. Three different PEEK percentages (20-10-5 %) in the mixture were then tested to assess the differences.

Table 4.10 summarizes the main parameters tested, commenting on the quality of the coating obtained in each condition. To define some terminology, “low” states that only a first layer could be produced, “decent” qualifies a coating with higher thickness than the previous but lacking homogeneity, “good” a coating without visible defect

but somehow limited in deposition efficiency, “excellent” a homogeneous and very thick coating.

| PEEK content (%vol) | Pressure (MPa) | Temperature (°C) | Stand-off distance (mm) | Transverse velocity (mm/s) | Deposition quality |
|---------------------|----------------|------------------|-------------------------|----------------------------|--------------------|
| 20 | 0.6 | <400 | 10-20 | 5-20 | Good |
| 20 | 0.6 | 400-450 | 10-20 | 5-20 | Very good |
| 20 | 0.6 | 450-500 | 10-20 | 5-20 | Excellent |
| 10 | 0.6 | <400 | 10-20 | 5-20 | Decent |
| 10 | 0.6 | 400-450 | 10-20 | 5-20 | Very good |
| 10 | 0.6 | 450-525 | 10-20 | 5-20 | Excellent |
| 5 | 0.6 | <400 | 10-20 | 5-20 | Low |
| 5 | 0.6 | 400-450 | 10-20 | 5-20 | Very good |
| 5 | 0.6 | 450-525 | 10-20 | 5-20 | Very good |

Table 4.10: Summary table of the differences in the main tested parameters for the LPCS

PEEK 20% results

The coating shown in 4.9 can be considered the best. It was produced with a total temperature of 450°C and a pressure of 0.6 MPa. The thickness is almost 500 μm . The microstructure of this coating, as visible from the SEM cross sectional images, shows aluminum particles that are not very deformed, embedded in a PEEK matrix. Only when an aluminum particle hit another one, a metallurgical bonding with strong deformation is present. This can be a problem when the purpose is to have good conductivity. The black spots are pores resulting from the metallographic preparation of the sample. In effect, during the polishing, some aluminum particles can detach from the PEEK matrix, leaving big pores in the images. The interface and the short fibers did not appear damaged.

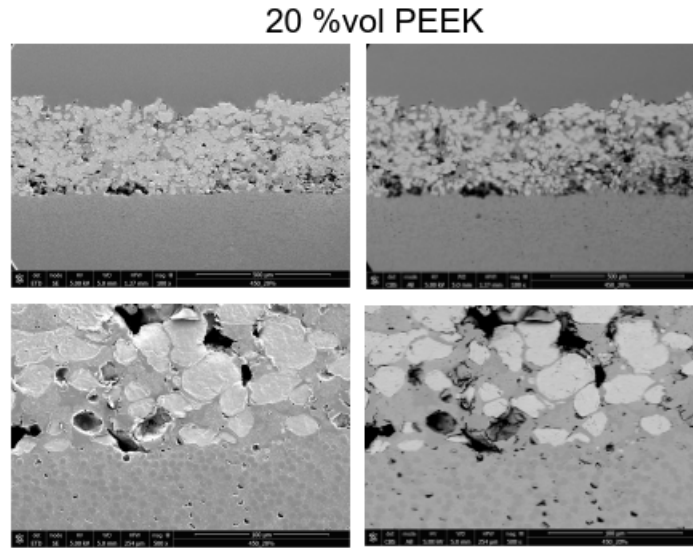


Figure 4.9: SEM cross sectional image of the best PEEK 20 %vol - Aluminum coatings.

Adhesion strength results are reported in Table 4.11. It can be noticed that the presence of the 20% vol of PEEK in the feedstock powder increases significantly the adhesion strength of coating onto the composite substrate, as compared to pure aluminum coatings. In the case of higher temperature, the adhesion strength increases

even further.

| Tensile strength (MPa) | | | | | | | |
|------------------------|------|------|------|------|------|------|----------|
| Parameters | 1 | 2 | 3 | 4 | 5 | Avg | Failure |
| 450°C 0.6 MPa | 2.24 | 1.37 | 1.58 | 1.30 | 2.20 | 1.7 | cohesive |
| 550°C 0.6 MPa | 7.61 | 6.76 | 6.37 | 6.35 | 6.83 | 6.80 | cohesive |

Table 4.11: Measured adhesion strength values of the LPCS 20%PEEK-aluminum mixed powders

Resistivity measurements shown in Table 4.12 show a surprisingly low dispersion in the case of 450°C. Indeed, this is usually not true in the case of composite coatings, where the different materials are not homogeneous in the volume. Unfortunately, in the case of 550°C the coating is not conductive at all. This can be due to PEEK particles that at high temperatures are semi-molten and surround completely aluminum particles in the coating, preventing percolation of the metallic phase and impeding the electric continuity.

| Average resistance (Ω) | | | | | | Resistivity ($\Omega \cdot m$) |
|---------------------------------|---------------------|---------------------|---------------------|---------------------|---------------------|-------------------------------------------|
| Parameters | 1 | 2 | 3 | 4 | R_{eq} | |
| 450°C 0.6 MPa | $6.6 \cdot 10^{-3}$ | $7.1 \cdot 10^{-3}$ | $6.8 \cdot 10^{-3}$ | $7.5 \cdot 10^{-3}$ | $7.1 \cdot 10^{-3}$ | $6.3 \cdot 10^{-5} \pm 1.9 \cdot 10^{-5}$ |
| 550°C 0.6 MPa | ∞ | ∞ | ∞ | ∞ | ∞ | ∞ |

Table 4.12: Electrical resistance measurements of LPCS 20% PEEK-aluminum mixed powders.

PEEK 10% results

The PEEK volume fraction in the feedstock powder was reduced to 10%. Three different spraying temperatures were tested, as before: 450°C, 500°C and 550°C. Results for are shown in Figure 4.10. A greater number of aluminum particles in this case succeeded in reaching the substrate surface. An increase in deposition efficiency with the spraying temperature could be noticed. A smaller fraction of aluminum particles are surrounded by PEEK, as compared to the 20% case. At 550temperature, there are several zones where aluminum particles in the interface are completely deformed and well connected. Even if those observations are 2D, a percolating network of the aluminum phase seems possible in this case, and so a better electrical conductivity can be expected.

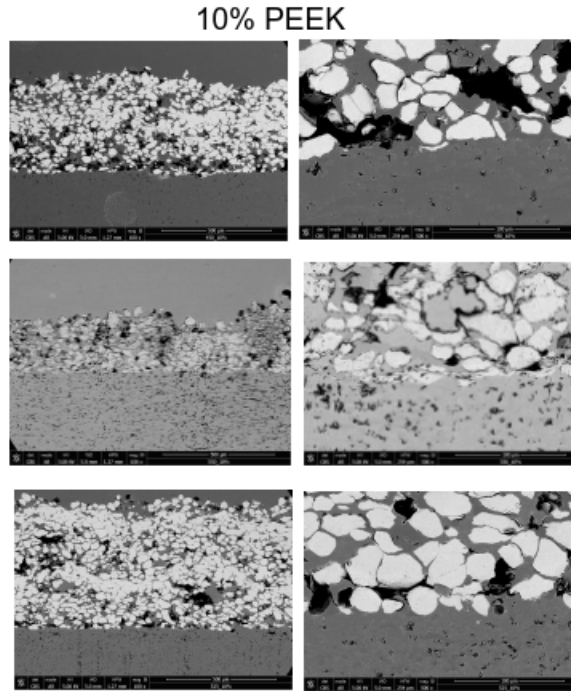


Figure 4.10: SEM cross sectional images of PEEK 10% - aluminum coatings for three different temperatures. From top to bottom: 450°C, 500°C and 550°C.

Adhesion strength measurements were performed and results are reported in Table 4.13. Unfortunately, the pull-off tests were affected by problems during sample preparation. The glue used for assembling the samples was not suitable and conducted to very poor adhesion. All samples broke at the interface with the glue. As a consequence, very little informations was obtained through these tests, capable of giving a low adhesion limit. Resistivity measurements are shown in Table 4.14 and can be considered good, as compared to pure aluminum and Al-20%PEEK coatings. This confirms the clues coming from microstructural observations. Some dispersion in the resistivity is present, again due to local inhomogeneities in the PEEK-Al local distribution.

| Tensile strength (MPa) | | | | | | | |
|------------------------|-------|-------|-------|------|------|-------|---------|
| Parameters | 1 | 2 | 3 | 4 | 5 | Avg | Failure |
| 450 °C 0.6 MPa | >0.43 | >0.85 | >0.32 | N/A | N/A | >0.5 | Glue |
| 500 °C 0.6 MPa | >0.48 | >0.53 | N/A | 0.61 | 0.53 | >0.5 | Glue |
| 550 °C 0.6 MPa | >0.94 | 0.87 | 0.30 | 1.55 | N/A | >0.91 | Glue |

Table 4.13: Measured adhesion strength values of the LPCS 10%PEEK-aluminum mixed powders

| Average resistance (Ω) | | | | | | Resistivity ($\Omega \cdot m$) |
|---------------------------------|---------------------|---------------------|---------------------|---------------------|-------------------------------------------|----------------------------------|
| Parameters | 1 | 2 | 3 | 4 | R_{eq} | |
| 450 °C 0.6 MPa | $1.2 \cdot 10^{-2}$ | $7.7 \cdot 10^{-3}$ | $2.6 \cdot 10^{-2}$ | $6.4 \cdot 10^{-3}$ | $1.3 \cdot 10^{-2} \pm 0.0055$ | $2.5 \cdot 10^{-5}$ |
| 500 °C 0.6 MPa | $4.7 \cdot 10^{-4}$ | $4.6 \cdot 10^{-4}$ | $4.3 \cdot 10^{-4}$ | $4.8 \cdot 10^{-4}$ | $4.6 \cdot 10^{-4} \pm 1.1 \cdot 10^{-4}$ | $9.2 \cdot 10^{-7}$ |
| 550 °C 0.6 MPa | $1.3 \cdot 10^{-3}$ | $1.4 \cdot 10^{-3}$ | $2.1 \cdot 10^{-3}$ | $1.3 \cdot 10^{-3}$ | $1.5 \cdot 10^{-3} \pm 4 \cdot 10^{-4}$ | $1.6 \cdot 10^{-6}$ |

Table 4.14: Electrical resistance measurements of LPCS 10% PEEK-aluminum mixed powders.

PEEK 5% results

The last PEEK volume fraction in the feed-stock powder was 5%. From SEM cross-sectional images shown in Figure 4.11, it can be noticed the prevalent presence of aluminum in the coating. Only a few PEEK particles are visible in the substrate-coating interface and in the coating thickness. Aluminum particles near the interface resemble those in a pure aluminum coating, with limited deformation and penetration into the substrate. Nevertheless, more deformed aluminum particles are visible within the coating, farther from the interface. As in the case of Al-10%PEEK mixtures, this is a clue for good electrical conductivity.

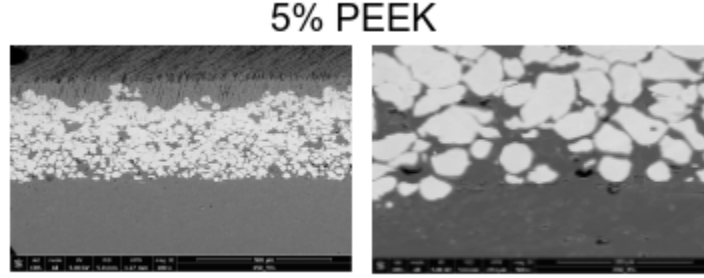


Figure 4.11: SEM cross sectional images of PEEK 5%-aluminum coatings for three different temperatures. From top to bottom: 450°C, 500°C and 550°C.

Table 4.15 presents pull-off results. As expected, adhesion values are lower, as compared to the 20% PEEK content. On the other hand, regarding resistivity measurements reported in 4.16, even better values than those of the 10% PEEK content case. On average, the conductivity of this mixture is just one order of magnitude lower compared to bulk aluminum.

| Tensile strength (MPa) | | | | | | | |
|------------------------|------|------|------|------|------|------|----------|
| Parameters | 1 | 2 | 3 | 4 | 5 | Avg | Failure |
| 450 °C 0.6 MPa | 0.84 | 0.87 | 0.69 | 0.62 | N/A | 0.75 | cohesive |
| 550 °C 0.6 MPa | 0.99 | 1.17 | 1.62 | 1.97 | 1.16 | 1.4 | cohesive |

Table 4.15: Measured adhesion strength values of the LPCS 5%PEEK-aluminum mixed powders

| Parameters | Average resistance (Ω) | | | | | Resistivity ($\Omega \cdot m$) |
|----------------|---------------------------------|---------------------|-------------------------------|---------------------|-------------------------------------------|----------------------------------|
| | 1 | 2 | 3 | 4 | R_{eq} | |
| 450 °C 0.6 MPa | $4.5 \cdot 10^{-4}$ | $4.7 \cdot 10^{-4}$ | $6.8 \cdot 10^{-4}$ | $4.8 \cdot 10^{-4}$ | $5.3 \cdot 10^{-4} \pm 5.1 \cdot 10^{-5}$ | $9.7 \cdot 10^{-7}$ |
| 550 °C 0.6 MPa | $2.1 \cdot 10^{-4}$ | $2.8 \cdot 10^{-4}$ | $2.5 \cdot 5.3 \cdot 10^{-4}$ | $2.3 \cdot 10^{-4}$ | $2.1 \cdot 10^{-4} \pm 1.1 \cdot 10^{-5}$ | $3 \cdot 10^{-7}$ |

Table 4.16: Electrical resistance measurements of LPCS 5% PEEK-aluminum mixed powders.

Figure 4.12 sums up conductivity and adhesion strength results for all the LPCS experiments with PEEK-aluminum feed-stock powder.

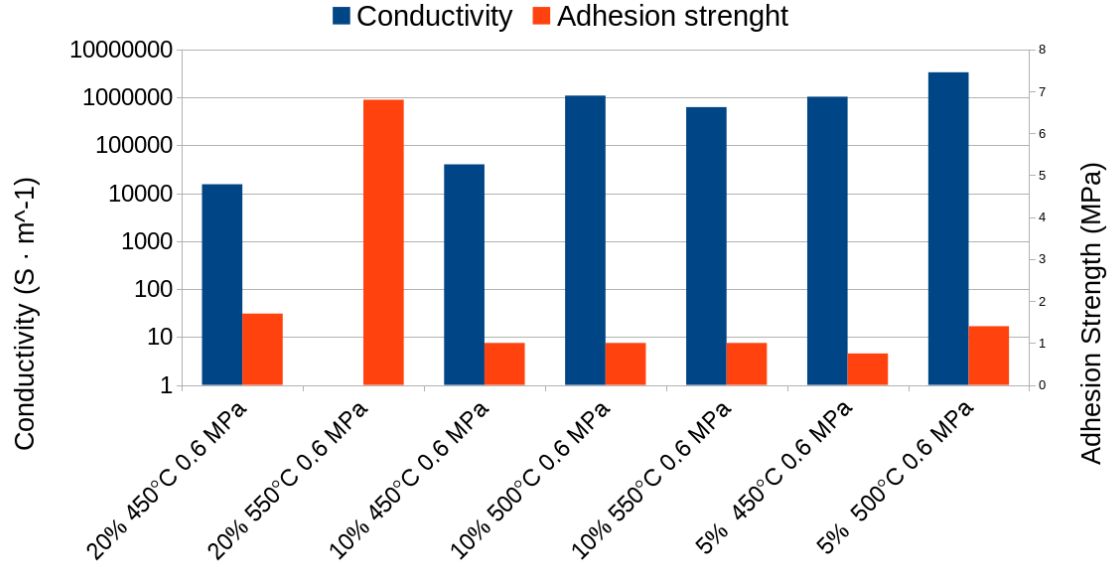


Figure 4.12: Bar chart of conductivity and adhesion strength values for different PEEK contents into the feed-stock powder mixture and spraying temperatures.

It can be noticed that, increasing the PEEK content, adhesion increases but conductivity decreases. This is due to a double effect of PEEK addition. Polymer particles help in coating adhesion, presenting a greater affinity with the substrate. The polymer-polymer bonding seems to be stronger than the metal-polymer one, especially in the case of aluminum. In effect, the penetration of aluminum particles in the substrate is limited, as well as the mechanical anchoring. On the other hand, the presence of PEEK in the coating has a detrimental effect on the electrical conductivity, especially after a certain threshold. This can be related to the tortuosity of conductive paths in the coating. When PEEK content increases, the length of the shortest path inside the metal phase becomes longer, decreasing the average conduc-

tivity. A certain inhomogeneity in the coating microstructure is also observed, with the presence of clusters of PEEK or of aluminum. This is somehow reflected by the dispersion of conductivity measurements. Inhomogeneity can be due to particle interactions in the feed-stock powder before spraying. Particles of the same type probably present more affinity and can form packs in the powder feeder which are transported together in the feeding pipe to the injector. Finally, due to the double effect of PEEK addition in the mixture, a different strategy can be proposed, consisting of a multi-layer coating with changing composition. The result would be a material presenting a gradient of composition through the thickness direction. Starting with layers richer in PEEK, a good adhesion to the substrate can be achieved. Using lower content of PEEK for the higher layers, or even a pure aluminum one, the electrical conductivity can be boosted. In the next part, this strategy will be tested, but using a different polymer powder addition, the PEKK.

4.3.2 Mixed PEKK - aluminum coatings

As already discussed, two different PEKK powders were received from Arkema: PEKK 8002, with melting temperature higher than PEEK, and PEKK 6002, with lower melting temperature than PEEK. In addition, the coefficient of thermal expansion (CTE) of PEKK differs from the aluminum one of only 34% and can contribute to a better coating cohesion. Four tests were performed, with two percentages of the two different powder grades. No conductivity tests were performed with the PEKK-aluminum mixture for these cases. In table 4.17 the results of the adhesion strength tests are reported.

| Tensile strength (MPa) | | | | | | | | |
|------------------------|----------------|-------|------|-------|------|------|------|----------|
| PEEK content | Parameters | 1 | 2 | 3 | 4 | 5 | Avg | Failure |
| 10% PEKK 8002 | 450 °C 0.6 MPa | 2.65 | 3.69 | 3.12 | 3.34 | 4.71 | 3.5 | Cohesive |
| 10% PEKK 8002 | 525 °C 0.6 MPa | >2.05 | 6.92 | >3.14 | 9.87 | 8.8 | 8.53 | Cohesive |
| 7.5% PEKK 6002 | 550 °C 0.6 MPa | 2.5 | 2.5 | 3 | >2.1 | >1.8 | 2.6 | Cohesive |
| 10% PEKK 6002 | 550 °C 0.6 MPa | 1.1 | 1.2 | 1.1 | >0.8 | >0.8 | 1.1 | Cohesive |

Table 4.17: Adhesion test results for LPCS of PEKK-Al mixed feed-stock powder.

The goal here is to evaluate the adhesion of a polymer similar to PEEK, but with possibly different chemical affinities and CTE closer to the one of aluminum. For example, in the case of higher melting temperature, the particles could be semi-molten, but at a temperature still higher than the PEEK melting temperature, increasing the chance to penetrate the surface and adhere. In fact, the PEKK 8002 at 525 °C gave the best results with an average value of 8.53 MPa.

A final experiment was performed to test the multi-layer strategy previously introduced. A first layer was cold sprayed using an aluminum-PEKK mixture as feed-stock powder. On top of that, a second layer of pure aluminum was sprayed. The SEM cross-sectional image shown in Figure 4.13 presents the result of this experiment.

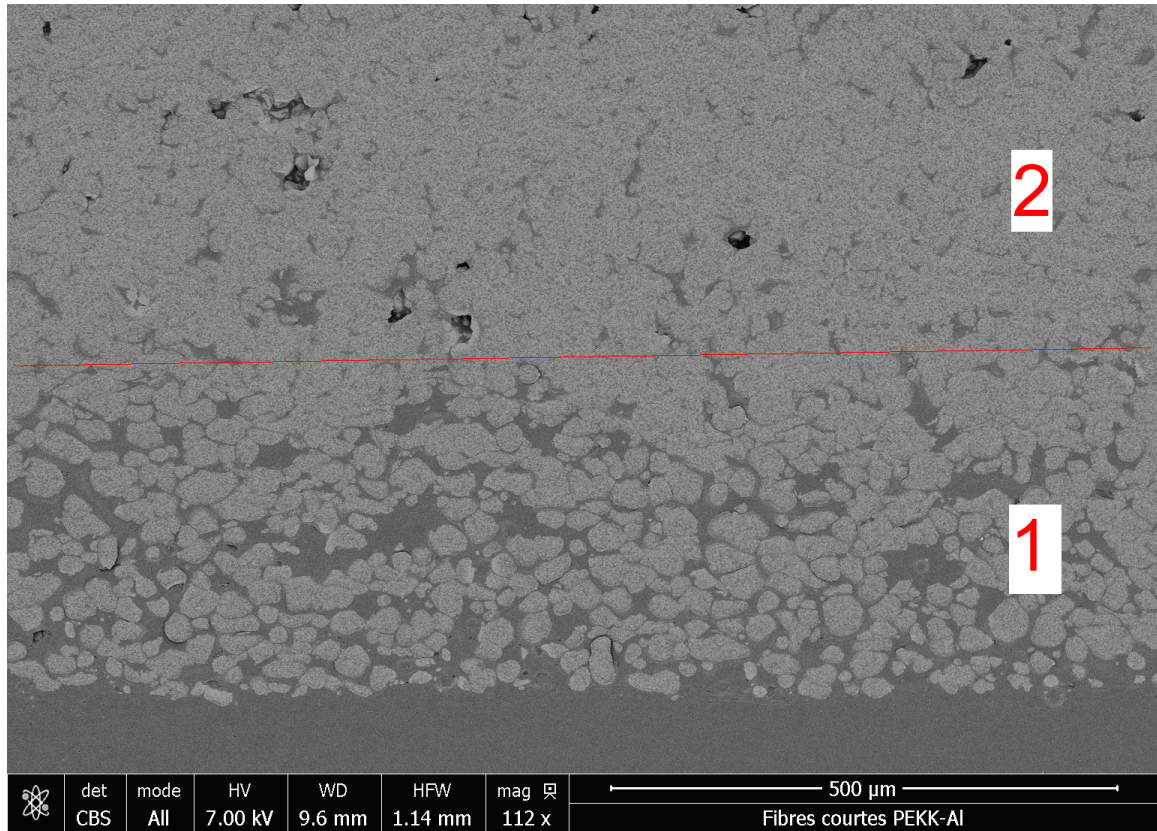


Figure 4.13: SEM cross sectional images of multilayered coating, consisting of a composite adhesion layer made of PEKK and aluminum (1) and in a pure aluminum top coating (2).

The results of the adhesion test are reported in Table 4.18. Failure in this case could be located between the two layers. The interface between the bonding PEKK-Al layer and the pure aluminum one revealed to be the weakest part in the assembly. The change in feed-stock powder composition was probably too abrupt. To go further in the development of an optimal material, a coating with a gradient of composition shall be proposed in future works, gradually reducing the percentage of PEKK from the substrate to the top layer. Hopefully, in this case, the smooth transition will help in increasing coating adhesion even further. Resistivity measurement is reported in Table 4.19. The value is the lowest among all the experiments performed. Compared to bulk aluminum, the difference is of less than an order of magnitude, confirming the need to have a pure aluminum layer on the top for an optimal coating conductivity.

| Tensile strength (MPa) | | | | | | |
|------------------------|------|------|-----|-----|-----|------|
| Parameters | 1 | 2 | 3 | 4 | 5 | Avg |
| 500 °C 0.6 MPa | 1.94 | 1.80 | 2.4 | 2.3 | 1.8 | 2.04 |

Table 4.18: Adhesion test results for for LPCS multilayered sample, made of a PEKK-Al bond coating and a pure Al top layer.

| Average resistance (Ω) | | | | | | Resistivity ($\Omega \cdot m$) |
|---------------------------------|---------------------|---------------------|---------------------|---------------------|-----------------------------------------|----------------------------------|
| Parameters | 1 | 2 | 3 | 4 | R_{eq} | |
| 500 °C 0.6 MPa | $6.1 \cdot 10^{-5}$ | $7.2 \cdot 10^{-5}$ | $6.1 \cdot 10^{-5}$ | $7.1 \cdot 10^{-5}$ | $6.5 \cdot 10^{-5} \pm 3 \cdot 10^{-6}$ | $1.1 \cdot 10^{-7}$ |

Table 4.19: Resistivity measurement by the Van der Pauw method for LPCS multilayered sample, made of a PEKK-Al bond coating and a pure Al top layer.

4.4 Conclusion

The cold spray of pure metals revealed some difficulties in obtaining a good adhesion. The addition of PEEK powder to the aluminum in a feedstock powder mixture resulted to be beneficial in this sense. The adhesion strength indeed increases with the amount of PEEK. From the experimental tests and observations, it seems that the polymer acts in two ways. The first effect is a better anchoring of aluminum particles onto the substrate. In fact, impacting PEEK particles increase the PEEK layer above carbon fibers in which the aluminium particles can penetrate. Furthermore, this is an increased protection layer for the short carbon fibers. This effect can be renamed as "mattress" effect.

Secondly, when a high temperature PEEK particle hits an aluminium one, it can trap the aluminium particle on the substrate forcing the adhesion. This effect was renamed "spiderman web" effect, because it can be visualized thinking about the way spiderman locks enemies to the wall by his spider webs.

The final microstructure is then composed of aluminum particles embedded in a PEEK matrix. In effect, a thin layer of molten/semi-molten highly deformed PEEK can be found in between aluminum particles. When a second cold spray pass is made, the new impacting aluminum particles destroy the PEEK layer preventing metal-metal contact. Once the layer is removed aluminum particles bond with the

others, with a good deformation and then percolation. In a composite metal-polymer coating, adhesion and conductivity are antagonist properties. When trying to increase one, the other will decrease. A compromise should thus be found. Alternatively, a multi-layer coating strategy can be adopted, with a composition gradient bringing the benefits of both solutions. The potential drawback could be an increased coating thickness (and weight) to complete the material transition. An interesting perspective is also to study different compositions for the polymer phase. The PEKK powders tested here, for example, revealed to be a good candidate to improve adherence. If the mechanism regulating polymer deposition in cold spray will be elucidated in future studies, other formulations can be developed to optimize the adhesion of polymer and polymer-metal composite coatings.

Another point of interest is the difference between high and low pressure cold spray. Comparing the results produced here by HPCS and LPCS onto short carbon fiber PEEK-based composites, it is clear that the adherence is better using the latter. The causes for a lesser performance of HPCS could be the higher speed and lower temperature of the particles. Indeed, even in these conditions, aluminum particles could not penetrate into the composite surface. Even if they deform at impact, rebounding is important. This is due to insufficient heating of the substrate surface. The same thermal issue is probably operating in the presence of PEEK particles when spraying a mixture. These are too cold to form a strong bonding with the substrate surface. Although the adhesion strength is increased by PEEK addition in the powder, it does not reach the same values as LPCS. In the latter, particles are slower and the temperature is higher. Several features, helping the adhesion and the creation of thick coatings, were observed:

- the presence of polymer links between PEEK particles and the substrate;
- a better adhesion of aluminum particles on the heated substrate surface;

- the “spiderman web” effect produced by semi molten PEEK particles around aluminum ones.

The next chapter will investigate by numerical CFD simulations the changes in particle speed and temperature related with the usage of the two different cold spray systems. Moreover, in the case of thermo-sensitive material, the effect of the cold spray gas on the coating build-up will be addressed. In the fifth chapter, instead, particle impact mechanical behavior onto the PEEK-based composite substrate will be investigated, trying to understand the elementary phenomena guessed in the experimental analysis.

CHAPTER 5

CFD ANALYSIS TOOL APPLIED TO COLD SPRAY PROCESS

Abstract

Several industrial processes involve biphasic gas-solid flows. To cite just a few of them, circulating fluidized beds, cyclones, solid propellant rocket motors and, of course, the cold spray process. This led to the need for opportune optimization and design methods for these flows, by means of experimental and numerical tools [100]. In recent years, thanks to the growth of computational resources, more and more numerical studies have tried to investigate the particle behavior in supersonic gas flow. In particular, CFD simulations revealed to be a powerful tool, capable of predicting phenomena involved in two-phase flows. As reported in chapter 1, an increasing number of works focused on the modeling of the cold spray process in the last years. In almost all of these works, the particulate phase was described as Lagrangian. Early studies found that the effect of solid phases on gas flow was neglected, in the so-called one-way Lagrangian description. Afterwards the increasing computational resources allowed to keep into account this effect (*i.e.* two-way coupling) as well as the particle-particle interaction (four-way coupling). In the paper of Samareh [101], an Eulerian description of the particle phase was adopted. This approach allowed the study to range from diluted to dense particulate flow in the cold spray process. In the case of dense flows, particle-on-gas and particle-particle effects are not negligible. The simulation shows strong effects in the flow regime where the particulate phase is present. Location and strength of Mach diamond shocks are both affected. Moreover, increased particle size and loading significantly reduce the particle impact speed. The Lagrangian description is not suitable to catch these phenomena. In the two-

way Lagrangian approach, gas and particle phases are coupled by means of source (*i.e.* exchange) terms in the momentum and energy equations, as well as in the fully Eulerian approach. Anyway, in the latter, the effect of the volume fraction of each phase is in the conservation laws. In this way, the interaction between the two phases is already present in convective terms. Then, in the case of denser particulate phases, an Eulerian description is preferable [102]. In the two-way Lagrangian description, stochastic differential equations (SDE) must be solved using notional-particle based Monte-Carlo mesh technique, increasing the complexity and the computational time when a great number of particles is considered [103]. A few works involved a Direct Numerical Simulation (DNS) model in simpler cases to obtain a real description of the cold spray process, due to very high computational cost. Instead, many preferred the Reynold Average Navier Stokes (RANS) approach, in which the Navier-Stokes equations are averaged. Different turbulence models have been chosen such as k-epsilon, the shear stress and many others. Several models for the drag coefficient, for the momentum exchange and for the heat transfer between the solid and the gas phase are available in the literature. All these works have as final common goal, which is the realization of a reliable tool to predict particle velocities and temperatures. An opportune optimization and new design of the cold spray equipment can be a natural extension of these studies.

Résumé en français

Plusieurs procédés industriels font intervenir des écoulements biphasiques gaz-solide. Pour n'en citer que quelques-uns, les lits fluidisés circulants, les cyclones, les moteurs de fusée à propergol solide et, bien sûr, le procédé de projection à froid. Cela a conduit à la nécessité de disposer de méthodes d'optimisation et de conception appropriées pour ces écoulements, au moyen d'outils expérimentaux et numériques [100]. Ces dernières années, grâce à l'augmentation des ressources informatiques, de

plus en plus d'études numériques ont tenté d'étudier le comportement des particules dans un écoulement gazeux supersonique. En particulier, les simulations CFD se sont révélées être un outil puissant, capable de prédire les phénomènes impliqués dans les écoulements diphasiques. Comme indiqué dans le chapitre 1, un nombre croissant de travaux se sont concentrés sur la modélisation de la projection à froid au cours des dernières années. Dans la quasi-totalité de ces travaux, la phase particulaire a été décrite comme lagrangienne. L'effet de la phase particulaire sur l'écoulement gazeux a été négligé dans les premières études dans la description lagrangienne dite à sens unique. Par la suite, l'augmentation des ressources de calcul a permis de prendre en compte cet effet (c'est-à-dire le couplage à deux voies) ainsi que l'interaction entre les particules (couplage à quatre voies). Cependant, dans l'article de Samareh [101], une description eulérienne de la phase particulaire a été adoptée. Cette approche a permis l'étude de l'écoulement de particules diluées à denses dans le spray froid. Dans le cas d'un écoulement dense, l'effet des particules sur le gaz et l'effet particule-particule ne sont pas négligeables. La simulation a montré un effet important de la phase particulaire sur le gaz. L'emplacement et la force des chocs mach diamant sont tous deux affectés. De plus, l'augmentation de la taille et du débit des particules réduit considérablement la vitesse d'impact des particules. La description lagrangienne ne permet pas de saisir ces phénomènes. Dans l'approche lagrangienne bidirectionnelle, les phases gazeuse et particulaire sont couplées au moyen de termes sources (c'est-à-dire d'échange) dans l'équation de quantité de mouvement et d'énergie, ainsi que dans l'approche totalement eulérienne. De toute façon, dans cette dernière, l'effet de la fraction volumique de chaque phase est inclus dans les lois de conservations. Cela permet que l'interaction entre les deux phases soit déjà présente dans les termes convectifs. Ainsi, dans le cas d'une phase particulaire plus dense, une description eulérienne est préférable [102]. De plus, dans la description lagrangienne à deux voies, l'équation différentielle stochastique (SDE) doit être résolue en

utilisant une technique de maillage de Monte-Carlo basée sur des particules fictives, ce qui augmente la complexité et le temps de calcul lorsqu'un grand nombre de particules est considéré [103]. Peu de travaux ont impliqué une modélisation DNS dans des cas plus simples pour obtenir une description réelle du processus de projection à froid, en raison du coût de calcul très élevé. Au lieu de cela, beaucoup d'autres ont préféré l'approche RANS dans laquelle les équations de Navier-Stokes sont moyennées. Différents modèles de turbulence ont été choisis tels que k-epsilon, la contrainte de cisaillement et bien d'autres. Différents coefficients de traînée pour l'échange de momentum et le modèle de transfert de chaleur entre la phase solide et la phase gazeuse sont disponibles dans la littérature. Tous ces travaux ont comme objectif commun final la réalisation d'un outil fiable pour prédire la vitesse et la température des particules sans système de mesure coûteux. Une optimisation opportune et une nouvelle conception de l'équipement de projection à froid peuvent être une extension naturelle de ces études.

5.1 Introduction

In this chapter, the CFD modeling approach and the obtained results of the simulation of high and low pressure cold spray systems will be presented. In the case of the HPCS, only the gas phase was analyzed while, for LPCS, a complete biphasic model was developed and its results were compared with experimental measurements. The goal of this study was not to build an accurate and predictive tool, but rather to investigate the gas-dynamic phenomena occurring in the two cold spray systems used, to better understand the difference in their behavior, in particular in the conditions for producing coatings onto PEEK based composites. Particle temperature and speed at impact are the most important parameters to take into account when dealing with classic cold spray onto metallic substrates. Nevertheless, when the substrate is thermo-sensitive, as the polymer-based composite studied in this thesis, gas

temperature is another important factor which must be considered. If particle velocity can be measured by experimental methods, particle temperature is much more difficult to assess experimentally. The classical infrared cameras are not suitable for cold spray high speed particles, due to the relatively low radiation and high speed. Eulerian approach and an open-source and customizable software, such as OpenFOAM, are the first two original ingredients in this work. A full 3D geometry of the rectangular-section nozzle provided by Dycomet for its LPCS has been implemented and results compared with HPCS model. In the latter, an axisymmetric geometry has been adopted. Aluminum and PEEK particle properties have been used for the solid phase to investigate the different behaviors. The presented models should be intended not as a replacement of the experimental measurements, always preferred to have reliable data, but only as an aid in a better understanding of the phenomena involved in the experiments. Some hypotheses about particle behavior in producing cold spray coatings onto thermo-sensitive substrates have been formulated and solutions envisaged.

5.2 Theoretical model

The theoretical aspects of the CFD model used in this thesis for cold spray nozzles is presented and discussed in this part, justifying the hypotheses and the assumptions that have been made.

5.2.1 Choice of the framework

First of all, when dealing with particles in a gas flow, three main model classes exist.

- one way behavior: the gas flow is resolved and used to calculate particle motion, while particles do not affect the gas behavior;
- two ways behavior: particles do affect gas behavior, so that gas and particle

flows are coupled, but particles do not interact with themselves;

- four ways behavior: as the two ways, but in addition particle-particle interactions are considered.

Depending on the volume fraction of the dispersed phase, solid-gas biphasic flows can be categorized as presented in Table 5.1. Considering the cold spray process, in the majority of spraying conditions the flow can be considered as dilute [31]. As shown in the introduction this led many works in literature to privilege the one way behavior, but in other works the effect of particle phase on the gas flow was found to be strong and not negligible. Leitz et al. in [44] indicated that a value of 10^{-6} as solid volume fraction is typical in cold spray experiments.

| Case | Solid volume fraction V_f |
|----------------|-----------------------------|
| Dilute flow | $V_f < 0.01\%$ |
| Kinetic Regime | $0.01\% < V_f < 10\%$ |
| Dense flow | $V_f > 10\%$ |

Table 5.1: Flow types depending on the volume fraction of the solid phase.

Another possibility is to adopt an Eulerian description for the solid phase too. Several possibilities are reported in 5.1 for the two different descriptions of the solid phase. In the case of Eulerian-Eulerian treatment, both phases are considered continuous fully inter-penetrating media. Conservation equations can be obtained by an opportune averaging process and the unclosed terms must be treated by means of constitutive relationships, such as the Kinetic Theory of Granular Flow (KTGF). In the Eulerian-Lagrangian description, several approaches are possible for the Lagrangian discrete solid phase. In the Discrete Phase Model (DPM) for dilute flow, a one-way and two-way effects can be considered, but no particle-particle interaction can be included. A mixed Eulerian-Lagrangian and Eulerian-Eulerian approach characterizes the Dense Discrete Phase Model with the Kinetic Theory of Granular Flow (DDPM-KTGF). This allows the treatment of particle-particle interactions, using the Lagrangian description only in the case of low solid volume fractions. The

Discrete Element Method, coupled with CFD, resulted to be more and more adopted to include all the bi-phase effects. In DEMm in fact, the collisions between particles are computed numerically, solving the equations of motion. This method is suitable for dense flows, but the computational effort is higher compared to the other methods. The latest and pretty new Eulerian-Lagrangian approach is the Computational Particle Fluid Dynamics (CPFD) numerical scheme, incorporated within the Multi-Phase Particle-in-Cell (MP-PIC) method. It seems to reduce the computational cost compared to the CFD-DEM involving particle parcels and a different way to compute particle collision forces. Considering the pros and cons of all these methods and approaches, in this work, as already reported, an Eulerian-Eulerian description of the bi-phase problem was chosen. Although the lack of works in literature adopting this choice for the cold spray process, except for the already mentioned work of Samareh [101], the better description of the interaction between the two phases and the particles themselves, together with a reduced computational cost were the reasons for such a choice.

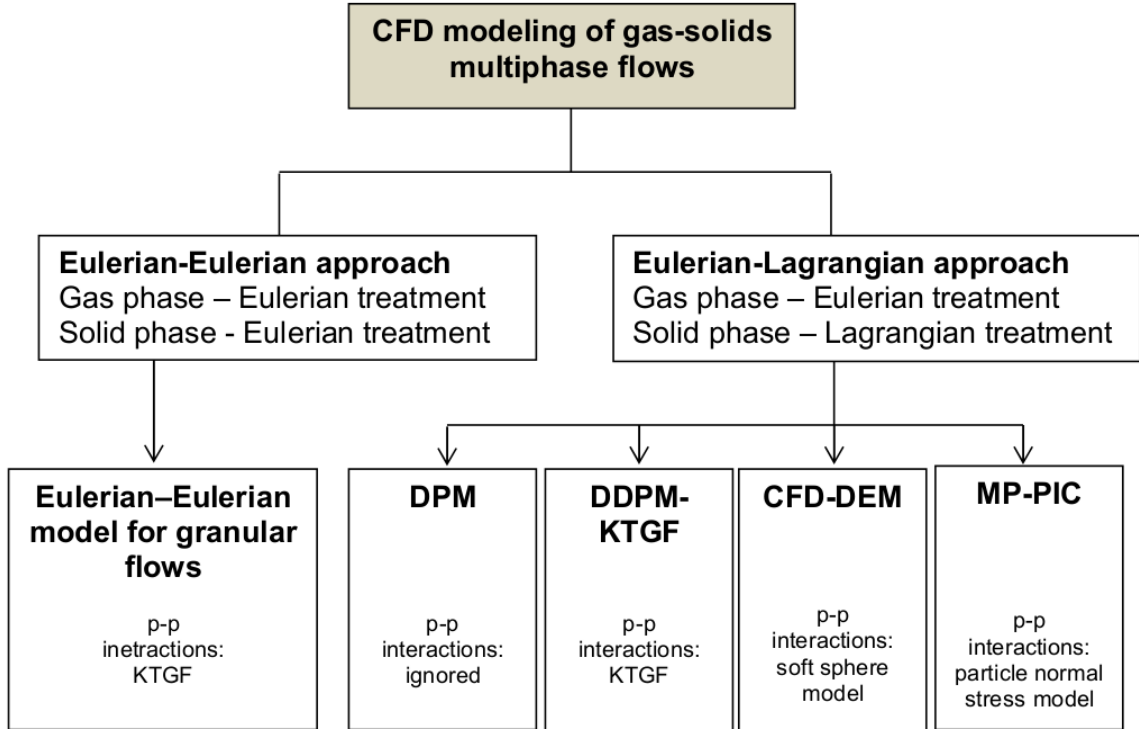


Figure 5.1: Summary of model approaches for gas-solids flows from [104]

High pressure and low pressure cold spray systems differ for the pressure and temperature ranges, but also for powder injection points. Although, in both equipments the acceleration of the gas is realized by means of a de Laval nozzle, as shown in Figure 5.2. In the high pressure system used in this study, the injection is axial and

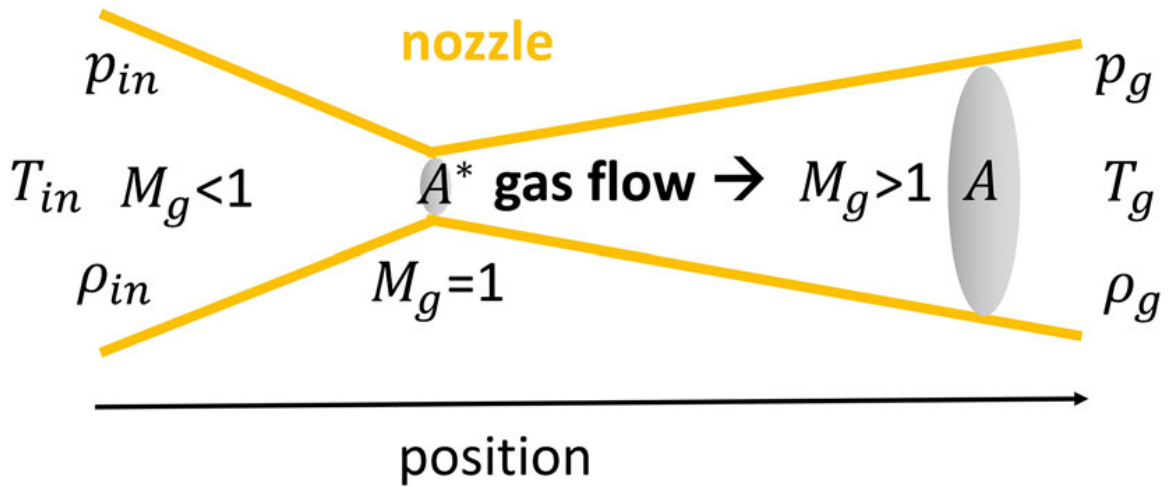


Figure 5.2: Gas flow in a nozzle (left), heating and acceleration of a particle in a gas flow (right).

located in the convergent part of the nozzle. In the low pressure system the injection is in the divergent part and it is radial. The nozzles used in the two equipment are different too. In HPCS the nozzle used is a polymeric convergent divergent, while in LPCS it is a stainless steel short convergent divergent nozzle base plus a circular or rectangular divergent insert. Several considerations have to be done in order to prepare a CFD simulation. The first issue is the computational cost. Axisymmetrical (wedge) geometry is the most used in the case of particle axial injection. It is also adopted in this work. In the case of the more complicated rectangular cross section geometry of the low pressure adapter, a full 3D model was developed. Regarding the model implementation, even if an in-house code is often preferable for specific problems, the effort and time to code the entire model were considered excessive with respect to the scope of this work. Commercial software, on the other hand, is expensive, especially for massive parallel super-computing needed to solve big problems in a reasonable time, and offer limited possibilities for customization. Open-source software seemed to be an interesting solution and OpenFoam (www.openfoam.com) was finally chosen.

5.2.2 Problem formulation

In the Eulerian-Eulerian case, gas and particles are both continuous phases and fully inter-penetrating [105]. They are considered in terms of volume fractions and are continuous functions of space and time. The sum of the two volume fractions is equal to one [106]. An averaging process allows to obtain the conservation equations for mass, momentum and energy for both phases [107]. In order to close out the model, the kinetic theory of granular flow [108] is used for the viscous solid stress tensor. The most important limitation is that variation of particle properties, distribution and shape could not be considered without increasing the number of equations and the computational cost.

In the case of a gas-solid two phase problem, the following assumption must be verified to ensure the continuity of the two phases:

$$\alpha_s + \alpha_g = 1 \quad (5.1)$$

where α_s is the solid volume fraction and α_g the gas volume fraction.

The three Navier-Stokes equations and a state equation define the gas dynamic problem. The first equation is the scalar mass conservation, the second is the vector momentum conservation and the third is the scalar energy conservation. A perfect gas state equation is used.

The mass continuity equation can be written for each phase, indicated by the subscript i , as follows:

$$\frac{\partial(\alpha_i \rho_i)}{\partial t} + \nabla \cdot (\alpha_i \rho_i \bar{u}_i) = 0 \quad (5.2)$$

where ρ_i is the density of phase i and u_i its velocity field. The momentum equations for both phases read as:

$$\frac{\partial(\alpha_i \rho_i \bar{u}_i)}{\partial t} + \nabla \cdot (\alpha_i \rho_i \bar{u}_i \bar{u}_i) = \nabla \underline{S}_i + (\alpha_i \rho_i \bar{g}_i) - \underline{I}_i \quad (5.3)$$

For the solid phase, S can be rewritten as:

$$\nabla \underline{S}_s = \nabla \cdot (\alpha_s \underline{\tau}_s - \alpha_s \nabla(p) - \nabla(p)_1) \quad (5.4)$$

where $\underline{\tau}_s = \mu_s \underline{D}_s + (\lambda_s - \frac{2}{3}\mu_s)(\nabla \cdot \bar{u}_s) \underline{I}_s$ is the solid stress tensor, $\nabla(p)_1$ the gradient of granular pressure, λ_s the solid bulk viscosity and $\underline{D}_s = \frac{1}{2}[\nabla \bar{u}_s + \nabla \bar{u}_s^T]$

For the gas phase, S can be rewritten as:

$$\nabla \underline{S}_g = \nabla \cdot (\alpha_g \underline{\tau}_g - \alpha_g \nabla(p)) \quad (5.5)$$

where $\underline{\tau}_g = \mu_g \underline{D}_g - \frac{2}{3} \mu_g (\nabla \cdot \bar{u}_g) \underline{I}_g$ is the gas stress tensor. Further equations, describing the flow regime, are necessary to complete the system for the global solid stress tensor. Three different regimes can be identified depending on the volume fraction of the solid phase. The simpler one is the kinetic one, suitable in the case of dilute flow. Here, particles and gas interact, but the very low solid volume fraction does not allow particle-particle interactions. Increasing the solid volume fraction, a collisional regime is considered and particles could collide among them. In the case of a dense flow, a frictional regime with a Coulombian friction has to be considered. In this work, only kinetic and collisional regimes have been considered. The constitutive relations are reported below [109].

- The total granular (solid) viscosity:

$$\mu_s = \mu_{s,kin} + \mu_{s,col} \quad (5.6)$$

- Kinetic ($\mu_{s,kin}$) and collisional ($\mu_{s,col}$) viscosities:

$$\mu_{s,kin} = \frac{4}{5} \alpha_s \rho_s g_{0,ss} d (1 + e_s) \sqrt{\psi_s / \pi} \quad (5.7)$$

$$\mu_{s,col} = \frac{1}{15} \sqrt{\psi_s} \pi \rho_s d g_{0,ss} \alpha_s^2 (1 + e_s) + \frac{1}{16} \sqrt{\psi_s} \pi \rho_s d_s \alpha_s + \frac{10}{96} \sqrt{\psi_s} \pi \frac{\rho_s d}{g_{0,s} (1 + e_s)} \quad (5.8)$$

- The total granular pressure (kinetic and collisional terms):

$$p_s = p_{s,kin} + p_{s,col} \quad (5.9)$$

- Kinetic ($\mu_{s,kin}$) and collisional ($\mu_{s,col}$) granular pressure terms:

$$p_{s,kin} + p_{s,col} = \alpha_s \rho_s \psi_s + 2 \rho_s (1 + e_s) \alpha_s^2 g_{0,s} \psi_s \quad (5.10)$$

- Radial distribution function:

$$g_{0,ss} = [1 - (\frac{\alpha_s}{\alpha_{s,max}})^{\frac{1}{3}}]^{-1} \quad (5.11)$$

- Solid bulk viscosity:

$$\lambda_s = \frac{4}{3}\alpha_s^2\rho_s d \quad (5.12)$$

- Conductivity of granular temperature:

$$k_{\Theta,s} = \frac{150\rho_s d \sqrt{\psi_s \pi}}{384(1+e_s)g_{0,ss}} [1 + \frac{6}{5}(1+e_s)\alpha_s g_{0,s}]^2 + 2\alpha_s^2 \rho_s d g_{0,s} (1+e_s) \sqrt{\frac{\psi_s}{\pi}} \quad (5.13)$$

- Kinetic energy dissipation due to inelastic collisions:

$$\gamma_{\Theta,s} = 3(1-e_s^2)\alpha_s^2\rho_s g_{0,ss}\psi_s (\frac{4}{d}\sqrt{\frac{\psi_s}{\pi}} - \nabla \bar{u}_s) \quad (5.14)$$

- Kinetic energy dissipation due to fluid friction:

$$\phi_{\Theta,s} = -3\beta\psi_s \quad (5.15)$$

The $I_{s,g}$ source terms in the momentum equation is the sum of the possible momentum interactions between the two phases, such as drag, lift, wall lubrication and turbulent dispersion force. In the case of solid and gas phases, only the drag force will be retained, the other terms being suitable only in a gas-liquid case. The drag force represents the interaction (*i.e.* the mutual aerodynamic exchange force) between the gas and the solid particles. It is a key issue in modeling the cold spray process and can be described in the following equation:

$$F_{drag} = \frac{1}{2}C_d Re_p \rho_g A_p (u_g - u_p)|u_g - u_p| \quad (5.16)$$

where $Re_p = \rho_g d_p |u_g - u_p| / \eta_g$ is the Reynolds number relative to the particle-gas motion, η_g the dynamic viscosity, d_p the particle diameter, A_p the particle cross sectional area, ρ_g the gas density, C_d the drag coefficient. Different models are proposed in the literature for the drag coefficient C_d , describing the force transfer between the gas and the particles. Following the article [44], the Plessis-Masliyah correlation seems to give the best results. Unfortunately, this model is available in OpenFOAM only in the Lagrangian formulation. An Eulerian implementation of this model was then coded in this work. This model is derived from the pressure drop for a gas flow through a porous medium and is valid for any solid volume fraction. The drag coefficient is expressed as:

$$C_d(Re_p) = 4 \frac{(1 - \alpha_s)}{3} \left(\tilde{A} \frac{\alpha_s}{1 - \alpha_s} + \tilde{B} \cdot Re_p \right) \quad (5.17)$$

with the coefficients:

$$\tilde{A} = \frac{26.8(1 - \alpha_s)^3}{\alpha_s^{2/3}(1 - \alpha_s^{1/3})(1 - \alpha_s^{2/3})^2}$$

$$\tilde{B} = \frac{(1 - \alpha_s)^2}{(1 - \alpha_s^{2/3})^2}$$

In order to evaluate the viscous dissipation in the fluid at high velocity in the internal energy and the flow compressibility, the energy equation must be solved for both phases:

$$\frac{\partial[\alpha_i \rho_i (h_i + k_i)]}{\partial t} + \nabla \cdot [\alpha_i \rho_i (h_i + k_i) \bar{u}_i] = \alpha_i \frac{\partial p}{\partial t} + \nabla \alpha_i \alpha_{eff} \nabla h_i + K_{ht} \Delta T \quad (5.18)$$

considering

$$h = e + pv$$

then

$$\frac{\partial[\alpha_i \rho_i (e_i + k_i)]}{\partial t} + \nabla \cdot [\alpha_i \rho_i (e_i + k_i) \bar{u}_i] = -\left[\frac{\partial \alpha_i}{\partial t} p + \nabla \alpha_i \bar{u}_i p\right] + \nabla \nabla \alpha_i \alpha_{eff} \nabla h_i + K_{ht} \Delta T \quad (5.19)$$

where e is the internal energy, k is the kinetic energy, α_{eff} is the effective thermal diffusivity and $K_{ht} \Delta T$ is the convective heat transfer between the solid and the gas phases. $h_t = (k_{gas} Nu)/d_s$ is the convective heat transfer coefficient, where k_{gas} is the thermal fluid conductivity, d_s the particle diameter and Nu is the Nusselt number. Before the definition of the Nusselt number, some assumptions about the internal temperature of the solid particles must be stated. The Biot number is defined as $Bi = \frac{k}{h} L$ where k $[[W/(m^2 \cdot K)]]$ is the thermal conductivity, h $[\frac{W}{m^2 \cdot K}]$ is the convective heat transfer coefficient and L $[m]$ a characteristic length of the considered geometry. This number evaluates the ratio between the internal solid particle thermal conductivity and the convective heat transfer coefficient with the flow. In the cold spray process, it presents a very low value [110]. For this reason, the majority of works in literature agree about the assumption of uniform temperature within particles, at least for metallic feed-stock powders. In contrast, this is not true in the case of polymer particles, as reported in [91], a work about the temperature evaluation of in-flight polymer particles in the cold spray process. Due to the low value of the thermal conductivity of polymer materials, a temperature gradient inside the particle exists. Due to the high sensitivity of polymer behavior on the temperature, this leads to a gradient of mechanical properties along the particle radius at the impact. In the present thesis, for the sake of simplicity, both metallic and polymer particles are treated with a uniform temperature. To evaluate the Nusselt number, needed for the convective heat transfer coefficient, a heat transfer model has to be chosen. In OpenFOAM, the only model available is the Ranz Marshall one, but it was found to be adequate only for particle Reynolds numbers up to 200. In cold spray conditions,

the Reynolds number can attain values up to 1000 [111]. Two new correlations were then implemented in the code, following the work of Li and Mason [112]. The first, suitable for particle Reynolds number between 200 and 1500, and the second for Reynolds number up to 1500. The Nusselt number will then be evaluated as follows.

- For Reynolds number less than 200 (Ranz Marshall):

$$Nu(Re_p) = 2 + 0.6Re_p^{0.5}Pr^{0.33} \quad (5.20)$$

- For Reynolds number within 200 and 1500 (Kempt et al.[113])

$$Nu(Re_p) = 2 + 0.5Re_p^{0.5}Pr^{0.33} + 0.02Re_p^{0.8}Pr^{0.33} \quad (5.21)$$

- For Reynolds number above 1500 (Frantz, J.F. [114])

$$Nu(Re_p) = 2 + 0.000045Re_p^{1.8} \quad (5.22)$$

where $Pr = \eta_g C_{p,g} / \lambda_g$ is the Prandtl number of the gas, η_g the dynamic viscosity of the gas, $C_{p,g}$ the gas heat capacity and λ_g the thermal conductivity of the gas.

The turbulence model adopted in this study is the $k - \epsilon$, in the Reynolds-averaged Navier-Stokes equations (RANS). This model allows for a considerable reduction in computational time compared to the Direct Numerical Simulation (DNS) approach. The basic assumption of the RANS model is to represent flow field variables, as for example the velocity $u(x, t)$, as the sum of a mean component $\bar{u}(x)$, which is only a function of the position in space, and fluctuating component $u'(x, t)$ varying with space and time. This is known in literature as the Reynolds decomposition.

$$u(x, y, z, t) = \bar{u}(x, y, z) + u'(x, y, z) \quad (5.23)$$

where

$$\bar{u}(x, y, z) = \frac{1}{t_0} \int_t^{t-t_0} u(x, t) dt$$

The $k-\epsilon$ turbulence model is characterized by a system of two equations and assumes that Reynolds stresses are proportional to the mean velocity gradients [115, 116]. This approach generally results in a good approximation of the turbulence kinetic energy and the turbulence dissipation rate for flows with a dominant continuous phase, such as the gas phase in our case. The two quantities mentioned above are then present in the equations below:

$$\frac{\partial \rho k}{\partial t} = \nabla \cdot (\rho D_k \nabla k) + T_p - \rho \epsilon \quad (5.24)$$

$$\frac{\partial \rho \epsilon}{\partial t} = \nabla \cdot (\rho D_\epsilon \nabla \epsilon) + \frac{c_1 \epsilon}{k} \left(T_p + c_3 \frac{2}{3} k \nabla \cdot u \right) - c_2 \rho \frac{\epsilon^2}{k} \quad (5.25)$$

where k is the turbulent kinetic energy, D_k the effective diffusivity for k , T_p the turbulent kinetic energy production rate, ϵ the turbulent kinetic energy production rate, D_ϵ the effective diffusivity for ϵ . c_1 , c_2 and c_3 are model coefficients, taking in our case the following values: $c_1 = 1.44$, $c_2 = 1.92$, $c_3 = 0$.

5.3 Model implementation in OpenFOAM

Several CFD commercial software programs are present on the market. Among them, Ansys Fluent and Autodesk CFD are probably the most popular ones. They have fancy end-user interfaces and tutorials and user-guides are easily available and complete. Despite these advantages, they are expensive and, even more importantly, they cannot be modified by the user. In this thesis, the choice of using open source software was made. OpenFOAM is a free and open-source CFD software package produced by OpenCFD Ltd [9]. It presents three main advantages: it is free of charge, it is open-source (*i.e.* the code can easily be modified to be improved by anyone) and peer

reviewed, it is object-oriented, so that users can introduce new models and solvers without changing the main code, independently from the discretization scheme used, providing great flexibility and simplicity of use. The programming language is C++.

OpenFOAM uses the Finite Volume Method (FVM) to discretize and solve complex fluid dynamics problems. It is based on the integral form of the conservation laws, rather than their differential form. FVM may also be based on unstructured (e.g. triangular) mesh and is thus suitable for irregular and complex geometries. Accuracy and stability are then improved even in the case of sharp gradients inside a domain (shock-capturing property) [117]. First of all, the volume of interest is created and divided into small volumes or cells, obtaining the so-called mesh. Then, the initial and boundary conditions necessary for solving the conservation equations are defined and applied to the geometry. OpenFOAM discretizes the equations using the previously built mesh.

In this work, the two-phase transient Eulerian-Eulerian solver, namely “twoPhaseEulerFoam”, is selected to model both high and low pressure cold spray systems. Gmsh, an open-source software, is used to draw sketches and to generate a structured mesh. High performance computing was necessary to run the simulations in an appropriate time. The cluster of the laboratory, running 43 nodes with 256 GB of RAM each, was used. OpenFOAM revealed to be prone to massive parallelization thanks to domain decomposition.

5.4 Simulations of high and low pressure cold spray systems

As already mentioned, two different strategies were adopted for modeling the two cold spray systems used in the present thesis. Since LPCS was the preferred choice in the experimental part of this work, the CFD analysis concentrated on this system. For HPCS, only a monophasic analysis was performed. Results are presented together with some considerations about particle temperatures. Nevertheless, experimental

velocity measurements for both systems are reported in this chapter, to validate the model in one case and provide data for a comparison between the HPCS and LPCS.

5.4.1 High pressure cold spray

Model setup

In the case of HPCS, taking advantage of the symmetry of the nozzle and of the powder injector, an axisymmetrical model is suitable. The simulation domain is illustrated in fig. 5.3 and corresponds to the real geometry of the system used in the experiments. It is constituted by a 7 cm long pre-chamber and by a convergent divergent nozzle, with the same sizes as the PBI33 nozzle. The injection point is located in the middle of the convergent part of the nozzle. The nozzle exit is located at $x = 0.224$ m. The area ratio (*i.e.* the nozzle exit section over the throat section area) is equal to 14.7, as in the HPCS system nozzle. In order to consider the evolution of particle temperatures and velocities outside the nozzle, an outflow region of 5 cm length is considered. Starting from a 2D sketch, an angular extrusion of less than 5° is required by OpenFOAM to consider an axisymmetrical geometry (wedge design). In Figure 5.3, the axisymmetrical geometry and the surface patches name are shown. Different mesh sizes are chosen for the various subdomains of the model, as shown in Figure 5.4. A coarser mesh (label C) is adopted for the pre-chamber, the first part of the convergent and for the left side of the openspace. A finer mesh (Label F) applies to the second part of the convergent, where the particle injector is located. Finally, the finest mesh (FF) is chosen for the divergent and for the adjacent part of the openspace. This choice was necessary in order to better catch all the rapid phenomena in the divergent part and in the outflow of a supersonic nozzle. A total of 297450 elements are present.

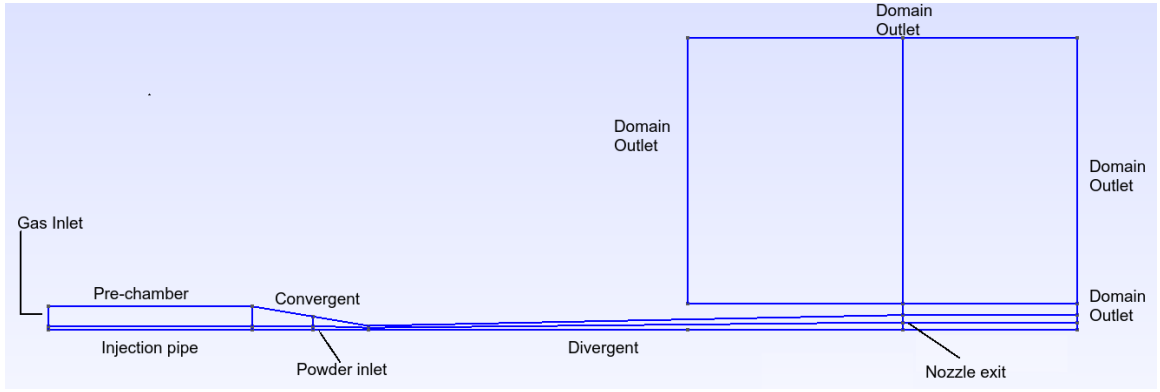


Figure 5.3: Simulation domain for HPCS.

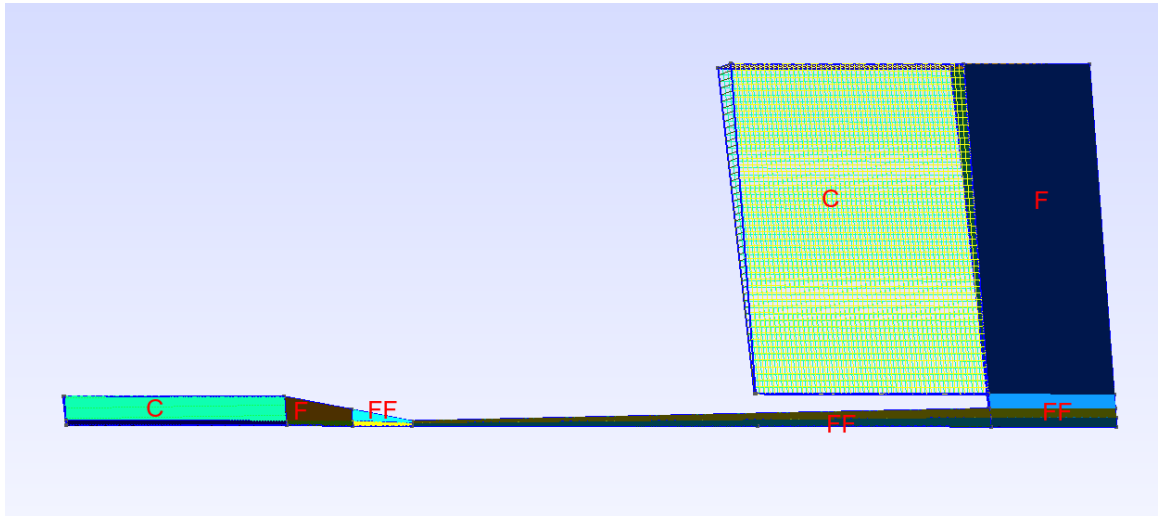


Figure 5.4: Mesh of the simulation domain for HPCS. Labels C, F and FF referred to different mesh size, respectively coarse, fine, finest. Values are reported in Table 5.2

| Meshsize (μm) | Label |
|----------------------|-------|
| 800 | C |
| 400 | F |
| 100 | FF |

Table 5.2: Meshsize of different parts for the HPCS case

In Tables 5.3 and 5.4, the boundary conditions for both phases and different patches are reported. The inlet values used correspond to the experimental pressure and temperature parameters of the HPCS system. On wall surfaces, a no-slip condition is chosen for gas velocity and a slip condition for particle velocity. On wedge surfaces, a special cyclic wedge condition is necessary to ensure axisymmetrical fields. The ambient conditions (pressure at 101325 Pa and temperature 300 K) are chosen for the top and left edges of the outflow space. A zero gradient condition is imposed on the other boundaries.

| Gas phase boundary conditions | | | |
|-------------------------------|-----------------------------------------|---------------------------------------------------------|---------------------------------|
| Patch | Pressure | Gas temperature | Gas velocity |
| Gas Inlet | $p_0 = p + \frac{1}{2}\rho u ^2 = cost$ | $T_0 = T(1 + \frac{\gamma-1}{2\gamma}\Psi u_2) = cost$ | $\frac{d\bar{u}}{d\bar{n}} = 0$ |
| Particle Inlet | $p_0 = p + \frac{1}{2}\rho u ^2 = cost$ | $T_0 = T(1 + \frac{\gamma-1}{2\gamma}\Psi u_2) = cost$ | $\frac{d\bar{u}}{d\bar{n}} = 0$ |
| Walls | $\frac{dp}{d\bar{n}} = 0$ | $\frac{dT}{d\bar{n}} = 0$ | $\bar{u} = (0, 0, 0)$ |
| Right Outlet | $\frac{dp}{d\bar{n}} = 0$ | $\frac{dT}{d\bar{n}} = 0$ | $\frac{d\bar{u}}{d\bar{n}} = 0$ |
| Top and Left Outlet | $p=cost$ | $T=cost$ | $\frac{d\bar{u}}{d\bar{n}} = 0$ |
| Wedge Surfaces | OpenFOAM wedge cyclic condition | | |

Table 5.3: Gas phase boundary conditions for the HPCS model

| Particle phase boundary conditions | | | |
|------------------------------------|---------------------------------|------------------------------------------------------|----------------------------------|
| Patch | Particle temperature | Particle velocity | Particle volume fraction |
| Gas Inlet | $\frac{dT}{d\bar{n}} = 0$ | $\frac{d\bar{u}}{d\bar{n}} = 0$ | $\alpha_s = 0$ |
| Particle Inlet | $T = cost$ | $\frac{d\bar{u}}{d\bar{n}} = 0$ | $\alpha_s = 10^{-6}$ |
| Walls | $\frac{dT}{d\bar{n}} = 0$ | $u - u_{wall} = \beta \frac{\partial u}{\partial n}$ | $\frac{d\alpha_s}{d\bar{n}} = 0$ |
| Right Outlet | $\frac{dT}{d\bar{n}} = 0$ | $\frac{d\bar{u}}{d\bar{n}} = 0$ | $\frac{d\alpha_s}{d\bar{n}} = 0$ |
| Top and Left Outlet | $T=cost$ | $\frac{d\bar{u}}{d\bar{n}} = 0$ | $\frac{d\alpha_s}{d\bar{n}} = 0$ |
| Wedge Surfaces | OpenFOAM wedge cyclic condition | | |

Table 5.4: Particle phase boundary conditions for the HPCS model

To impose the initial conditions, the domain is divided into two parts. The first ranges from the prechamber to the throat, the second from the throat to the end of the domain. This allows the simulations to speed up and avoid convergence problems close to inlet surfaces. In the first part of the domain, pressure and temperature initial values are set equal to the respective boundary conditions and the initial velocity is zero. In the second part of the domain, ambient pressure, temperature and zero velocity have been imposed.

Simulation results

During a transient simulation it is not always obvious to reach a steady state. This is not the case here. A steady state solution could be reached after 0.02 seconds in all the simulated cases. The time step is of the order of 10^{-7} seconds and the computing time on the cluster is about twelve hours to reach the steady state solution. Stability was assured, imposing an under-relaxation factor. The latter works by limiting the variation of a variable from one iteration to the next. A factor of 0.7 assured the convergence of the solution.

As explained in the previous section, the inlet total pressure and total temperature correspond to the experimental parameters imposed to the cold spray equipment. Four different combinations are tested, as reported in Table 5.5. The inlet total pressure in the powder injector is 10% higher than the total pressure, as in the experimental case.

| Inlet pressure (MPa) | Inlet temperature ($^{\circ}\text{C}$) |
|----------------------|------------------------------------------|
| 3 | 300 |
| 3 | 350 |
| 2.5 | 300 |
| 2.5 | 350 |

Table 5.5: Inlet cold spray parameters for HPCS.

Let's come now to the analysis of simulation results. The pressure computed in the exit section of the nozzle is lower than the ambient pressure, so the resulting field is an over-expanded flow. A Mach diamond structure and a series of oblique and rarefaction waves alternate until the ambient conditions are reached.

The maximum speed can be obtained only in the case of a nozzle designed for each specific condition, so that the pressure in the exit section of the nozzle is equal to the ambient one. Instead, the over-expanded flow of the HPCS nozzle allows confinement of the jet that could be desirable for many cold spray applications. Due to higher inlet pressure in the injector, the carrier gas is faster than the cold spray gas and it enters

the nozzle throat with a temperature very close to the ambient one. In this simulation, it seems that the the hot inlet cold spray gas does not affect the temperature of the carrier gas as visible in the Figure 5.7. In these simulations the heat exchange between this hot gas and the injector wall was neglected. Moreover, in the real case the cold spray gas is not injected in the whole nozzle section, but by means of a small hole close to the pre-chamber wall. This means that a swirling effect on the cold spray gas can be present, increasing the carrier gas reheating in the convergent nozzle. Unfortunately, this aspect was impossible to be verified experimentally. The axy-symmetrical profiles of velocity and temperature are reported respectively, in Figures 5.5 and 5.6.

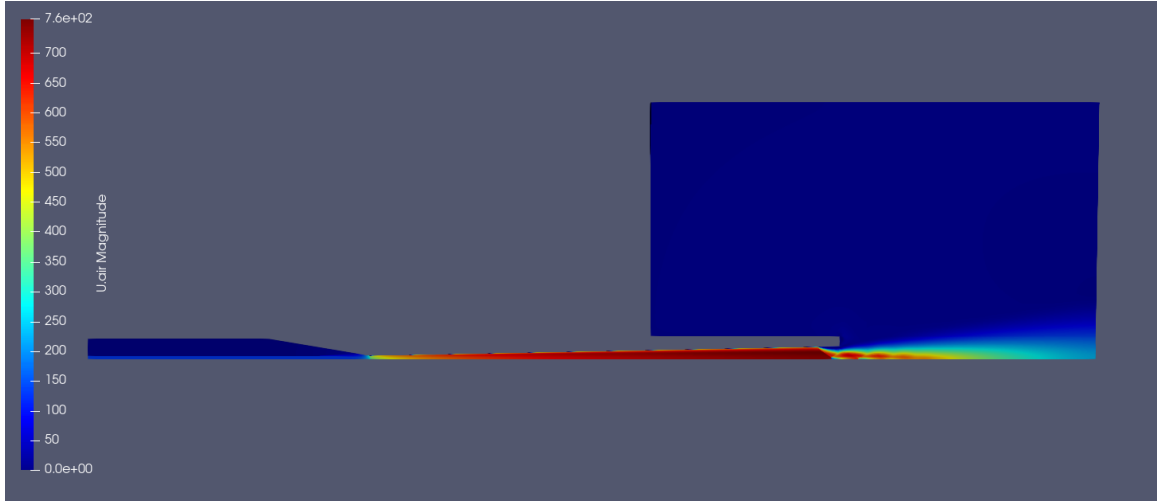


Figure 5.5: Axy-symmetrical gas velocity profile

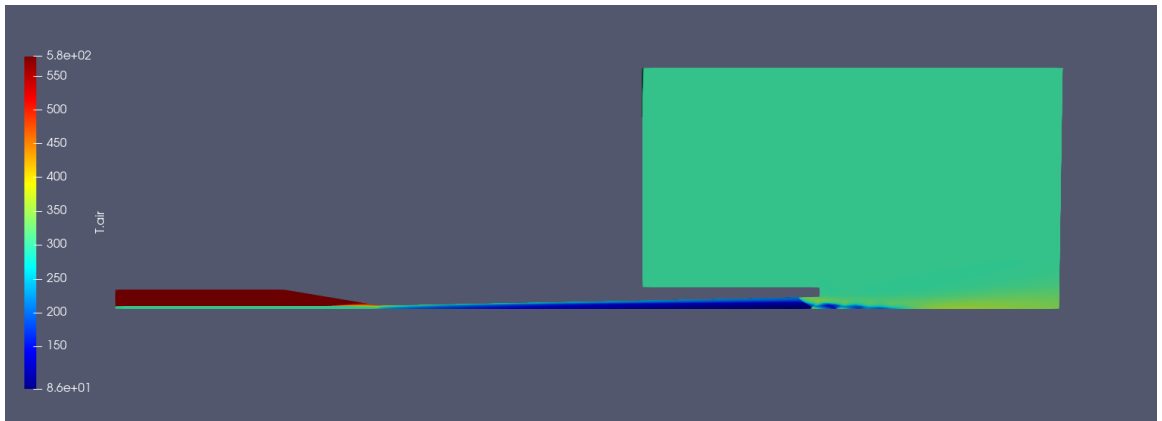


Figure 5.6: Axy-symmetrical gas temperature profile

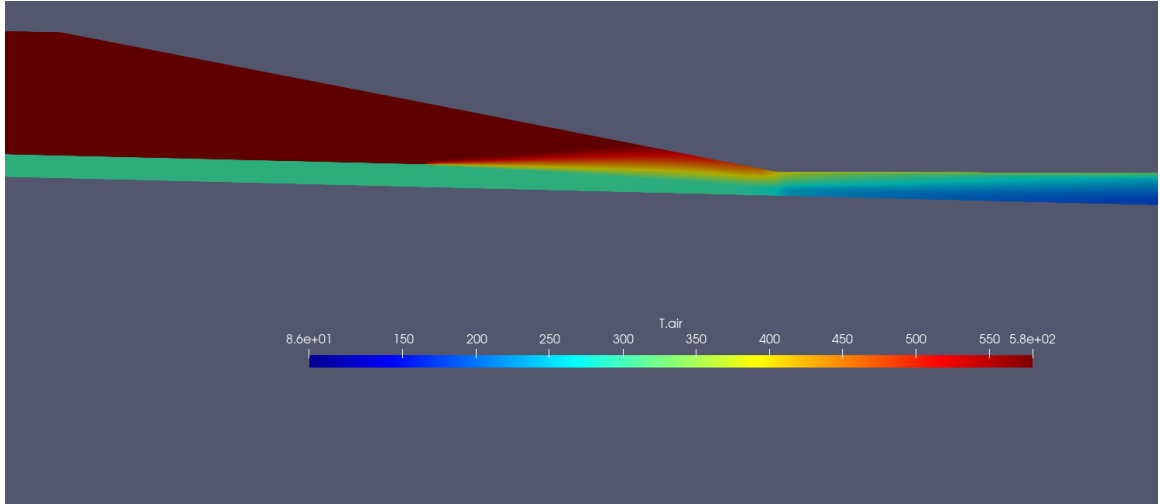


Figure 5.7: Close up of gas temperature profile on the particle injection point

Results for velocity and temperature of the gas phase along the nozzle axis are reported, respectively, in Figures 5.8 and 5.9.

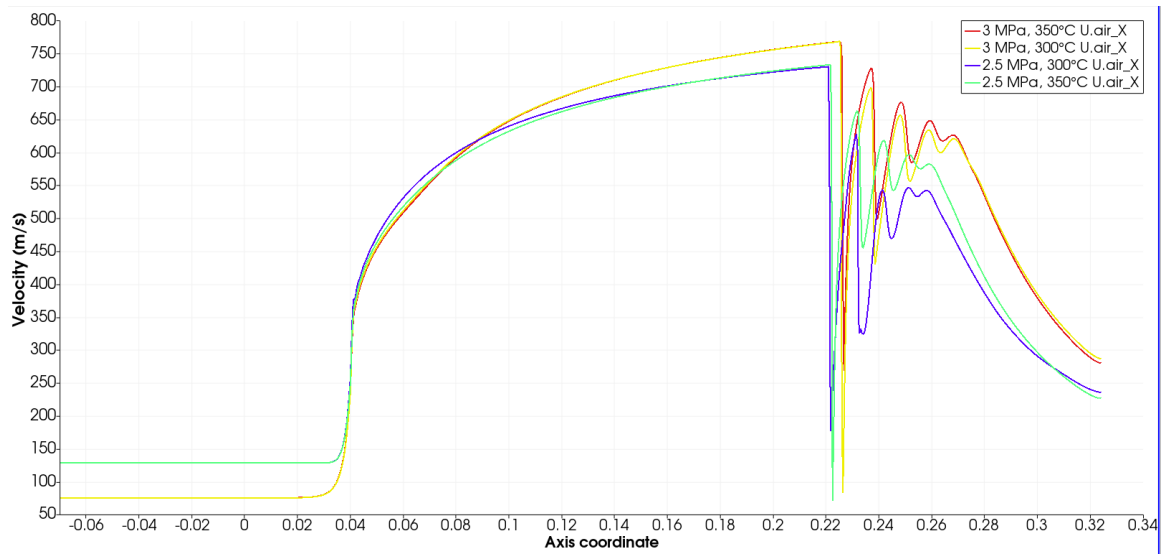


Figure 5.8: Gas velocity along the nozzle axis for the four different setups.

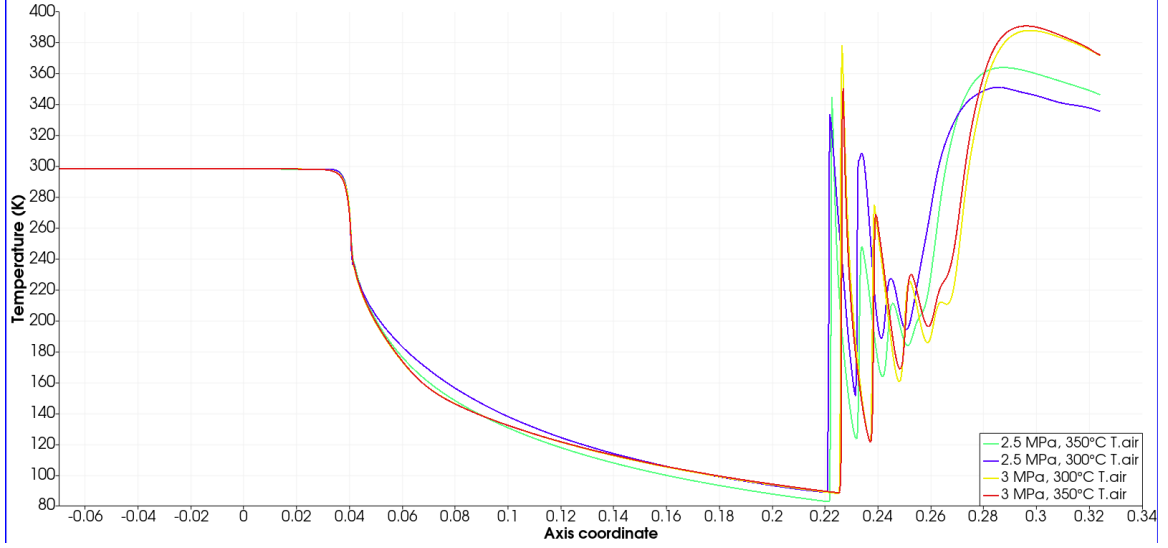


Figure 5.9: Gas temperature along the nozzle axis for the four different setups.

Attempts to include an Eulerian solid particle phase were performed but did not bring reliable results in this configuration and were not reported in the manuscript. Probably, the strong oblique shock at the nozzle exit led to non-physical behavior of the drag force model, heavily perturbing particle motion. To compensate the lack of information in the model on particle in-flight characteristics, some experimental measurements are reported in the next part.

Particle velocity experimental measurements

DPV2000 particle velocity measurements reported here were collected during the PhD thesis work of Pierre Emmanuel Leger [95], who worked in the same conditions and with the same material. In the case of $35\ \mu\text{m}$ average particle diameter, total pressure of 3 MPa and temperature of 300°C , the average speed is $600 \pm 150\text{m/s}$. This will be the reference value used, in the next chapter, in particle impact simulations for HPCS conditions. For what concerns particle temperature, some simple considerations can be done here based on simulation results for the gas phase. Gas temperature along the axis is very low in the divergent part of the nozzle. As a consequence, although the wall-gas heat transfer phenomenon is not taken into account in this simulation

and, thus, the simulated temperature field underestimates the real one, particle temperature at impact should be not far from the ambient one (25°C).

5.4.2 Low pressure cold spray

Model setup

Among LPCS nozzle inserts available and used in the experiments, only the rectangular section divergent insert is modeled in this thesis. In effect, the most interesting experimental results, as presented in chapter 3, were obtained with this type of insert. This nozzle is composed of a first short convergent-divergent part, with a circular section and a finite throat length. The latter allows, according to [118], to reduce the turbulence. At the divergent exit, a radial injection point for the powder is present, followed by a long divergent insert with a rectangular section, that completes the nozzle geometry. In LPCS, thus, powder injection is not axial but radial, lacking the requirements for an axisymmetrical model. For this reason, a full 3D model needs to be adopted. To avoid an excessively complex geometry, with rounded and squared geometries to be connected, and to have a structured mesh in the whole domain, the first part of the nozzle was modeled as having a rectangular cross sections too. Even if the shape of those sections is changed, the original nozzle area ratio is maintained, to preserve the same gas dynamic behavior as the real system. An outflow region outside the nozzle is considered to take into account ambient conditions and observe the evolution of particle velocities and temperatures at the experimental stand-off distance.

The simulation domain is illustrated in Figure 5.10. It is constituted by a 4 cm long pre-chamber, a 1.2 cm long convergent, a 0.7 cm long finite throat, a first 0.6 cm long divergent nozzle, a 0.07 cm constant section where the powder injection point is located, the 14 cm long divergent insert. The area ratio (*i.e.* the nozzle exit section over the throat area) is equal to 6.2, as in the real nozzle. The simulation domain

ends with an outflow region 4 cm long. Starting from a 2D sketch, a 0.3 cm extrusion is realized. Different mesh sizes were chosen for the sub-domains mentioned above. Figure 5.11 illustrates the meshed domain.

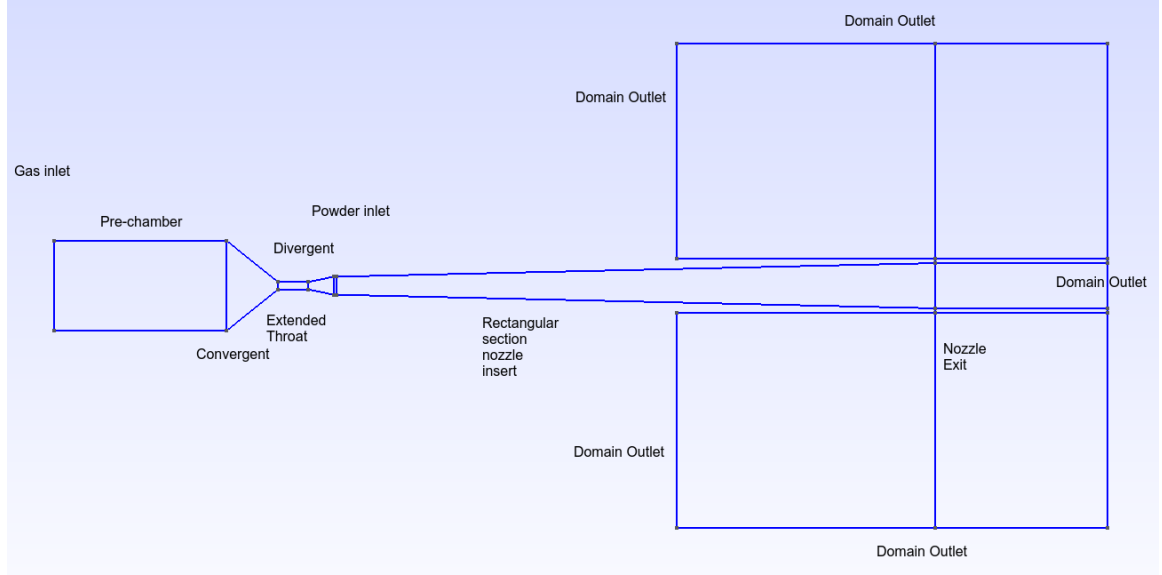


Figure 5.10: Simulation domain for LPCS.

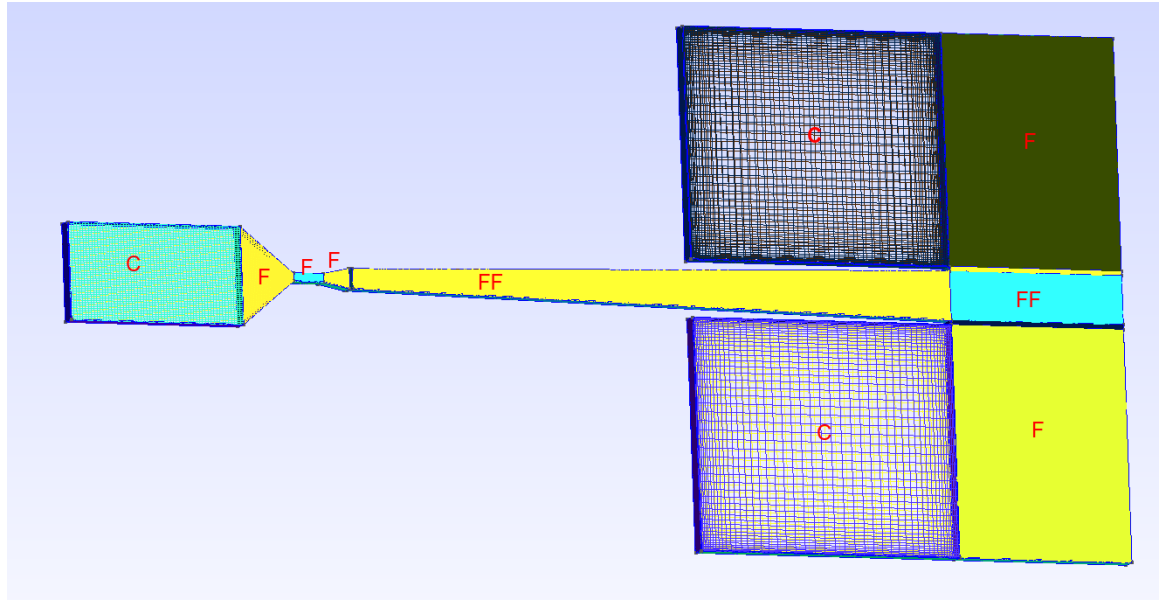


Figure 5.11: Mesh of LPCS model

Different mesh sizes are chosen for the various subdomains of the model, as reported in Table 5.6. A coarser mesh (label C) is adopted for the pre-chamber, the first part of the convergent and for the left side of the openspace. A finer mesh (Label

| Meshsize (μm) | Label |
|----------------------|-------|
| 700 | C |
| 300 | F |
| 100 | FF |

Table 5.6: Meshsize of different parts for the LPCS case

F) is applied for the second part of the convergent, where particle injection is located. Finally, the finest mesh (FF) is reserved for the divergent and to the adjacent part of the openspace. In the thickness direction, a mesh size of $300\mu m$ is set, to limit the computational cost. A total of 1857132 elements are present in the meshed domain.

In Tables 5.7 and 5.8 the boundary condition applied to the different patches are reported. The inlet values used correspond to the actual cold spray machine pressure and temperature parameters. On the wall surfaces, a no-Slip condition is set for gas velocity and a slip condition for particle velocity. The ambient conditions are assumed for the top, left, rear and front surfaces of the outflow space. On the right boundary of the openspace, the same conditions as those of the nozzle walls are imposed, considering this surface as the substrate. The physical parameters for the solid phase are shown in Table 5.9.

| Gas phase boundary conditions | | | |
|-------------------------------|-----------------------------------------|---------------------------------------------------------|---------------------------------|
| Patch | Pressure | Temperature | Velocity |
| Gas Inlet | $p_0 = p + \frac{1}{2}\rho u^2 = cost$ | $T_0 = T(1 + \frac{\gamma-1}{2\gamma}\Psi u_2) = cost$ | $\frac{d\bar{u}}{d\bar{n}} = 0$ |
| Particle Inlet | $p_0 = p + \frac{1}{2}\rho u^2 = cost$ | $T_0 = T(1 + \frac{\gamma-1}{2\gamma}\Psi u_2) = cost$ | $\frac{d\bar{u}}{d\bar{n}} = 0$ |
| Walls | $\frac{dp}{d\bar{n}} = 0$ | $\frac{dT}{d\bar{n}} = 0$ | $\bar{u} = (0, 0, 0)$ |
| Right Outlet | $\frac{dp}{d\bar{n}} = 0$ | $\frac{dT}{d\bar{n}} = 0$ | $\frac{d\bar{u}}{d\bar{n}} = 0$ |
| Top,Left,Front,Rear Outlet | $p=cost$ | $T=cost$ | $\bar{u} = (0, 0, 0)$ |

Table 5.7: Gas phase boundary conditions for the HPCS model

| Particle phase boundary conditions | | | |
|------------------------------------|---------------------------|------------------------------------------------------|----------------------------------|
| Patch | Temperature | Velocity | Volume fraction |
| Gas Inlet | $\frac{dT}{d\bar{n}} = 0$ | $\frac{d\bar{u}}{d\bar{n}} = 0$ | $\alpha_s = 0$ |
| Particle Inlet | $T = cost$ | $\frac{d\bar{u}}{d\bar{n}} = 0$ | $\alpha_s = 10^{-6}$ |
| Walls | $\frac{dT}{d\bar{n}} = 0$ | $u - u_{wall} = \beta \frac{\partial u}{\partial n}$ | $\frac{d\alpha_s}{d\bar{n}} = 0$ |
| Right Outlet | $\frac{dT}{d\bar{n}} = 0$ | $\frac{d\bar{u}}{d\bar{n}} = 0$ | $\frac{d\alpha_s}{d\bar{n}} = 0$ |
| Top,Left,Front,Rear Outlet | $T=cost$ | $u - u_{wall} = \beta \frac{\partial u}{\partial n}$ | $\frac{d\alpha_s}{d\bar{n}} = 0$ |

Table 5.8: Particle phase boundary conditions for the HPCS model

| Material | Density [$\frac{kg}{m^3}$] | Heat capacity [$\frac{J}{kg \cdot K}$] | Diameter [μm] | Volume Fraction |
|-----------|------------------------------|------------------------------------------|----------------------|-----------------|
| Aluminium | 2700 | 921 | 25 | 10^{-6} |
| PEEK | 1300 | 320 | 50 | 10^{-6} |

Table 5.9: Physical parameters of the solid phase.

Simulation results

A steady state solution is reached after 0.04 seconds in all the simulated cases. The time step is $6 \cdot 10^{-8}$ seconds and the computing time on the cluster is about twelve hours to reach the steady state solution. Stability was assured imposing an under relaxation factor. Under-relaxation works by limiting the amount in which a variable changes from one iteration to the next. In this case, a factor 0.8 assured the convergence of the solution. In low pressure experiments, presented in chapter 3, the main process parameter studied was the gas stagnation temperature. In fact, differently from the high pressure system, here the gas pressure range available is rather reduced. All experiments were performed at 0.6 MPa, with different temperatures. To reproduce the experimental parameters, in CFD simulations, the pressure is fixed at 0.6 MPa and three different temperatures (450, 500 and 550 °C) are imposed. In this presentation of the results, only the simulation for 500 °C will be shown for the sake of brevity. Indeed, changing the temperature in the range given above will affect quantitatively, but not qualitatively, the observed fields. The solid phase is not present from the beginning of the simulation. Instead, it is introduced by radial feeding when the gas flow begins to approach a steady state. In the steady state, as shown by the Mach number field in Figure 5.12, the gas flow field reaches sonic condition all along the finite length throat and becomes supersonic at the beginning of the divergent zone. In the first half of the divergent nozzle insert, the repeated reflection of oblique shocks can be observed. After this reflection zone, a flow separation occurs and, through another series of shocks, the flow reaches subsonic conditions. This means that the gas velocity decreases and is accompanied by a sudden increase

in temperature, as can be observed, respectively, in Figures 5.13 and 5.14.

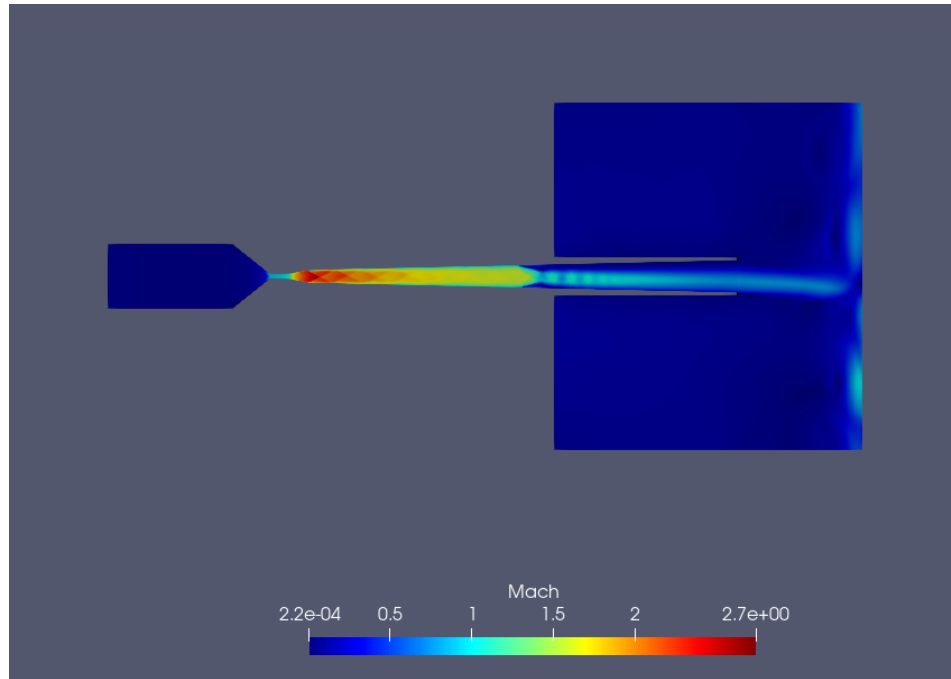


Figure 5.12: Mach number field for an inlet temperature of 500 °C.

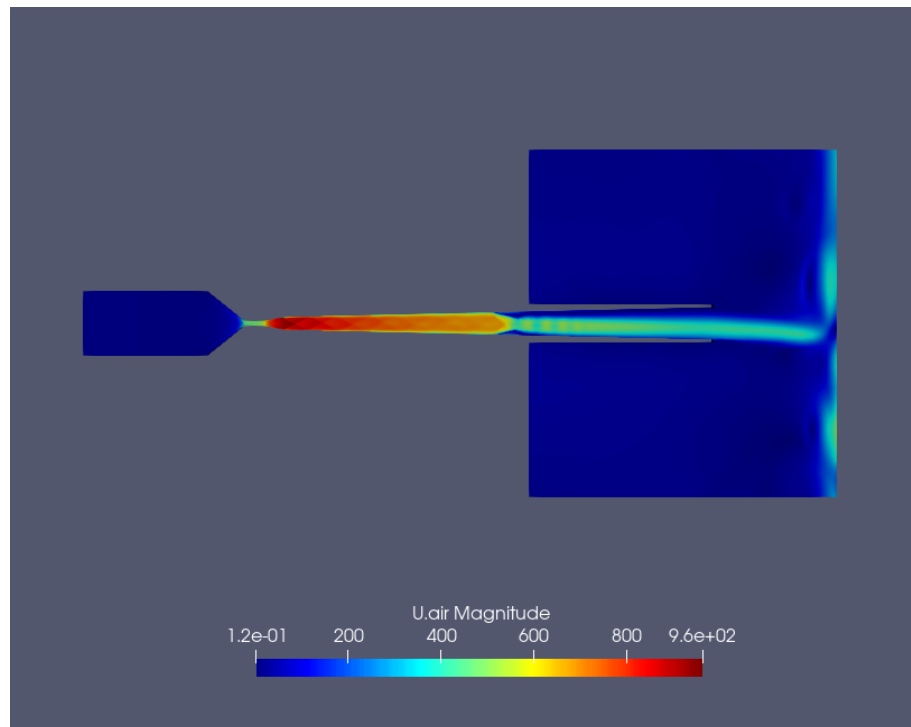


Figure 5.13: Gas velocity field [m/s] for an inlet temperature of 500 °C.

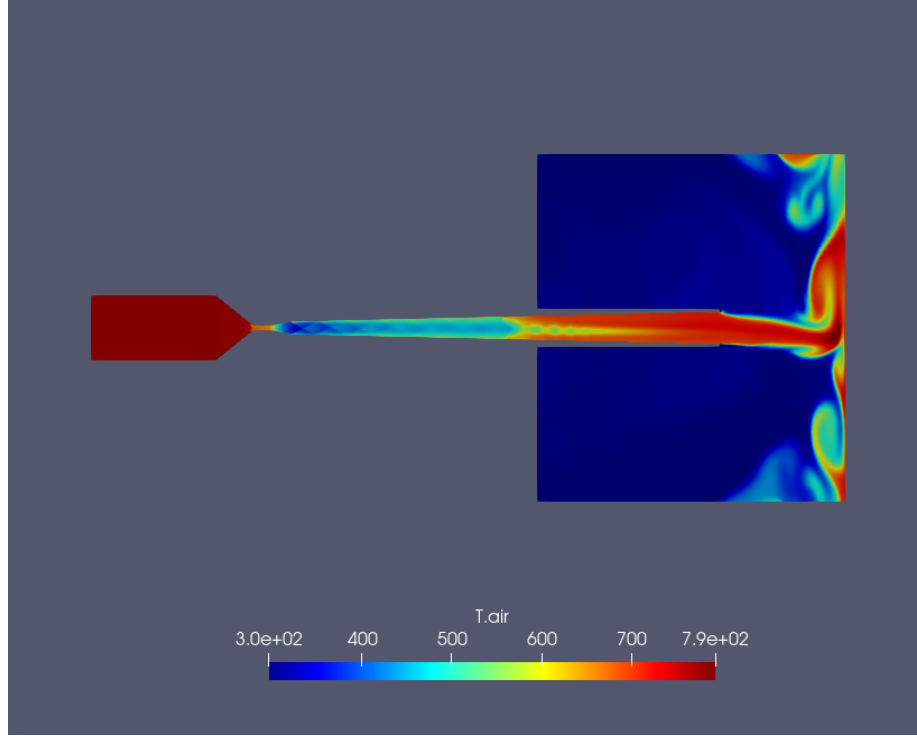


Figure 5.14: Gas temperature field [K] for an inlet temperature of 500 °C.

The effect of the total temperature on the gas temperature and velocity can be easily compared in 1-D profiles along the nozzle axis. These are reported in Figures 5.15 and 5.16. Axial velocity increases of about 30m/s for every 50 K increment of the inlet total temperature. The decrease of velocity values after fluid detachment is here more evident. On the other hand, temperature values rise after the fluid detachment, leading to very hot gas impacting on the substrate.

Powder injection begins once the gas fields reach a steady-state. At this moment, the simulation must be stopped and the OPENfoam “case file” modified in order to change the boundary condition on the powder injection surface patch. Thus, the wall condition is removed to allow an inflow through this patch. Here, total pressure and temperature conditions are set to ambient. A final boundary condition must be added here, imposing a fixed particle volume fraction. After the modification of the “case file”, the simulation is restarted. The positive difference between the ambient pressure and the very low pressure, due to gas expansion in the divergent

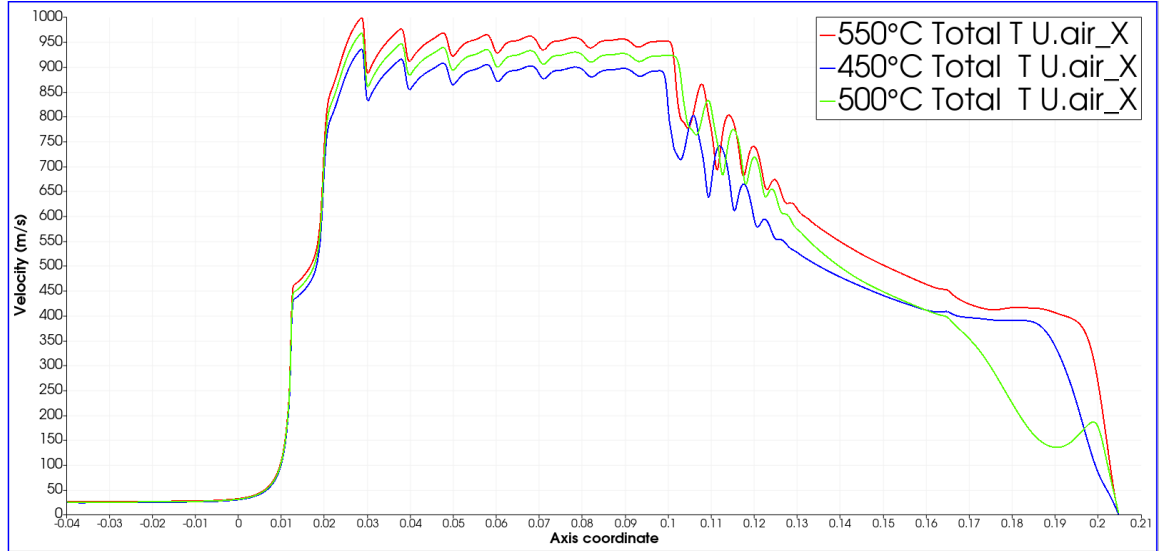


Figure 5.15: Velocity field on the axis for three inlet temperatures.

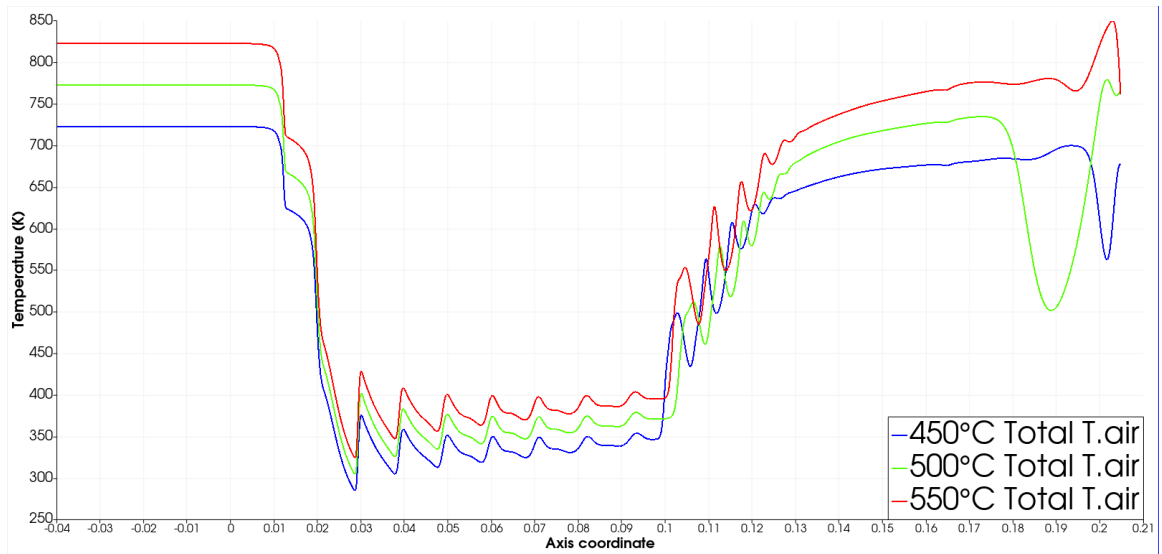


Figure 5.16: Temperature field on the axis for three inlet temperatures.

part, creates a suction allowing particle injection. This is the working principle of LPCS without a pressurized powder feeder. In any case, even in the presence of a pressurized powder feeder, the pressure value should never be more than 1.1 times the ambient pressure, otherwise particles could go upstream with dangerous consequences for the equipment. Powder injection affects both velocity and temperature gas fields, decreasing the former and increasing the latter, as can be seen in nozzle axis profiles reported in Figures 5.17 5.18.

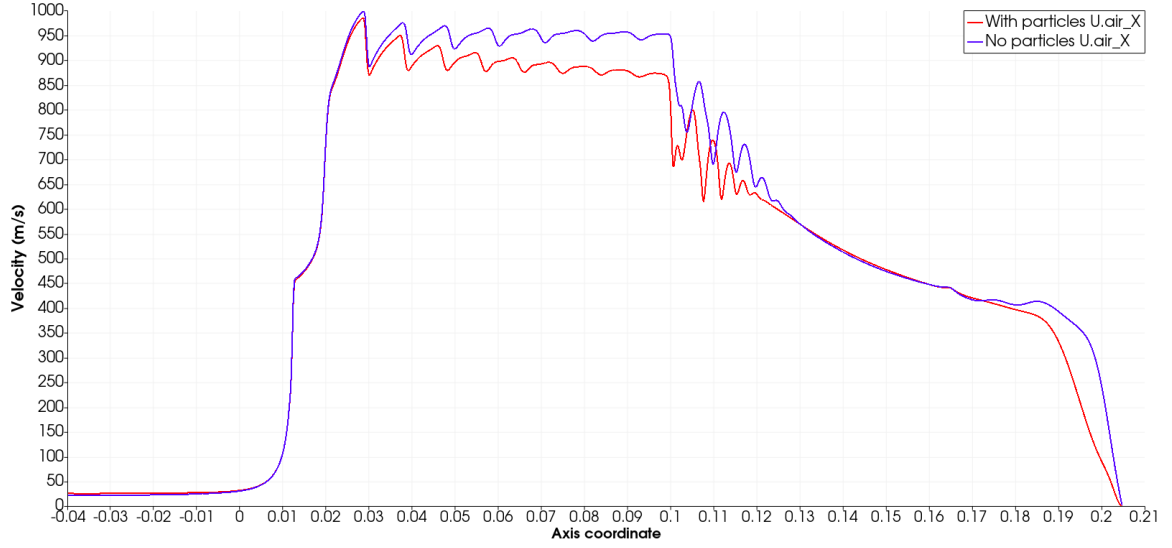


Figure 5.17: Change in gas velocity field due to particle injection for an inlet temperature of 500 °C.

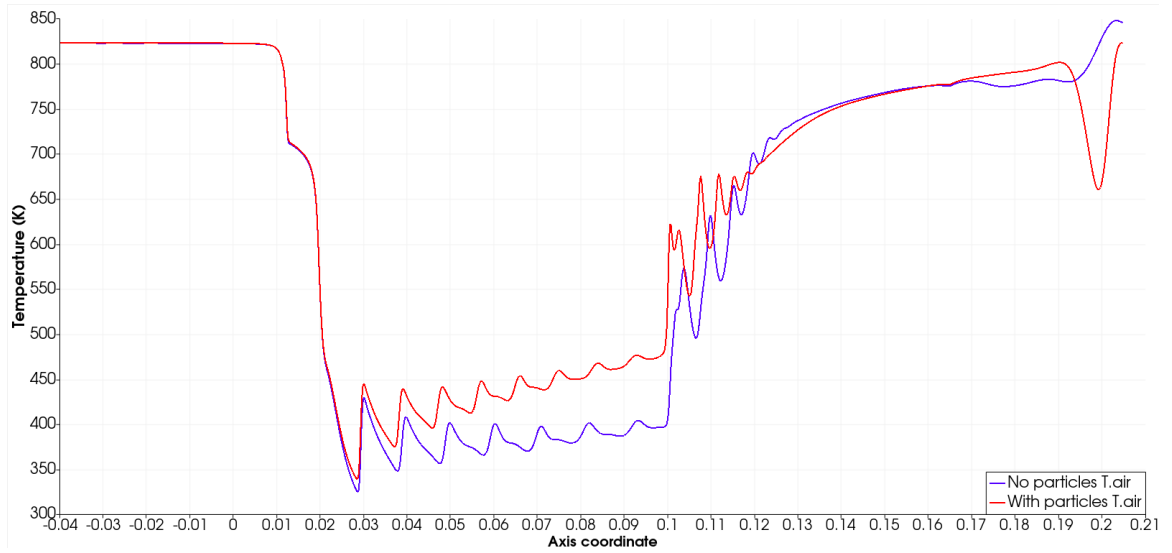


Figure 5.18: Change in gas temperature field due to particle injection for an inlet temperature of 500 °C.

Particle phase analysis

This part presents results on simulated particle velocities and temperatures, for the three cases with stagnation temperatures of, respectively, 450 °C, 500 °C 550 °C. Figures 5.19 and 5.20 show, respectively, the velocity and temperature of the solid phase in the biphasic flow, along the nozzle axis. First of all, it must be noted

that in the Eulerian framework it is not possible to follow and analyze velocity and temperature of a single particle, as in the Lagrangian one. Therefore, the computed quantities must be intended as an average of all the particles in the volume fraction considered.

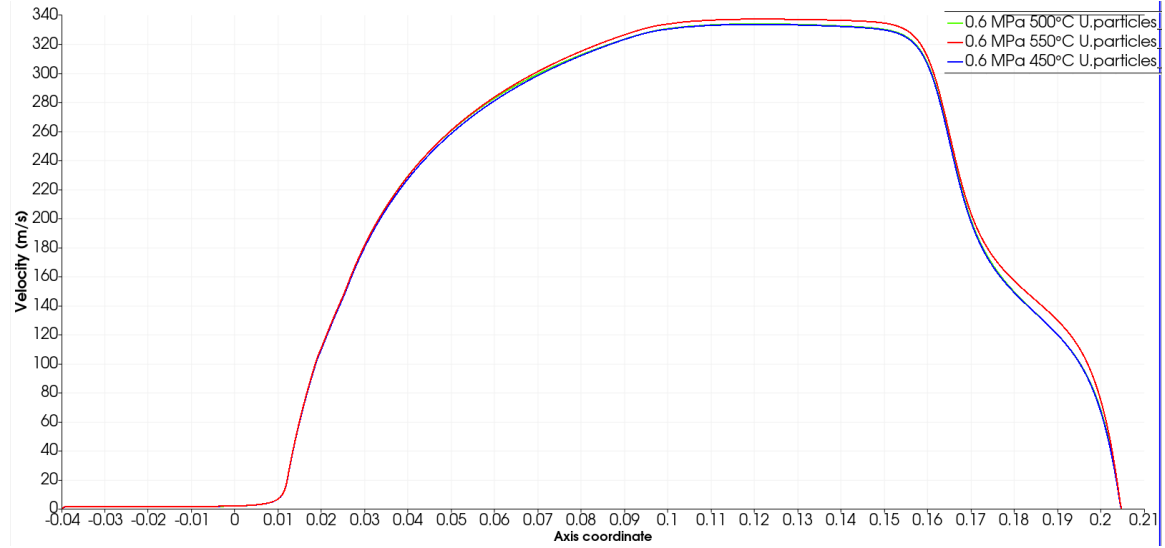


Figure 5.19: Particle velocity for three different inlet temperatures.

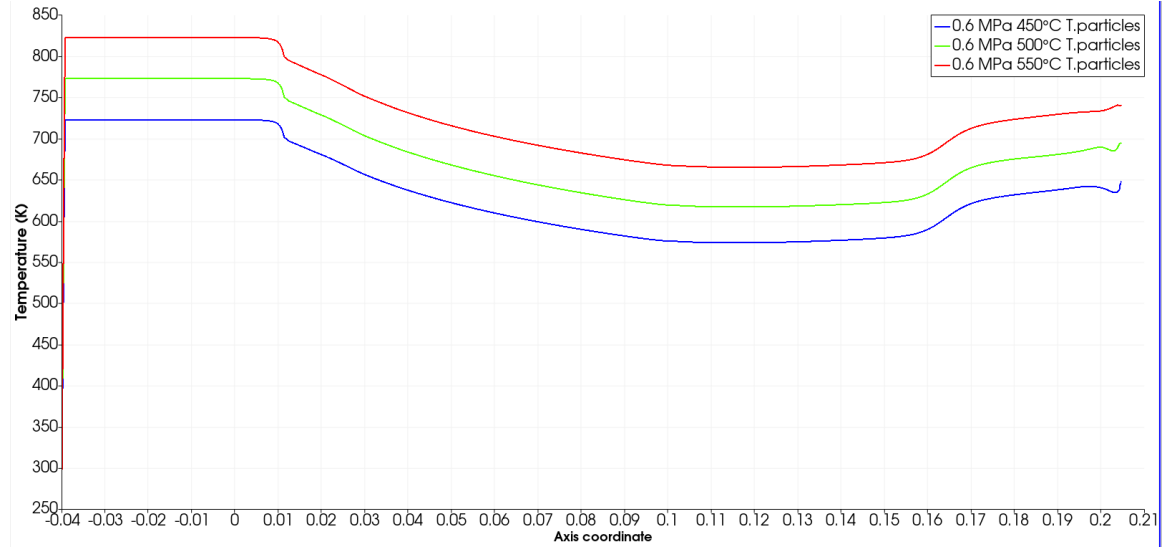


Figure 5.20: Particle temperature for three different inlet temperatures.

Variations in the stagnation temperature affect only slightly the gas velocity field, as already seen in Figure 5.15. As a consequence, particle velocity is also similar. In the same fashion as the gas phase, only the temperature of the solid phase is

significantly affected by the stagnation temperature. From an experimental point of view, then, when using LPCS with a rectangular-section nozzle and setting the total temperature to high values, particle impact temperatures are then much higher than in the HPCS case. This characteristic is desirable to improve penetration and mechanical anchoring on thermo-sensitive substrates. Unfortunately, no experimental measurements of particle temperatures are available in this work, so all these simulation results shall be considered only as an indication of the particle state. In OpenFOAM, when the particle volume fraction is equal to zero, its temperature will be considered the same as the gas one. This explains why in Figure 5.20, before the powder injection point, no difference can be noticed.

A single simulation was realized to catch some differences between aluminum and PEEK behavior as solid phases. The PEEK particle was bigger and lighter, so an increase in velocity is expected. For what concerns the temperature evolution, a different behavior is expected due to the lower specific heat and thermal diffusivity of PEEK as compared to aluminum. PEEK particle velocity, shown in Figure 5.20, has a similar tendency as the aluminum particle, even if the maximum value is about $100m/s$ greater for PEEK, due to its lower density. The temperature field is more difficult to dispute. Several factors can be called into question to explain the different behavior of the two materials. The gas flow field is definitely one of the main actors. Differences in gas-particle friction coefficients can lead to dissimilar gas-particle heat exchanges at higher velocities. Heat capacity can play another important role, through the Li-Mason heat exchange model. Further discussions can be made, but this is far from the aim of this work. Moreover, the lack of accessible experimental methods to measure particle temperatures inhibits a purely theoretical discussion on the results obtained. At the end of the day, it seems likely that particle temperature at typical cold spray stand-off difference should lie not far from the inlet gas total temperature. For this reason, in the next chapter dealing with particle impact sim-

ulations, several initial particle temperatures will be used, from the ambient up to 600K.

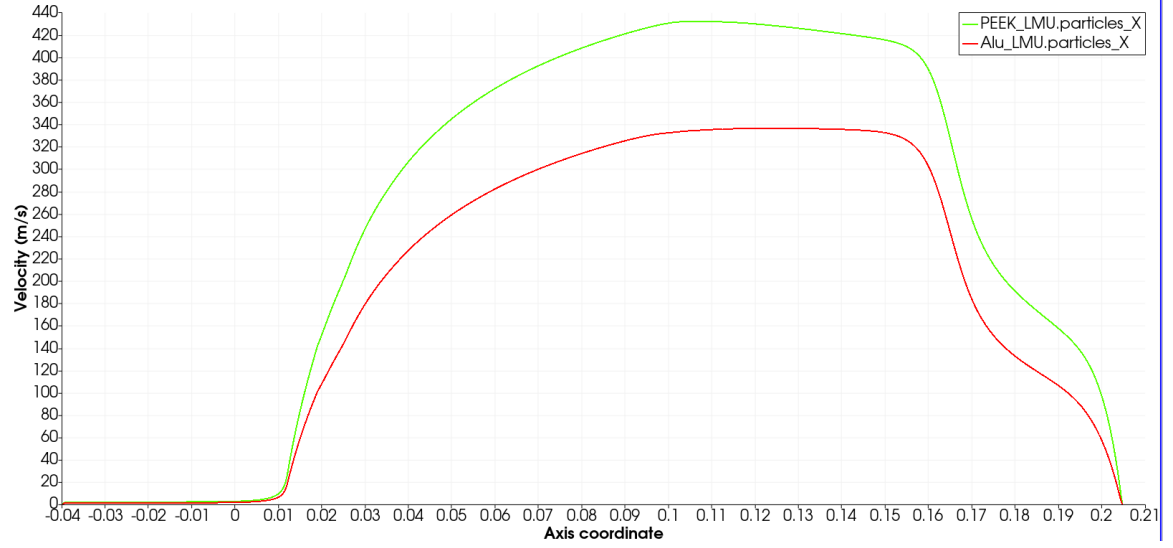


Figure 5.21: Particle velocity evolution along the symmetry axis for aluminum and PEEK.

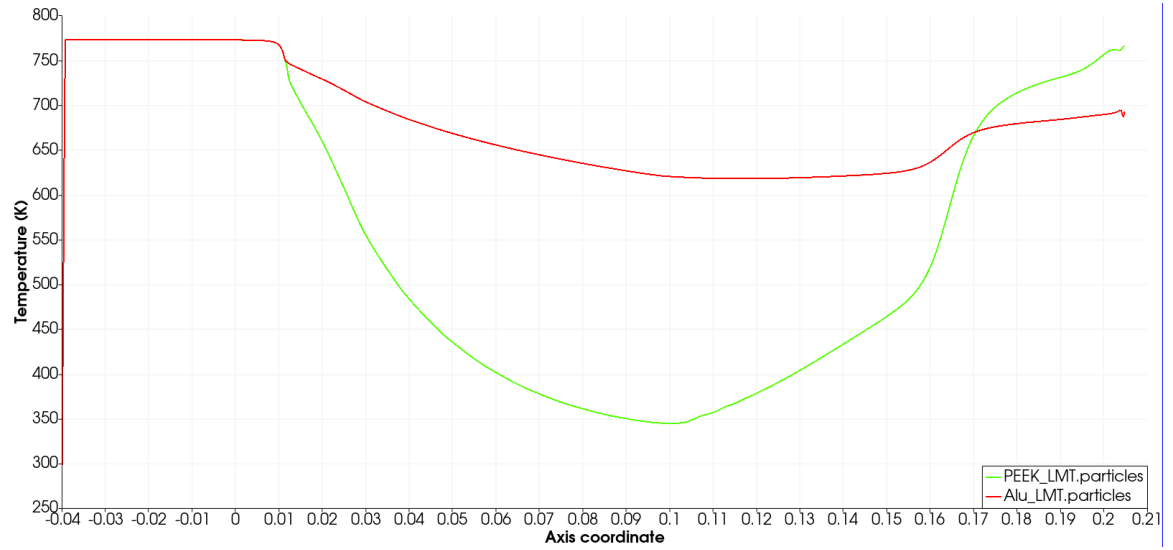


Figure 5.22: Particle temperature evolution along the symmetry axis for aluminum and PEEK.

Experimental particle velocity measurements

Experimental measurements of in-flight particle velocities in LPCS were performed by means of a shadowgraphy technique. As explained in Chapter 2, this system is

composed of a high speed camera and an illuminating laser. Several images were taken, allowing the velocity measurement for about one hundred particles. This technique seems to be very promising for accurate velocity measurements. Moreover, the same set-up with some modifications can potentially be transformed into a fast Schlieren imaging system, capable of capturing density variations in the gas phase and, thus, of revealing the shock structure within the cold spray flow. This modification was not developed during the work presented here, and only particle velocities were measured for a specific spraying condition, reported in Table 5.10.

| | |
|--------------------|---------------------------|
| Total pressure | 0.6 MPa |
| Total temperature | 500 °C |
| Nozzle type | Rectangular insert nozzle |
| Stand-off distance | 5 mm |

Table 5.10: LPCS parameters for the experimental measurement of particle velocities.

The imaging system delivers a series of images, such as those shown in Figure 5.23. The nozzle exit is evidenced on the right of the images and particles are visible as darker gray spots, circled in red in the figure. To compute the velocity of a particle, first it has to be identified on two subsequent images. The distance traveled can then be measured, counting the number of pixels and knowing the pixel size. Finally, the velocity is computed by dividing the distance by the time interval separating the two images. For example, the particle taken as reference in Figure 5.23 travelled 34 pixels. Since the pixel size is calibrated at $40.2 \mu\text{m}$ and the camera frequency is 200 kHz, corresponding to a time interval of $5 \mu\text{s}$, particle speed is evaluated at 273 m/s. If an uncertainty of 1 pixel is assumed for the distance, then the uncertainty on particle velocity is about $\pm 8 \text{ m/s}$. The procedure was applied to over one hundred particles and the average velocity was estimated at 270 m/s, at a distance of 8 mm from the nozzle exit.

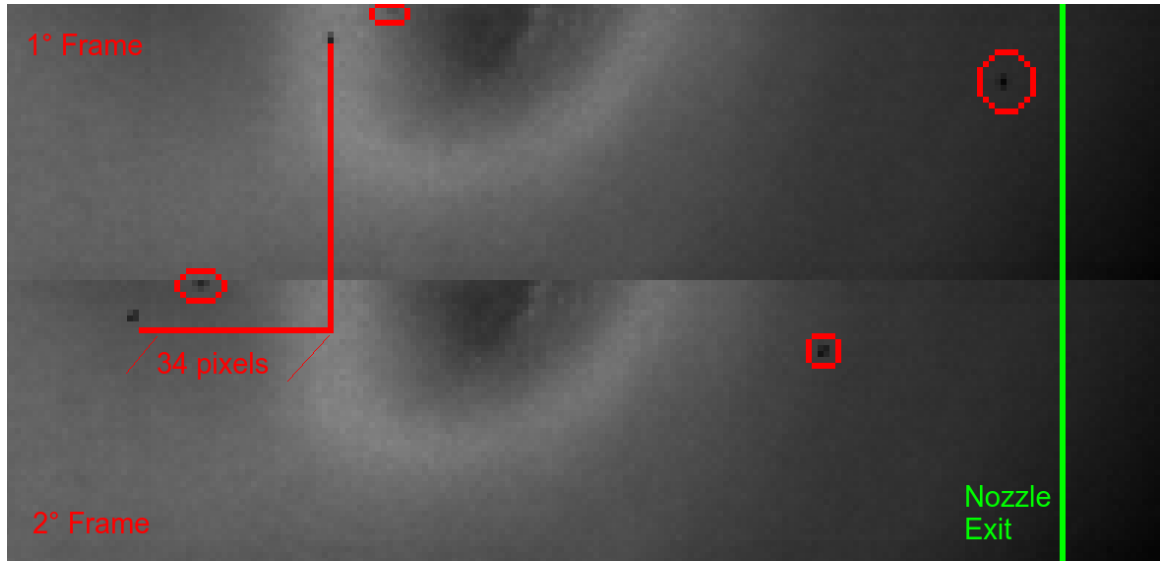


Figure 5.23: Particle velocity experimental measures.

In the CFD simulation corresponding to the same set of experimental parameters (stagnation pressure 0.6 MPa, stagnation temperature 500 °C), at 8 mm from the nozzle exit, simulated particle velocity was about 240 m/s, as shown in Fig. 5.24.

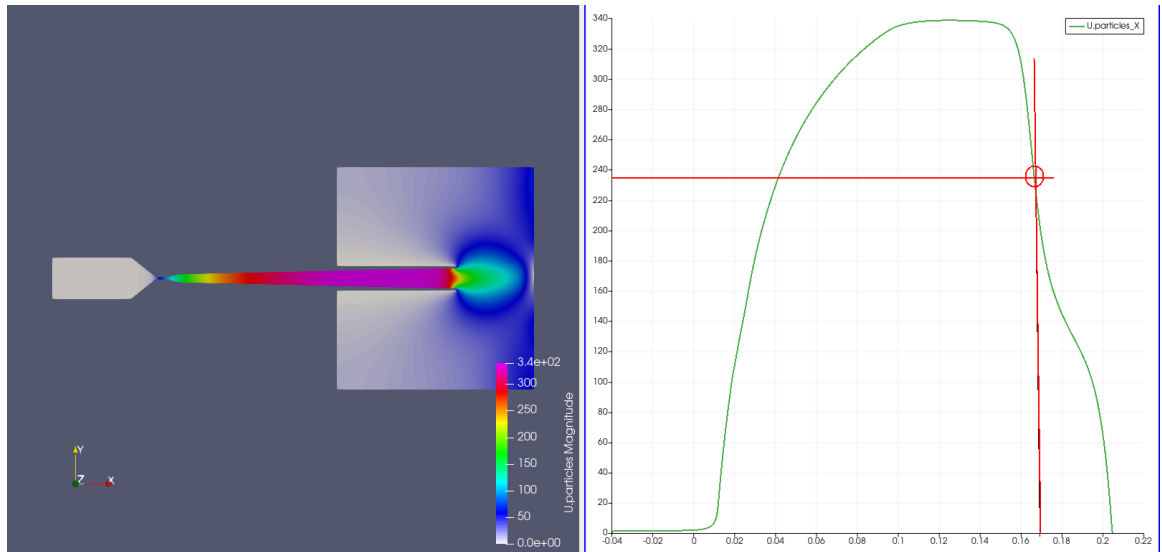


Figure 5.24: Simulated LPCS particle velocity, with a stagnation pressure of 0.6 MPa, a stagnation temperature of 500 °C, at 8 mm from the nozzle exit.

Even if this cannot be considered as a full validation of the CFD code, the comparison is very encouraging. This means that, at least, the CFD model developed produces reasonable results. Further experimental measurements, in different spray-

ing conditions and also in HPCS, and further improvements of the numerical code in terms of drag and turbulence modeling are necessary before claiming a reliable predictive tool. Moreover, an automated procedure should be envisaged in order to process all the observed particles velocities and to have larger data sets and statistical analysis.

5.5 Discussion

The results of CFD simulations of both high and low pressure cold spray systems led to the estimation of the important physical parameters of gas (and solid in LPCS) phases, allowing to identify the advantages of each equipment with respect to the application targeted in the present thesis. As expected, in HPCS, the gas velocity resulted to be much higher than in LPCS. In contrast, the temperature is dramatically lower in the first one. In LPCS, a particular rectangular-section nozzle allows flow separation inside the nozzle itself, leading to significant particle reheating. Simulation results indicate that the flow at nozzle exit is subsonic, so the jet is not as confined as in HPCS. This leads to a wider spread of particles in the outcoming jet. Nevertheless, this means that there is no formation of a bow shock in the proximity of the substrate. The sudden fall in particle velocity after the nozzle exit in LPCS suggests, as also found experimentally, that a stand-off distance of maximum 15 μm should be envisaged to have sufficient velocities to promote particle adhesion and coating growth.

5.6 Conclusion

CFD modeling was revealed to be a precious tool to investigate fluid-dynamic phenomena occurring in high and low pressure cold spray systems. An Eulerian-Eulerian approach was adopted to reduce the computational time and to account for all the interactions within the gas-solid biphasic flow. Using a Lagrangian model for these

interactions would have led to increased difficulties and to longer computational time. OpenFOAM was an interesting choice, being free and open-source, even if a certain lack of documentation limited the possibilities of this powerful tool. In particular, it would have been meaningful to test other models for the drag force and for the heat transfer between the two phases. This implies a lot of coding and testing and was too ambitious for the scope of this thesis work. Even if some parts of the model can still be improved, the model developed captured quite well the physical structures in the supersonic overexpanded flow of the high pressure cold spray and the subsonic transition inside the divergent rectangular-section insert of the low pressure one.

Concerning the modeling of the particle phase, the Eulerian approach offered different considerations from the Lagrangian one. Even if some issues should be fixed in the computation of particle velocity and temperature, the CFD model prediction differed only by few percentage points from the experimental measurements. In the case of high pressure cold spray this comparison was not possible, but some information of the gas phase was exploited. The high pressure system with axial injection allows (considering experimental data on the particles too) to accelerate particles to supersonic speed, but their temperature is rather low. In effect, the low temperature carrier gas accelerates and decreases its temperature without an opportune mixing with the hotter cold spray gas all around. A low pressure cold spray system, instead, allows a good reheating of the powder, with a significant beneficial effect of the hot gas on the composite substrate too. The thermoplastic substrate softens when hit by the hot gas, allowing better particle penetration. This could provide an indication of the cause of the higher adhesion value, measured in the pull-off test. The drawback is weaker bonds between aluminum particles, due to the lower speed. A possible solution could be to combine the two processes, with a first layer produced by low pressure assuring the adhesion and a subsequent layer by high pressure to boost the conductivity. The information obtained by CFD analysis, together with the exper-

imental measurements, helped to choose the initial conditions for the modeling of particle impact which will be treated in the next chapter.

CHAPTER 6

FINITE ELEMENT SIMULATION OF PARTICLE IMPACTS ONTO A COMPOSITE SUBSTRATE

Abstract

It is very challenging to observe and characterize experimentally the fundamental events at the basis of the cold spray process, *i.e.* the impact of high speed particles. Even more complex is to observe and understand the coating creation and growth, due to the high repetition rate of these fundamental events, with hundreds of thousands of particles impacting and rebounding each second. In this context, numerical simulation of particle impact is a precious tool to recover crucial information, such as temperature, plastic deformation and stress, to characterize the cold spray process. If the modeling of high speed metal particles impacting onto metal substrates has been the object of numerous studies, this is still not the case for polymers and polymer-based composites. As reported in chapter 1, polymers exhibit mechanical properties highly dependent on temperature and, for crystalline and semi-crystalline ones, on the degree of crystallinity. Moreover, their behavior at high deformation rates, as in the cold spray process case, is not well understood yet. In the experimental part of this thesis, presented in Chapter 3, polymer materials underwent very high deformation rates, produced either by the impact of high speed metal particles onto the PEEK-based substrate, or by the PEEK particles cold sprayed in mixture with aluminum ones. If experimental methods answered some questions quantifying adhesion and conductivity, the high speed behavior and the bonding mechanism of polymers largely remain to be understood. In chapter 4, the CFD analysis of both cold spray systems, as well as the experimental measurements of in-flight particles,

resulted in a data set consisting of particle temperatures and velocities at impact. Varying pressure and temperature cold spray machine parameters, notable differences in particle impact values for the two cold spray systems were evidenced. In this chapter, those particle temperatures and velocities are used as initial conditions for FEM simulations. The aim of this part is to investigate the differences in the elementary mechanisms when using high and low pressure cold spray for the production of coatings onto a SCRP substrate. To obtain this result, Finite Element Models is developed and applied to different cases. The behavior of the substrate, subjected to particle impacts in low and high pressure cold spray conditions are investigated, as well as the influence of the substrate initial temperature. The completely disparate behavior of PEEK particles compared to the metal ones when cold sprayed is a specific point of interest of these simulations. Moreover, pure PEEK and the short carbon reinforced PEEK substrate are both modeled. Fibers increase the stiffness of the PEEK polymer, potentially leading to increased particle deformation. An analysis of the fiber stress generated by impacts can help in understanding the possible fiber damage. Two different strategies are envisaged for preventing this issue. The first is to modify the substrate characteristic by adding a thicker PEEK layer on the top over the fibers. The second strategy, experimentally tested, involves a powder mixture containing a small percentage of PEEK particles. The beneficial effect of these two strategies are evaluated in terms of fiber stress, compared to the case of metal particles.

The pull-off experimental adhesion strength test revealed that the PEEK powder addition increases coating adhesion. A dual effect can be identified considering the relative position of PEEK and aluminum particles. If an aluminum particle hits a previously deposited PEEK one, the latter acts as a protection for the substrate. In this work, this is called “mattress effect”. On the contrary, in the case of a PEEK particle impacting onto a previously deposited aluminum one, the former traps the

latter on the substrate. This effect is called “spiderman web effect”. FEM simulations were revealed to be able to capture both effects. Finally, multi-particle simulations involving both PEEK and aluminum particles are presented, trying to reproduce a composite microstructure similar to the one observed experimentally.

Résumé en français

Il est très difficile d’observer et de caractériser expérimentalement les événements fondamentaux à la base du processus de projection à froid, c’est-à-dire l’impact d’une particule à grande vitesse. Il est encore plus complexe d’observer et de comprendre la création et la croissance du revêtement, en raison du taux de répétition élevé de ces événements fondamentaux, avec des centaines de milliers de particules impactant et rebondissant chaque seconde. Dans ce contexte, la simulation numérique de l’impact des particules est un outil précieux pour récupérer des informations cruciales, comme par exemple la température, la déformation plastique et la contrainte, pour caractériser le processus de projection à froid. Si la modélisation de l’impact de particules métalliques à grande vitesse sur des substrats métalliques a fait l’objet de nombreuses études, ce n’est pas encore le cas pour les polymères et les composites à base de polymères. Comme indiqué au chapitre 1, les polymères présentent des propriétés mécaniques fortement dépendantes de la température et du degré de cristallinité. De plus, leur comportement à des taux de déformation élevés, comme dans le cas du procédé de projection à froid, n’est pas encore bien compris. Dans la partie expérimentale de cette thèse, présentée au chapitre 3, les matériaux polymères ont subi des taux de déformation très élevés, produits soit par l’impact de particules métalliques à haute vitesse sur le substrat à base de PEEK, soit par les particules de PEEK pulvérisées à froid en mélange avec des particules d’aluminum. Si les méthodes expérimentales ont répondu à certaines questions quantifiant l’adhésion et la conductivité, le comportement à haute vitesse et le mécanisme de liaison des polymères

restent largement à comprendre. Dans le chapitre 4, l'analyse CFD des deux systèmes de pulvérisation à froid, ainsi que les mesures expérimentales des particules en vol, ont permis d'obtenir un ensemble de données comprenant les températures et les vitesses des particules à l'impact. En faisant varier les paramètres de pression et de température de la machine de projection à froid, des différences notables dans les valeurs d'impact des particules pour les deux systèmes de projection à froid ont été mises en évidence. Dans ce chapitre, ces températures et vitesses de particules sont utilisées comme conditions initiales pour les simulations FEM. L'objectif de cette partie est d'étudier les différences dans les mécanismes élémentaires lors de l'utilisation de la projection à froid haute et basse pression pour la production de revêtements sur un substrat SCRP. Pour obtenir ce résultat, des modèles d'éléments finis ont été développés et appliqués pour les différents cas. Le comportement du substrat soumis à des particules pulvérisées à froid à basse et haute pression impactant à différentes vitesses et températures a été étudié, ainsi que l'influence de la température initiale du substrat. Le comportement complètement disparate des particules de PEEK par rapport à celles de métal lors de la projection à froid était un point d'intérêt spécifique de ces simulations. De plus, le PEEK pur et le substrat PEEK renforcé de carbone court ont été modélisés. Les fibres augmentent la rigidité du polymère PEEK, ce qui peut conduire à une augmentation des déformations des particules. Une analyse de la contrainte des fibres générée par les impacts pourrait aider à comprendre l'endommagement éventuel des fibres. Deux stratégies différentes ont été envisagées pour prévenir ce problème. La première consiste à modifier la caractéristique du substrat en ajoutant une couche plus épaisse de PEEK sur le dessus des fibres. La seconde stratégie, testée expérimentalement, consiste à utiliser un mélange de poudres dont un faible pourcentage est composé de particules de PEEK. L'effet bénéfique de ces deux conceptions a été évalué en termes de contrainte sur les fibres par rapport au cas classique de la particule métallique sur le substrat original.

Le test expérimental de résistance à l'arrachement a révélé que l'ajout de poudre de PEEK augmentait l'adhérence du revêtement. Un double effet peut être identifié en considérant la position relative des particules de PEEK et d'aluminium. Si une particule d'aluminium heurte une particule de PEEK précédemment déposée, cette dernière agit comme une protection pour le substrat. Dans ce travail, cet effet a été appelé effet "matelas". Au contraire, dans le cas où une particule de PEEK heurte une particule d'aluminium précédemment déposée, la première piège l'aluminium sur le substrat. Cet effet a été renommé "effet toile d'araignée". La simulation FEM s'est révélée capable de capturer les deux effets. Enfin, un test multi-particules, impliquant à la fois des particules de PEEK et d'aluminium, a été présenté afin d'essayer d'obtenir une micro-structure composite similaire à celle trouvée expérimentalement.

6.1 Model foundations

Concerning the mechanical simulations of particle impact in cold spray conditions, several approaches are presented in literature. In this work, a finite element analysis (FEA) is chosen. FEA approaches can be divided into three main categories: Lagrangian, Eulerian and mixed. In the Lagrangian framework, nodes are fixed on the material and elements deform with it. In the Eulerian one, instead, nodes are fixed in the space and materials flow through the mesh. In this case, elements are not deforming at all. For this reason, Eulerian or mixed Eulerian-Lagrangian approaches improve the possibilities of avoiding convergence problems due to large deformations, as reported in [119] and [120]. This is particularly useful in the cold spray process, where materials can deform heavily. The Abaqus commercial software is adopted to perform all the simulations. Explicit solvers are used, in particular, where the integration scheme is more suitable to solve non-linear, highly dynamic problems. The Combined Eulerian Lagrangian (CEL in the following) approach is finally chosen. Lagrangian and Eulerian elements coexist in the analysis and the contact formulation

between Eulerian and Lagrangian domains is computed if they are embedded. [121]. This choice allows to avoid problems of excessive mesh distortion and convergence.

Several input conditions are needed for the analyses. Constitutive models, one for each material involved in the simulations, allow the computation of responses to different thermo-mechanical loading conditions. The Johnson-Cook model, together with the Mie-Gruneisen equation of state, is chosen in this case. For what concerns the initial state conditions of particles and substrates, such as velocity and temperature, CFD simulations and experimental measurements of chapter 4 provide the data.

6.1.1 CEL approach

In order to setup a CEL analysis in Abaqus all the parts must be embedded in an Eulerian domain. Particles and substrate matrix are treated as Eulerian parts. Carbon fibers, instead, are considered Lagrangian parts. Abaqus allows parts to be defined in the Eulerian domain via the Volume Fraction Tool (VTF in the following). Figure 6.1 illustrates the principle of the method:

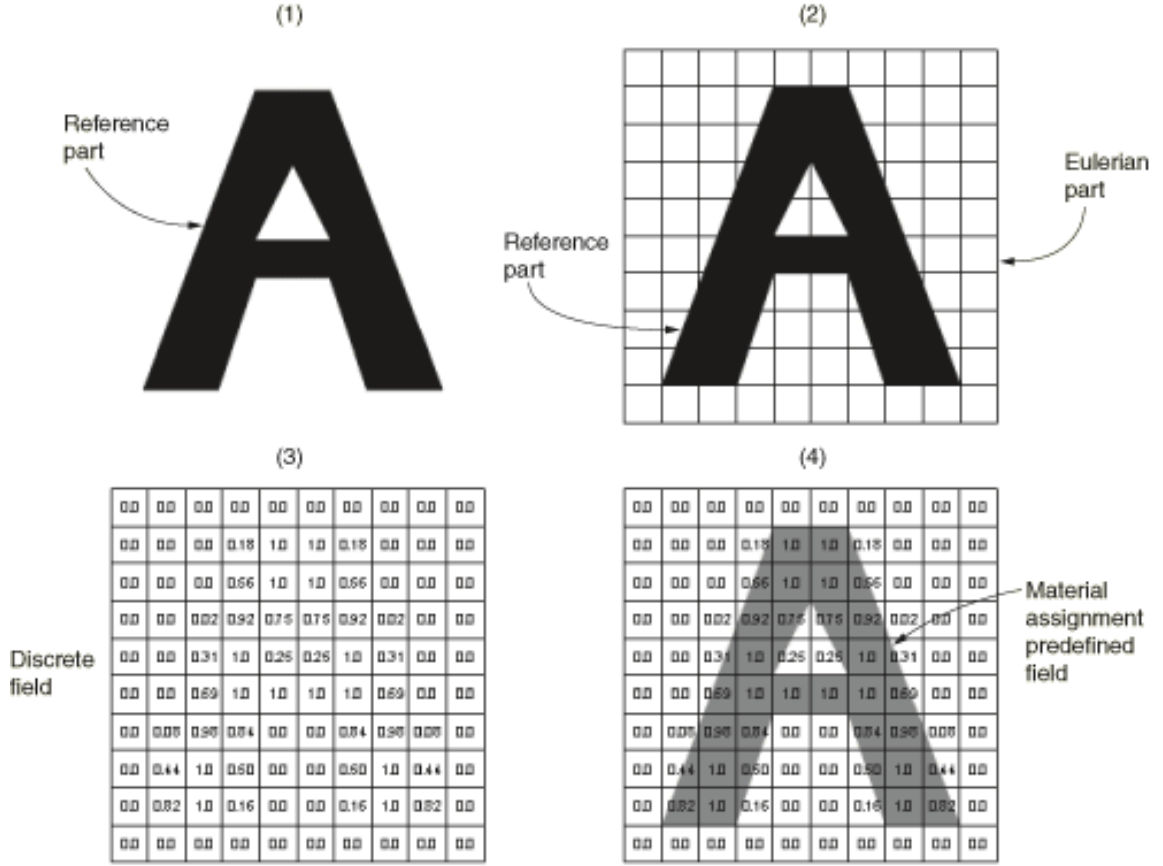


Figure 6.1: Schematic view of Volume Fraction Tool DS Simulia, after [59].

The VFT algorithm works in the following way:

1. parts are created in the Abaqus GUI or by a python script;
2. an Eulerian domain is created and meshed;
3. parts are placed inside the Eulerian volume (already meshed);
4. the VFT tool creates a discrete field in the intersection between the Eulerian volume and each part. The volume fraction is then calculated for each element (1 full intersection, 0 void);
5. a material is assigned to each of these discrete fields.

Material distribution fields are thus necessary in the Eulerian framework. Each material in the model has its own variable, namely Eulerian Volume Fraction (EVF in

the following), describing the volume fraction of the given material in each element.

Description of the model

Fibers are also embedded in the Eulerian domain but, differently from particles and the substrate matrix, they are meshed apart. Then, the material model chosen is assigned. The interaction module defines the contact properties between Eulerian and Lagrangian parts. Abaqus checks for contact between all the surfaces in the whole model and manages its evolution.

Some assumptions must be made before starting the simulation. They are reported below:

- full 3D simulation,
- aluminum and PEEK particles are perfectly spherical,
- particle velocity is normal to the substrate surface,
- the substrate is perfectly flat,
- the initial temperature is homogeneous inside the particles and the substrate,
- no adhesion model is added to the normal Eulerian contact behavior,
- the friction between particle and substrate is modeled with a Coulomb law, $\tau = \mu \cdot N$, with τ the tangential frictional force, $\mu = 0.3$ the friction coefficient and N the normal force.

In Abaqus, there is no predefined unit system for physical quantities. It must be defined by the user, in a consistent way. The system adopted in this study is presented in table 6.1.

| Quantity | SI | Adopted unit |
|--------------|------------------|--------------------|
| Distance | m | mm |
| Mass | kg | $tonne$ |
| Energy | J | mJ |
| Time | s | s |
| Stress | Pa | MPa |
| Volumic mass | $\frac{kg}{m^3}$ | $\frac{ton}{mm^3}$ |
| Temperature | K | K |
| Power | W | mW |

Table 6.1: Unit system for Abaqus simulations.

6.1.2 Constitutive laws

Aluminum and PEEK

In the cold spray process, impacting particles deform very quickly with strain rates locally up to 10^7 - 10^9 s^{-1} [122], depending on the material and impacting velocity. Several material models are able to account for strain rate effects. For example, in [122] six different constitutive models were compared. In the present thesis, the Johnson-Cook visco-plastic model [68] (JC in the following) is chosen. The main advantage with respect to other models is the small number of material parameters. JC parameters are typically obtained by means of the Hopkinson Pressure Bar Test, in which strain rates in the order of 10^3 - 10^4 s^{-1} are explored. In addition to the JC model, the Mie-Grüneisen Equation of State (EOS in the following), accounts for the hydrostatic response of solid materials in shock conditions. The EOS (Equation 6.1) links the pressure and the internal energy.

$$p - p_H = \Gamma_\rho(E - E_H) \quad (6.1)$$

where P is the pressure, E the internal energy, p_H the Hugoniot pressure, E_H the Hugoniot internal energy. Γ is the Grüneisen parameter, defined as $\Gamma\rho = \Gamma_0\rho_0$, ρ is the density and the 0 subscript means quantities in a reference state. Γ_0 can be considered as a material dependent constant. Hugoniot energy and pressure are linked

by the relation:

$$E_H = \frac{P_H \eta}{2\rho_0} \quad (6.2)$$

Where $\eta = 1 - \frac{\rho_0}{\rho}$. The pressure can be written as follows:

$$p = p_H \left(1 - \frac{\Gamma_0 \eta}{2\rho_0} \right) + \Gamma_0 \rho_0 E \quad (6.3)$$

The EOS used in this work is the so called “Us-Up” formulation, based on the hypothesis that the shock wave velocity is linked to the material speed as:

$$U_s = c_0 + sU_p \quad (6.4)$$

where U_s is the shock velocity, U_p the material velocity, c_0 is the speed of sound, and s is the slope of the relation, determined experimentally for each material. The Hugoniot pressure is defined by the following relationship:

$$p_H = \frac{\rho_0 c_0^2 \eta}{(1 - s\eta)^2} \quad (6.5)$$

The equation linking the pressure to the internal mass energy is:

$$p = \frac{\rho_0 c_0^2 \eta}{(1 - s\eta)^2} \left(1 - \frac{\Gamma_0 \eta}{2\rho_0} \right) + \Gamma_0 \rho_0 E \quad (6.6)$$

The Us-Up Mie-Grüneisen EOS has four material dependent parameters: ρ_0, Γ_0, c_0 and s .

In addition to the EOS, the semi-empirical model of Johnson-Cook, widely used in cold spray impact simulations [123], is chosen as a constitutive law. The yield stress is expressed as a function of the plastic deformation, the deformation rate and

the temperature, as shown in Equation 6.7 below.

$$\sigma = (A + B\epsilon^n)(1 + C \ln(\frac{\dot{\epsilon}}{\dot{\epsilon}_0}))(1 - T_*^m) \quad (6.7)$$

where ϵ , $\dot{\epsilon}$, $\dot{\epsilon}_0$ are, respectively, the equivalent plastic deformation, deformation rate, reference deformation rate, A the initial elastic limit, B, n , respectively, the hardening coefficient and exponent, C the strain rate hardening coefficient. T_* is a normalized temperature, defined as:

$$T_* = 0 \text{ if } T < T_0$$

$$T_* = \frac{T - T_0}{T_m - T_0} \text{ if } T_0 \leq T \leq T_m$$

$$T_* = 1 \text{ if } T > T_m$$

where T_0 , T_m , m are, respectively, the reference temperature, melting temperature, and thermal softening exponent.

Eight material dependent parameters are necessary for the JC model, often available in literature even if, as already discussed in Chapter 1, these are not necessarily appropriate for the deformation regime characteristic of the cold spray process. The JC parameters for aluminum rely on [124]. The m parameter is generally set to unity, as explained in [125]. The Mie-Grüneisen parameters for aluminium come from [126]. In the case of PEEK, all material parameters rely on [87].

Table 6.2 presents all the material dependent parameters used for impact simulations.

| Quantity | Value (SI) | |
|------------------------------------------|------------|-------|
| - | Aluminum | PEEK |
| Thermo-mechanical parameters | | |
| Density [kg/m^3] | 2700 | 1304 |
| Shear Modulus [GPa] | 26.4 | - |
| Young Modulus [GPa] | - | 3.9 |
| Poisson Modulus | - | 0.4 |
| Thermal conductivity [$Wm^{-1}K^{-1}$] | 229 | 0.23 |
| Specific Heat [$JK^{-1}kg^{-1}$] | 889 | 2180 |
| Johnson-Cook Parameters | | |
| $AMPa$ | 110 | 132 |
| $BMPa$ | 150 | 10 |
| n | 0.36 | 1.2 |
| C | 0.014 | 0.034 |
| $\dot{\epsilon}_0$ | 1 | 1 |
| m | 1 | 0.7 |
| T_0K | 293 | 293 |
| T_fK | 931 | 616 |
| Mie -Gruneisen | | |
| $C_0 [ms^{-1}]$ | 5300 | 2520 |
| S | 1.34 | 1.71 |
| Γ_0 | 2.16 | 1.5 |

Table 6.2: Material dependent parameters for aluminum and PEEK.

Carbon fibers

Concerning the carbon fibers reinforcing the PEEK matrix, a pure elastic model is chosen. Damage and failure models are not considered. It was difficult to find appropriate thermophysical properties for the short carbon fibers of the composite material, because of a large variety of different types of fibers in literature. For this reason, average values were chosen. For a pure elastic analysis, the few material properties required are reported in Table 6.3.

| Quantity | Value (SI) |
|------------------------------|---------------------|
| Thermo-mechanical parameters | |
| Density | $2000kg/m^3$ |
| Young Modulus | $228GPa$ |
| Poisson Modulus | 0.3 |
| Thermal conductivity | $100Wm^{-1}K^{-1}$ |
| Specific Heat | $800JK^{-1}kg^{-1}$ |

Table 6.3: Material dependent parameters for the carbon fibers.

6.1.3 Mesh and element types

Eulerian domain

The Eulerian domain is defined by a rectangular cuboid including the particle(s) and the substrate. Following the Ph.D. work of Sébastien Weiller, who applied a CEL analysis for aluminum particles impacting on an aluminum substrate, the mesh size is fixed to 1 micrometer. This allowed for reliable results with reduced computational time. 3D elements with 8 nodes, full thermo-mechanical coupling and reduced integration were adopted. In Abaqus/Explicit this element type has the code EC3D8RT.

Lagrangian domain

The Lagrangian domain is limited to carbon fibers. The same mesh size as for the Eulerian domain is chosen. These elements are embedded inside the Eulerian domain and, in particular, within the substrate part. 3D elements with 8 nodes, full thermo-mechanical coupling and reduced integration were adopted. In Abaqus/Explicit, an element with reduced integration (one integration point) and full thermo-mechanical coupling has the code C3D8RT. The contact zone between the Eulerian and the Lagrangian domains is automatically calculated by Abaqus with a penalty tangential behavior and a “hard” type contact behavior for the normal component.

6.2 Impact simulations

The goal of this part is to recognize and possibly understand the differences between HPCS and LPCS cold spray in producing adherent and conductive coatings onto short fiber reinforced PEEK composites. In the experiments reported in Chapter 3, strong differences were highlighted in the coating produced by the two different equipments. The addition of PEEK powder to the aluminum led to better results, but the adhesion mechanism deserves to be investigated further. The presence of short carbon fibers represents another point of interest. Its effect on particle impact behavior has to be evaluated. All the initial particle conditions are provided by experimental measurements and CFD analysis. For the substrate, ambient temperature is chosen for HPCS and two different temperatures, respectively lower and higher compared to the PEEK glass transition one, are tested for LPCS. To summarize, various simulations are carried out to investigate the phenomena reported above. The different simulation types performed are listed below:

- impact of an aluminum particle onto a pure PEEK substrate with different velocities and temperatures;
- impact of an aluminum particle onto a short carbon reinforced PEEK substrate with different velocities and temperatures;
- impact of a PEEK particle onto a short carbon reinforced PEEK substrate with different velocities and temperatures;
- bi-particle impacts, to study the fundamental effects taking place when spraying metal/polymer powder mixtures. In particular, a PEEK particle followed by an aluminum one and *vice versa* are studied;
- multi-particle impacts, to study collective effects taking place when spraying metal/polymer powder mixtures.

In all cases, both HPCS and LPCS conditions are tested and compared. In order to fix a final time for the simulations, a criterion based on the total kinetic energy of the system is adopted. Looking at the history output of the total kinetic energy of the system (ALLKE variable in Abaqus/Explicit), it was noticed that after $1 \cdot 10^{-7}$ s the value drops of about 2 orders of magnitude. Then it continues to decrease slightly toward zero. A conservative choice was made, fixing the end-time for the simulations to $3 \cdot 10^{-7}$ s, which assures that the kinetic energy is almost zero, for all the simulations, independent of the number of particles.

6.2.1 Single aluminum particle onto a pure PEEK substrate

This simulation can be considered as a numerical splat test. It aims to study the behavior of PEEK polymer when hit by an aluminum particle in HPCS and LPCS conditions. The results can then be compared to the case of the composite substrate, where the short carbon fiber reinforcement changes the substrate properties. In HPCS, particles have velocities over 500 m/s and temperatures close to the ambient. In LPCS instead, particle velocities are half of the HPCS case, but particle and gas temperatures can easily be higher than 500 K. Both temperatures affect the PEEK properties. In effect, thermoplastic polymers generally undergo softening when the temperature exceeds the glass transition temperature. This can allow a better particle penetration into the substrate and, as a consequence, a better mechanical anchoring. In the absence of fibers, a full Eulerian analysis is performed in this case. The particle diameter is fixed to $25\mu m$ for all simulations. The substrate is a parallelepiped measuring $70 \times 70 \times 35 \mu m$. The particle and substrate are embedded in an Eulerian box parallelepiped of $70 \times 70 \times 65 \mu m$. For the HPCS simulation, ambient temperature is chosen for the particle and substrate as initial conditions. In the case of LPCS, two different initial temperatures are tested for the substrate, to keep into account the effect of the hot gas on the substrate. All the initial conditions are

reported in Table 6.4

| Equipment | Particle velocity (m/s) | Particle temperature (K) | Substrate temperature (K) |
|-----------|-----------------------------|---------------------------|----------------------------|
| HPCS | 500 | 300 | 300 |
| LPCS | 280 | 500 | 300 |
| LPCS | 280 | 500 | 450 |

Table 6.4: Initial conditions for impact simulations of an aluminum particle onto a pure PEEK substrate.

Figure 6.2 presents particle and substrate shapes in the last frame of the simulation ($3 \cdot 10^{-7}$ s). To show in the same graph the three materials, a special user defined variable is plotted, the modified EVF. It is defined as the sum of PEEK EVF and 2 times Al EVF. In this way, it takes a zero value in empty elements, 1 in full PEEK elements and 2 in full aluminum ones. Near the boundaries, where elements contain two or more materials (void included), the interpretation is more complex.

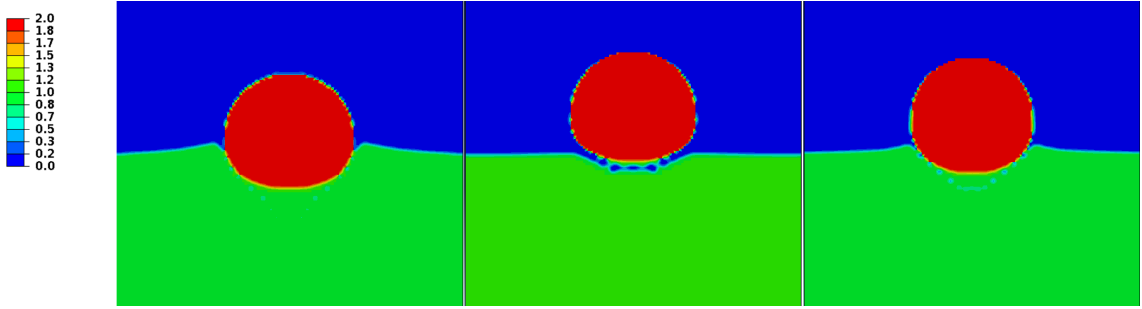


Figure 6.2: Modified EVF field in cross sectional view for the impact simulation of an aluminum particle onto a pure PEEK substrate. Last frame of the simulation ($3 \cdot 10^{-7}$ s). From the left to the right, HPCS, LPCS with substrate initial temperature at 300 K and LPCS with substrate initial temperature at 450 K.

To help the comparison of the three cases, a particle flattening ratio is computed. The expression chosen, well suited for spherical particles, is the following:

$$\epsilon = \frac{w}{h} \quad (6.8)$$

where w and h are, respectively, the width and height of deformed particles. In the case of HPCS $\epsilon = 1.16$, for the LPCS with a lower substrate temperature $\epsilon = 1.14$ and in the last case $\epsilon = 1.07$. Thus, HPCS particles are subject to more deformation

even when impacting a polymer. In LPCS, when the substrate temperature is lower, the material is stiffer and makes the particle deform more. Concerning particle penetration, it is highest in HPCS ($7\mu m$). In LPCS, an increased substrate temperature improves the penetration of the particle ($5.5\mu m$ vs $3\mu m$). Anyway, as shown by the presence of a partial void between the particle and the substrate, the particle seems to rebound in LPCS with the lower temperature substrate. As in the experimental part of this work, where some erosion was noticed, it seems that a layer of PEEK remains attached to the rebounded particle.

Figure 6.3 shows the temperature field in the last frame of the simulation. In the CS process, the kinetic energy of the particle dissipates at impact in plastic deformation, distributed between the particle and the substrate depending on the respective material properties. Plastic deformation induces a temperature increase, which depends on the duration of the deformation and on thermal properties of the materials. Polymer and polymer based materials are thus more prone than metals to the temperature increase due to lower thermal diffusivities. In HPCS the temperature rise is about 100 K on the interface between the substrate and the particle. A similar value was found in LPCS with a substrate at ambient temperature. In the last case, the increase in temperature is limited to about 50 K. In both LPCS cases, temperatures in the contact zone exceed the PEEK glass transition one, considerably softening substrate material.

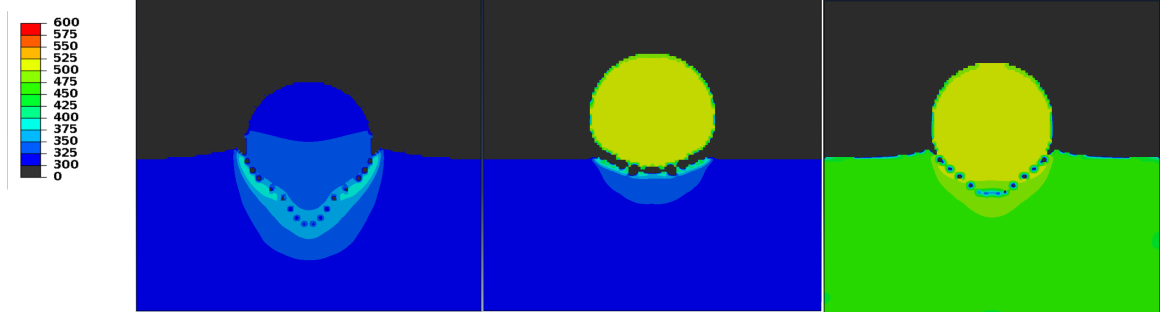


Figure 6.3: Temperature field in cross sectional view for the impact simulation of an aluminum particle onto a pure PEEK substrate. Last frame of the simulation ($2 \cdot 10^{-7}$ s). From the left to the right, HPCS, LPCS with substrate initial temperature at 300 K and LPCS with substrate initial temperature at 450 K.

6.2.2 Single particle onto SCRP substrate

In this part, the behavior of HP and LP cold sprayed single particles, either aluminum or PEEK, onto a composite substrate is evaluated. The differences between the pure PEEK and the SCRP substrate can then be enlightened by comparing these results with those of the previous part. In addition, at the end of this part, a modified substrate is modeled with an increased PEEK top layer. This allows investigating the beneficial effects of an additional PEEK top layer in terms of mechanical anchoring and fiber protection.

Aluminum particle test

As in the previous part, three initial conditions were chosen, one for HPCS and two for LPCS. In the HPCS case, the parameters are the same as the pure PEEK substrate case. In the LPCS case, two different temperature sets were chosen. The aim is to evaluate the process temperature effect, acting on the particles and on the substrate through heat exchange with the gas. The initial conditions are reported in Table 6.5.

| Equipment | Particle velocity (m/s) | Particle temperature (K) | Substrate temperature (K) |
|-----------|-----------------------------|--------------------------|---------------------------|
| HP | 500 | 300 | 300 |
| LP | 280 | 500 | 300 |
| LP | 280 | 600 | 450 |

Table 6.5: Initial conditions for the aluminum particle impacting onto the composite substrate.

Figure 6.4 presents the modified EVF field in the last frame of the three simulations. Particles are more deformed than in the pure PEEK substrate case. This is certainly due to the overall increased stiffness of the composite. In this case, the flattening ratios of the three particles are almost the same: $\epsilon = 1.6$. Moreover, the penetration is lower compared to the pure PEEK case, possibly inhibiting the mechanical anchoring effect, which is the main mechanism for the adhesion of such dissimilar materials. As in the pure PEEK case, in LPCS the effect of temperature is again beneficial for a higher particle penetration in the PEEK top layer. In Figure 6.5 the temperature fields of the three cases are shown. For HPCS, a rise of more than 100 K is visible in the bottom part of the particle and the upper PEEK layer. The LPCS particle temperature, starting at 600 K, overcomes 700 K after the impact. The PEEK matrix near the interface can thus be considered melted.

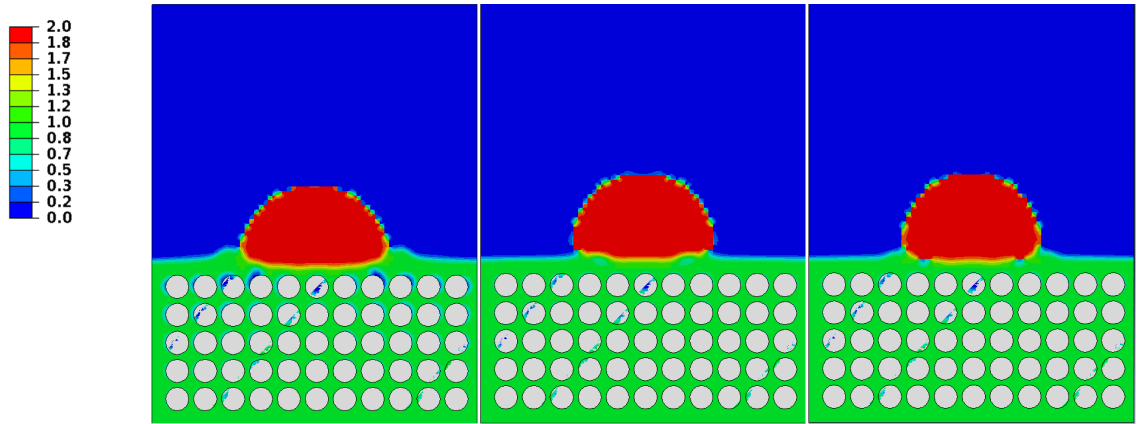


Figure 6.4: Modified EVF field in cross sectional view for the impact simulation of an aluminum particle onto a SCRP substrate. Last frame of the simulation ($2 \cdot 10^{-7}$ s). From the left to the right, HPCS, LPCS with substrate initial temperature at 300 K and LPCS with substrate initial temperature at 450 K.

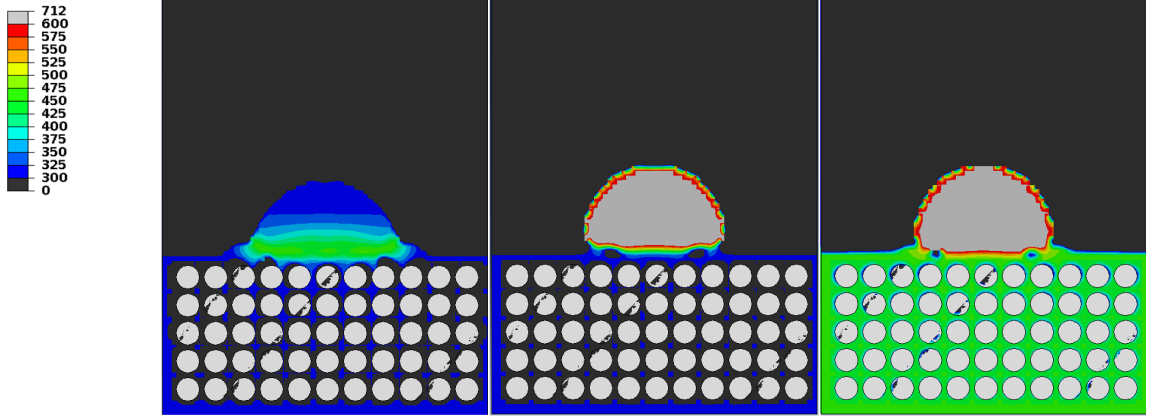


Figure 6.5: Temperature field [K] in cross sectional view for the impact simulation of an aluminum particle onto a SCRP substrate. Last frame of the simulation ($2 \cdot 10^{-7}$ s). From the left to the right, HPCS, LPCS with substrate initial temperature at 300 K and LPCS with substrate initial temperature at 450 K.

In HPCS, the particle reaches the fiber surface. Carbon fibers are modeled with a linear elastic law, so their damage is not considered in the model. Nevertheless, the maximum absolute value of the stresses, shown in Figure 6.6, can give an idea of the possibility of damaged fibers. These values cannot be considered as real, because fibers can debond from the matrix or break at lower values. Anyway, the comparison of the three cases shows that the computed maximum stress in HPCS is more than the double of the LPCS cases. It is thus likely that fibers are damaged in HPCS, as also observed experimentally.

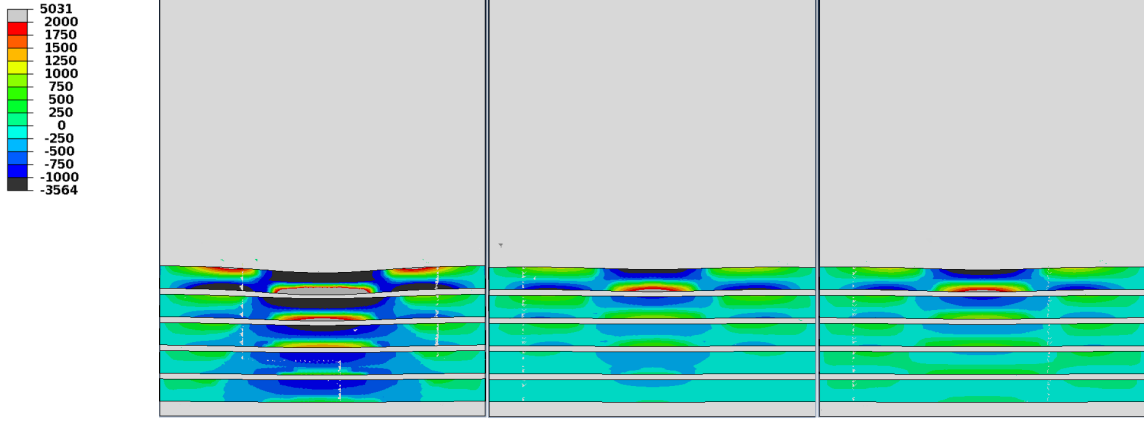


Figure 6.6: Max stress (absolute value) [MPa] field of fibers in cross sectional view for an aluminum particle impact onto a SCRP substrate. From the left to the right, HPCS, LPCS with substrate initial temperature at 300 K and LPCS with substrate initial temperature at 450 K.

Aluminum particle onto a substrate with a thicker top layer

The substrates used in the experimental campaign were produced by injection molding technique. A PEEK top layer of about $3 \mu m$, without fibers, was measured. Since both experimentally and numerically the aluminum particles reached the fiber surfaces with possible damage, a numerical evaluation of the effect of a thicker PEEK top layer is performed here, to assess the validity of such a strategy in protecting the substrate. The goal is to reduce the stress on the fiber beneath and to promote a better mechanical anchoring of impinging particles. The thickness of this layer is now increased to $10 \mu m$. The initial conditions are reported in Table 6.6.

| Equipment | Particle velocity (m/s) | Particle temperature (K) | Substrate temperature (K) |
|-----------|-----------------------------|--------------------------|---------------------------|
| HPCS | 500 | 300 | 300 |
| LPCS | 280 | 450 | 450 |

Table 6.6: Initial conditions for the simulations with a thicker top PEEK layer.

From the modified EVF field in 6.7 it can be noticed that, in both HPCS and LPCS, a thicker PEEK layer allows a better penetration of the particle and, due to the increased contact surface, a better mechanical anchoring. Moreover, even in the HP case, particles are not reaching the fibers, that are protected by the PEEK layer.

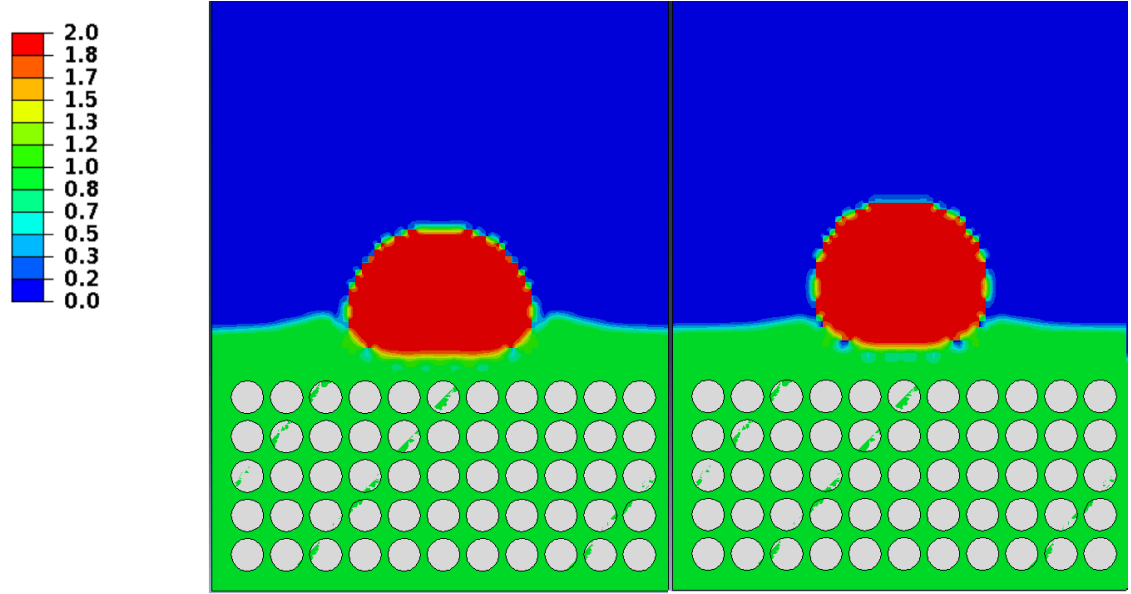


Figure 6.7: Modified EVF field in cross sectional view for the impact simulation of an aluminum particle onto a SCRP substrate with increased PEEK layer. Last frame of the simulation ($2 \cdot 10^{-7}$ s). On the left, HPCS. On the right, LPCS.

Single PEEK particle impact

In the experiments, the addition of PEEK to the aluminum feed-stock powder helped to improve the adhesion and to preserve the substrate from damage. In the rest of the chapter, simulations related to this strategy will be presented. Being the cold spray of polymer powders, a new field to be explored both experimentally and numerically, it seems reasonable to begin with the simulation of the impact of a single PEEK particle onto the SCRP substrate, for both HPCS and LPCS. Initial conditions for the simulations are reported in Table 6.7.

| Equipment | Particle velocity (m/s) | Particle temperature (K) | Substrate temperature (K) |
|-----------|-----------------------------|--------------------------|---------------------------|
| HPCS | 500 | 300 | 300 |
| LPCS | 280 | 450 | 300 |
| LPCS | 280 | 450 | 450 |

Table 6.7: Initial conditions for impact simulations of a PEEK particle onto a SCRP substrate.

The EVF profile in Figure 6.8 shows that the PEEK particle is highly deformed at impact, especially in HPCS. The flattening ratio in all three cases overcomes 1.8

and is equal to 2.1 for HPCS. The particle does not penetrate into the substrate and no signs of erosion are present.

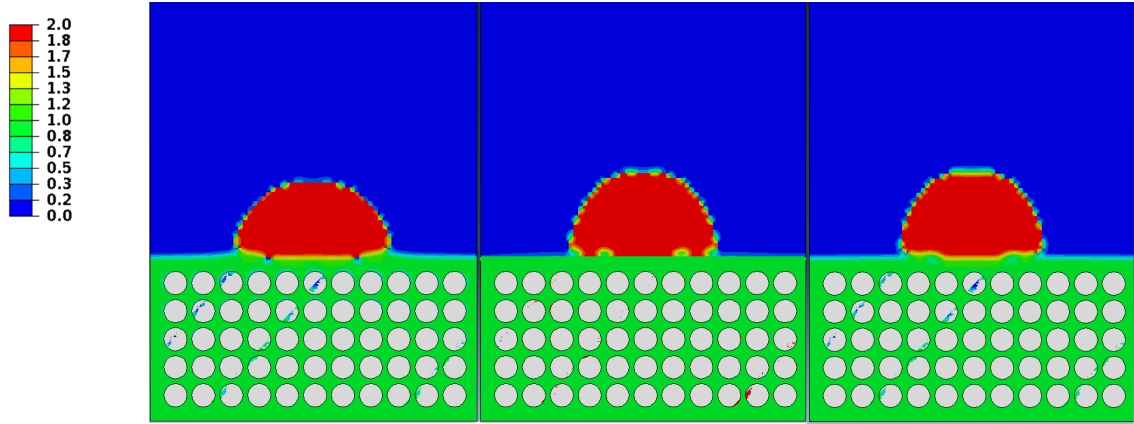


Figure 6.8: Modified EVF field in cross sectional view for the impact simulation of an PEEK particle onto a SCRP substrate. Last frame of the simulation ($2 \cdot 10^{-7}$ s). On the left, HPCS. On the center and on the right, LPCS.

The temperature field illustrated in Figure 6.9 reports a rise of more than 50 K inside the particle. It should be noted that we assumed a homogeneous temperature for the impacting PEEK particle. In reality, as suggested by Bernard in [91], in the cold spray of polymer powders, the temperature inside flying particles should not be considered as homogeneous. Simulation results would then be different if such a hypothesis was implemented. Further investigations should be envisaged in order to catch the real behavior of a cold sprayed PEEK particle. Anyway, even in the case of homogeneous temperature, the PEEK glass transition temperature is overcome and a local melting could occur in the warmer zones.

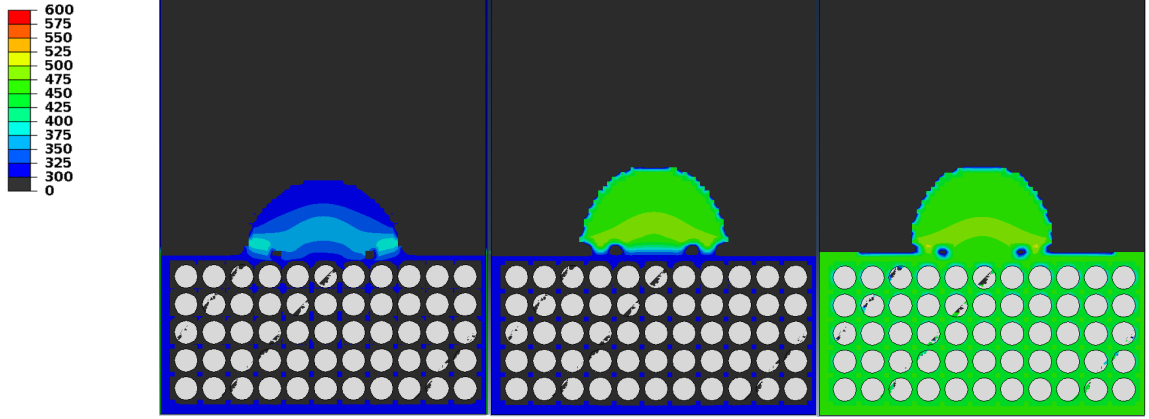


Figure 6.9: Temperature field [K] in cross sectional view for the impact simulation of an PEEK particle onto a SCRP substrate. Last frame of the simulation ($2 \cdot 10^{-7}$ s). On the left, HPCS. On the center and on the right, LPCS.

6.2.3 Bi-particle impact

A further step towards understanding of the cold spray of a metal-polymer powder mixture is to elucidate collective phenomena. The simplest case when representing a two-component mixed powder concerns the interaction of two particles of different nature. In this part, thus, two different elementary cases are presented. The first is an aluminum particle hitting a PEEK one, flying just below it. In the second, materials are inverted: a PEEK particle hits an aluminum one.

Aluminum over PEEK

Initial conditions are reported in 6.8. From CFD results of Chapter 4, PEEK particles resulted to be a little faster than aluminum ones, due to their low weight. Instead, the initial temperature is the same for the two materials.

| | Aluminum | | PEEK | | Substrate |
|-----------|--------------------|-----------------|--------------------|-----------------|-----------------|
| Equipment | Velocity (m/s) | Temperature (K) | Velocity (m/s) | Temperature (K) | Temperature (K) |
| HPCS | 500 | 500 | 300 | 300 | 300 |
| LPCS | 280 | 300 | 450 | 450 | 450 |
| LPCS | 280 | 300 | 600 | 600 | 450 |

Table 6.8: Initial conditions for the simulation of bi-particle impacts, with a PEEK particle below an aluminum one.

The results are presented in Figures 6.10, 6.11 and 6.12. In all cases, the PEEK

particle acts as an anchoring site for the aluminum particle. The PEEK particle heavily deforms and begins to wrap the aluminum one. This is more evident in HPCS due to higher velocities. In LPCS, the PEEK particle is less deformed by the particle above and the wrapping effect is less pronounced. In the case of an initial particle temperature of 600 K, the PEEK particle is completely melted. The PEEK particle acts as an increased PEEK layer, reducing the stress in the composite substrate and protecting the fibers from the impact, as shown in Figure 6.12. It is also clear that the aluminum particle deformation is very low, as seen in the experimental test in chapter three. For these reasons, the dampening effect of the PEEK particles, when they are hit by metallic ones, is nicknamed the "mattress effect". In addition, the aluminum particle can penetrate more into the PEEK material. In this way, the contact surface is increased, as well as the mechanical anchoring. This mechanism helps in explaining the experimental results when spraying aluminum-PEEK powder mixtures. Indeed, it was found that the substrate surface is preserved and that the adhesion strength and the deposition efficiency increase.

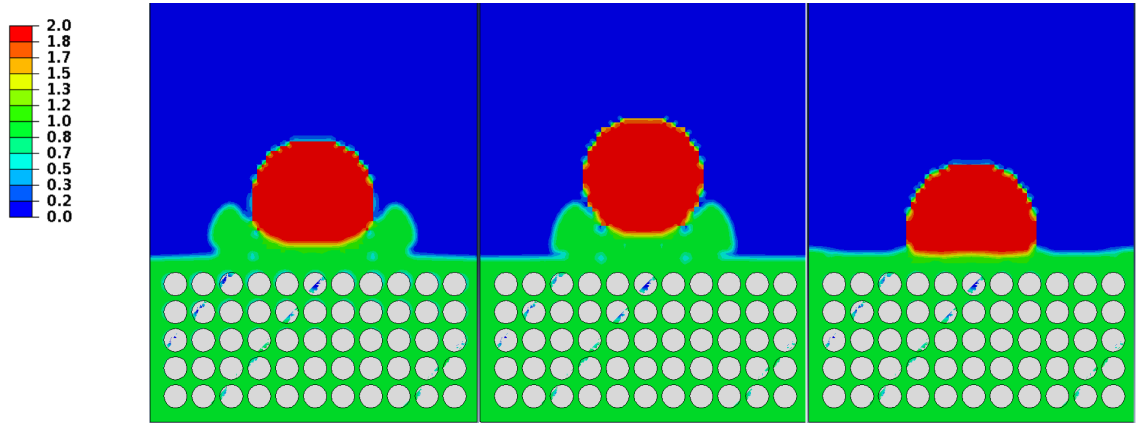


Figure 6.10: Modified EVF field in cross sectional view for the impact simulation of two particles onto a SCRP substrate. The lower particle is PEEK, the upper aluminum. Last frame of the simulation ($2 \cdot 10^{-7}$ s). From the left to the right, HPCS, LPCS lower temperature and LPCS higher temperature.

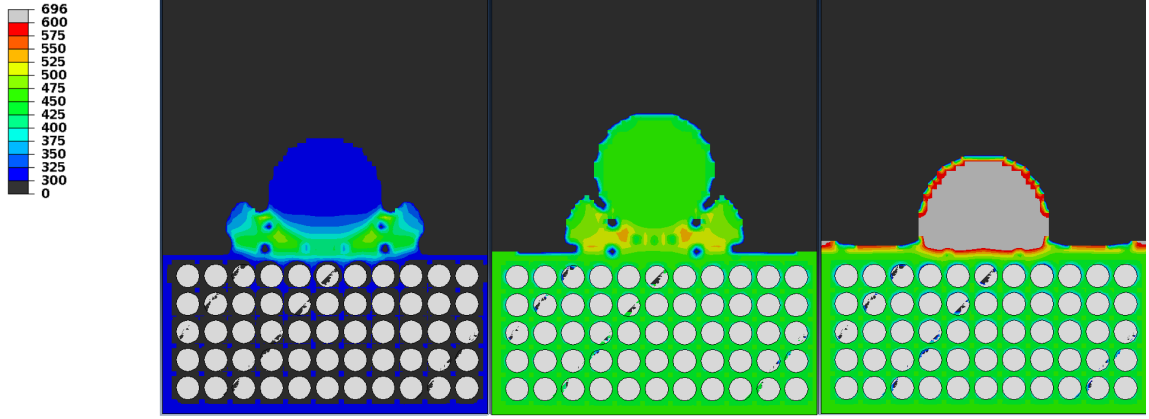


Figure 6.11: Temperature field [K] in cross sectional view for the impact simulation of two particles onto a SCRP substrate. The lower particle is PEEK, the upper aluminum. Last frame of the simulation ($2 \cdot 10^{-7}$ s). From the left to the right, HPCS, LPCS lower temperature and LPCS higher temperature.

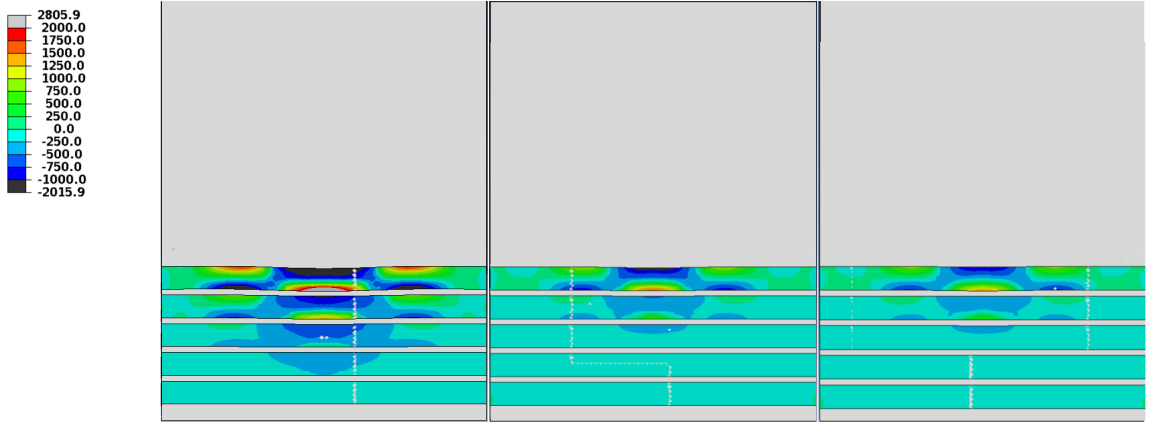


Figure 6.12: Max stress (absolute value) [MPa] field of fibers in cross sectional view for two particles onto a SCRP substrate. The lower particle is PEEK, the upper aluminum. Last frame of the simulation ($2 \cdot 10^{-7}$ s). From the left to the right, HPCS, LPCS lower temperature and LPCS higher temperature.

PEEK over aluminum

These simulations consider a PEEK particle impacting onto an aluminum one. The initial conditions are the same as in Table 6.8 The EVF fields illustrated in Figure 6.13 shows a deformed PEEK particle over the aluminum one in HPCS and LPCS at a lower temperature. For LPCS at an initial temperature of 600 K, the PEEK particle melts and spreads over the aluminum one, which is completely covered. It finally

reaches the substrate, probably adhering to it due to the high temperature. The temperature fields are shown in Figure 6.14. The high temperature PEEK behaves as a glue film capturing the metallic particle, so the effect is nicknamed as “Spider-Man web effect”. Similar behaviors were observed in Chapter 3. This effect is also probably contributing to the increased adhesion and deposition efficiency obtained when mixing PEEK and aluminum particles.

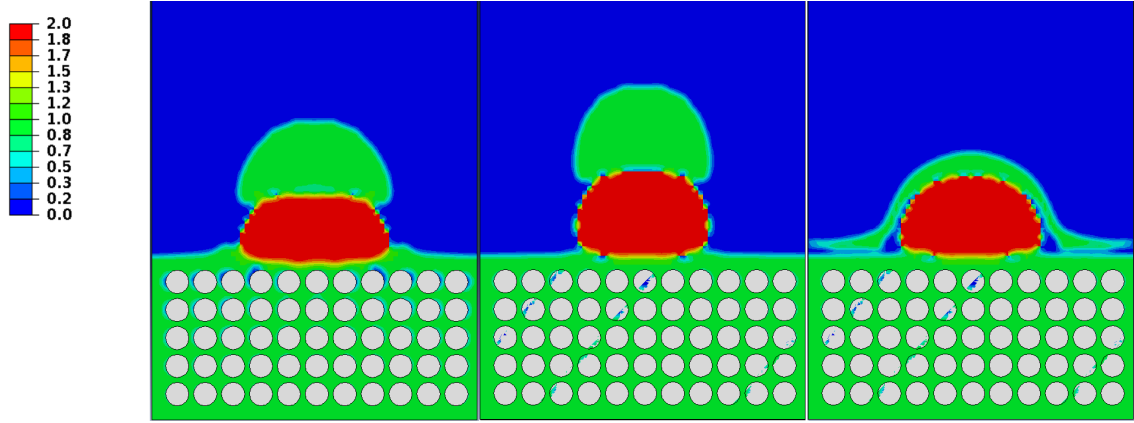


Figure 6.13: Modified EVF field in cross sectional view for the impact simulation of two particles onto a SCRP substrate. The lower particle is aluminum, the upper PEEK. Last frame of the simulation ($2 \cdot 10^{-7}$ s). From the left to the right, HPCS, LPCS lower temperature and LPCS higher temperature.

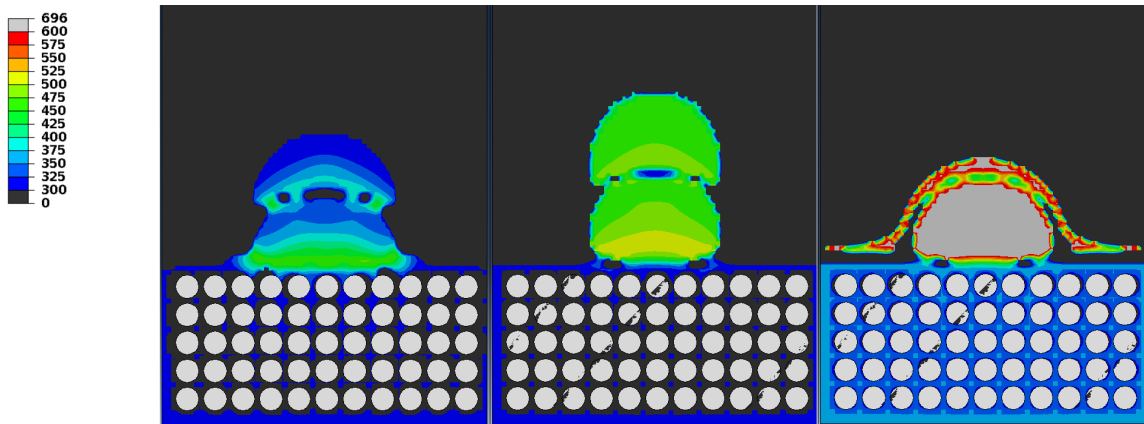


Figure 6.14: Temperature field [K] in cross sectional view for the impact simulation of two particles onto a SCRP substrate. The lower particle is aluminum, the upper PEEK. Last frame of the simulation ($2 \cdot 10^{-7}$ s). From the left to the right, HPCS, LPCS lower temperature and LPCS higher temperature.

6.2.4 Multi-particle impact

To further push the study of collective behaviors of polymer-metal mixed powders, a simulation with 32 impacting particles is carried out. The aim is to observe how the previously explained mattress and Spider-Man web effects take place in a particle cluster and to catch the composite coating structure observed in the experiments. The choice of the number of particles is a compromise to limit the already heavy computational cost of multi-particle simulations and to gather representative results of a large group of particles. Particle velocity and temperature were set respectively to 300 m/s and 600 K, corresponding to the LPCS case with high temperature, as in previous simulations. Half of the number of particles were modeled as PEEK and the other half as aluminum. Even if the real volume ratio between aluminum and PEEK powder is much different, this configuration allows to observe globally all the mechanisms previously singularly modeled. Four eight particle layers were created, the first layer is composed of six PEEK particles in the center and two aluminum at the opposite edge. Instead, the second layer presents six aluminum particles in the center and two PEEK particles at the opposite edge. The third is identical to the first and the fourth to the second. By doing so, it can be observed:

- the effect of aluminum and PEEK particles impacting on the raw substrate
- the effect of aluminum particles impacting onto previously deposited PEEK particles
- the effect of PEEK particles impacting onto previously deposited aluminum particles
- the effect of aluminum particles that bonds to other aluminum particles breaking the PEEK film due to PEEK particles
- the final composite PEEK-aluminum micro-structure

,

The initial configuration is reported in Figure 6.15, where PEEK particles appear in pink color. The final frame of the simulation is presented in Figure 6.16.

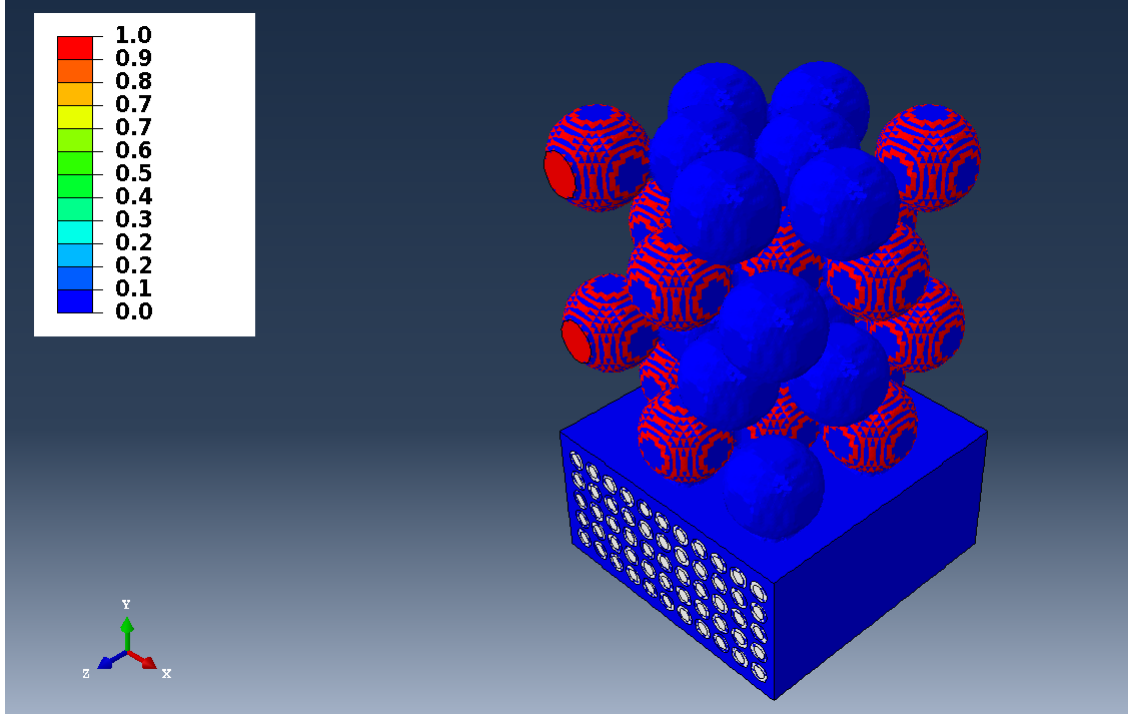


Figure 6.15: PEEK EVF field. Initial configuration of the multi-particle impact simulation.

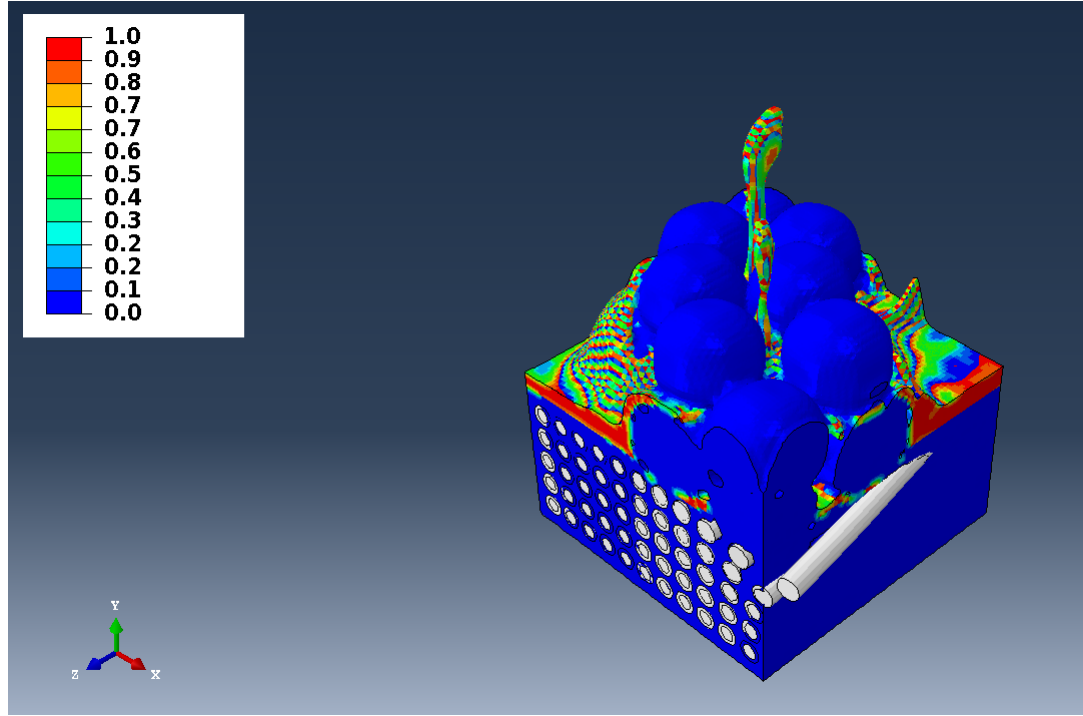


Figure 6.16: PEEK EVF field. Final frame of the multi-particle impact simulation. Aluminum particles, as well as the PEEK matrix, appear in blue. Carbon fibers are in white.

It can be noticed that the aluminum particle on the edge caused a fiber debonding. This is due also to the limited size of the simulation domain. The fiber expulsion from the matrix, thus, is helped by the absence of material outside the domain. PEEK particles are completely deformed and probably melted. A PEEK layer seems to cover inner aluminum particles.

Figure 6.17 illustrates how the previously reported effects operate in a multi-particle case. An aluminum particle (in red) is completely embedded with PEEK (in green), due to the Spider-Man web effect. Other aluminum particles hit PEEK ones, attenuating the impact and preserving the substrate top layer. This illustrates the mattress effect. It can also be noticed that, even if PEEK surrounds many particles, a percolating path within the aluminum phase is possible. In conclusion, although the comparison is only qualitative at this stage, the microstructure resulting from the multi-particle impact simulation is similar to those found in the experiments.

Further work is needed, with more accurate simulations (*e.g.* with a larger substrate and simulation domain, with different proportions of PEEK and aluminum particles) and with the development of quantitative comparison criteria, to transform this kind of model into a predictive tool to be used for optimization purposes.

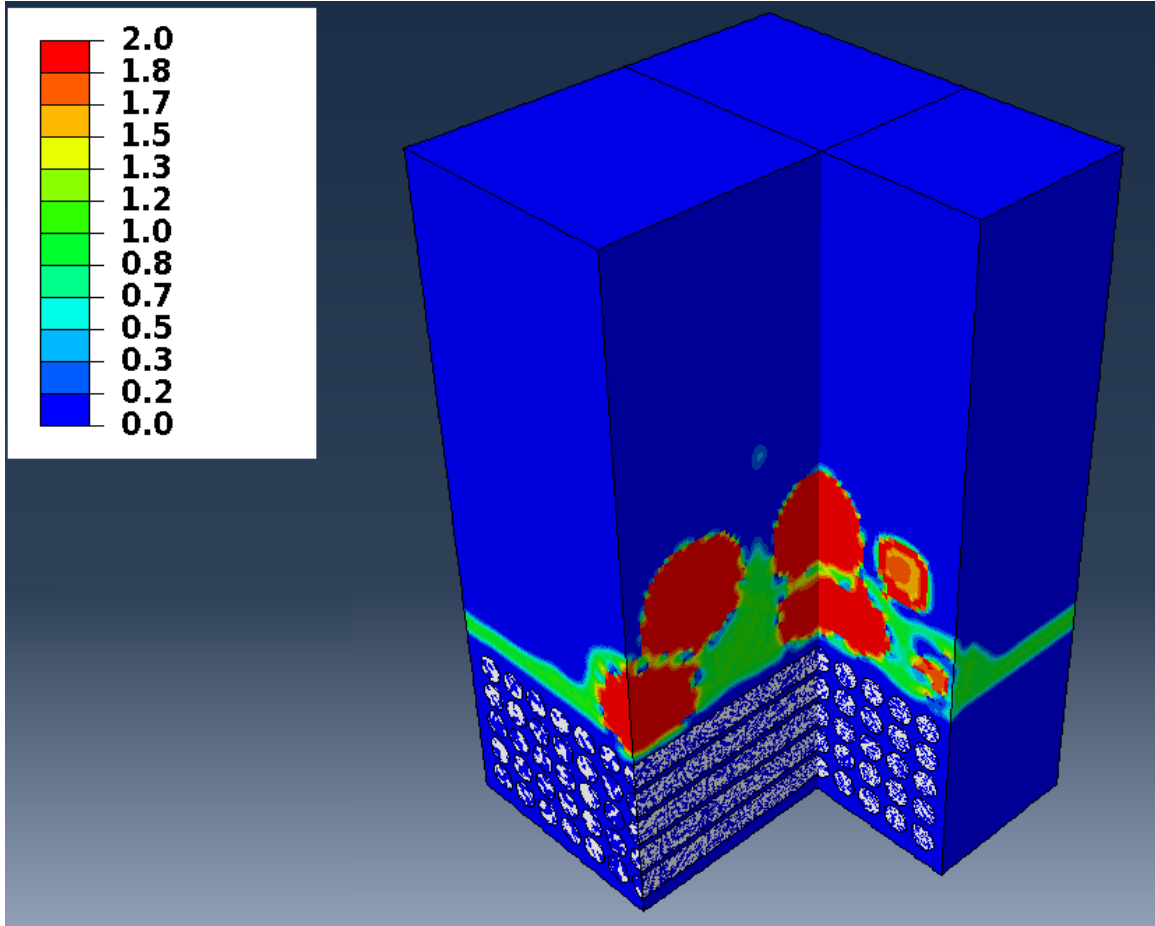


Figure 6.17: Modified EVF field in double cross sectional view for the multi-particle impact simulation.

6.3 Conclusion and perspectives

FEM analyses were carried out to investigate the cold spray particle impact by means of the Abaqus/Explicit commercial software. A full Eulerian approach in the case of pure PEEK substrate and a coupled Eulerian Lagrangian approach in the case of composite substrate were adopted. Single and multi-particle impacts with aluminum and PEEK materials were successfully modeled. Different strategies for reducing short carbon fiber damage were presented. Some clues about the dissimilar behavior of the particles sprayed by high and low pressure cold spray could be obtained. For what concerns HPCS, the high speed particles penetrate further into the substrate, as compared to LPCS. Nevertheless, in LPCS higher particle temperatures can reduce this gap. In effect, when substrate and particle temperatures are increased, particles can reach the same penetrations as in HPCS. This happens when the substrate temperature overcomes the PEEK glass transition temperature. HPCS particles can erode the top surface, reaching and probably damaging the carbon fibers. Compared to LPCS, in HPCS the fiber stress is more than double. Two different strategies were envisaged to protect the composite, no matter which equipment it is used. The first one is an increased top layer of pure PEEK. Experimentally, this could not be tested, but simulation results encourage to examine this possibility. The protective PEEK layer reduces the stress induced on carbon fibers, preserving them from damage. Moreover, it can possibly improve the penetration and mechanical anchoring of particles. The second strategy, used in the experiments, involves again PEEK, this time in the form of powder, to be added to the aluminum one. Two main effects were identified. In the mattress effect, when an aluminum particle hits a PEEK one, the latter permits to reduce the stress on the fibers and to increase the mechanical anchoring. This mechanism is similar to the one acting in the case of a PEEK protective layer. The second effect, namely the Spider-Man web, appears when a PEEK

particle impacts on an aluminum one. The former embeds the entire aluminum particle, trapping it to the substrate, as Spider-Man does with people or objects on the walls. A multi-particle simulation illustrated how these effects operate when a group of particles impacts the substrate. In the real cold spray, where millions of aluminum and PEEK particles impinge onto a SCRP substrate, similar microstructures were observed. Indeed, aluminum particles result embedded in a PEEK matrix that acts as a glue. When aluminum particles impact on other aluminum particles, they are more deformed and bond with each other, creating a high-conductivity pathway for electrons. Thus, considering the small percentage of PEEK in the mixtures sprayed in experiments, statistically the fraction of metal-on-metal impacts is dominating. Anyway, the best strategy to optimize both adhesion and conductivity is to use the mixture only as a sub-layer. Further improvements in the approach developed in this thesis concerns the PEEK material model. Here, a JC model was adopted, even if it is more suitable for metals. Different models should be envisaged for a better understanding of the behavior of PEEK powders and substrates in high speed dynamics. An interesting constitutive model is presented in [63]. It keeps into account thermal softening, strain rate, pressure sensitivities, and temperature evolution in the cold spray process regime. A tentative of implementing the model in Abaqus user subroutine was done during this PhD work and first tests were performed. Unfortunately, due to time limitations, this work could not be applied to particle impact simulations. New tests with a rheological model, as well as simulations with increased domain size and number of particles, should be envisaged to improve the approach towards the development of a predictive tool intended for optimization.

CHAPTER 7

INDUSTRIAL APPLICATIONS

Abstract

This concluding chapter briefly presents a possible industrial application for the metallization of PEEK based short carbon fiber composites by cold spray. In addition, the expertise acquired and the methods developed open new perspectives for other thermo-sensitive and brittle substrates. In particular, the very first composite material used by mankind, the wood, was studied in cold spray experiments to explore the possibility to produce metal coatings onto this organic material. Finally, cold spray was applied to PA66 samples produced by a 3D printing technique to assess the possibilities of the process onto the complex surfaces and geometries that additive manufacturing can develop.

Résumé en français

Les chapitres présentés jusqu'à présent ont montré la possibilité d'obtenir des revêtements adhérents et conducteurs sur des composites à fibre courtes de carbone. Les meilleurs résultats ont été obtenus avec une poudre mixte contenant une majorité d'aluminium et une plus petite fraction de PEEK. Ensuite, des études de simulation CFD et FEM ont permis de mieux comprendre les phénomènes impliqués et de confirmer certaines intuitions déjà formulées dans la partie expérimentale. Le rôle principal de la température a été évalué, les particules pénètrent davantage si la température de transition vitreuse du PEEK est atteinte. Ceci est dû à la fois à la température élevée des particules et des gaz comme le montrent les chapitres 4 et 5. L'expertise acquise et les méthodes développées ont ouvert de nouvelles perspectives pour d'autres

substrats thermosensibles et fragiles. Dans ce travail, le tout premier composite, le bois, a été utilisé comme substrat pour comprendre si le procédé CS pouvait convenir pour produire des revêtements métalliques sur ce matériau organique. Ensuite, des échantillons de PA66, produits par la technique FFF, ont été testés pour évaluer le processus CS sur ce matériau et surtout sur les différentes surfaces et géométries qu’une technologie d’impression 3D peut développer.

7.1 Introduction

The chapters presented so far showed the possibility of obtaining adherent and conductive coatings onto short carbon fiber reinforced PEEK composite. The best results were obtained with a mixed powder containing a majority of aluminum and a smaller fraction of PEEK. Then, fluid dynamics and mechanical models allowed to better understand the phenomena involved and to confirm some intuitions already formulated in the analysis of the experiments. This concluding chapter rapidly overviews some of the potential industrial applications of cold spraying onto thermo-sensitive substrates. In particular, after presenting the industrial application of the cold spray metallization of short carbon fibre reinforced PEEK composites, the metallization of wood and of 3D printed PA66 parts by cold spray is presented.

7.2 Cold spray metallization of short carbon fibre reinforced PEEK composite for the aerospace industry

The substrate studied in the previous chapters, the short carbon fibre reinforced PEEK composite, has potential applications in the aerospace industry, among other sectors. One of the partners of this study envisaged using this PEEK-based composite to replace of some metallic components in a turbopump system used for air conditioning in the airplane. The targeted parts are turbo-machinery volute and air bleed valves. Both elements are connected to aluminum pipes and various metallic

components. Air friction can cause static charges to create and accumulate on PEEK components, with possible damage due to the Joule effect during electrical discharge. The evacuation of electric currents coming from other airplane components could lead to the same issues. Cold spray was chosen due to the very low working temperature compared to other thermal spray technologies. Moreover, homogeneous coatings can be produced, bringing then homogeneous conductivity.

The following requirements and recommendations are formulated by the industrial partner for the coating:

- in the case of evacuation of static charges, resistance should be lower than $100m\Omega$;
- in the case of evacuation of electric currents, resistance should be lower than $20m\Omega$;
- good adhesion strength (no range provided);
- thickness lower than $500\mu m$;
- no damage to the substrate;
- coating stability, in terms of adhesion and integrity, for temperature variations between -55 and $+85$ C;
- resistance to salt spray test (96h);
- resistance to vibrations and to most acidic products.

For what concerns the first two requirements, they were matched with a value always below $10m\Omega$ as shown in Chapter 3. The adhesion strength, especially in the case of high PEEK content in the feed-stock powder, can be considered satisfactory as compared to literature values. Electrical conductivity and adhesion strength were shown, in Chapter 3, to be two antagonistic properties. The increase in PEEK percentage

in the mixture led to higher adhesion strengths and lower electrical conductivities. An optimal solution could be the development of a gradient composition coating, in order to take the best properties from the two solutions. This could be realized by varying the feed-stock mixture composition during the spraying process, gradually decreasing the PEEK powder percentage. In this way the first layers closer to the substrate will assure a better adhesion, while the superficial ones, richer in metal will assure an optimal conductivity. The process allows one to adapt the coating thickness by tuning the gun transverse velocity, the flow rate, and the stand-off distance. Being the goal of this application to have thin and lightweight conductive coatings, it was demonstrated that $400\mu m$ thick coatings could reach the required resistance. Moreover, the PEEK substrate does not seem to be affected and mechanical properties of the composite are preserved. In conclusion, the cold spray technology revealed a possibility to replace conductive painting and metal grids to add electrical conductivity to polymer based composite materials. For perspective, a mechanical tensile test as well as thermal cycling test should be envisaged. Also, an economic analysis will be necessary to complete the case study before the application. Proper validation to match the aeronautical requirements should be envisageable. Finally, non-destructive testing, such as 3D observations by microtomography, could confirm the lack of damage in the composite substrate.

7.3 Metallization of wood for luxury and design applications

7.3.1 Introduction

Wood is an heterogeneous and anisotropic material, which obliges to analyze phenomena both at the micro scale and at the macro scale. Wood is hygroscopic, porous and strongly affected by the environment and aging. Ultraviolet radiation and fungal growth are the main causes of loss of structural and aesthetic properties, as reported for example in [127], [128] and [129]. Several techniques are commonly used for wood

protection, involving structural measures, superficial protection, by lacquers, or a deep protection by wood impregnation procedures. All these solutions are either expensive or not environmentally sustainable. Thermal spray could be a feasible way to protect, improve and add functionalities to wooden substrates. Plasma spray of copper resulted in a very good way to preserve the materials against UV rays and microbial activity. Anti-wearing and conductivity functionalities could be added to the wooden samples as well aesthetic design . In [94], a thin copper layer was successfully deposited by means of plasma spray technology onto different species of wood. The purpose was to evaluate if this copper coating could preserve wood in different scenarios. The mildew growth resistance was assessed as well as the water vapor permeability and the weathering protection, thanks to the copper layer. Anyway, this coating does not appear to be not water repellent. The adhesion was excellent, even more so with a sanding surface preparation method before spraying. Another work, presented in the ITSC 2019 conference [130], tried to begin a discussion about the usage of cold spray on wooden substrates. Various potential applications can be envisaged for cold spray on wood. First, an anti-weathering layer, preserving the substrate for outdoor applications, or adding conductivity and wear resistance. Another possibility is the assembly of wooden parts without glue to create innovative multi-materials.

7.3.2 Cold spray experiments

The experience gained with the SCRP opens new perspectives for the usage of the CS process on thermo-sensitive and brittle materials, such as wood. The brittle behavior of carbon fibers is somehow similar to that of wood fibers. This can help to understand the phenomena involved in particle impact onto wooden surfaces. Moreover, the solutions retained for the thermo-sensitive PEEK can be useful to choose the right setup of cold spray parameters for wood. The different sections and the

micro-structures of the wooden substrate must be kept in account especially when the impacting particles have sizes in the same order of magnitude. Vessels, fibers and rays behave in dissimilar ways along the different axes when subjected to the high speed particle flow. For this reason all sections are tested and analyzed to understand the phenomena involved. Four different wooden species, namely oak, sycamore, ash and walnut, were tested, with both HPCS and LPCS. An exploratory work was done using a wide range of spraying parameters to find a suitable setup for the wood substrate. The received tablets were cut into cubes with 1 cm long edges, to test as many cold spray parameters as possible. The powders used were commercially-purity aluminum, tin, copper and zinc, with average particle sizes of, respectively, 45, 63, 17 and 20 μm . During HPCS tests only aluminum and tin powders were employed. All materials were tested in LPCS. In addition, a 20%vol.PEEK-copper mixture was tried. HPCS and LPCS parameters are presented in Tables 7.1 and 7.2.

| Powder | Pressure (MPa) | Temperature (C) | s.o.d (mm) | Gun speed (mm/s) |
|----------|----------------|-----------------|------------|------------------|
| Aluminum | 1-2.5 | 100-350 | 20-40 | 100-200 |
| Tin | 0.8-1.5 | 50-250 | 20-40 | 100-200 |

Table 7.1: HPCS parameters with a wooden substrate.

| Powder | Pressure (MPa) | Temperature (C) | s.o.d. (mm) | Gun speed (mm/s) |
|-------------|----------------|-----------------|-------------|------------------|
| Aluminum | 0.4-0.6 | 400-600 | 10-30 | 100 |
| Tin | 0.4-0.6 | 250-400 | 10-30 | 100 |
| Copper | 0.4-0.6 | 400-600 | 10-30 | 100 |
| Copper/zinc | 0.4-0.6 | 400-500 | 10-30 | 100 |
| Zinc | 0.4-0.6 | 400-500 | 10-30 | 100 |

Table 7.2: LPCS parameters with a wooden substrate.

HPCS tests revealed that aluminum powder was not a suitable choice for wooden substrates. In fact, despite the spraying parameters adopted, in all cases no coating could be grown. All the surfaces and wooden species were completely eroded. An example is reported in Figure 7.1.

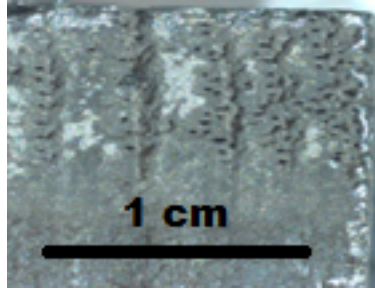


Figure 7.1: Top view of a wood sample cold sprayed with aluminum powder.

Although, some useful information could be extracted about the different behavior of the four wood species and the three surfaces. Transversal sections and particularly the sycamore species showed better behavior in terms of resistance to erosion. It was then decided to continue the HPCS study only onto the transverse section of sycamore samples. Further experiments were conducted by HPCS, using tin as feed-stock powder with the purpose of avoiding the erosion experienced with aluminum. Tin is in fact softer than aluminum and easily deformable at impact. Being careful not to exceed the melting point of tin (230 C) and to reduce as possible the HPCS pressure to limit erosion, some results were obtained. Thick tin coatings were successfully produced onto sycamore transverse surface, as shown in Figure 7.2.

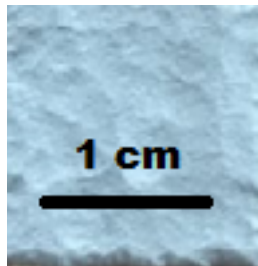


Figure 7.2: HPCS tin coating onto wood sample.

Starting with this exploratory HPCS session, the following conclusions are drawn:

- harder and faster particles erode the brittle wood structure;
- higher temperature promotes adhesion and coating build-up;
- low melting temperature metals are easier to spray and can be used to create a bond coat.

To reduce particle velocity while preserving or increasing the temperature, LPCS is chosen. Aluminum and tin were sprayed, to compare the results with HPCS. Here, deposition onto all the wood species and surfaces is obtained. Zinc presents an interesting compromise between mechanical properties and the low melting temperature. It was sprayed alone and in a mixture with copper. Moreover, following the strategy used for composites, a mixture of 20% PEEK and copper was tested. If copper alone could not be directly sprayed onto the wood, a tin bond coat allowed its deposition. The results are shown in Figure 7.3.

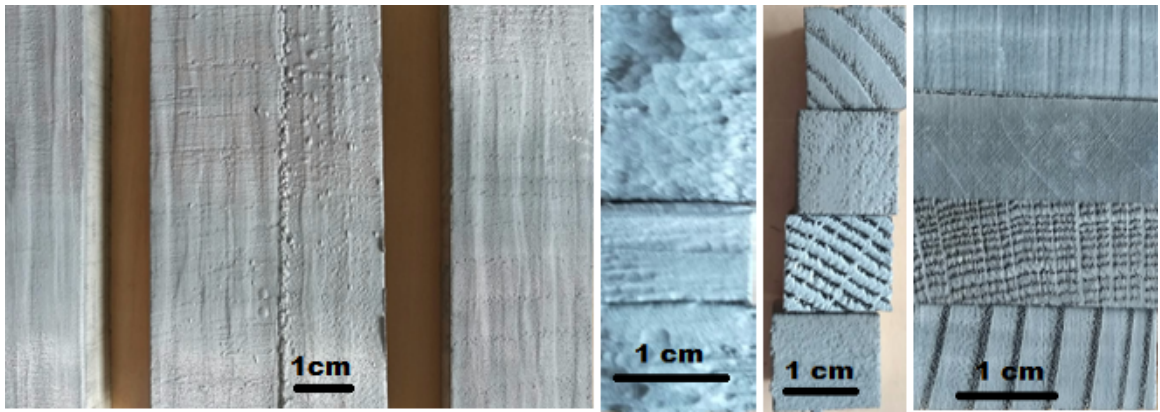


Figure 7.3: LPCS of metals on wood. From the left to the right, tin (bond layer) and copper, tin, aluminum, zinc.

Characterization of top surfaces and of the metal-wood interfaces of sprayed samples by means of optical and SEM microscopes is not an easy task. Because of the porous nature of the wood, classical polishing techniques revealed to be deleterious. The water used as a lubricant, in fact, penetrates into the inner structure of wood, changing its properties. This can be solved by embedding wooden samples into resin and using ethanol as the polishing fluid. To increase the quality of SEM images, a final polishing session with a colloidal silica gel is recommended.

SEM observations of the coated samples show the different mechanisms in coating formation, depending on the type of surface. When a transverse surface is exposed to LPCS, the sprayed particles begin to fill up the vessels, which can be considered as elongated holes. This can be seen in Figure 7.4. At the same time, they begin to

depose on the fibers, but cannot penetrate inside, since these are smaller than the particles. As a consequence, fiber compaction is observed. The modified structure then offers an increased resistance to impacting particles, allowing the coating build-up to begin. The filling of vessels can be better understood by looking at Figure 7.5. Aluminum particles penetrate far inside the vessels, without deformation. No coating was created in this case, since the sprayed particles revealed to be too hard for the wooden substrate.

When spraying onto the radial section, fibers are hit on their longitudinal surface and no vessels are present. The results are shown in Figure 7.6. The first layer of fiber is destroyed by impacting particles, while those below begin to compress, increasing the stiffness of the structure. At this point, the coating build-up begins.

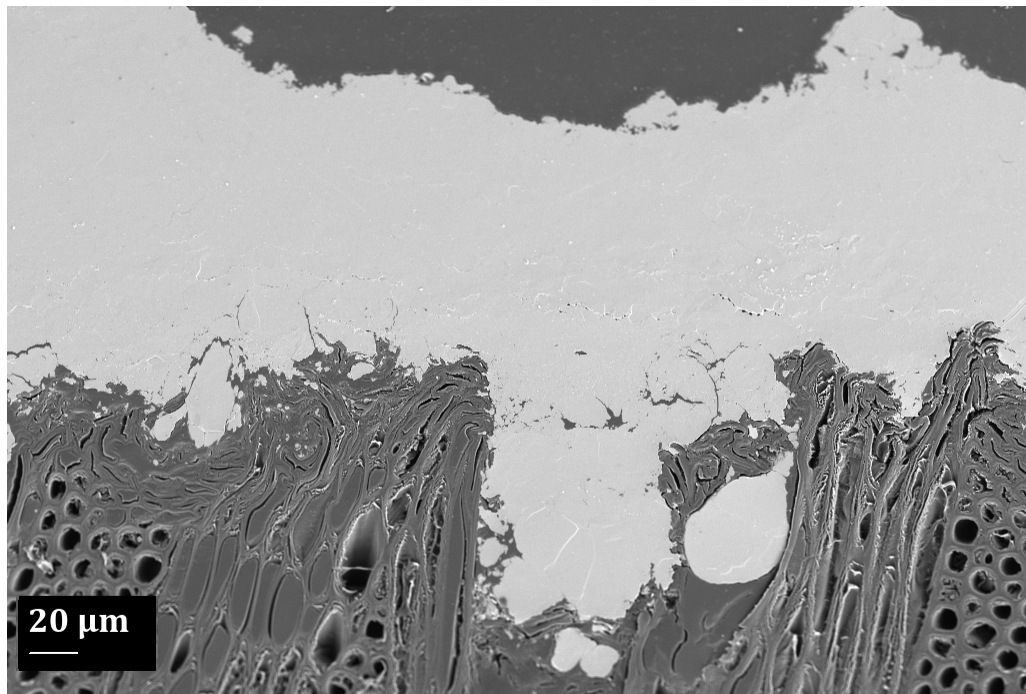


Figure 7.4: SEM cross section of LPCS tin bond coat onto the transverse surface of a sycamore sample.

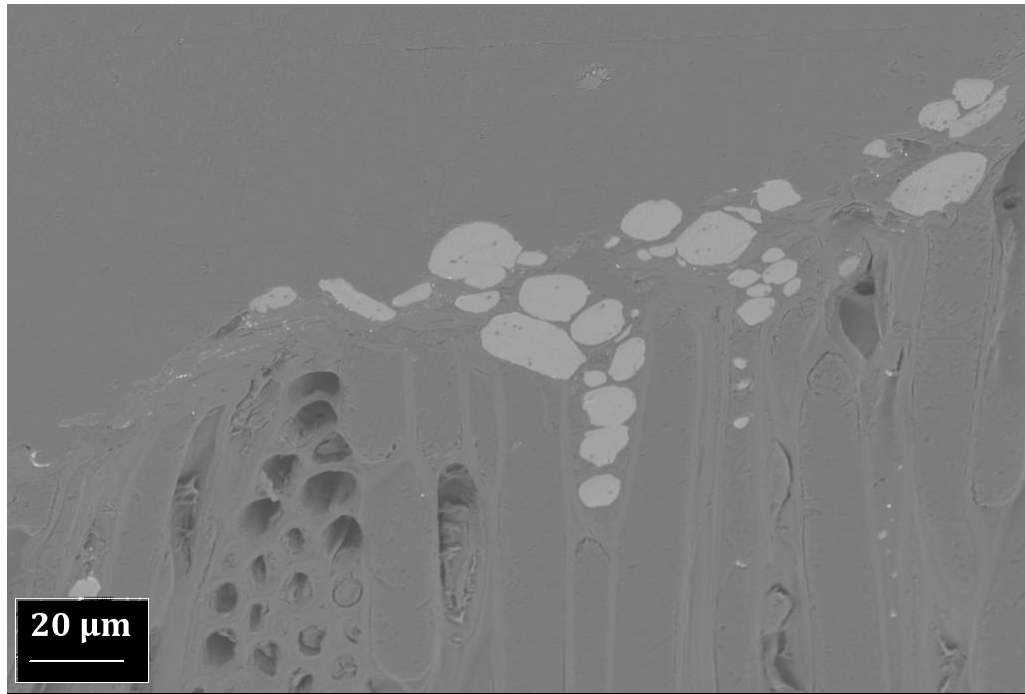


Figure 7.5: LPCS of aluminum particles onto the transverse surface of a sycamore sample.

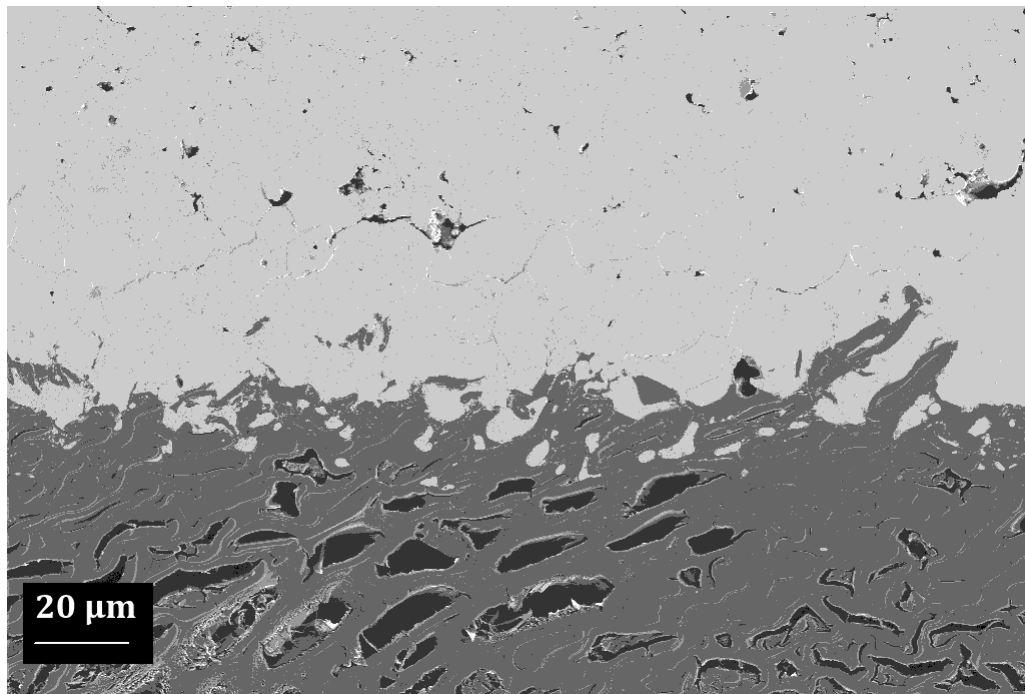


Figure 7.6: SEM cross section of LPCS tin bond coat onto the radial surface of a sycamore sample.

A mixture of zinc and copper powders is well tolerated by the wooden surface and a very thick coating can be obtained on the radial surface, as shown in Figure 7.7.

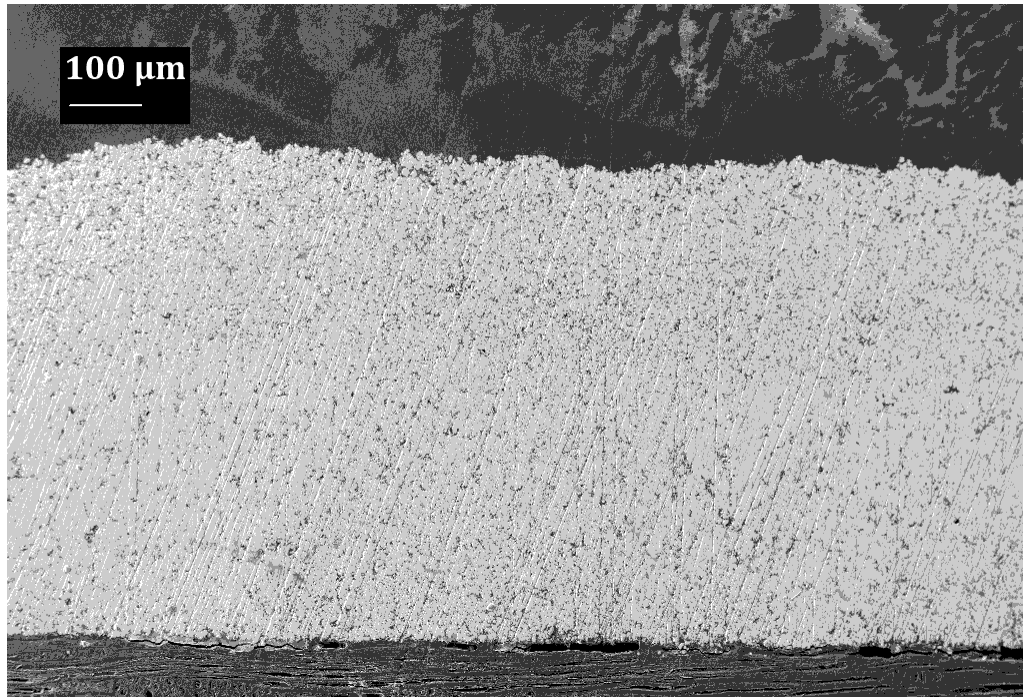


Figure 7.7: SEM cross section of a copper-zinc coating onto radial surface of sycamore specimen.

7.3.3 Modelling of particle impact onto the wood surface

The behavior of wood is hard to predict due to the complex multiscale structure of the material. In [131], an innovative approach to numerical modelling of wood has been proposed, using the commercially available finite element software Abaqus. This work was taken as a reference for the modeling of the deformation of wooden microstructures under particle impact. Instead of modeling wood with macroscopic homogenized properties, the cellular microstructure was considered, at the scale of the fibers. The model uses shell elements, is assigned to the microscopic material properties of the cell walls and loaded with transverse compression. The cell structure of wood was idealized for simplicity as a regular honeycomb pattern. This is not the case in the real wood material because not every cell is not hexagonal or equally sized.

For practical purposes, irregularities in the cell structure were neglected. In Figure 7.8, the response of the structure to the imposed transverse compression is shown. First, as shown in Figure 7.8 on the left, the honeycomb pattern deforms elastically. Then, the cell walls begin to buckle, causing cell layers to cave in on themselves, as illustrated in Figure 7.8 in the middle. When the cells collapse, as in Figure 7.8 on the right, their inner walls go into self-contact, with an increase in global stiffness.

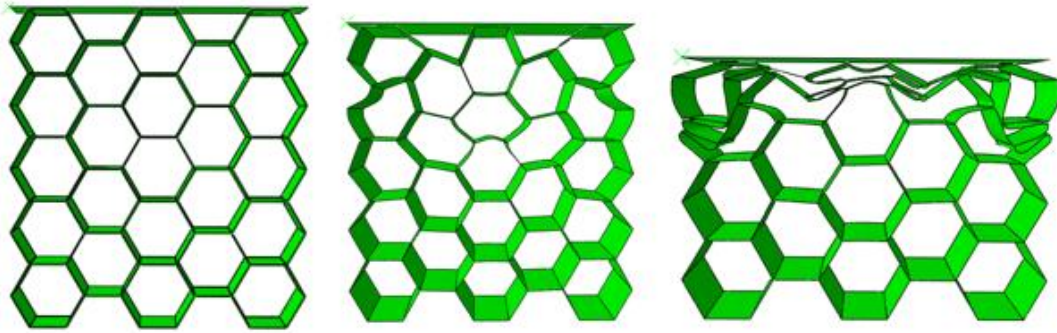


Figure 7.8: Mechanical behavior of the honeycomb structure of wood under a compressive load from the top, after [132]. The structure is shown in different subsequent states: undeformed (left), slightly deformed with small bending and buckling of cell walls (middle) and severely crushed, with self-contact of cell walls (right).

The first identified aim of numerical simulations is to catch and investigate elementary phenomena that led to strong wood erosion, in the case of aluminum powders, or to coating formation, when spraying tin. In particular, the interaction of metal particles with the surface structure of the wood, at particle scale, is crucial. For this purpose, the data required for the modeling are the shape, velocity, temperature and material for the particles, as well as, for wood substrates, geometry and mechanical properties of its structural constituents, at the particle scale ($10 - 100\mu m$). SEM observations and literature review, as for example [132], provide data for the representation of a simplified structure, starting from real observations of the wood. The finite element method was chosen as the tool for the simulation of elementary impacts of particles onto the wood surface, using the commercial software Abaqus/Explicit as in the previous chapter. The size of the 3D modeling domain was identified as

slightly larger than that of the cold sprayed particles. This corresponds to the so-called meso-level structure of the wood, where fibers and vessels are present. At this scale, the material appears as a structure made up of objects of $10\mu m$ (fibers) and $150\mu m$ (vessels), as shown in Figure 7.9.

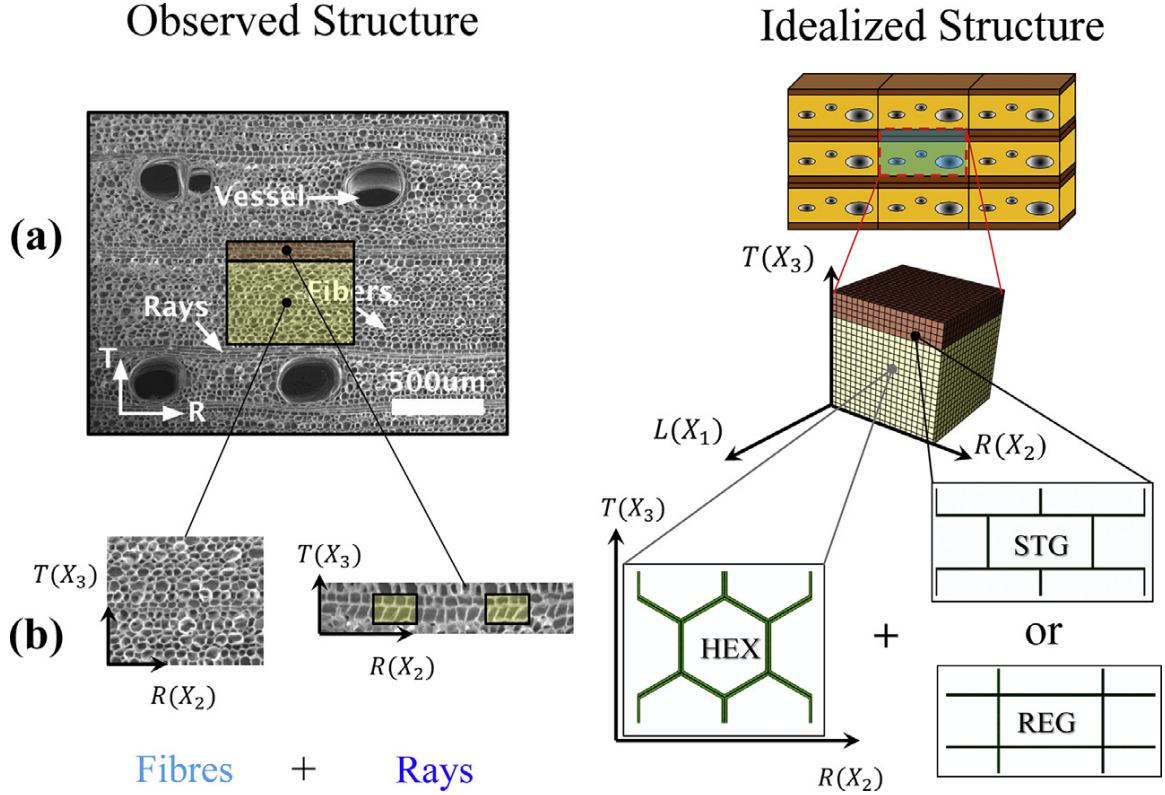


Figure 7.9: Unit cell geometries representing fibers and rays at the macro-scale (a) and meso-scale (b)

At the first level of approximation, a simplified wood structure can be imagined as made up of extruded hexagonal cells (i.e. the fibers). This simplification is particularly useful when trying to build up a mechanical model of wood, as done in literature for example in the already cited work [132] shown in Figure 7.8. In a first approach, the interaction of an aluminum particle with a single fiber is considered, oriented as in a typical radial section. A damage model is included for fiber material, with values obtained from [132]. The results are shown in Figure 7.10. At impact, the lateral surface of the fiber is heavily damaged and the particle penetrates into it. A more complex simulation was then developed, trying to replicate the honey-

comb structure of wood with multiple hexagonal fibers. Here, the damage model is excluded to concentrate on the buckling mechanism also observed experimentally. A result is reported in Figure 7.11. Several fibers have to buckle completely to absorb all the kinetic energy of the impinging particle. Fiber compaction leads to an increased stiffness, so it is likely that forthcoming particles will not produce such severe deformations of the structure. Even if this would need further work to be elucidated, it seems that this mechanism allows particle deposition on the wooden radial surfaces. This modeling approach, with its extreme simplifications, is simply a starting point to understand the behavior of wood under cold spray particles.

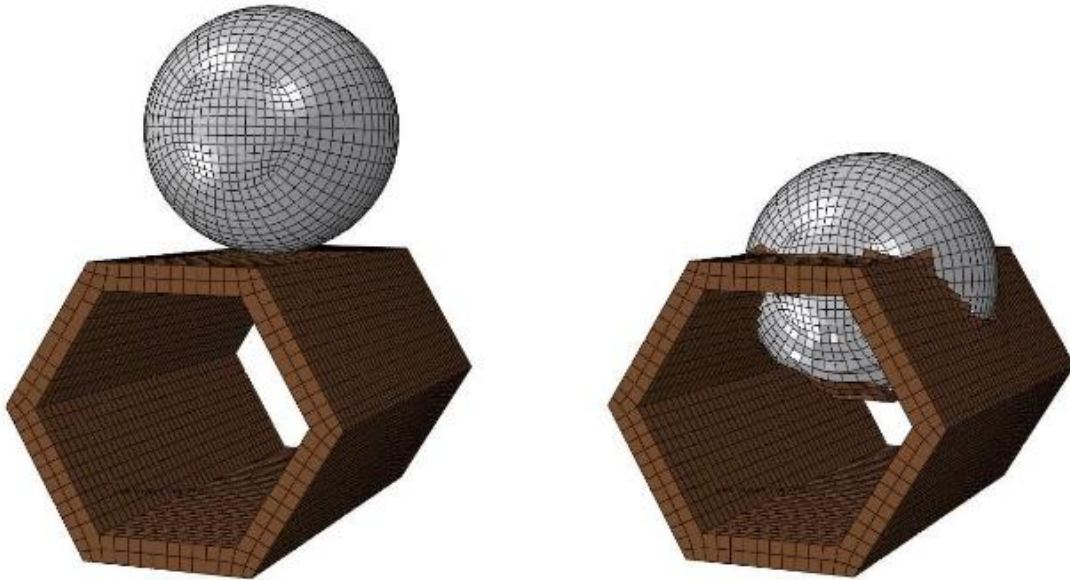


Figure 7.10: Particle (diameter $20\mu m$) impacting onto a single wood fiber at $500ms^{-1}$.

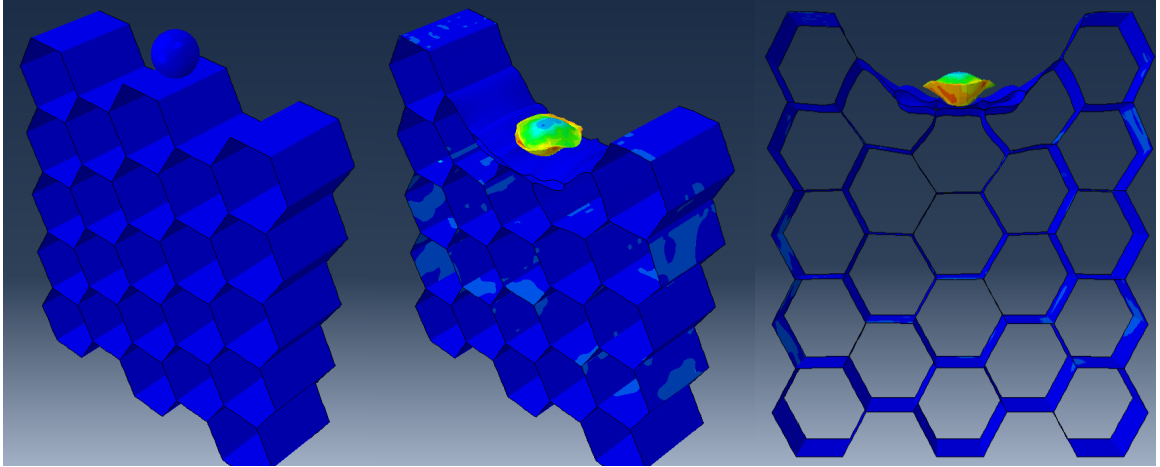


Figure 7.11: Particle (diameter $20\mu\text{m}$) impacting onto an hexagonal array of wood fibers at 500ms^{-1} .

7.3.4 Conclusions

The idea of using cold spray onto wood is an innovative way to produce new material assemblies made of metals and organic substrates. This was an exploratory work and the obtained results should be considered preliminary. As for PEEK-based composites, LPCS revealed to be more suitable in producing metal coatings wood. Transverse sections revealed to be more apt to receive a coating due to the orientation of vessels and fibers. Sycamore showed better behavior compared to the other three species in both HPCS and LPCS. Tin can be deposited without particular difficulties and it can be used as bond coat for copper and harder metals. The zinc and zinc-copper mixture was deposited directly without the usage of tin. To conclude, several metals were sprayed successfully on wood, but for the moment only an aesthetic purpose can be achieved. In order to have a glue-free assembly, aluminum coating should be produced without damaging the wooden substrates. Nevertheless with further improvement and test, better results can be achieved in future works.

7.4 Metallization of PA66 additively manufactured substrates

The 3D printing method, alternatively known as additive manufacturing (AM in the following), is promising for rapid prototyping and layered micro-manufacturing. Using this technique, complex structures can be produced with polymers and polymer-based composites, reinforced with fibers. In the case of the Fused Filament Fabrication (FFF) process, the machine prints samples by extruding a polymer filament through a heated nozzle in a specific pattern onto a substrate. A schematic view of this type of machine is shown in Figure 7.12.

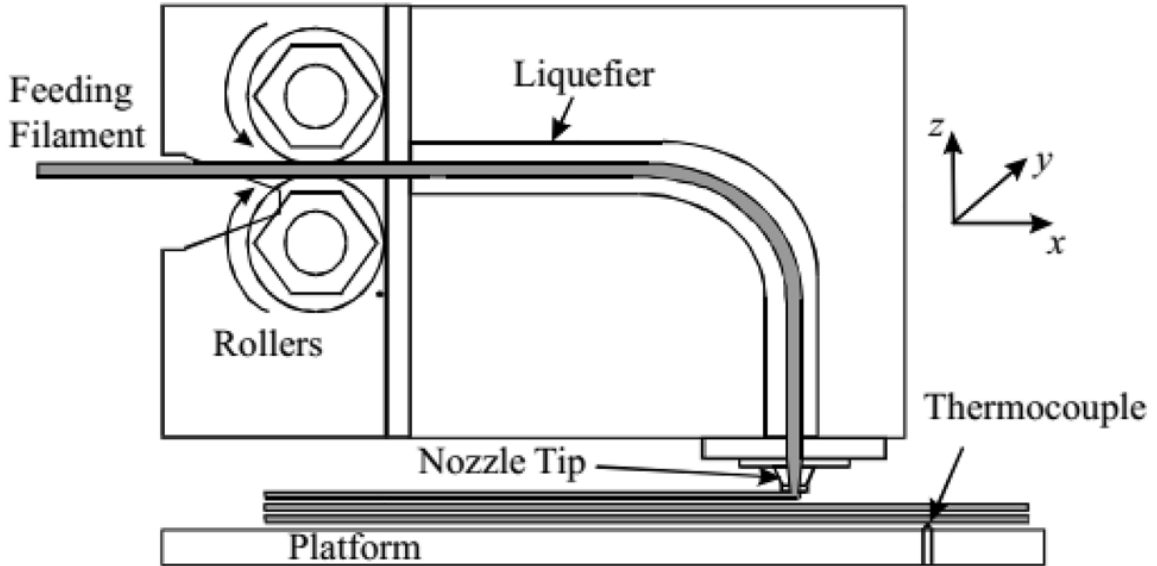


Figure 7.12: Schematic view of a FFF machine, after [133].

Once the material is deposited in liquid form, it starts immediately to solidify, bonding with the substrate or previously deposited material. Repeating this process layer-by-layer, the part is built up. Printing parameters (*e.g.* layer height, nozzle, print-bed temperature, trace width) and possible geometries depend on the material used, which can be a polymer, pure or charged with fillers and fibers.

The cold spray process is a possible solution for the metallization of FFF parts, to apply a conductive coating to protect the part from wear. Taking advantage of the results exposed in the rest of this thesis, LPCS was chosen as the most promising

technique. One of the partners involved in this thesis provided PA66 samples manufactured by FFF, with a complex shape, different surface topographies and numbers of layers. Each face of the sample presents a particular feature, as illustrated in Figure 7.13. The following six topographies can be listed:

- flat on the building platform;
- flat on the top;
- vertical on the side;
- 30° positive (stair effect);
- 30° negative (overhang);
- channel aspect.

Moreover, different printing parameters are used:

- thickness layer: 0.1, 0.125;
- number on contour and top/bottom layers: 1, 2, 3 and 4.

Not every combination of topography and printing parameters was systematically tested in cold spray. Instead, only some trials were performed, to benchmark the cold spray process as a metallization technique for FFF parts. It is particularly challenging to spray on those surfaces, because of the sudden changes in height, slope and shapes. As a consequence, the stand-off distance changes continuously, making it more difficult for the particles to adhere to the surface.

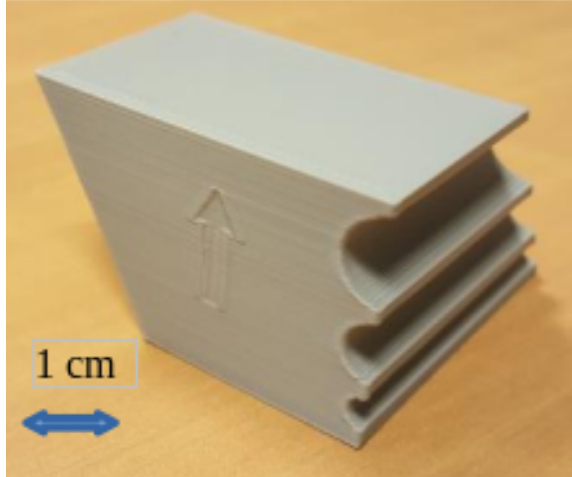


Figure 7.13: Sample produced by FFF to test different surfaces features.

To better cope with the special shape of the specimens, the LPCS gun was not mounted on the robot but kept by hand. Aluminum was chosen as a feed-stock powder, because it was already assessed onto PA66 substrates, as reported for example in [134]. Several tests with pure aluminum and mixtures of aluminum and 10% vol PEEK. Pressure was set at 0.6 MPa and the temperature range between 250 and 400 was explored, with the aim of obtaining a coating and avoiding damage of the PA66.

Due to limited time for these experiments, only uncharged samples (pure PA66) were tested. The results are very encouraging. A coating could be deposited onto all six different surfaces. Particles penetrated into the substrate material, creating at least a first layer on all the surfaces. On the flatter surfaces, a coating with a thickness of about $500\mu m$ was obtained, as shown in Figure 7.14.

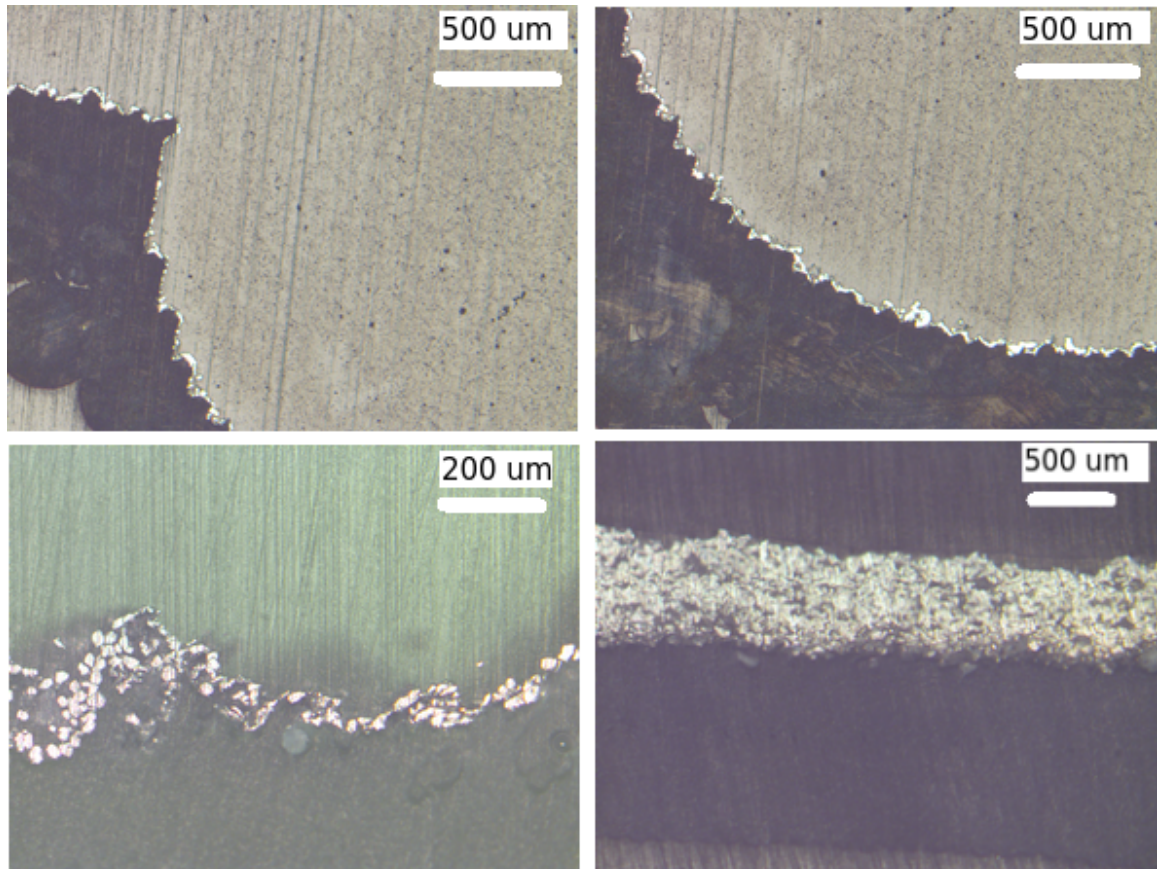


Figure 7.14: Optical microscope cross section of an aluminum sprayed PA66 samples.

Pull-off adhesion tests were performed to assess variations of the adhesion strength among the different surfaces. The only one that could not be tested is the channeled one, where the pin could not be glued. The results are presented in Figure 7.16. On the x axis, the labels 1-5 refer to the following surfaces: 1 is the flat top surface, 2 is the flat on the building platform, 3 is the vertical on the side surface, 4 is the 30° positive (stair effect), 5 is the 30° negative (overhang). The failure was always adhesive, *i.e.* taking place between the coating and the substrate, as shown for example in Figure 7.15. Rather, the measured adhesion strengths are dispersed. It must be noticed that the manual utilization of the LPCS gun did not allow for precise control of certain parameters, as the spraying distance and the gun speed. The results are very encouraging, with an average value of more than 1 MPa.



Figure 7.15: Photographic images of the pull-off test. On the left, sample preparation with all the pins glued to the metallized surfaces. On the right, the adhesive failure of an aluminum-PEEK coating.

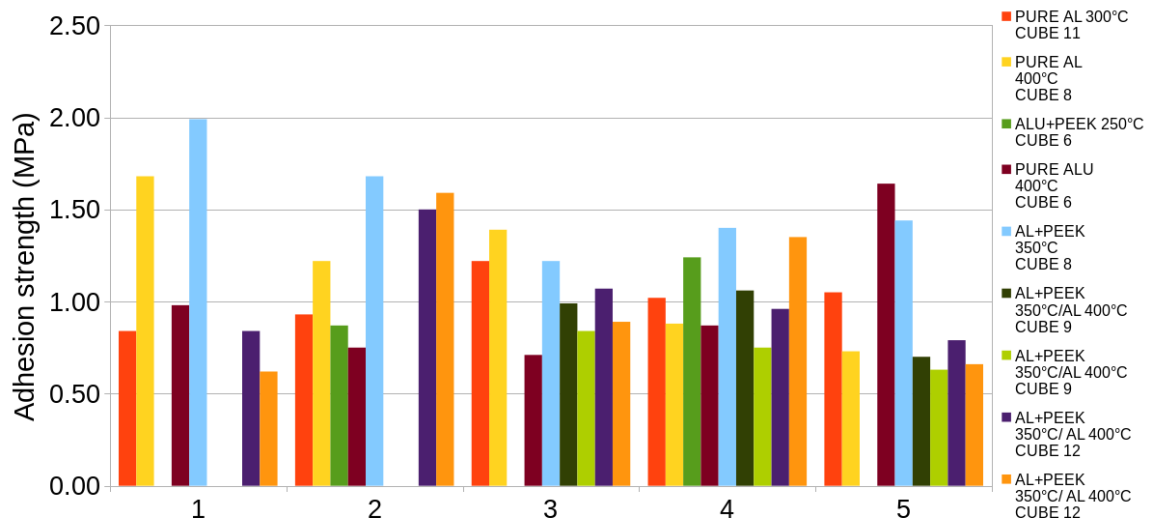


Figure 7.16: Adhesion strength results for 9 different specimens and spraying parameters.

The best values are given by aluminum sprayed at 400°C and by the mixture of aluminum and 10% vol PEEK, sprayed at 350° C. Further cold spray tests must be envisaged to improve these results and fiber reinforced PA66 samples should be realized and tested. Conductivity measurements should also be carried out for each surface topography.

CHAPTER 8

CONCLUSION AND PERSPECTIVES

8.1 Conclusion

The results presented in this work showed the possibility to create conductive coatings onto composite and thermo-sensitive materials by means of the cold spray technology. Several steps have been taken in order to experimentally assess the conductivity and adhesion of these coatings. Moreover, the involved phenomena have been investigated by numerical simulations. A metal powder was obviously the only choice in order to have a conductive layer onto a polymer based composite. Thermo-sensitivity of the polymeric matrix, together with the brittleness of the fibers, needed an opportune choice of cold spray parameters. In chapter 1 a state-of-the-art of cold spray process, particularly in the case of thermo-sensitive substrates, was reported. All the materials and the methods adopted in this work have been presented in chapter 2. In chapter 3, an extensive series of cold spray experiments was presented. Short carbon fiber reinforced PEEK was the substrate. Aluminium powder has been chosen as coating material, because of its high conductivity and low weight properties. Both HPCS and LPCS were used to assess the differences between the two equipments. Experimental tests revealed that LPCS was more effective compared to HPCS in producing coatings onto thermo-sensitive substrates, due to the combined effect of high temperature and low velocity particles as well as the gas temperature at impact. In effect, PEEK is a thermoplastic polymer and it becomes softer when its glass transition temperature is overcome. Particles can then penetrate further into the substrate, with improved mechanical anchoring. HPCS particles instead are faster and colder. In this case, PEEK acts as a brittle material, being eroded by particle impacts. Short carbon

fibers are hit and damaged as well. The strategy to add a percentage of PEEK particles to the aluminum powder improved considerably the deposition efficiency and the adhesion strength. The drawback was the reduction in coating conductivity. A trade-off has been found with a percentage of 10 %. In chapter 4, a CFD analysis of the two cold spray systems was conducted, implementing an Eulerian-Euleria bi-phase model in OpenFOAM software. Particle velocity and temperature were computed and a comparison with experimental measurements was possible for LPCS. The predicted velocity slightly differed from the measured one. For HPCS, only the gas phase was modeled, revealing that gas temperature drops along the nozzle and is close to ambient at impact. In LPCS with a rectangular section insert, the gas detaches in the middle of the nozzle starting to decelerate and to reheat. The final temperature reaches the inlet temperature value. Thus, particles impact at low speed (about 300 m/s) and high temperature. This could explain the better behaviour of LPCS onto the composite. The experimental velocity values in the case of HPCS and the computed velocity and temperature values in the case of LPCS were used as initial conditions for the particle impact simulations developed in chapter 5. An explicit analysis, either in full Eulerian or coupled Eulerian-Lagrangian framework, was chosen. A set of different cases encountered during the experimental phase were simulated. Single particle impacts of aluminium onto a pure PEEK and onto a composite substrate helped to understand the differences in the case of fiber reinforcement. In the latter, particles penetrate less because of the increased rigidity of the substrate. In HPCS, fibers underwent more stress than in LPCS. A thicker PEEK top layer prevented particles from reaching the fibers and facilitated their penetration, increasing the mechanical anchoring. Furthermore, the spraying of a metal-polymer powder mixture was studied by multi-particle simulations. When an aluminium particle follows a PEEK one, the impact is damped, the fibers protected and the mechanical anchoring increased. When, on the contrary, a PEEK particle impacts onto an aluminium

one, if its temperature is high enough, the first covers the latter, trapping it onto the substrate. This mechanism can increase the adhesion strength of the composite coating. Finally, in a simulation with more than thirty particles, PEEK particles under the effect of aluminium ones hammering and due to the high temperature, reach a quasi-melting state. This allows the creation of a PEEK layer embedding aluminium particles, providing adhesion strength but limiting conductivity. In the last chapter a potential industrial application was presented, which is the replacement of some metal components in the airplane air conditioning system by means of composite ones. Then, the extension of the process to other substrate materials was studied. First, the cold spray process was used to coat wooden substrates. Several metals were successfully sprayed onto four different wooden species. The multiscale structure of the wood was studied to better understand bonding mechanisms. This analysis showed that results depended on the surface type and on the species. Promising results were obtained for diffuse ring porous species, such as the walnut and the sycamore. Moreover, the transverse surface was more apt for receiving a cold spray coating, due to the filling of vessels and fibers by particles. Numerical simulations were also presented, showing a stiffness increase due to the folding of fibers. This exploratory work may open the way to new perspectives for the wood industries and cabinet makers, among which innovative aesthetic effects, anti-weathering properties and the possibility of assembling metal and wood without any glue. To conclude, the cold spray was applied to PA66 substrates produced by 3D printing. LPCS was revealed to be capable of producing aluminium and aluminium-PEEK coatings onto a variety of different surface morphologies. Adhesion strength measurements confirmed that an adherent coating can be produced on these samples, showing the possibility of joining 3D printing and cold spray to produce complex and conductive parts.

8.2 Perspectives

Cold spray is a very versatile process. The number of possibilities for both feed-stock powders and substrates is one of the most valuable features of this technique. In this work the final goal was to produce a conductive layer onto thermo-sensitive substrate and this task was completely fulfilled. Composite aluminium-PEEK coating offers an original solution for the creation of adherent and conductive coatings. To go further in the work started in this thesis, a coating with a composition gradient can be envisaged. The first layer rich in PEEK could increase the adhesion onto the composite substrate and protect the carbon fibers. A top pure aluminium layer will assure a conductivity value close to one of the bulk aluminium. For what concerns the different behaviour between HPCS and LPCS, further development in the model is necessary to include all the important phenomena involved in the process. In particular, drag models including both turbulence and compressibility terms should be implemented and validated by means of experimental measurements of particle speed. If particle speed is experimentally accessible, as shown for example by the shadowgraphy methodology in this thesis, an important work is needed for the characterization of particle temperature. On the modeling side, new heat transfer models should be envisaged for the correct estimation of particle temperature. Experimental tests with fast thermal cameras should be carried out to obtain precious measurements and model validation. Accurate knowledge of the particle state at impact is, in effect, the starting point for particle impact simulations. In this field, constitutive models more suitable for polymers should be adopted, keeping into account the particular behavior of these materials in high temperature and dynamic conditions. Moreover, fiber modeling at the microscale should be envisaged to study the conditions bringing to their damage or debonding from the matrix. With an improved knowledge of the cold spray process on thermo-sensitive substrates, new materials could be coated. The

exploratory work presented here on wooden substrates and 3D printed parts should be followed by new tests and numerical simulations.

Résumé en français

Les résultats présentés dans ce travail ont montré la possibilité de créer des revêtements conducteurs sur des matériaux composites et thermosensibles au moyen de la technologie de projection à froid. Plusieurs étapes ont été réalisées afin d'évaluer expérimentalement la conductivité et l'adhérence de ces revêtements. De plus, les phénomènes impliqués ont été étudiés par des simulations numériques. Une poudre métallique était manifestement le seul choix possible pour obtenir une couche conductrice sur un composite à base de polymère. La thermosensibilité de la matrice polymère, ainsi que la fragilité des fibres, ont nécessité un choix judicieux des paramètres de projection à froid. Le chapitre 1 présente un état de l'art du procédé de projection à froid, en particulier dans le cas de substrats thermosensibles. Tous les matériaux et les méthodes adoptés dans ce travail ont été présentés dans le chapitre 2. Dans le chapitre 3, une série extensive d'expériences de projection à froid a été présentée. Le substrat était du PEEK renforcé par des fibres de carbone courtes. La poudre d'aluminium a été choisie comme matériau de revêtement, en raison de ses propriétés de haute conductivité et de faible poids. Le HPCS et le LPCS ont été utilisés pour évaluer les différences entre les deux équipements. Les tests expérimentaux ont révélé que le LPCS était plus efficace que le HPCS pour produire des revêtements sur des substrats thermosensibles, en raison de l'effet combiné de la haute température et de la faible vitesse des particules ainsi que de la température du gaz à l'impact. En effet, le PEEK est un polymère thermoplastique et il devient plus mou lorsque sa température de transition vitreuse est dépassée. Les particules peuvent alors pénétrer plus profondément dans le substrat, avec un meilleur ancrage mécanique. Les particules HPCS, au contraire, sont plus rapides et plus froides. Dans ce cas, le PEEK se comporte comme

un matériau fragile, érodé par les impacts des particules. Les fibres de carbone sont également touchées et endommagées. La stratégie consistant à ajouter un pourcentage de particules de PEEK à la poudre d'aluminium a considérablement amélioré l'efficacité du dépôt et la force d'adhérence. L'inconvénient était la réduction de la conductivité du revêtement. Un compromis a été trouvé avec un pourcentage de 10 %. Dans le chapitre 4, une analyse CFD des deux systèmes de projection à froid a été réalisée, en implémentant un modèle biphasé Eulerian-Euleria dans le logiciel OpenFOAM. La vitesse et la température des particules ont été calculées et une comparaison avec les mesures expérimentales a été possible pour le LPCS. La vitesse prédite différait légèrement de celle mesurée. Pour le HPCS, seule la phase gazeuse a été modélisée, révélant que la température du gaz chute le long de la buse et est proche de la température ambiante à l'impact. Dans le cas du LPCS avec insert à section rectangulaire, le gaz se détache au milieu de la buse et commence à décélérer et à se réchauffer. La température finale atteint à nouveau la valeur de la température d'entrée. Ainsi, l'impact des particules se fait à faible vitesse (environ 300 m/s) et à haute température. Cela pourrait expliquer le meilleur comportement des LPCS sur le composite. Les valeurs de vitesse expérimentales dans le cas du HPCS et les valeurs de vitesse et de température calculées dans le cas du LPCS ont été utilisées comme conditions initiales pour les simulations d'impact de particules développées dans le chapitre 5. Une analyse explicite, soit dans un cadre eulérien complet, soit dans un cadre couplé eulérien-lagrangien, a été choisie. Un ensemble de différents cas rencontrés lors de la phase expérimentale ont été simulés. Les impacts de particules uniques d'aluminium sur un PEEK pur et sur un substrat composite ont permis de comprendre les différences de renforcement des fibres. Dans ce dernier, les particules pénètrent moins en raison de la rigidité accrue du substrat. Dans le HPCS, les fibres subissent plus de contraintes que dans le LPCS. Une couche supérieure en PEEK plus épaisse a empêché les particules d'atteindre les fibres et a facilité leur pénétration,

augmentant ainsi l'ancrage mécanique. Par ailleurs, la projection d'un mélange de poudre métal-polymère a été étudiée par des simulations multi-particules. Lorsqu'une particule d'aluminium suit une particule de PEEK, l'impact est amorti, les fibres protégées et l'ancrage mécanique augmenté. Lorsque, au contraire, une particule de PEEK percute une particule d'aluminium, si sa température est suffisamment élevée, la première recouvre la seconde, la piégeant sur le substrat. Ce mécanisme peut augmenter la force d'adhésion du revêtement composite. Enfin, dans une simulation avec plus de trente particules, les particules de PEEK, sous l'effet du martèlement de celles d'aluminium et en raison de la température élevée, atteignent un état de quasi-fusion. Ceci permet la création d'une couche de PEEK enrobant les particules d'aluminium, fournissant une force d'adhésion mais limitant la conductivité. Dans le dernier chapitre, une application industrielle potentielle a été présentée, à savoir le remplacement de certains composants métalliques du système de climatisation d'un avion par des composants composites. Ensuite, l'extension du procédé à d'autres matériaux de substrat a été étudiée. Tout d'abord, le procédé de projection à froid a été utilisé pour revêtir des substrats en bois. Plusieurs métaux ont été pulvérisés avec succès sur quatre espèces de bois différentes. La structure multi-échelle du bois a été étudiée pour mieux comprendre les mécanismes de liaison. Cette analyse a montré que les résultats dépendaient du type de surface et de l'essence. Des résultats prometteurs ont été obtenus pour les espèces poreuses à anneau diffus, comme le noyer et le sycomore. De plus, la surface transversale était plus apte à recevoir un revêtement par projection à froid, en raison du remplissage des vaisseaux et des fibres par les particules. Des simulations numériques ont également été présentées, montrant une augmentation de la rigidité due au pliage des fibres. Ce travail exploratoire peut ouvrir la voie à de nouvelles perspectives pour les industries du bois et les ébénistes, parmi lesquelles des effets esthétiques innovants, des propriétés anti-corrosion et la possibilité d'assembler métal et bois sans colle. Enfin, la projection à froid a été

appliquée sur un substrat PA66 produit par impression 3D. Le LPCS s’est révélé capable de produire des revêtements en aluminium et en aluminium-PEEK sur une variété de morphologies de surface différentes. Les mesures de la force d’adhérence ont confirmé qu’un revêtement adhérent peut être produit sur ces échantillons, ce qui montre la possibilité de combiner l’impression 3D et la projection à froid pour produire des pièces complexes et conductrices. La projection à froid est un procédé très polyvalent. Le nombre de possibilités pour les poudres et les substrats est l’une des caractéristiques les plus précieuses de cette technique.

Dans ce travail, l’objectif final était de produire une couche conductrice sur un substrat thermosensible et cette tâche a été entièrement remplie. Le revêtement composite aluminium-PEEK offre une solution originale pour la création de couches adhérentes et conductrices. Pour aller plus loin dans le travail entamé dans cette thèse, un revêtement avec un gradient de composition peut être envisagé. Une première couche riche en PEEK pourrait augmenter l’adhérence sur le substrat composite et protéger les fibres de carbone. Une couche supérieure en aluminium pur assurera une valeur de conductivité proche de celle de l’aluminium massif. En ce qui concerne les différences de comportement entre HPCS et LPCS, des développements supplémentaires du modèle sont nécessaires pour inclure tous les phénomènes importants impliqués dans le processus. En particulier, des modèles de traînée comprenant à la fois des termes de turbulence et de compressibilité devraient être mis en œuvre et validés au moyen de mesures expérimentales de la vitesse des particules. Si la vitesse des particules est accessible expérimentalement, comme le montre par exemple la méthodologie de la shadowgraphie dans cette thèse, un travail important est nécessaire pour la caractérisation de la température des particules. Du côté de la modélisation, de nouveaux modèles de transfert de chaleur devraient être envisagés pour une estimation correcte de la température des particules. Des tests expérimentaux avec des caméras thermiques rapides devraient être réalisés pour obtenir des mesures

précieuses et valider les modèles. La connaissance précise de l'état des particules à l'impact est, en effet, le point de départ des simulations d'impact de particules. Dans ce domaine, des modèles constitutifs plus adaptés aux polymères devraient être adoptés, en tenant compte du comportement particulier de ces matériaux à haute température et dans des conditions dynamiques. De plus, la modélisation des fibres à l'échelle microscopique devrait être envisagée pour étudier les conditions amenant à leur endommagement ou à leur décollement de la matrice. Avec une meilleure connaissance du procédé de projection à froid sur des substrats thermosensibles, de nouveaux matériaux pourraient être revêtus. Les travaux exploratoires présentés ici sur des substrats en bois et des pièces imprimées en 3D devraient être suivis de nouveaux tests et de simulations numériques.

REFERENCES

- [1] Anatolii Papyrin et al. *Cold Spray Technology*. Elsevier, 2007.
- [2] Surinder Singh et al. “Influence of Cold Spray Parameters on Bonding Mechanisms: A Review”. In: *Metals* 11.12 (2021).
- [3] S. Kumar, M. Kumar, and Jindal. “Overview of cold spray coatings applications and comparisons: a critical review”. In: *World Journal of Engineering* 17.1 (2020).
- [4] NV Nayak. “Composite materials in aerospace applications”. In: *International Journal of Scientific and Research Publications* 4 (Sept. 2014).
- [5] Kumar Sardiwal et al. “Advanced Composite Materials in Typical Aerospace Applications”. In: *Global Journal of Research In Engineering* 14 (2014).
- [6] S Du. “Advanced composite materials and aerospace engineering”. In: *Acta Mater. Compos. Sin.* 24 (2007).
- [7] A.P Mouritz et al. “Review of advanced composite structures for naval ships and submarines”. In: *Composite Structures* 53.1 (2001), pp. 21–42.
- [8] Brigitte Zimmerli et al. “Composite materials: composition, properties and clinical applications. A literature review.” In: *Schweizer Monatsschrift für Zahnmedizin = Revue mensuelle suisse d’odonto-stomatologie = Rivista mensile svizzera di odontologia e stomatologia* 120 11 (2010), pp. 972–86.
- [9] Andrzej Katunin et al. “Electrically conductive carbon fibre-reinforced composite for aircraft lightning strike protection”. In: *IOP Conference Series: Materials Science and Engineering* 201 (May 2017), p. 012008.
- [10] D Rosato. *Designing with plastics and composites: a handbook*. Springer Science Business Media, 2013.
- [11] Hirohide Kawakami and Paolo Feraboli. “Lightning strike damage resistance and tolerance of scarf-repaired mesh-protected carbon fiber composites”. In: *Composites Part A: Applied Science and Manufacturing* 42.9 (2011), pp. 1247–1262.
- [12] E. Rupke. *Lightning Direct Effects Handbook*. Lightning Technologies Inc., 2002.

- [13] J.A. Plumer F.A. Fisher. *Aircraft Lightning Protection Handbook*. FEDERAL AVIATION ADMINISTRATION TECHNICAL CENTER, 1989.
- [14] J.M. Welch. *Repair design, test and process considerations for lightning strikes*. 3rd FAA/EASA/Boeing/Airbus Joint Workshop on Safety and Certification, Federal Aviation Administration, 1989.
- [15] L. Chemartin et al. “Direct Effects of Lightning on Aircraft Structure: Analysis of the Thermal, Electrical and Mechanical Constraints”. In: 5 (Dec. 2012).
- [16] Hasim Mulazimoglu. “Recent Developments in Techniques to Minimize Lightning Current Arcing Between Fasteners and Composite Structure”. In: 2011.
- [17] Bangwei Zhang et al. “Galvanic corrosion of Al/Cu meshes with carbon fibers and graphene and ITO-based nanocomposite coatings as alternative approaches for lightning strikes”. In: *The International Journal of Advanced Manufacturing Technology* 67 (July 2012).
- [18] S. Celotto et W. O’Neill A. Sturgeon B. Dunn. “Cold spray coatings for polymer composite substrates”. In: *10th International Symposium on Materials in a Space Environment and The 8th International Conference on Protection of Materials and Structures in a Space Environment, ESA SP 616*. 2006.
- [19] R. Lupoi and W. O’Neill. “Deposition of metallic coatings on polymer surfaces using cold spray”. In: *Surface and Coatings Technology* 205.7 (2010), pp. 2167–2173.
- [20] X.L. Zhou et al. “Preparation of metallic coatings on polymer matrix composites by cold spray”. In: *Surface and Coatings Technology* 206.1 (2011), pp. 132–136.
- [21] Jon Affi et al. “Fabrication of Aluminum Coating onto CFRP Substrate by Cold Spray”. In: *MATERIALS TRANSACTIONS* 52 (Aug. 2011), 1759 to 1763.
- [22] Amirthan Ganesan, Motohiro Yamada, and Masahiro Fukumoto. “Cold Spray Coating Deposition Mechanism on the Thermoplastic and Thermosetting Polymer Substrates”. In: *Journal of Thermal Spray Technology* 22 (2013), pp. 1275–1282.
- [23] Hanqing Che et al. “Metallization of Various Polymers by Cold Spray”. In: *Journal of Thermal Spray Technology* 27.1 (Jan. 2018), pp. 169–178.

- [24] V. Gillet et al. “Development of low pressure cold sprayed copper coatings on carbon fiber reinforced polymer (CFRP)”. In: *Surface and Coatings Technology* 364 (2019), pp. 306–316.
- [25] M. R. Rokni et al. “Depositing Al-Based Metallic Coatings onto Polymer Substrates by Cold Spray”. In: *Journal of Thermal Spray Technology* 28.7 (Oct. 2019), pp. 1699–1708.
- [26] Vincent Bortolussi et al. “Cold spray of metal-polymer composite coatings onto carbon fiber-reinforced polymer (CFRP)”. In: (2016).
- [27] L.J. Van der Pauw. “A Method of Measuring Specific Resistivity and Hall Effect of Discs of Arbitrary Shape”. In: 13 (1958), pp. 1–9.
- [28] E. P. Mamunya, V. V. Davidenko, and E. V. Lebedev. “Percolation conductivity of polymer composites filled with dispersed conductive filler”. In: *Polymer Composites* 16.4 (1995), pp. 319–324. eprint: <https://onlinelibrary.wiley.com/doi/pdf/10.1002/pc.750160409>.
- [29] R C McCune et al. “An exploration of the cold gas-dynamic spray method for several materials systems”. In: (Dec. 1995).
- [30] R. C. Dykhuizen and M. F. Smith. “Gas dynamic principles of cold spray”. In: *Journal of Thermal Spray Technology* 7.2 (June 1998), pp. 205–212.
- [31] Shuol Yin et al. “Gas Flow, Particle Acceleration, and Heat Transfer in Cold Spray: A review”. In: *Journal of Thermal Spray Technology* 25.5 (June 2016), pp. 874–896.
- [32] A. P. Alkhimov, V. F. Kosarev, and S. V. Klinkov. “The features of cold spray nozzle design”. In: *Journal of Thermal Spray Technology* 10.2 (June 2001), pp. 375–381.
- [33] V. F. Kosarev et al. “On some aspects of gas dynamics of the cold spray process”. In: *Journal of Thermal Spray Technology* 12.2 (June 2003), pp. 265–281.
- [34] B. Samareh et al. “Assessment of CFD Modeling via Flow Visualization in Cold Spray”. In: *Journal of Thermal Spray Technology* 18 (Dec. 2009), pp. 934–943.
- [35] Champagne VK et al. “Theoretical and Experimental Particle Velocity in Cold Spray”. In: *Journal of Thermal Spray Technology* 20 (2011), pp. 425–431.
- [36] R.N. Raelison et al. “Turbulences of the supersonic gas flow during cold spraying and their negative effects: A DNS CFD analysis coupled with experi-

- mental observation and laser impulse high-speed shadowgraphs of the particles in-flight flow”. In: *International Journal of Heat and Mass Transfer* 147 (2020), p. 118894.
- [37] N. Zuckerman and N. Lior. “Jet Impingement Heat Transfer: Physics, Correlations, and Numerical Modeling”. In: 39 (2006), pp. 565–631.
 - [38] Muhammad Faizan Ur Rab et al. “Development of 3D Multicomponent Model for Cold Spray Process Using Nitrogen and Air”. In: *Coatings* 5.4 (2015), pp. 688–708.
 - [39] Saden H. Zahiri et al. “Development of Holistic Three-Dimensional Models for Cold Spray Supersonic Jet”. In: *Journal of Thermal Spray Technology* 23 (2014), pp. 919–933.
 - [40] Muhammad Faizan-Ur-Rab et al. “3D CFD Multicomponent Model for Cold Spray Additive Manufacturing of Titanium Particles”. In: *CFD Modeling and Simulation in Materials Processing 2016*. Ed. by Laurentiu Nastac et al. Cham: Springer International Publishing, 2016, pp. 213–220. ISBN: 978-3-319-65133-0.
 - [41] O. C. Ozdemir and C. A. Widener. “Influence of Powder Injection Parameters in High-Pressure Cold Spray”. In: *Journal of Thermal Spray Technology* 26 (2017), 1411–1422.
 - [42] A. Sova et al. “Deposition of aluminum powder by cold spray micronozzle”. In: *The International Journal of Advanced Manufacturing Technology* 95.9 (Apr. 2018), pp. 3745–3752.
 - [43] W. E. Ranz and W. R. Marshall. “Evaporation from drops”. In: *Chemical Engineering Progress* 48.3 (1952), pp. 141–146.
 - [44] K.-H. Leitz et al. “OpenFOAM Modeling of Particle Heating and Acceleration in Cold Spraying”. In: *Journal of Thermal Spray Technology* 27.1 (Jan. 2018), pp. 135–144.
 - [45] H. G. Weller et al. “A tensorial approach to computational continuum mechanics using object-oriented techniques”. In: *Computers in Physics* 12.6 (1998), pp. 620–631.
 - [46] L. Schiller and A. Naumann. “Unungen bei der Schwerkraftaufbereitungs”. In: *Zeitschrift des Vereins Deutscher Ingenieure* 77 (1935), 318–320.
 - [47] L. Schiller and A. Naumann. “Fluid Flow Through Packed Columns”. In: *Chemical Engineering Progress* 48 (1952), pp. 89–94.

- [48] A. Haider and O. Levenspiel. “Drag coefficient and terminal velocity of spherical and nonspherical particles”. In: *Powder Technology* 58.1 (1989), pp. 63–70.
- [49] J. Prieur Du Plessis and Jacob H. Masliyah. “Mathematical modelling of flow through consolidated isotropic porous media”. In: *Transport in Porous Media* 3.2 (Apr. 1988), pp. 145–161.
- [50] “Front Matter”. In: *Theory of Elasticity and Stress Concentration*. John Wiley Sons, Ltd, 2016, pp. i–xxvi. ISBN: 9781119274063. eprint: <https://onlinelibrary.wiley.com/doi/pdf/10.1002/9781119274063.fmatter>.
- [51] Wenya li et al. “Modelling of impact behaviour of cold spray particles: Review”. In: *Surface Engineering* 30 (June 2014), pp. 299–308.
- [52] M Grujicic et al. “Adiabatic shear instability based mechanism for particles/substrate bonding in the cold-gas dynamic-spray process”. In: *Materials Design* 25.8 (2004), pp. 681–688.
- [53] Wenya li et al. “Modeling Aspects of High Velocity Impact of Particles in Cold Spraying by Explicit Finite Element Analysis”. In: *Journal of Thermal Spray Technology* 18 (May 2009), pp. 921–933.
- [54] Wenya li and Wei Gao. “Some aspects on 3D numerical modeling of high velocity impact of particles in cold spraying by explicit finite element analysis”. In: *Applied Surface Science* 255 (June 2009), pp. 7878–7892.
- [55] Baran Yildirim, Sinan Muftu, and Andrew Gouldstone. “Modeling of high velocity impact of spherical particles”. In: *Wear* 270 (Apr. 2011), pp. 703–713.
- [56] Shuo Yin et al. “Numerical Investigation on Effects of Interactions Between Particles on Coating Formation in Cold Spraying”. In: *Journal of Thermal Spray Technology - J THERM SPRAY TECHNOL* 18 (Dec. 2009), pp. 686–693.
- [57] Shuo Yin et al. “Examination on the Calculation Method for Modeling the Multi-Particle Impact Process in Cold Spraying”. In: *Journal of Thermal Spray Technology* 19 (Sept. 2010), pp. 1032–1041.
- [58] Gang Qiu, Sascha Henke, and Jürgen Grabe. “Application of a Coupled Eulerian–Lagrangian approach on geomechanical problems involving large deformations”. In: *Computers and Geotechnics* 38.1 (2011), pp. 30–39.
- [59] Dassault Systemes. *ABAQUS Analysis User’s Manual, 6.11 ed.* Simulia, Providence, 2011.

- [60] Gang Qiu, Sascha Henke, and Jürgen Grabe. “Application of a Coupled Eulerian-Lagrangian approach on geomechanical problems involving large deformations”. In: *Computers and Geotechnics* 38 (2011), pp. 30–39.
- [61] I. Smojver and D. Ivančević. “Bird strike damage analysis in aircraft structures using Abaqus/Explicit and coupled Eulerian Lagrangian approach”. In: *Composites Science and Technology* 71.4 (2011), pp. 489–498.
- [62] Saeed Rahmati and Bertrand Jodoin. “Physically Based Finite Element Modeling Method to Predict Metallic Bonding in Cold Spray”. In: *Journal of Thermal Spray Technology* 29.4 (Apr. 2020), pp. 611–629.
- [63] M. Nazem, J.P. Carter, and D.W. Airey. “Arbitrary Lagrangian–Eulerian method for dynamic analysis of geotechnical problems”. In: *Computers and Geotechnics* 36.4 (2009), pp. 549–557.
- [64] Jing Xie et al. “Simulation of the Cold Spray Particle Deposition Process”. In: *Journal of Tribology* 137.4 (Oct. 2015). 041101. eprint: https://asmedigitalcollection.asme.org/tribology/article-pdf/137/4/041101/6285630/trib_137_04_041101.pdf.
- [65] Baran Yildirim et al. “On Simulation of Multi-Particle Impact Interactions in the Cold Spray Process”. In: vol. ASME/STLE 2012 International Joint Tribology Conference. International Joint Tribology Conference. Oct. 2012, pp. 83–85.
- [66] Xu Song et al. “Coupled Eulerian-Lagrangian (CEL) simulation of multiple particle impact during Metal Cold Spray process for coating porosity prediction”. In: *Surface and Coatings Technology* 385 (2020), p. 125433.
- [67] Matteo Terrone et al. “A numerical Approach to design and develop free-standing porous structures through cold spray multi-material deposition”. In: *Surface and Coatings Technology* 421 (2021), p. 127423.
- [68] Gordon R. Johnson and W. Howard Cook. “A CONSTITUTIVE MODEL AND DATA FOR METALS SUBJECTED TO LARGE STRAINS, HIGH STRAIN RATES AND HIGH TEMPERATURES”. In: 2018.
- [69] Saeed Rahmati and A. Ghaei. “The Use of Particle/Substrate Material Models in Simulation of Cold-Gas Dynamic-Spray Process”. In: *Journal of Thermal Spray Technology* 23 (Nov. 2013).
- [70] Hopkinson Bertram. “A method of measuring the pressure produced in the detonation of high explosives or by the impact of bullets.” In: *Proc. R. Soc. London* 89 (1914).

- [71] *Combined Laser Shock and Micro-Compression Approach to the Mechanical Behavior of Powders for Cold Spray*. Vol. Thermal Spray 2021: Proceedings from the International Thermal Spray Conference. International Thermal Spray Conference. May 2021, pp. 627–634. eprint: <https://dl.asminternational.org/itsc/proceedings-pdf/ITSC2021/83881/627/487998/itsc2021p0627.pdf>.
- [72] Francesco Delloro et al. “Characterization of mechanical behaviour of aluminum powders under fast dynamic conditions”. In: *European Physical Journal Web of Conferences*. Vol. 250. European Physical Journal Web of Conferences. Sept. 2021, 01036, p. 01036.
- [73] Qian Wang et al. “Development of a material model for predicting extreme deformation and grain refinement during cold spraying”. In: *Acta Materialia* 199 (2020), pp. 326–339.
- [74] G. Regazzoni, U.F. Kocks, and P.S. Follansbee. “Dislocation kinetics at high strain rates”. In: *Acta Metallurgica* 35.12 (1987), pp. 2865–2875.
- [75] S.E. Gad. “Polymers”. In: (2014). Ed. by Philip Wexler, pp. 1045–1050.
- [76] H.-H. Kausch. *Matériaux polymères : propriétés mécaniques et physiques*. PPUR Presses Polytechniques, 2001.
- [77] N. Billon et J.-L. Bouvard. *Propriétés et comportement mécanique des polymères thermoplastiques*. 2015.
- [78] N. Billon. *Chapitre XVII : comportement mécanique des polymères*. 2014.
- [79] Jorgen Bergstrom and Jeffrey Bischoff. “An advanced thermomechanical constitutive model for UHMWPE”. In: *International Journal of Structural Changes in Solids* 2 (Jan. 2010), pp. 31–39.
- [80] David J. Quinn, Jorgen Bergstrom, and Sam Chow. “Development and Experimental Validation of an Advanced Nonlinear, Rate-Dependent Constitutive Model for Polyether Ether Ketone (PEEK)”. In: *Journal of Medical Devices* 7.4 (Dec. 2013).
- [81] Daniel Garcia Gonzalez et al. “Mechanical impact behavior of polyether-etherketone (PEEK)”. In: *Composite Structures* 124 (Jan. 2015), pp. 88–99.
- [82] JS Bergström, CM Rimnac, and SM Kurtz. “Prediction of multiaxial mechanical behavior for conventional and highly crosslinked UHMWPE using a hybrid constitutive model”. In: *Biomaterials* 24.8 (Apr. 2003), 1365—1380.

- [83] A. Maurel-Pantel et al. “A thermo-mechanical large deformation constitutive model for polymers based on material network description: Application to a semi-crystalline polyamide 66”. In: *International Journal of Plasticity* 67 (2015), pp. 102–126.
- [84] Michael J. Kendall and Clive R. Siviour. “Experimentally simulating adiabatic conditions: Approximating high rate polymer behavior using low rate experiments with temperature profiles”. In: *Polymer* 54.18 (2013), pp. 5058–5063.
- [85] Michael J. Kendall, Richard F. Froud, and Clive R. Siviour. “Novel temperature measurement method thermodynamic investigations of amorphous polymers during high rate deformation”. In: *Polymer* 55.10 (2014), pp. 2514–2522.
- [86] D. Garcia-Gonzalez, R. Zaera, and A. Arias. “A hyperelastic-thermoviscoplastic constitutive model for semi-crystalline polymers: Application to PEEK under dynamic loading conditions”. In: *International Journal of Plasticity* 88 (2017), pp. 27–52.
- [87] Nand Kishore Singh et al. “Analyzing the Effects of Particle Diameter in Cold Spraying of Thermoplastic Polymers”. In: *Journal of Thermal Spray Technology* 30.5 (June 2021), pp. 1226–1238.
- [88] Taylor Geoffrey Ingram and Quinney H. “The latent energy remaining in a metal after cold working”. In: *Proc. Roy. Soc.* (1934).
- [89] J C F Millett, N K Bourne, and G T GrayIII. “The response of polyether ether ketone to one-dimensional shock loading”. In: *Journal of Physics D: Applied Physics* 37.6 (Feb. 2004), pp. 942–947.
- [90] Andrew Roberts, Gareth Appleby-Thomas, and Paul Hazell. “Experimental determination of Grüneisen gamma for polyether ether ketone (PEEK) using the shock-reverberation technique”. In: *AIP Conference Proceedings* 1426 (Mar. 2012), pp. 824–827.
- [91] C.A. Bernard et al. “Thermal gradient of in-flight polymer particles during cold spraying”. In: *Journal of Materials Processing Technology* 286 (2020), p. 116805.
- [92] Lukas Scherer. “COLD GAS DYNAMIC SPRAY PROCESS, AN MD SIMULATION SINGLE PARTICLE IMPACT ANALYSIS”. PhD thesis. June 2020.
- [93] Vincent Bortolussi. “Etude expérimentale et numérique de la conductivité de revêtements composites métal-polymère déposés par projection dynamique par gaz froid sur substrat composite à matrice organique”. Theses. Université Paris sciences et lettres, Dec. 2016.

- [94] Mojgan Nejad et al. “Thermal Spray Coating: A New Way of Protecting Wood”. In: *Bioresources* 12 (Jan. 2017), pp. 143–156.
- [95] Pierre-Emmanuel Leger. “Rôle de la microstructure sur les mécanismes de corrosion marine d’un dépôt à base d’aluminium élaboré par projection dynamique par gaz froid (cold spray)”. Thèse de doctorat dirigée par Jeandin, Michel Sciences et génie des matériaux Paris Sciences et Lettres (ComUE) 2018. PhD thesis. 2018.
- [96] ASM Thermal Spray Society and Accepted Practices Committee. “Accepted Practice for Testing Bond Strength of Thermal Spray Coatings”. In: *Thermal Spray Technology: Accepted Practices*. ASM International, June 2022. ISBN: 978-1-62708-428-4. eprint: <https://dl.asminternational.org/book/chapter-pdf/619054/t56040101.pdf>.
- [97] Rogerio Varavallo et al. “Adhesion of Thermally Sprayed Metallic Coating”. In: *Journal of ASTM International* 9 (Feb. 2012), p. 103414.
- [98] Reza Rokni et al. “Depositing Al-Based Metallic Coatings onto Polymer Substrates by Cold Spray”. In: *Journal of Thermal Spray Technology* 28 (Sept. 2019).
- [99] P. Feng, M. R. Rokni, and S. R. Nutt. “Depositing Aluminum onto PEKK Composites by Cold Spray”. In: *Journal of Thermal Spray Technology* 30.1 (Jan. 2021), pp. 385–393.
- [100] Hamid Arastoopour. “Numerical simulation and experimental analysis of gas/solid flow systems: 1999 Fluor-Daniel Plenary lecture”. In: *Powder Technology* 119.2 (2001), pp. 59–67.
- [101] Babak Samareh and Ali Dolatabadi. “Dense Particulate Flow in a Cold Gas Dynamic Spray System”. In: *Journal of Fluids Engineering-transactions of The Asme - J FLUID ENG* 130 (Aug. 2008).
- [102] A. Dolatabadi, J. Mostaghimi, and V. Pershin. “Modeling Dense Suspension of Solid Particles in Highly Compressible Flows”. In: *International Journal of Computational Fluid Dynamics* 18.2 (2004), pp. 125–131. eprint: <https://doi.org/10.1080/10618560310001634221>.
- [103] S.N.P. Vegendla, G.J. Heynderickx, and G.B. Marin. “Comparison of Eulerian–Lagrangian and Eulerian–Eulerian method for dilute gas–solid flow with side inlet”. In: *Computers Chemical Engineering* 35.7 (2011), pp. 1192–1199.
- [104] W.K. Ariyaratne et al. “CFD Approaches for Modeling Gas-Solids Multiphase Flows – A Review”. In: Sept. 2016.

- [105] Yinghui Zhang, Xingying Lan, and Jinsan Gao. “Modeling of gas-solid flow in a CFB riser based on computational particle fluid dynamics”. In: *Petroleum Science* 9.4 (Dec. 2012), pp. 535–543.
- [106] Alireza Abbasi, Paul E. Ege, and Hugo I. de Lasa. “CFD simulation of a fast fluidized bed steam coal gasifier feeding section”. In: *Chemical Engineering Journal* 174.1 (2011), pp. 341–350.
- [107] Xizhong Chen and Junwu Wang. “A comparison of two-fluid model, dense discrete particle model and CFD-DEM method for modeling impinging gas–solid flows”. In: *Powder Technology* 254 (2014), pp. 94–102.
- [108] C. K. K. Lun et al. “Kinetic theories for granular flow: inelastic particles in Couette flow and slightly inelastic particles in a general flowfield”. In: *Journal of Fluid Mechanics* 140 (1984), 223–256.
- [109] Dyrney Araújo dos Santos, Shivam Baluni, and Andreas Bück. “Eulerian Multiphase Simulation of the Particle Dynamics in a Fluidized Bed Opposed Gas Jet Mill”. In: *Processes* 8 (Dec. 2020).
- [110] Louis-Vincent Bouthier and Elie Hachem. *Analysis and comparisons of various models in cold spray simulations : towards high fidelity simulations*. 2020.
- [111] H. Assadi et al. “On Parameter Selection in Cold Spraying”. In: *Journal of Thermal Spray Technology* 20.6 (Dec. 2011), pp. 1161–1176.
- [112] Jintang Li, David J. Mason, and Arun Sadashiv Mujumdar. “A Numerical Study of Heat Transfer Mechanisms in Gas–Solids Flows Through Pipes Using a Coupled CFD and DEM Model”. In: *Drying Technology* 21 (2003), pp. 1839–1866.
- [113] I.C. Kemp, R.E. Bahu, and H.S. Pasley. “MODEL DEVELOPMENT AND EXPERIMENTAL STUDIES OF VERTICAL PNEUMATIC CONVEYING DRYERS”. In: *Drying Technology* 12.6 (1994), pp. 1323–1340.
- [114] J.F Frantz. *Design for fluidization, part 2*. Elsevier, 1962.
- [115] B.E. Launder and D.B. Spalding. “The numerical computation of turbulent flows”. In: *Computer Methods in Applied Mechanics and Engineering* 3.2 (1974), pp. 269–289.
- [116] Florian R. Menter. “Two-equation eddy-viscosity turbulence models for engineering applications”. In: *AIAA Journal* 32 (1994), pp. 1598–1605.

- [117] Simon P. Neill and M. Reza Hashemi. “Chapter 8 - Ocean Modelling for Resource Characterization”. In: *Fundamentals of Ocean Renewable Energy*. Ed. by Simon P. Neill and M. Reza Hashemi. E-Business Solutions. Academic Press, 2018, pp. 193–235. ISBN: 978-0-12-810448-4.
- [118] Lida Zhao, Xiang Wang, and Jingfeng Xu. “Structural design and application analysis of Laval nozzle”. In: *Journal of Physics: Conference Series* 1549 (June 2020), p. 042117.
- [119] Jing Xie et al. “Simulation of the Cold Spray Particle Deposition Process”. In: *Journal of Tribology* 137 (Oct. 2015), pp. 041101–041101.
- [120] Xu Song et al. “Coupled Eulerian-Lagrangian (CEL) simulation of multiple particle impact during Metal Cold Spray process for coating porosity prediction”. In: *Surface and Coatings Technology* 385 (2020), p. 125433.
- [121] *Abaqus Analysis User’s Guide*. Version Version 6.14.x. DS Simulia. 2014. 10 pp. Octobre, 2020.
- [122] Peter King, Saden Zahiri, and Mahnaz Jahedi. “Microstructural Refinement within a Cold-Sprayed Copper Particle”. In: *Metallurgical and Materials Transactions A* 40 (Sept. 2009), pp. 2115–2123.
- [123] V. Lemiale et al. “Temperature and strain rate effects in cold spray investigated by smoothed particle hydrodynamics”. In: *Surface and Coatings Technology* 254 (2014), pp. 121–130.
- [124] Anne-Claire Jeanson et al. “Identification du comportement mécanique dynamique de métaux par un essai d’expansion électromagnétique de tube”. In: (May 2013).
- [125] P. E. Leger et al. “Multiscale Experimental and Numerical Approach to the Powder Particle Shape Effect on Al-Al₂O₃ Coating Build-Up”. In: *Journal of Thermal Spray Technology* 26.7 (Oct. 2017), pp. 1445–1460.
- [126] Quentin Blochet et al. “Effect of the Cold-Sprayed Aluminum Coating-Substrate Interface Morphology on Bond Strength for Aircraft Repair Application”. In: *Journal of Thermal Spray Technology* 26.4 (Apr. 2017), pp. 671–686.
- [127] Yutaka Ishimaru et al. “Physical and mechanical properties of wood after moisture conditioning”. In: *Journal of Wood Science* 47.3 (June 2001), pp. 185–191.
- [128] Franziska Weichelt et al. “ZnO-Based UV Nanocomposites for Wood Coatings in Outdoor Applications”. In: *Macromolecular Materials and Engineering*

295.2 (2010), pp. 130–136. eprint: <https://onlinelibrary.wiley.com/doi/pdf/10.1002/mame.200900135>.

- [129] Özlem Gezici-Koç et al. “Bound and free water distribution in wood during water uptake and drying as measured by 1D magnetic resonance imaging”. In: *Cellulose* 24.2 (Feb. 2017), pp. 535–553.
- [130] Patrizio Lomonaco et al. “Cold spray metal coating of wood for cabinet making applications”. In: *Proceedings of the International Thermal Spray Conference and Exposition* (May 2019).
- [131] A. C. Wiedenhoeft and R. B. Miller. *The structure and function of wood*. R. M. Rowell (ed.), CRC Press, Boca Raton, FL, USA, 2005.
- [132] Trygve Stenrud Nilsen. “Numerical modelling of Wood Microstructure”. Master’s Thesis. Norwegian University of Science and Technology, 2015.
- [133] F. Górski et al. “Experimental Determination of Critical Orientation of ABS Parts Manufactured Using Fused Deposition Modelling Technology”. In: *Journal of Machine Engineering* Vol. 15, No. 4 (2015), pp. 121–132.
- [134] Giraud Damien et al. “Metallization of a polymer using cold spray: Application to aluminum coating of polyamide 66”. In: *Proceedings of the International Thermal Spray Conference* (May 2012).

RÉSUMÉ

Le procédé de projection à froid n'est évalué industriellement que pour l'assemblage de métal sur métal. Néanmoins, il offre plusieurs avantages technologiques par rapport aux autres procédés de projection thermique car il est basé sur l'énergie cinétique plutôt que thermique. Cette caractéristique augmente les possibilités de déposer des revêtements sur des substrats fragiles et thermosensibles, tels que les polymères et les composites à base de polymères. L'objectif principal de cette thèse était de développer des stratégies pour réaliser la métallisation de composites PEEK renforcés de fibres de carbone courtes par projection à froid à haute et basse pression. Les phénomènes impliqués dans un tel processus ont été étudiés. Afin d'augmenter l'adhérence et de réduire la délamination des revêtements en aluminium pur, une stratégie de mélange de poudre a été employée. Des tests d'adhérence par arrachement et des mesures de conductivité électrique ont été effectués pour comprendre l'effet de la teneur en poudre de PEEK dans le mélange. Un modèle de dynamique des fluides a été développé pour mieux comprendre les phénomènes impliqués dans les processus de projection à froid à haute et basse pression. Les mesures expérimentales des vitesses des particules, ainsi que les températures calculées des particules, ont été utilisées comme conditions initiales pour les simulations par éléments finis de l'impact des particules sur le composite. Une approche couplée eulérienne-lagrangienne dans une analyse explicite a été utilisée pour simuler l'impact de particules simples et multiples. Dans la dernière partie de ce travail, quelques applications industrielles ont été mises en avant. En conclusion, ce travail de thèse a fait appel à plusieurs techniques, à la fois expérimentales et numériques, et des approches originales ont été proposées pour étudier et améliorer le processus de projection à froid dans le cas de matériaux substrats thermosensibles et fragiles.

MOTS CLÉS

Projection à froid, PEEK, composite, CFD analyses, CEL simulation d'impact, PA66, Bois.

ABSTRACT

The cold spray process is industrially assessed only for the assembly of metal onto metal. Nevertheless, it offers several technological advantages over the other thermal spray processes because it is based on kinetic rather than thermal energy. This feature increases the possibilities to deposit coatings onto brittle and thermo-sensitive substrates, such as polymer and polymer based composites. The main goal of this PhD thesis was to develop strategies to achieve the metallization of short carbon fiber reinforced PEEK composites by both high pressure and low pressure cold spray. The phenomena involved in such a process were investigated. To increase the adherence and reduce the delamination of pure aluminium coatings, a powder mixing strategy was employed. Pull-off adhesion tests and electrical conductivity measurements were carried out to understand the effect of PEEK powder content in the mixture. A fluid dynamic model was developed to better understand the phenomena involved in both high and low pressure cold spray process. Experimental measurements of particle velocities, together with computed particle temperatures, were used as initial conditions for finite element simulations of particle impact onto the composite. A coupled eulerian-lagrangian approach in an explicit analysis was used to simulate single and multiple particle impact. In the final part of this work, some industrial applications were brought to attention. In conclusion, this PhD work engaged several techniques, both experimental and numerical, and original approaches were proposed to investigate and improve the cold spray process in the case of thermo-sensitive and brittle substrate materials.

KEYWORDS

Cold spray, PEEK, composite, CFD analysis, CEL Impact simulation, PA66, WOOD.